(12)

DTNSRDC-82/035

AD A117740

DTIC FILE COPY

MEASUREMENT OF THE PRESSURE DISTRIBUTION ON TWO MODEL PROPELLERS

DAVID W. TAYLOR NAVAL SHIP RESEARCH AND DEVELOPMENT CENTER

Bethesda, Maryland 20084

MEASUREMENT OF THE PRESSURE DISTRIBUTION ON TWO MODEL PROPELLERS

by

Stuart D. Jessup

APPROVED FOR PUBLIC RELEASE: DISTRIBUTION UNLIMITED

SHIP PERFORMANCE DEPARTMENT
RESEARCH AND DEVELOPMENT REPORT

July 1982

DTNSRDC-82/035

MAJOR DTNSRDC ORGANIZATIONAL COMPONENTS

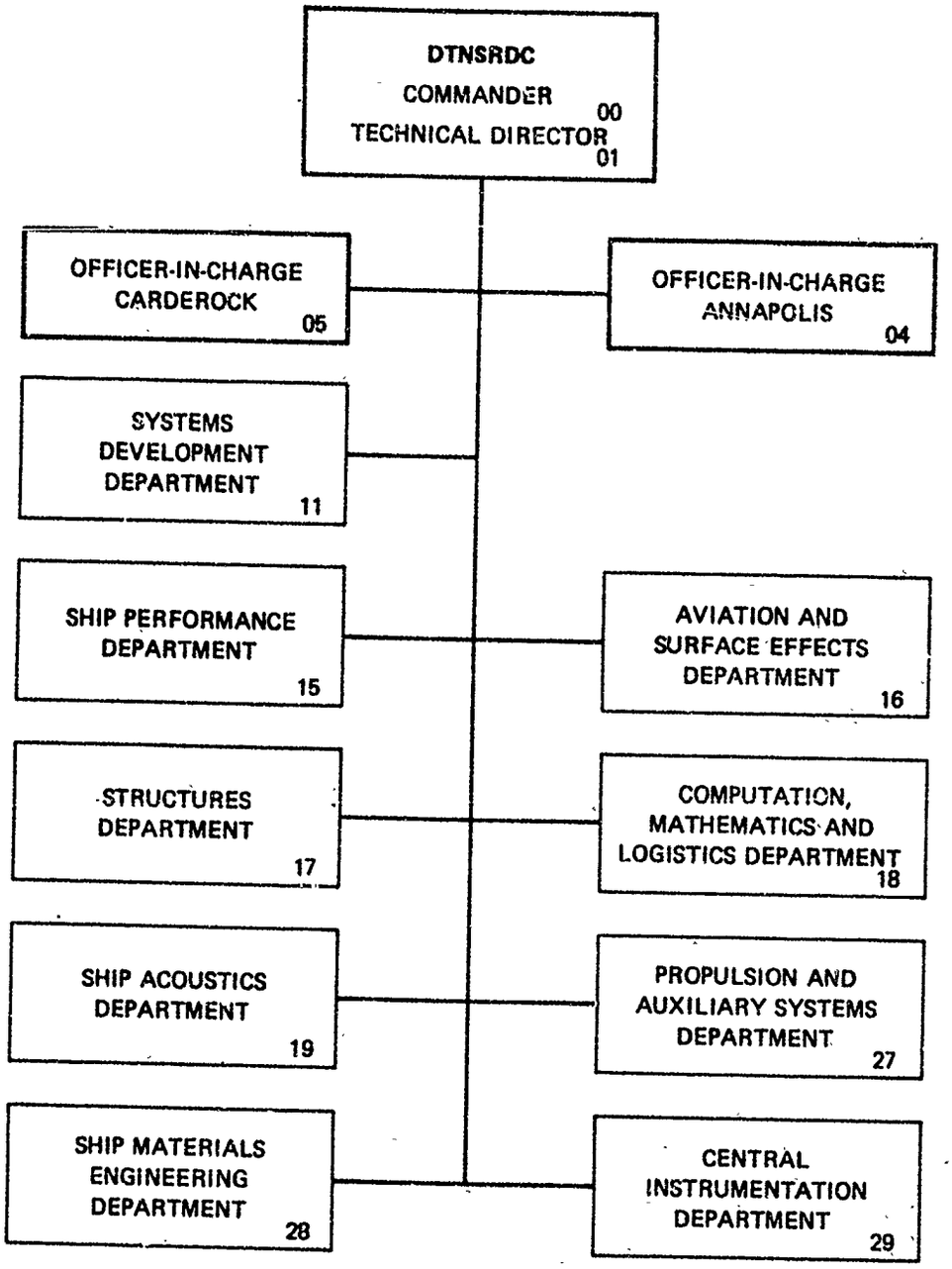

UNCLASSIFIED

SECURITY CLASSIFICATION OF THIS PAGE (When Data Entered)

REPORT DOCUMENTATION PAGE		READ INSTRUCTIONS BEFORE COMPLETING FORM
1 REPORT NUMBER DTNSRDC-82/035	2 GOVT ACCESSION NO. AII7740	3 RECIPIENT'S CATALOG NUMBER
4 TITLE (and Subtitle) MEASUREMENT OF THE PRESSURE DISTRIBUTION ON TWO MODEL PROPELLERS		5 TYPE OF REPORT & PERIOD COVERED Final 6 PERFORMING ORG. REPORT NUMBER
7 AUTHOR(s) Stuart D. Jessup		8 CONTRACT OR GRANT NUMBER(s)
9 PERFORMING ORGANIZATION NAME AND ADDRESS David W. Taylor Naval Ship Research and Development Center Bethesda, Maryland 20084		10 PROGRAM ELEMENT, PROJECT, TASK AREA & WORK UNIT NUMBERS (See reverse side)
11 CONTROLLING OFFICE NAME AND ADDRESS Naval Sea Systems Command (05R) Ship Systems Research and Technology Group Washington, D.C. 20362		12 REPORT DATE July 1982 13 NUMBER OF PAGES 240
14 MONITORING AGENCY NAME & ADDRESS(if different from Controlling Office) Naval Sea Systems Command (524) Propulsion Line, Shafting Equipment Division Washington, D.C. 20362		15 SECURITY CLASS. (of this report) UNCLASSIFIED 15a DECLASSIFICATION/DOWNGRADING SCHEDULE

16 DISTRIBUTION STATEMENT (of this Report)

APPROVED FOR PUBLIC RELEASE: DISTRIBUTION UNLIMITED

17 DISTRIBUTION STATEMENT (of the abstract entered in Block 20, if different from Report)

18 SUPPLEMENTARY NOTES

19 KEY WORDS (Continue on reverse side if necessary and identify by block number)

Marine Propeller
Controllable-Pitch Propeller
Pressure Distribution
Propeller Research
Unsteady Pressure Distribution
Model Experiments

20 ABSTRACT (Continue on reverse side if necessary and identify by block number)

Experiments are described in which the pressure distribution on two model controllable-pitch propellers was measured. The pressure was measured at 40 locations on the blade surface with the propeller operating in both uniform and inclined flow. The discussion of the experimental technique includes a description of the hardware and data analysis systems.

(Continued on reverse side)

DD FORM 1 JAN 73 1473 EDITION OF 1 NOV 65 IS OBSOLETE
S/N 0102-LF-014-6601

UNCLASSIFIED

SECURITY CLASSIFICATION OF THIS PAGE (When Data Entered)

(Block 10)

Task Area S0379-SL001
Task 19977
Work Units 1544-350 and 1544-296

(Block 20 continued)

The accuracy of the measured pressures was comparable to the measured calibration accuracy, excluding unexpected loading effects observed on some of the gages.

The measured mean pressure distributions produced fair correlation with predictions based on equivalent two-dimensional blade-section methods at the design advance coefficient. The measured pressure coefficients at certain blade locations were observed to be dependent upon Reynolds number for a given advance coefficient. Boundary-layer separation is thought to have caused the Reynolds-number effect. These viscous effects were greater than previously anticipated.

The variation of the mean pressure distributions with advance coefficient produced the expected trends. At a given location, C_p generally varied linearly with advance coefficient with increased sensitivity toward the leading edge.

Measurements of the unsteady pressure were performed with the propeller shaft inclined 7.5 degrees to the flow direction. Quasi-steady predictions of the fluctuating pressures underestimated the measured values by 30 percent to 50 percent, but generally followed the measured fluctuation pressure distribution along the chord. Over a range of advance coefficients, the quasi-steady predictions matched the general trends in the measured fluctuating pressures.

TABLE OF CONTENTS

LIST OF FIGURES

LIST OF TABLES

NOTATION

A_E	Expanded area, $\int_{r_h}^{R} c\,dr$
A_o	Disk area of propeller, πR^2
C_D	Drag coefficient of section
C_L	Lift coefficient of section at ideal angle of attack, $L/((1/2)\rho V_L^2 c)$
C_p	Local pressure coefficient, $(p-p_o)/((1/2)\rho V_R^2)$
C_{pL}	Loading pressure coefficient, $\frac{\text{(gage output) (calibration factor)}}{1/2\rho V_R^2}$
C_{PS}	Power coefficient based on ship, speed $P_D/[(\rho/2)\pi R^2 V^3]$
C_{PSI}	Inviscid power coefficient based on ship speed
C_{PTI}	Inviscid thrust power coefficient
C_{Th}	Thrust loading coefficient, $T/((1/2)\rho V_A^2 A_o)$
C_{ThS}	Thrust loading coefficient based on ship speed, $T/((1/2)\rho V^2 A_o)$
C_{ThSI}	Inviscid thrust loading coefficient based on ship speed
c	Section chord length
c_{LE}	Expanded distance from generator axis to leading edge
c_{TE}	Expanded distance from generator axis to trailing edge
D	Propeller diameter
D	Drag of section

E_c	Meanline ordinate of blade section
E_T	Half-thickness ordinate of blade section
F	Factor for estimating local equivalent two-dimensional angles of attack, $1/(1+2\pi\tan(\beta_I-\beta)/C_L)$
f_M	Camber of section
f_{M2D}	Camber required to produce specified lift coefficient at ideal angle of attack in two-dimensional flow
G	Nondimensional circulation, $\Gamma/\pi DV$
g	Acceleration due to gravity
H	Hydrostatic head at local position (absolute)
h	Hydrostatic head at local position minus vapor head
I	Record number, I = 1 to 75
i_G	Blade Rake
J	Advance coefficient, V/nD
L	Local effective lift per unit area, $(1/2)\ \rho\ V_R^2 C_L$
K_Q	Propeller torque coefficient, $K_Q/(\rho n^2 D^5)$
K_T	Propeller thrust coefficient, $K_T/(\rho n^2 D^4)$
k_c	Camber correction factor, f_M/f_{M2D}
N	Gage number, N = 1 to 40
n	Propeller revolutions per unit time
p	Total pressure at local position on blade
P	Propeller section pitch
P_D	Delivered power at propeller, $2\pi nQ$

P_E	Effective power, RV
p_n	nth harmonic amplitude of pressure
p_o	Static pressure at shaft centerline
pL	Measured pressure signal due to loading effects
Q	Quasi-steady loading correction, equivalent to the slope of C versus J curve for a given blade location
R	Propeller radius
R_n	Reynolds number of propeller, based on inflow speed along 0.7 radius $V_{R_{0.7}}$ c/ν
R_T	Total resistance of hull
r	Radial distance
r_h	Radius of hub
T	Propeller thrust
t	Maximum total thickness of blade section
t	Thrust deduction fraction, $(T-R_T)/T$
U_A	Axial induced velocity at lifting line
U_T	Tangential induced velocity at lifting line
V	Ship speed
V_A	Speed of advance of propeller, $V(1-w_T)$
V_c	Carriage speed
V_{L_o}	Inflow velocity corresponding to baseline, design J condition
V_R	Resultant inflow velocity to blade section, $[V^2(1-w_x)^2 + (2\pi nr+V_T)^2]^{1/2}$

V_T	Tangential component of propeller inflow velocity
V_T	Local tangential wake velocity
V_x	Local longitudinal wake velocity
W_H	Wave height
w_T	Taylor wake fraction determined from thrust identity
w_x	Local wake fraction
x	Fraction of chord from leading edge
Y	Blade section offset
Y_{2D}	Blade section offsets adjusted to have the camber producing the required lift coefficient in two-dimensional flow
Z	Number of blades
α	Section equivalent angle of attack in two-dimensional flow
α	Ideal angle of attack required to produce specified lift coefficient in two-dimensional flow
β	Circumferential mean advance angle, $\tan^{-1} [V(1-w_x)/2nr\pi]$
β_I	Hydrodynamic flow angle
Γ	Circulation about blade section
$\Delta\overline{C}_p$	Difference in pressure coefficient across blade, $\overline{C}_p$ on face minus $\overline{C}_p$ on back
η_B	Propeller behind efficiency, TV_A/P_D
η_D	Propulsive efficiency, P_E/P_D
θ	Position angle about propeller axis in propeller plane, measured from vertical upward, positive clockwise looking upstream, in direction of propeller rotation

θ_s Skew angle in the projected plane measured from spindle axis to the radial line through the midchord of the section at the local radius, positive in direction opposite to ahead rotation

ν Kinematic viscosity of water

ρ Mass density of water

ρ_P Mass density of propeller

σ Local cavitation number, $2gh/V_R$

σ_o Cavitation number at shaft centerline, based on speed of advance, $2gh/V_A^2$

ϕ Pitch angle of propeller blade section $\tan^{-1}(P/(2\pi r))$

ϕ_{Ln} nth harmonic phase angle of pressure signal due to loading effects, based on a cosine series

ϕ_n Phase angle of nth harmonic of P based on a cosine series representation,

$$P(r,x,\theta) = \overline{P}(r,x) + \sum_{n=1}^{N} P_n(r,x) \cos(n\theta - \phi_n)$$

ϕ_n^* Phase angle of nth harmonic of P based on a sine series representation,

$$P(r,x,\theta) = \overline{P}(r,x) + \sum_{n=1}^{N} P_n(r,x) \sin(n\theta + \phi_n)$$

ϕ_T Phase angle of nth harmonic of thrust per blade based on a cosine series representation,

$$T(\theta) = \overline{T} + \sum_{n=1}^{N} T_n \cos\left(n\theta - \phi_{T_n}\right)$$

SUBSCRIPTS

avg Average value for two or more experimental runs

cal Value determined during calibration

cor Corrected value

des Design values

exp	Value determined during experiment
h	Value of hub radius
meas	Measured value
n	Value of nth harmonic

SUPERSCRIPTS

–	Time average value per revolution

ABSTRACT

Experiments are described in which the pressure distribution on two model controllable-pitch propellers was measured. The pressure was measured at 40 locations on the blade surface with the propeller operating in both uniform and inclined flow. The discussion of the experimental technique includes a description of the hardware and data analysis systems.

The accuracy of the measured pressures was comparable to the measured calibration accuracy, excluding unexpected loading effects observed on some of the gages.

The measured mean pressure distributions produced fair correlation with predictions based on equivalent two-dimensional blade-section methods at the design advance coefficient. The measured pressure coefficients at certain blade locations were observed to be dependent upon Reynolds number for a given advance coefficient. Boundary-layer separation is thought to have caused the Reynolds-number effect. These viscous effects were greater than previously anticipated.

The variation of the mean pressure distributions with advance coefficient produced the expected trends. At a given location, C_p generally varied linearly with advance coefficient with increased sensitivity toward the leading edge.

Measurements of the unsteady pressure were performed with the propeller shaft inclined 7.5 degrees to the flow direction. Quasi-steady predictions of the fluctuating pressures underestimated the measured values by 30 percent to 50 percent, but generally followed the measured fluctuating pressure distribution along the chord. Over a range of advance coefficients, the quasi-steady predictions matched the general trends in the measured fluctuating pressures.

ADMINISTRATIVE INFORMATION

The work reported herein was funded by the Naval Sea Systems Command (NAVSEA 05R), Task Area S0379-SL001, Task 19977. The work was performed at the David W. Taylor Naval Ship Research and Development Center (DTNSRDC) under Work Units 1544-296 and 1544-350.

INTRODUCTION

With the increasing use of controllable-pitch (CP) propellers for high powered ships,[1,2*] the U.S. Navy has been conducting a research and development (R&D) program to establish the technology for producing reliable CP propellers. The program undertaken at DTNSRDC included:

1. Blade Loading of CP Propellers
   a. Model measurement and theoretical prediction of blade loading on CP propellers
   b. Model and full-scale wake measurements and theoretical predictions of wake
   c. Full-scale measurements of forces, pressures, and strains in CP propellers components.
2. Structural Design of CP Propeller Blade Attachments.
3. Development of Materials for CP Propeller Systems.

The current report presents the results of work conducted under Section 1a of the CP Propeller Research and Development Program, i.e., model measurement and theoretical prediction of blade loading of CP propellers. Work under the other sections of this program will be reported separately.

An accurate estimate of the maximum time-average and alternating loads under all operating conditions is necessary in order to design the blades and pitch-changing mechanisms of high-power CP propellers so that they possess adequate strength with regard to both yield and fatigue stresses. High time-average and alternating loads occur at steady full-power ahead conditions and during high-speed maneuvers, including full-power crash astern, full-power crash ahead, and full-power turns.

The total unsteady and time-average propeller blade loads, as represented by three force components and three moment components, have been evaluated[3-7] in other portions of Section 1a of the CP Propeller R&D program. These results have demonstrated that the currently available analytical techniques substantially underpredict periodic propeller blade loads for operation in inclined flow. However, these available results do not yield significant information on the distribution of the periodic loadings over the blade.

---

*A complete listing of references is given on page 217.

Information on the detailed distribution of loads (or pressures) is necessary in both uniform flow and inclined flow in order to isolate the reasons for the under-prediction of the periodic propeller blade loads in inclined flow and the poor prediction of time-average propeller blade loads at substantially off-design conditions. This further information is necessary in order to provide guidance for improving the analytical predictions. To the author's knowledge, no detailed reliable information of this type is presently available.

A number of attempts to measure the pressure distribution on marine propellers have been reported. These attempts are summarized in Table 1. As outlined in Table 1, several techniques have been used including air or water tubes leading to either manometer tubes[8,9] or remote pressure transducers,[10-16] and pressure transducers[17-18] in the blade including transducers which extend beyond the blade surface, fully-embedded flush-mounted transducers,[19-23] and transducers[24] embedded in cavities in the blades with a small hole to the blade surface. Various experiments have been conducted in wind tunnels, water tunnels, and towing tanks in both uniform flow and circumferentially nonuniform flow.

All of these data have shortcomings of commission or omission, and thus their accuracies are suspect to varying degrees. None of the generally available documentation of pressures measured on marine propeller blades[9-23] describes the experimental procedure in sufficient detail to demonstrate the experimental accuracy. Further, none of these documents, except the paper by Takei et al.,[21] describes the propeller geometry in sufficient detail to allow one to theoretically calculate the pressure distribution.

Therefore, an experimental program was undertaken in an attempt to obtain accurate and reliable measurements of the pressure distribution on CP propellers in uniform and inclined flow over a range of advance coefficients. This report presents results from the program. The results of some exploratory experiments conducted under this program were reported in Reference 25. Experimental data are presented from uniform and inclined flow configurations over ranges of advance coefficient and Reynolds numbers. Steady and unsteady pressure coefficients are presented and compared to theoretical predictions.

PROPELLER DESIGNS

The objective of this project dictated somewhat conflicting constraints on the propeller design. On the one hand, the design should be somewhat representative of recent CP propeller designs for surface combatants. These designs usually have five blades and possess nonlinear radial distributions of skew and rake. The radial distributions of blade thickness, chord length, and load distribution for these propellers are selected from considerations of cavitation, strength, and propulsive efficiency. On the other hand, the propeller geometry for the present investigation must allow insertion of recessed, commercially available pressure transducers over a wide area of the propeller blade,* built to a model scale which can be handled readily by available facilities at DTNSRDC. This dictated relatively thick blades and a total propeller diameter of 2 ft (0.61 m).

The propeller design was based on typical realistic CP propellers[26,27] with adjustments as necessary to meet the constraints imposed by the model experiments. The adjustments are as follows:

1. The chord-diameter ratio, c/D, and thickness-diameter ratio, t/D, at each radial station were increased by a factor of 5/3. This allows sufficient thickness to embed the gages in the model propeller while retaining the thickness-to-chord ratio t/c, and to expand the area ratio A_E/A_o of the five-bladed FFG-7 propeller on a three-bladed model propeller.

2. A balanced distribution of skew** was used with somewhat larger magnitudes of skew angle than on the FFG-7 propeller. The projected skew angle θ_s extended from -10 deg at the 50 percent radius to +41 deg at the tip.

Propeller 4679 was designed for the same advance coefficient J_A and thrust loading coefficient C_{Th} as the FFG-7 propeller.

After preliminary experiments were completed on DTNSRDC Propeller 4679, a second propeller, DTNSRDC Propeller 4718, was designed to investigate the surface pressure on a more conventional propeller geometry. The modifications for this second propeller are as follows:

---

*The configurations of the pressure transducers are described in the section on Instrumentation.

**A balanced skew distribution has forward skew at the inner radii and aft skew at the outer radii to keep the moment about the spindle axis as low as practical.

1. The c/D at each radius was the same as that on the FFG-7 propeller; however, the t/c was increased to up to 5/3 times the value on the FFG-7 in order to allow sufficient thickness in which to recess the gages.

2. A balanced distribution of skew was used with slightly smaller magnitudes of skew than on the FFG-7 propeller. The projected skew angle θ_s extended from -5 deg at the 50 percent radius to +20 deg at the tip.

3. The design advance coefficient J_A was reduced from a value of 1.077 on both the FFG-7 propeller and Propeller 4679, to 0.751 on Propeller 4718. Therefore, at design J_A, the experimental propeller rotational speed n is increased for a given speed of advance V_A. This increases the local Reynolds number R_n at a given V_A and increases the number of propeller revolutions for a given pass down the towing basin. The increased number of runs provided improved statistical data.

4. The design thrust loading coefficient C_{Th} was reduced to approximately 3/5 times the value on the FFG-7 propeller so that the design thrust loading coefficient per blade is approximately the same as on the FFG-7 propeller.

The propellers were designed using the lifting line procedure of Caster et al.[28] for the preliminary design, and the lifting surface procedure of Kerwin[29] for the final design. The results of the lifting line calculations are shown in Table 2. The geometric details of the model propellers are presented in Figure 1 and Table 3. Photographs of the propellers are shown in Figure 2.

EXPERIMENTAL TECHNIQUE

FACILITY

All experiments were conducted on DTNSRDC Carriage 4. The propeller was driven from downstream using the drive system and housing of the DTNSRDC 1000 hp dynamometer. This dynamometer system uses two 500 hp (0.372 MW) electric drive motors located in a pod attached to the lower end of a strut. The test arrangement is shown in Figure 3.

The 1000 hp dynamometer was mounted to the carriage in two different orientations:

1. With the propeller shaft parallel to the direction of the carriage advance so that the propeller operated in uniform flow, and

2. With the propeller shaft inclined 7.5 deg downward from the direction of the carriage advance so that the propeller operated in inclined flow.

INSTRUMENTATION

The propellers were instrumented with 40 semiconductor pressure transducers (gages); 20 transducers were mounted on the pressure side (face) of one blade (Blade 2) and 20 transducers were mounted in the same radial and chordal positions on the suction side (back) of another blade (Blade 3); see Figure 4 and Table 4.

The pressure transducers were mounted in Helmholtz cavities. A hole 0.040 in. (1.0 mm) in diameter connected each cavity to the surface of the blade. This configuration was accomplished in one of two ways. Where the thickness of the blade permitted, the transducer was installed from the opposite side of the blade (Figure 5a). O-rings isolated the transducer from the blade in order to essentially eliminate the effects of blade deflection, as discussed in the section on Experimental Results. A set screw secured the assembly, and the remainder of the hole was filled with a clear resin.

Near the leading and trailing edges, and at the 90 percent radius, there was not sufficient thickness to permit such an installation. At these locations the transducer was set into a 0.625 in. (15.9 mm) diameter cavity which was milled into the blade from the surface on which the pressure was to be measured (Figure 5b). The transducer was held in place with teflon tape and the tape was epoxied in place at its edges, so that the transducer was not directly attached to the blade. A faired coverplate with a 0.040 in. (1.0 mm) diameter hole was cemented over the cavity.

Dynamic calibrations were conducted using an enclosed column of liquid vibrated by a shaker. The natural frequency of the pressure gage cavity arrangement was above 1600 Hz. This ensured a flat response with no dynamic effects in the 5 to 20 Hz shaft rate frequency range investigated during the experiment.

Transducers recessed in Helmholtz cavities were used rather than flush-mounted transducers for the following reasons:

1. Recessed transducers are better protected from damage arising from cavitation collapse pressures or from accidental damage due to handling the blades than are flush-mounted transducers.

2. Recessed transducers produce less disturbance to the blade contour than do surface mounted transducers. However, this advantage of recessed transducers has been partially mitigated by smaller transducers which have become available since these recessed transducers were installed (July 1976).

For Propeller 4769, two of the pressure transducers in Helmholtz cavities were replaced by flush-mounted transducers, one to each surface of the blade at 50 percent chord at the 0.70 radius. These transducers are the recently-developed extremely small type. The total diameter is 0.050 in. (1.3 mm) and the diameter of the sensing element is 0.023 in. (0.58 mm). These flush-mounted transducers were found to be unsatisfactory in terms of durability and accuracy.

The instrumentation components used in a single pressure measurement channel are shown in Figure 6.*

The pressure transducer sensing elements are contained in a resistance Wheatstone bridge circuit which produces an output signal voltage proportional to the applied pressure. Power is supplied to the pressure transducer through a slip ring on the propeller shaft and is regulated by four integrated circuit voltage regulators, one for each group of ten pressure transducers. Only two arms of the Wheatstone bridge are actually located at the pressure transducer; there are two bridge completion resistors per transducer located inside the propeller hub.

The bridge output voltage is fed through a semiconductor analog switch into a voltage controlled oscillator (VCO). The VCO produces a frequency modulated (FM) output signal in which a deviation in the VCO center frequency is proportional to the voltage level of the input signal.

The FM output signal from 20 of the VCO modules, corresponding to the 20 pressure signals on one blade, are fed into a common mixer circuit module. The FM multiplexed signal at the output of the mixer is then telemetered via a single slip-ring and a single coaxial cable from the propeller hub to a bank of 20 discriminator channels located on the towing carriage. There are two identical but separate mixer circuit modules and banks of discriminators, each of which carries the signals from 20 pressure transducers. Therefore, the signals from all 40 pressure transducers are transmitted simultaneously using only two coaxial cables and two slip rings.

Each discriminator channel converts the associated FM signal into a high level dc voltage proportional to a corresponding pressure transducer signal; i.e., it demultiplexes the signal. The resulting voltages are digitized, averaged, and stored by an Interdata Minicomputer, as discussed later.

---

*Details of the instrumentation are shown on DTNSRDC Drawings C-543-1, C-543-2, C-543-3, and C-543-4.

The transducer bridge circuit sensitivity for each channel was adjusted so that a full-scale pressure of approximately ±15 psig (103 kPa), with respect to atmospheric pressure, produces a ±10 mV output signal. The VCO accepts a ±10 mV full-scale input signal and produces ±2 kHz (constant bandwidth) deviation in center frequency. The discriminator gain for each channel was adjusted to convert a ±2 kHz center frequency deviation into a full-scale output signal of ±5 V. Therefore, the overall sensitivity of each channel was designed so that an applied full-scale pressure of ±15 psig (103 kPa) produced approximately ±5 V at the output of a discriminator unit. Thus, the overall system sensitivity was approximately 0.33 V/psi (48V/MPa).

A Baldwin optical shaft-angle encoder, geared to the propeller shaft, was used to determine shaft angular position. Two types of pulses were generated; a single-pulse per revolution and a multipulse per revolution (60 equally spaced pulses). The single pulse is referred to a known angular position relative to the propeller. The pulses generated by this encoder are accurate to within ±0.01 deg.

An ultrasonic wave-height probe was used to measure changes in the water level above the propeller. This measurement permitted a correction to the initial pressure zeros taken at the beginning of the run due to any variation in the average water level during the run. The wave probe was zeroed out at the start of a day's running, when the basin's water surface was undisturbed. The instrument zero was checked between runs by inserting a flat plate a known distance below the probe, but above the disturbed water level.

CALIBRATION

An extensive calibration program was conducted to arrive at accurate calibrations for test purposes, and to investigate possible systematic errors in pressure measurement instrumentation.

This program was based on a computer-automated calibration system. A cylindrical aluminum pressure tank was constructed to house the entire propeller and hub assembly. Pressure inside the tank was monitored with a precision pressure standard and used to calibrate the 40 pressure gages simultaneously. The tank pressure was stepped automatically by computer through a range from -5 to 10 psig (-34 to 69 kPa).

The minicomputer automatically performed the entire calibration in a consistent fashion, based on programed variations such as the number and order of pressure steps, and the averaging and settling time for each pressure reading. After calibration data were obtained, the computer calculated a straight line least-squares curve fit based on the recorded pressures for each gage, providing gage sensitivity and the standard deviation from the straight-line calculated values. This system permitted consistently run, quick calibrations conducive to statistical analysis and the identification of possible systematic errors.

An exhaustive series of calibrations was conducted on Propeller 4679 to investigate possible systematic errors in the pressure measurement instrumentation. Initial calibrations were conducted in the laboratory without the 1000 hp dynamometer cabling and sliprings connected through the measurement system. The propeller pressure gages were calibrated under conditions with both water and air in the pressure tank, and in the gage cavities. The procedure for filling the cavities with water involved injecting water mixed with a wetting solution through the gage hole. The wetting solution eliminated the adhesion of air bubbles to the cavity interior. The procedure was used throughout the experimental program to remove air from the cavity. Combinations of air and water in the cavities and pressure tank had no effect on the gage sensitivities.

Calibrations were also conducted with the propeller and pressure tank mounted on the 1000 hp dynamometer. This arrangement most closely resembled actual test conditions by including the dynamometer cabling and sliprings in the calibrations. The pressure tank was also designed to be rotated with the propeller on the dynamometer shaft, allowing calibration to include the effects of centrifugal loading, propeller drive motor noise, and slipring noise. Calibrations were conducted with air in the pressure tank and gage cavities while the propeller was rotating at 300-500 rpm, representing typical test rotational speeds. Rotation had no effect on the gage sensitivities. Some additional noise, developed on selected gage signals, attributed to drive motor transmission noise because of its dependency upon the FM multiplexing frequency of the gage channels. Because the source of noise did not influence the sensitivity of the gage, it was assumed to average out in the data collection process.

The final calibrations used during the test were conducted in the laboratory with water in the pressure tank and gage cavities. A series of automated calibrations were performed, and averaged. A second series of calibrations was conducted midway through the test which resulted in a slight variation in sensitivity of the gages, which was attributed to exercising the gages during the first part of the test. From these calibrations, the degree of expected accuracy of the pressure measurements was obtained. For any single calibration, the error band, based on a 95 percent confidence level was calculated from the standard deviation relative to a straight line calculated sensitivity. The average error band of all gages for the pretest calibrations was $\pm$0.035 psi (0.24 kPa). The average difference between the pretest and midtest calibration sensitivity was 0.022 psi/V (0.15 kPa/V). For a typical measured pressure coefficient of -0.4 this variation in calibration sensitivity corresponded to 0.015 psi (0.10 kPa) at low test speeds (V_c = 6 knots) and 0.035 psi (0.24 kPa) at high test speeds (V_c = 11 knots). An expected upper and lower bound on a given pressure measurement could be formulated by simply adding the above sources of error.

1. Expected error at low test speeds - $\pm$0.050 psi (0.34 kPa)
2. Expected error at high test speeds - $\pm$0.070 psi (0.48 kPa)

EXPERIMENTAL CONDITIONS

All experiments on Propellers 4679 and 4718 were conducted with the blades set at the design pitch. Table 5 indicates the test conditions. The values of carriage speed V_c, rotational speed n, resultant inflow speed at 0.7 radius $V_{R0.7}$, Reynolds number R_n, and advance coefficient J are nominal values. Generally, the final measured quantities were averaged over the number of runs at each condition and varied slightly from the quantities indicated. Most conditions were run at the three indicated configurations of uniform flow, 7.5 deg inclined flow, and uniform flow with the static pressure taps covered with tape to determine loading effects on the pressure gage output.

DATA COLLECTION

The data which were recorded during the experiment included 40 channels of blade-surface pressure, propeller rotational speed, carriage speed, and wave height

above the propeller. The pressures were recorded 60 times per revolution, at every six-degrees of blade angular position, as triggered by the shaft encoder. The other quantities were recorded once per revolution.

Zeros were recorded before each experimental run. The zero before each run was subtracted from the data recorded during the run as part of the data analysis. Zeros recorded on consecutive runs were compared to observe zero drift.

Zeros were collected by recording the gage pressures with the propeller at rest. Each static pressure value was corrected to its shaft centerline value in the computer analysis by accounting for the static head difference between an individual gage location at zero collection and the shaft centerline. This computation was based on the propeller angular position which was recorded during the zero collection, and the individual gage angle relative to the propeller shaft reference angle which was stored in the analysis program.

This procedure was an improvement over a preliminary experiment,[25] where zeros were collected by averaging pressure values during slow propeller rotation.

After the carriage had reached the desired speed and the propeller rotational speed had been set, pressure data were recorded at each of the 60 blade angular positions over 75 records. Each record involved collecting data from 20 pressure side gages on Blade 2 in the first revolution, 20 suction side gages on Blade 3 in the second revolution, and 3 once per revolution signals on the third revolution (V_c, n, and wave height WH). Therefore, each of the 75 records included data from three revolutions. It was not feasible to obtain all of the data simultaneously due to computer limitations.

After completion of a run, the computer analysis was performed. As part of the analysis, the cyclic variation in hydrostatic head, p_o, produced during each propeller revolution, was subtracted from the measured pressure at each of the 60 blade angular positions. This procedure produced essentially constant measured pressure with angular position in uniform flow. The analysis provided the following output after each run:

1. Quantities averaged over one record:

   $V_c(I)$, $n(I)$, $J(I)$, $p(\theta,N,I)$, $WH(I)$, I = 1 to 75 records, N = 1 to 40 gages

2. Quantities averaged over one run:
$\bar{p}_o(N)$, $\bar{V}$, $\bar{n}$, $\overline{WH}$, $\bar{J}$, $\bar{p}(N)$, $\bar{C}_p(N)$, N = 1 to 40 gages where

$$\bar{C}_p(N) = [\bar{p}(N) - p_o(N)] \Big/ 1/2\rho\ [\bar{V}^2 + (2\pi\bar{n}r)^2]$$

3. First harmonic analysis of averaged variation of pressure coefficients with blade angular position

$$C_p(N,\theta) = \bar{C}_p(N), + \tilde{C}_{p1} \cos\ (\theta - \phi_1)$$

4. Graphs of average pressure variation with blade angular position, $p(N,\theta)$ versus θ

5. Graph of mean pressure coefficients as a function of chordwise station, $\bar{C}_p(N)$ versus x/c

EXPERIMENTAL RESULTS

LOADING CORRECTIONS

The pressure-gage installations were designed for minimum interactions due to loading. Propeller 4679, constructed first in the program, demonstrated small loading effects on the gage pressure measurements. Propeller 4718 was constructed later using the same gage installation procedures, but was found to have significant loading interactions for gages installed in the thicker portions of the blades, as shown in Figure 5a. The cause was thought to be related to variation in the details of the gage installation procedure. In this configuration the pressure gage was seated against an o-ring with a set screw, and then covered with potting resin. Variations in the torque applied to the set screw would cause variations of the pressure acting on the o-ring, therefore, causing variations in the ability of the o-ring to isolate loading interactions. Unfortunately, there is no practical method of checking this because of the permanence of the potting material covering the set screw.

To account for the loading effect, both propellers were load tested at the various test conditions in uniform flow. To eliminate the gage response to pressure, 2-mil thick Mylar tape was applied over the gage holes. Pressure calibrations were conducted with the taped over gages, resulting in a reduction in gage sensitivity to less than one percent of the sensitivity without the tape applied. Rerunning the test matrix (shown in Table 5 in uniform flow) with the tape applied over the gage holes provided a direct measure of the loading effects on gage output. The gage signal due to loading was nondimensionalized in the same way as the original pressure signal and represented as a pressure coefficient. This coefficient is defined as the loading pressure coefficient. Its mean value is $\overline{C}_{pL}$:

$$\overline{C}_{pL} = p_L/(1/2\rho V_R^2)$$

where p_L is the measured pressure signal produced when the gage holes were covered with tape.

Figure 7 shows the variation of $\overline{C}_{pL}$ for each gage over a range of J for inflow speeds listed in Table 5. Each figure shows all repeat runs at each condition and a third-order least-squares polynomial fit through the measured values. From Figure 7, the repeatability observed was good with $\overline{C}_{pL}$ varying by ± 0.01 for repeat conditions at constant J. Certain gages (at the inner radii) had substantial loading coefficients at design J with large variations over the range of J measured. To correct the measured pressure for loading effects at a given J, the polynomial describing the loading coefficient for each gage was solved and subtracted,

$$\overline{C}_{pL}(J) = A + BJ + CJ^2 + DJ^3$$

$$\overline{C}_{pcor}(J) = \overline{C}_p(J) - \overline{C}_{pL}(J)$$

where A, B, C, D, are the polynomial coefficients. This corrective procedure eliminated the loading effect on most of the gages over the range of test conditions.

To further correct the measured pressure for loading, a second-order effect of inflow speed was investigated. Conditions were run at design J over a range of inflow speeds. Figure 8 shows the variation of $\overline{C}_{pL}$ over ranges of inflow speed at design J. Again, all test spots are shown, including repeat runs, and a third-order polynomial was fitted to the measured loading coefficients over the range of V_R. Even with relatively expanded scales for $\overline{C}_{pL}$ (see Figure 8), the variation with V_L was small except at two gage locations. To adjust for loading effects as accurately as possible, the second-order effect of speed was considered in a fashion similar to the first-order effect of advance coefficient. In this case the curve-fit polynomial in Figure 8 was used to analytically describe the variation of $\overline{C}_{pL}$ with V_R at constant design J,

$$\overline{C}_{pL}\ (J_{des},V_R) = A + BV_R + CV_R^2 + DV_R^3$$

where A, B, C, D, are polynomial coefficients. The above quantity was then subtracted from the measured pressure coefficient to correct for the second order loading effect due to speed, as

$$\overline{C}_{pcor}(J) = \overline{C}_p(J) - \overline{C}_{pL}(J) - \overline{C}_{pL}(J_{des},V_R)$$

To avoid accounting for the loading effect twice in the two loading terms above, $\overline{C}_{pL}(J_{des},V_{Ro})$ was added to the right side of the above equation, where V_{Ro} was the primary inflow speed tested in the range of J runs, as shown in Figure 7. Rewriting the above equation, one obtains

$$\overline{C}_{pcor}(J,V_R) = \overline{C}_p(J,V_R) - \overline{C}_{pL}(J,V_{Ro}) - \overline{C}_{pL}(J_{des},V_R) + \overline{C}_{pL}(J_{des},V_{Ro})$$

Each pressure coefficient term is a function of both J and V_L, where,

1. $\overline{C}_{pL}(J,V_{Ro})$ is the polynomial function from Figure 7
2. $\overline{C}_{pL}(J_{des},V_R)$ is the polynomial function from Figure 8

3. V_{Ro} is the primary inflow speed used in Figure 7

4. J_{des} is the design advance coefficient held constant in Figure 8

A similar loading correction was made to the fluctuating pressure coefficients. Because the runs conducted with the taped-over gage holes were performed in uniform flow only, the loading corrections to the fluctuating pressure coefficients had to be approximated. The approximation is based on an assumed quasi-steady variation in the local loading pressure coefficient $C_{pL}(\theta)$, with local advance coefficient $J(\theta)$, calculated from the variation of the mean loading pressure coefficient $\overline{C}_{pL}$, with advance coefficient J from Figure 7. The procedure was identical to that used (see page 32) to calculate predicted unsteady pressure coefficients. In the present case, the C_{pL} versus J curves were used instead of C_p versus J curves, as described in the later section. For each pressure gage, a first-harmonic loading pressure coefficient amplitude $\tilde{C}_{pL1}$ and phase ϕ_{L1} were calculated for each run conducted and were vectorially subtracted from the measured fluctuating first harmonic pressure coefficient. The propeller shaft inclination produced a constant tangential wake, producing a first-harmonic phase angle due to load effects, called the loading phase, ϕ_{L1} of 270 deg. To more accurately approximate the unsteady correction, the phase of $\tilde{C}_{pL1}$, ϕ_{L1}, was shifted from the quasi-steady prediction of ϕ_{L1} = 270 deg to ϕ_{L1} = 300 deg. This adjustment was based on a similar phase lag in previously measured unsteady propeller blade loads in inclined flow by Jessup and Boswell.[7]

Figures 9 and 10 show the uncorrected and corrected first harmonic pressure coefficients and phases. Loading effects did not occur at the 0.9 radial positions, so comparisons there were deleted. Note that on some gages the correction is considerable and is only an approximation. When analyzing results from these gages, consideration must be made for the uncertainty of the correction. (Some discussion of this point will be given subsequently.) Fortunately, most gages show little or no loading correction.

MEASURED MEAN PRESSURE DISTRIBUTIONS

Figure 11 depicts the measured and predicted mean pressure distributions for Propellers 4718 and 4679 at design advance coefficient at the 0.5, 0.7, and 0.9 radial positions. The measured mean pressure coefficients represent average values over the range of speeds tested for each propeller to allow general comparisons with theory.

The predictions were calculated by a combination of the propeller design procedure[28,29] and equivalent two-dimensional blade section methods.[30] Initially, from the lifting-line prediction,[28] the radial loading distribution was obtained, providing the required lift coefficient for a given section of chord length. Assuming a NACA 66 thickness airfoil section, with an $\alpha = 0.8$ meanline, a two-dimensional camber ratio and ideal angle of attack were calculated to produce the desired loading.* The two-dimensional theoretical pressure distribution was calculated by the method of Brockett[30] using the assumed thickness shape, meanline, and ideal angle of attack.

Before comparing results of the two propellers, one should note the qualitative geometric differences. Propeller 4718 was designed to resemble a conventional CP propeller with moderate skew and planform. Propeller 4679 was designed with increased skew, increased pitch, and increased expanded area ratio, producing much larger chord lengths for an equivalent overall diameter. In planar-wing terminology, Propeller 4679 resembles a delta wing, especially at the outer radial positions. Therefore, the pressure distribution at the outer radii of Propeller 4679 could be dominated by the real fluid effects of cross-flow and tip-vortex roll-up observed on low-aspect ratio wings, and would be less likely to match predicted two-dimensional pressure distributions. At the inner radii, the measured flow characteristics of the two propellers would be expected to be similar due to the effect of the hub and the close similarity of the local planforms.

On the suction side, at the 0.5 radius, both propellers display similar measured results. The measured negative pressure coefficient, $-\overline{C}_p$, is less than the theoretical value near the leading edge region, and greater than the theoretical value near the trailing edge.

On the pressure side, at the 0.5 radius, the measured results on Propeller 4718 more closely resemble the theory with irregular peaks in the measured result at the 10 percent and 50 percent chord positions. Measured magnitudes of $\overline{C}_p$ on Propeller 4679 are generally less than theoretical predictions over the forward portion of the

*The final propeller geometry is determined using lifting surface techniques[29] to arrive at the corrected camber, and ideal angle of attack to produce a chordwise load distribution equivalent to that calculated in two dimensions.

chord, and greater towards the trailing edge. There, a large negative pressure coefficient implies an acceleration of flow at the trailing edge on the pressure side, in somewhat better agreement with the suction-side pressure coefficients at the trailing edge.

A possible explanation for some of the irregularities in the measured pressures at the 0.5 radius involves the flow perturbation produced by the fairwater and hub of the propeller. The propellers were operated on a downstream shaft, with a hemispherical fairwater ahead of the blades. The blades were mounted to a protruding spherical section intersecting the cylinder to which the fairwater was attached, as shown in Figures 1b and 2. The hub would disturb the flow into the blades near the root and the perturbation velocity would depend on the axial position of the blades relative to the hub and fairwater. The increased axial speed would increase the advance coefficient locally at the blade-section leading edge near the hub, thus causing a decrease in $-\overline{C}_p$ on the suction side and an increase in $-\overline{C}_p$ on the pressure side. Potential flow calculations on a hemispherical headform predicted a maximum axial velocity increase of 3 percent of free stream speed at the 0.5 propeller radius. A 3 percent increase in advance coefficient changed the measured pressures at the leading edge only slightly, but in the direction of the theoretical result. Therefore, this effect could only partially explain the trends of the measured pressures near the leading edge at the 0.5 radius.

Image effects of the hub are another possible explanation for the trends of the measured pressure distribution on the suction side at the 0.5 radius. Unfortunately, there is no simple way to approximate the effect. Any influence would be tied to the roll-up process of the hub vortex and the boundary condition on the hub. At present, there is no available lifting-surface design computer code that takes the hub into account.

At the 0.7 radius, data from Propeller 4718 match the theory reasonably well, but there is a theoretical over-prediction of pressure magnitudes in the midchord regions.

At the 0.7 radius, the flow over Propeller 4679 produces irregular pressure distributions. On the suction side, the measured pressure distribution has a suction peak at the leading edge followed by a drop across the midchord, and an increase

matching theory in the trailing-edge region. The measured pressure at midchord may be in error because it was obtained with a questionable surface mounted gage which proved unreliable in unsteady flow. The bracket indicates a more credible result from earlier tests before the surface gage was installed. The measurements on the pressure side have similar irregularities across the chord, with values greater than theory near the leading edge, then dropping below theory further aft.

Results of this type are questionable, since one expects smoother variations in pressure along the chord. Irregular variations along the chord could be explained by the effect of crossflow and rollup processes of the tip vortex. The leading edge at the 0.7 radius is positioned at the start of the extreme sweepback of the leading edge, which could be the start of streamwise vortex generation and rollup. Strong vortex formation in this leading-edge region will induce high local velocities in the chordwise direction along the leading edge from the 0.7 radius to the tip, thus producing suction peaks in the surface pressures. Also, any degree of crossflow would greatly change the effective blade-section shape traversed by the flow over the gage of interest. It is believed that an extremely complex lifting-surface flow model with advanced numerical-analysis techniques is required to predict the pressure distributions in these regions.

At the 0.9 radius, measured pressure coefficients on Propeller 4718 are generally less than the theoretical predictions. On the suction side, measured values are less than predictions except near the trailing edge where measured values are slightly greater than predictions. On the pressure side, measured values are less than theoretical predictions uniformly across the chord. On Propeller 4679, theory and experiment are in good agreement on the pressure side; however, on the suction side the experimental pressure distribution is greater than the theoretical prediction. This result is much different than that of Propeller 4718, again implying possible differences in flow patterns near the tip.

Again, the difference in correlation between theory and experiment for Propellers 4679 and 4718 may relate to different rollup and tip-vortex positions near the tip not accounted for in the mathematical model. The greater skew on Propeller 4679 may cause tip vortex formation further inboard of the tip, resulting in a decrease in pressures on the suction side near the tip. Also tip-vortex separation may occur, influencing the local pressures.

Summarizing, correlation of mean pressure distributions with data from existing analytical methods produces poor results compared to similar measurements on planar wings. It is thought that improved correlation could be obtained with theories accounting more completely for observed three-dimensional flow effects.

INFLUENCE OF REYNOLDS NUMBER ON MEASURED PRESSURE DISTRIBUTIONS

It was thought that over the range of Reynolds numbers covered by the tests ($6\times10^6 > R_n > 2\times10^6$) the pressure distributions would be essentially independent of Reynolds number at a given design point. With an absence of cavitation and boundary-layer separation, it was expected that the measured pressure coefficients at constant J would match a potential flow model, being independent of Reynolds number or, in this case, carriage speed V_c, resultant inflow speed V_R, or rotational speed n.

To investigate this, runs were conducted at design advance coefficients over ranges of carriage speeds in a Reynolds number range of 2.50×10^6 to 4.63×10^6 for Propeller 4718, and 3.08×10^6 to 6.20×10^6 for Propeller 4679. A limited number of speed runs were also made at off-design conditions. Results shown in Figures 12 and 13 indicate a relatively large speed dependence of the pressure coefficients in various chordwise regions of the blade.

At the 0.5R radial position, a dramatic increase in pressure coefficient occurred on the suction side with increasing speed in the mid-to-aft chord region on Propeller 4718, representing the greatest speed effect observed. A variation, similar in effect, occurred in a similar region on Propeller 4679, but to a lesser degree. On the pressure side of Propeller 4718, a pressure increase with increasing speed occurred near the leading edge; however, for the gage nearest the leading edge the $\overline{C}_p$ was essentially constant. The pressure side of Propeller 4679 showed less of a speed effect than Propeller 4718 with the exception of increased values of $\overline{C}_p$ on the lowest speed run, contradicting the usual trend of increasing $\overline{C}_p$ with increasing speed.

At the 0.7 radial position on Propeller 4718, values of C_p increased on the suction side with increasing speed in the fore- to mid-chord regions. On the pressure side, a similar variation occurred. In both cases, little or no variation occurred at the leading and trailing edges. Propeller 4679 produced a similar trend

on the suction side, but to a lesser degree. The pressure side showed irregularities at the lowest speed, similar to those at the 0.5 radius, but produced a large increase in $\overline{C}_p$ with speed at the trailing edge.

At the 0.9 radial position on the suction side of Propeller 4718, C_p increases with speed, with increasing magnitudes toward the trailing edge. On the pressure side, only a slight speed effect occurred at the leading and trailing edges. The suction side of Propeller 4679 had pressures increasing with speed in the fore-chord region. The pressure side had little speed dependency except for, again, irregularities at the lowest and highest speed condition.

Generalizing the pressure-coefficient speed-dependence trends are as follows:

1. Consistent direction of speed dependence - The pressure coefficients increased with increasing speed on both sides of the blade with the exception of the pressure side of Propeller 4679, at the lowest speed run.

2. $\overline{C}_p$ versus V_R was a smooth function - In most cases, pressure coefficients plotted against V_R produced smooth monotonically varying curves, as shown in Figure 14.

3. Propeller 4718 exhibited slightly greater speed effects for $\overline{C}_p$ than did Propeller 4679.

4. Speed dependence of $\overline{C}_p$ occurred in both uniform and inclined flows.

5. Speed dependence appeared to be independent of J (from results to be discussed subsequently).

6. No speed dependence was observed in unsteady pressure measurements (from results to be discussed subsequently).

POSSIBLE MEASUREMENT ERRORS CAUSING C_p VARIATION WITH REYNOLDS NUMBER

The above trends do not obviously point to any real flow effects, so the feasibility of an instrumentation error as the cause of the speed effects should be considered. The form of the pressure coefficient is:

$$C_p = \frac{p - p_o}{1/2\ \rho V_R^2}$$

Because of the speed squared term in the relation, any constant or variable error in p, p_o, or V_R will produce a speed effect on the calculated value of C_p. For example, if the static pressure, p_o as measured is greater than actually occurred, then the measured value of $p - p_o$ will be decreased over the range of speeds by a given increment. When nondimensionalized by V_R^2, a monotonically decreasing pressure coefficient will result over the given speed range.

Errors in measurement of p_o were possible due to the many corrections performed before the final value was reached. As stated previously, zeros were taken when the propeller was stationary. The value was then corrected for wave height deviations from zero and the hydrostatic correction to the propeller axis based on the angular position of the propeller. Corrected static zeros were compared over twenty range-of-speed runs with variations observed from 0.02 to 0.07 psi (0.14 to 0.48 kPa). No correlation of speed with pressure variation was observed. This variation was within the expected gage error, and did not approach a p_o error of 0.2 - 10 psi (1-69 kPa) which is necessary to produce the observed speed effect. The small variation in p_o values demonstrated the proper zero correction, because each zero collection was performed with the propeller at a different angular position.

Errors in the measured pressure p were possible due to uncertainties in the loading corrections. As stated earlier, some gages, primarily on Propeller 4718, exhibited a sensitivity to blade loading. To correct the data for this effect, the test conditions were repeated with tape over the gages (which then measured the cavity air pressure) to desensitize the gage output to pressure. The measured loading effect was subtracted from the measured pressures. The loading effect was found to be sensitive to advance coefficient, but relatively insensitive to Reynolds number or speed when nondimensionalized by $1/2\rho V_R^2$. Because the loading effect was independent of speed, it was thought not to be the cause of the observed speed effect.

Correlations between gages with large loading and speed effects indicated a possible cause for some of the large speed dependency. A measure of the relative loading effect was represented by the quasi-steady loading correction Q, which is the slope of the C_{pL} versus J curves at design J shown in Figure 7. Figure 15 shows the magnitude of the loading correction Q against the speed dependency, as the difference in pressure coefficient at two inflow speeds. For Propeller 4718 it

appeared that many of the gages with large loading corrections also had large speed effects. Also, most of these gages were the back-mounted type used in the thicker sections of the blade. Propeller 4679 did not have as large a speed effect or as great a loading effect as Propeller 4718, but showed similar correlation between the two effects, and indicated greater problems with the back-mounted gages.

From this observation it was thought that some errors existed in the loading correction procedure. The most probable error was a coupling effect between the gage calibrations for loading and pressure. When the loading sensitivities were measured, the gage holes were taped over, producing approximately constant atmospheric pressure acting on the gage. During pressure measurements, additional non-atmospheric pressures acted on the gage, therefore, the same conditions occurring during the loading effect measurements were not reproduced. If the loading effects were caused by gage diaphram deflection, produced by displacements of the blade in contact with a gage, then that effect could be dependent upon the initial deflection of the gage, before the blade was strained by the loading. The dependence of the loading sensitivity on gage deflection or pressure was checked in the laboratory by hanging a weight from the end of the blade while applying known pressures to the gage of interest. The gage output due to loading was independent of the pressure on the gage. The lack of interaction effects between loading and pressure eliminated the loading effect as a possible cause of the observed speed effect. The correlation between loading effects and speed effects, if not due to instrumentation, could be caused indirectly by systematic real flow effects for the speed-affected gages and may be influenced by their location in the thicker mid-chord region of the blade.

In future pressure measurement tests, closer attention should be paid to the loading effects on the gages. It appears that on both propellers, the coverplate configuration produced little or no loading effect, while the back-mounted configuration produced large loading effects on Propeller 4718, and lesser effects on Propeller 4679. As stated earlier, it is suspected that the back-mounted configuration is very sensitive to slight variations in installation. In the future, a new gage mounting configuration could be designed incorporating the advantages of both types.

The remaining source of instrumentation error possibly causing the speed variation was in V_R, the inflow speed, calculated from carriage speed V_C, and propeller rotational speed n. Error in these measured quantities was highly unlikely for the following reasons:

1. An error in either n or V_C would have shown up as a variation in advance coefficient, causing variations in C_p near the leading edge. That did not occur.

2. An error in V_R would cause a systematic variation in C_p over speed identical for all the gages on both propellers.

With the elimination of possible instrumentation errors in measured p, p_o, and V_R, only real flow effects can explain the large pressure variations with speed observed at the design test condition.

POSSIBLE REAL FLOW EFFECTS CAUSING C_p VARIATION WITH REYNOLDS NUMBER

The variation in measured pressure coefficients at design J with Reynolds number could be related to variations in flow regime over the blade. Reynolds number will influence the development of the blade boundary layer, including laminar to turbulent transition and flow separation, and perhaps the formation of the tip vortex. If boundary-layer development leads to separation, then the pressure field will be altered in the separated flow region of the blade, and adjustments in circulation will cause some change in the pressure field ahead of the separated region. Changes in tip-vortex formation and position will alter pressures at the 0.9 radius on the suction-side of the blade. Also leading-edge separation and reattachment could occur over much of the outboard radius, altering the pressures near the leading edge.

It was suggested that part of the boundary layer on the blades might be laminar, making separation more likely than for a turbulent boundary layer at increased values of the Reynolds number. To check this, sand of 400 grit size (60 μm) was glued to the leading edges of the blades with shellac. Upon rerunning the test matrix, it was found that no appreciable change in measured pressure coefficients occurred. Table 6 shows values of pressure coefficients for Propellers 4718 and 4679 with sand, and the difference produced when the sand was applied. The differences measured were generally within the largest standard deviation produced from repeat runs conducted

for the two cases. Inspection of runs at other speeds also produced no effect of the tripped boundary layer. It was concluded that the boundary layer was essentially fully turbulent without the sand, even for the run at the lowest Reynolds number of 2.5×10^6 for Propeller 4718, and 3.08×10^6 for Propeller 4679. This result agrees with data from Meyne[31] who predicts a fully turbulent boundary-layer to occur for Reynolds number values greater than about 10^6.

Attempts to correlate the speed effects at certain gage locations with possible separation could be advisible without a better understanding of three-dimensional separation and other boundary-layer flow phenomena, as could be determined with flow visualization on the two propellers. Unfortunately, little insight can be drawn from experiments correlating the effects of two-dimensional separation phenomena with static surface pressures.

Three-dimensional separation could be influenced by many effects. At the root of the blade, local separation forms and is dependent upon the thickness and mean-line of the inner radius sections and on the fairness of the blade fillets. Also, a secondary-flow horseshoe vortex is formed around the root of the blade, and is shed downstream, inducing flow on the blade. The rotation of the blades produces a boundary-layer flow component radially outward, directing the surface shear stress also radially outward. The effect is more pronounced for laminar than turbulent flow.[31] The large thickness ratios at the inner radii, especially on Propeller 4718, could also contribute to possible three-dimensional separation related to strong adverse pressure gradients in the radial and chordwise directions. At the tip, the formation of the tip vortex could cause extreme local pressure gradients contributing to separation. Influences from these effects could lead to separation in various regions of the blade.

More detailed predictions of boundary-layer flow and separation could be made only through boundary-layer flow visualization techniques. By applying a paint (or oil) to the leading edge of the blades,[31] the paint-film flow patterns produced after running can indicate the details of the boundary-layer flow. This would provide a base to compare variations in pressure coefficients with Reynolds number.

VARIATION IN PRESSURE COEFFICIENTS OVER A RANGE OF J

As the propeller advance coefficient is reduced, the increased loading will be a result of increasing pressures on the pressure side of the blade and decreasing pressures on the suction side. Analogous to a planar wing, pressure coefficients toward the leading edge will be most influenced by angle-of-attack changes. For a propeller, variations in J are closely related to variations in blade section angle-of-attack.

Graphs were constructed presenting the variation of pressure coefficient with advance coefficient for each pressure gage location. Initial plots revealed problems on certain gages due to the effect of speed on the measured pressure coefficient. The uncorrected pressure coefficients plotted in Figures 16a and 16b demonstrate how the speed effect shifted $\overline{C}_p$ values based on the operating speed of each J condition. By matching speed runs from Table 5 to the plotted $\overline{C}_p$ values, it was apparent that the values of $\overline{C}_p$ corresponding to higher speed runs at low advance coefficients were uniformly shifted below the values extrapolated from measurements of C_p corresponding to high J, low speed runs.

To better describe the relationship between $\overline{C}_p$ and J, it was hypothesized that the variation of $\overline{C}_p$ with speed was independent of J and only dependent upon the local inflow speed, V_L. This assumption permitted the pressure coefficient to be corrected for the observed speed effect. Third-order, least-squares polynomials were fitted to the $\overline{C}_p$ versus V_R relationships shown in Figure 14 representing the observed speed effect at design J. All measured pressure coefficients were corrected to a baseline condition at design J of 7.88 rps for Propeller 4718 and 8.20 rps for Propeller 4679. The correction was made by subtracting from the measured $\overline{C}_p$ the difference in $\overline{C}_p$ from Figure 10. This difference is between that at the base condition and that corresponding to the local speed of the $\overline{C}_p$ to be corrected. Again, this assumed that the speed effect was independent of J.

The improvement to the C_p versus J relationship can be seen in the plots corrected for speed; see Figure 16. The pressure coefficients shown with relatively large speed effects tend to collapse to approximately straight lines indicating a generally linear relationship. Similar relationships resulted with gages with little or no speed effects, differing primarily by the slope of the line. Because of the substantial improvement obtained, the assumption was considered accurate.

Figure 17 represents the variation of the speed corrected pressure coefficients with J for uniform and inclined flow. Along with the measured pressure coefficients for each run, first- and second-order least-squares curves are shown. There are no significant differences in the curves for the cases of uniform and inclined flow, as expected, except when numerous bad runs shifted the shape of the curve. Generally, the slopes of the curves increased in magnitude from trailing edge to leading edge, as expected.

Some gages produced obvious second-order nonlinear C_p versus J curves. On Propeller 4718, nonlinearity occurred mainly at the leading edge and at the 0.9 radius. On Propeller 4679, nonlinearity occurred, with some exceptions, at all blade positions, clouded to some extent by scatter of the data at some gage positions. The nonlinearity which occurred may be associated with effects caused by the tip-vortex separation or crossflow over the blade surface. Comparisons with lifting-surface theories may provide insights into this possibility.

The variation of the pressure distribution along the chord over a range of J is shown in Figures 18 and 19. As expected, increased sensitivity of the pressure coefficients to J occur towards the leading edge of the blade. From two-dimensional theory, the sensitivity should be zero at the trailing edge and monotonically increase towards the leading edge. This generally occurs except on the suction side of both propellers at the 0.5R and 0.7R radius positions, where the point of insensitivity to J occurs forward of the trailing edge. In each of these cases, this point is shown by the location at which a reversal occurs in the direction of $\overline{C}_p$ variation with J at the 90 percent chord position. This could be due to viscous effects or by induced velocities from a variable "tip" vortex and the trailing-vortex sheet.

The results for Propeller 4718 appear consistent with expected trends, with the exception of the 50 percent chordwise position at the 0.5 radius on the pressure side of the blade. A reversal in the direction of the $\overline{C}_p$ variation with J occurs there, completely inconsistent with surrounding gage results. A polarity error in the gage output would seem obvious, except for the proper polarity of the measured $\overline{C}_p$ at design J. Also, this gage has no speed effect or loading correction, and the measured unsteady pressures, as explained later, support this result. All this supports a real flow effect, but given the expected behavior over the rest of propeller, this seems unlikely.

Propeller 4679 showed behavior similar to Propeller 4718, with some noticeable variations. At the 0.7 radius on the suction side, the suction peak that occurred at the leading edge at design J remained even at the high J condition, implying not a simple angle of attack cause, but perhaps a local effect due to blade geometry at the leading edge. Also, the dip in $-\overline{C}_p$ at the 50 percent chord corresponds to a questionable surface mounted gage. The bracket at that position represents the range of pressures recorded in earlier tests, before the surface gage was installed. On the pressure side of the blade, a constant sensitivity of $\overline{C}_p$ to J was observed in the aft chord region. This appeared only at the 0.9 radius and could be related to tip-vortex separation and rollup occurring on the opposite side of the blade.

At the 0.9 radius of Propeller 4679, dramatic tip effects appeared to dominate the variation of pressure coefficient with J. On the suction side, variations with J occurred to a greater degree than for Propeller 4718. Also, from Figure 7c, the measured pressure coefficients at design J were larger than the theoretical predictions, contrary to data for Propeller 4718. As J was reduced, large decreases in $\overline{C}_p$ occurred near the leading edge. On the pressure side, variation in $\overline{C}_p$ was small, and the data were mostly uniform across the chord. This behavior was substantially different from the expected sensitivity of $\overline{C}_p$ to J occurring over most of the blade sections, including the 0.9 radius of Propeller 4718.

It is hypothesized that the formation and position of the tip vortex on Propeller 4679 produced the unconventional pressure distributions at the tip. Figure 20 shows Propeller 4679 operating in uniform flow at advance coefficients of 1.077, 0.8, and 0.6. The carriage speed in this preliminary test series was slightly greater than test values reported herein, causing a visible tip vortex even at design J. All three conditions shown were at approximately the same Reynolds number. As J was reduced, a thicker vortex core formed on the back of the blade migrating forward along the broad tip. At J = 0.6, the tip-vortex formation seemed to begin close to the leading edge at the 0.7 radius. Increased tip-vortex separation may have occurred also, but this is unclear from the photographs. If the tip vortex formed well ahead of the 0.9 radius, the tip vortex would have induced higher velocities along the 0.9 radius, causing a decrease in the pressure coefficients on the suction side which are strongly dependent on J. The pressure coefficients on the pressure

side seem little affected by the vortex, and perhaps are desensitized to J by its position on the back. This effect at the tip occurred only on Propeller 4679 which is characcerized by swept-back blades with wide, swept tips.

An attempt was made to compare the sensitivity of $\overline{C}_p$ with J along the chord with the two-dimensional theory[30] used to predict the pressure distributions at design. From Figure 17, the slopes of the first-order curve fits of $\overline{C}_p$ versus J were plotted against chord position in Figures 21 and 22. The magnitude and sign of the slope are proportional to the magnitude and direction of the sensitivity of $\overline{C}_p$ to J. At the 0.5 and 0.7 radii, the pressure coefficients on the pressure side of the blade were more sensitive to J than those on the suction side, while at 0.9 radius, the pressure coefficients on the suction side appeared more sensitive on both propellers. Also, the sensitivity reversal at the trailing edge on the suction side can be seen as a negative slope.

Similar slope distributions along the chord were approximated from the two-dimensional theory. With the same propeller blade sections, pressure distributions were calculated over a range of assigned angles of attack α. Slopes of these approximately linear relationships between $\overline{C}_p$ and α were calculated. The predicted slopes on each side of each section were then normalized by a constant factor so that the predicted and experimental slopes were equal for the gages nearest to the leading edge. This procedure was used to make simple approximate predictions of the slope or sensitivity distribution of $\overline{C}_p$ to J along the chord, because no simple relationship between effective two-dimensional angle of attack and advance coefficient is known. The predictions show roughly similar distributions of slope, but do not predict the differences between the measured slopes on the suction and pressure sides. Also, as expected, the predictions do not indicate any sensitivity reversal near the trailing edge. One might conclude from the gross similarity between prediction and measurements, that the effective three-dimensional camber distribution is similar to that of the equivalent two-dimensional model. More accurate comparisons with a lifting surface model should be made to confirm this hypothesis.

ACCURACY OF MEASURED DATA

At the time of earlier evaluations, attempts to quantify the accuracy of the measured mean pressures were hindered by small variations in advance coefficient. Because the carriage speed and the propeller rotational speed are set manually, a precise value of J cannot be set. The prescribed test matrix produced a series of runs at values close to the specified test conditions. The dependence of certain gages on speed or Reynolds number further hindered an quantification of the accuracy of the measurement system.

To overcome these problems, an error analysis was conducted based on the $\overline{C}_p$ versus J curves in Figure 17. The mean pressure coefficient represented in these curves had been corrected for Reynolds number dependence, as described earlier. Therefore, this accepted Reynolds number effect, whether being an instrumentation error or a real-flow phenomenon, had been eliminated in these figures. First- and second-order curves were least squares fit to these speed-corrected pressure coefficients over a range of J, and then a standard error for each curve was calculated. The standard error represents the standard deviation of the measured pressure coefficients from the least squares curve-fit values. The standard error was multiplied by 1.96 to represent the standard error at a 95 percent confidence level. This implies that, if one assumes a normal distribution of the variation of measured pressure coefficients from the curve fit values, then 95 percent of the measured pressure coefficients fall within plus or minus the value of the standard error from the curve-fit result. This procedure permitted the use of the entire test matrix, over a range of J and carriage speed, in calculating a statistical error band. Also, small variations in J, for a given test condition, were properly accounted for. The resulting nondimensional error bands in $\pm\overline{C}_p$, are shown in Table 7.

These results were extended to provide a dimensional error band in terms of a dimensional pressure. The standard error process was modified to calculate dimensional pressures and arrive at a 95 percent confidence level error band in psi that could be compared to the approximated error band of the measured pressures during calibration. These results, shown in Table 8 for the two propellers tested, indicate, in the best case of Propeller 4718 in uniform flow with a second-order curve fit, an average error band very close to the predicted error from the calibrations. Most other cases indicate a test error band up to twice the predicted error based on calibration error.

These results, especially in the best case, are very encouraging, indicating an observed test accuracy similar to the expected accuracy of the gages. The only discrepancy in the overall result is the Reynolds number effect, which when corrected for, produces test accuracy similar to the expected accuracy of the instrumentation.

The runs conducted with Propeller 4718 in inclined flow produced noticeably larger error bands than the uniform flow runs. Some of the increase was due to the inclusion of one or two questionable runs in the inclined flow case. The general policy was to remove bad runs from results if justifying errors where found. If errors were concluded to be random for given gages, then the result was not removed. This type of error can be seen in Figure 13. Another possible error in the inclined flow runs was the use of speed corrections generated from the uniform flow runs. Any difference in the speed dependence between inclined and uniform flow runs would show up as an error in the inclined flow result. It appeared that on some gages with large speed corrections, for example, Gage 25, the $\overline{C}_p$ values in inclined flow did not collapse onto the fitted curve as well as in uniform flow. Another possible source of error in inclined flow could have resulted from instrumentation problems associated with maintaining and measuring carriage speed that occurred at the beginning of the inclined-flow measurements with Propeller 4718.

The average error bands generated from runs of Propeller 4679 in inclined flow and uniform flow are both noticeably larger than the best case. Table 8b indicates many gages having numerous bad runs that were not removed from the error analysis, implying no obvious gage malfunction. It was generally felt that the gages on Propeller 4679 were less reliable due to previous use on two other tests. These gages were more prone to zero shifts during a given run, which would cause random errors in the pressure measurements. Fortunately, most gages performed properly in both uniform and inclined flow so that $\overline{C}_p$ versus J measurements were available. Speed correction problems did not occur in the error analysis due to the small speed dependence of most of the gages.

Generally, error bands were reduced on both propellers when the second-order curve fit was used. From Figure 17 it is obvious that certain gages displayed a nonlinear behavior that was better fitted by the second-order curves. Where no improvement occurred using a higher order fit, then the $\overline{C}_p$ versus J relationship could be assumed linear.

Accuracy in the measurement of carriage speed and propeller rotational speed would also affect the overall accuracy of the pressure measurements. No determination was made to evaluate the accuracy of these measured quantities, but given the good results of the best-case test error, it was felt these measurements were accurately made.

The only remaining assumption in the measurement process that could be questioned was the equating of the carriage speed to the advance speed V_A through the propeller disk. This assumption is always made in basin testing; however, with the large size of the dynamometer, small amplitude, low-frequency standing waves were setup after a few runs. These standing waves caused small additional velocities in the basin. It was assumed that this effect would average out over a run, and given the accuracy of the best case, was neglected.

The accuracy of the measured fluctuating pressures was generally good. Repeatability was the only indication of accuracy in this case because no consistent governing trend existed for unsteady pressures. Error bands with a 95 percent confidence level were calculated for first harmonic amplitude C_{p1} and first harmonic phase ϕ_1 from the repeat runs conducted at each given test condition in inclined flow. Propeller 4718 produced an average error band of $\Delta C_{p1} = \pm 0.002$ and $\Delta\phi_1 = \pm 4$ deg, while Propeller 4679 produced expected larger average error values of $\Delta C_{p1} = \pm 0.005$ and $\Delta\phi_1 = \pm 8$ deg. This average error band was relatively small for typical first harmonic amplitudes in a range greater than $C_{p1} = 0.0150$, but in some cases on the pressure side of the propeller blade, values of C_{p1} were less than 0.0050, thus causing uncertainty in the measured amplitude and also in the measured phase.

FLUCTUATING PRESSURE MEASUREMENTS AT DESIGN J

Periodic pressure measurements were obtained when the propellers were operated in inclined flow. The 7.5 deg shaft inclination produced a first harmonic, once per revolution variation in the measured pressure. A typical variation of pressure with gage angular position is shown in Figure 23. As expected, the pressure variation was primarily first harmonic, with negligible higher harmonics observed, attributed to noise. The fluctuating pressure is represented as the first harmonic pressure

coefficient amplitude $\tilde{C}_{p1}$ and the corresponding lagging cosine series phase, ϕ_1:

$$\tilde{C}_p(\theta) = \tilde{C}_{p1} \cos(\theta - \phi_1)$$

This result at design J is presented for Propellers 4679 and 4718 in Figures 24 and 25. Included in the figures are fluctuating and quasi-steady predictions. The small effect of speed or Reynolds number is depicted by the similarity in C_{p1} and ϕ_1 at two speeds. There appears to be no correlation between the Reynolds number dependency of certain pressure gages measuring mean pressure and the same gages measuring unsteady pressures.

The corrections to the fluctuating pressure measurements due to loading are shown in Figures 9 and 10 for Propellers 4679 and 4718 at design J. Note that no corrections due to loading occur at r/R = 0.9 on either propeller attributed to the use of the coverplate gage installations. The locations of the largest corrections are the 0.5 and 0.7 radius positions on the suction side of Propeller 4718. These loading corrections were determined from a quasi-steady analysis of the measured mean load corrections in uniform flow. This approximation places some uncertainty on the unsteady measurements associated with gage positions with large corrections, and the difference between the corrected and uncorrected pressure measurement could, conservatively, provide an envelope for the actual measured result.

Before correlating the measured fluctuating results to the unsteady and quasi-steady predictions, a detailed description of the quasi-steady technique is necessary.

QUASI-STEADY PROCEDURE FOR PREDICTING FLUCTUATING PRESSURE DISTRIBUTIONS

The quasi-steady analysis for predicting the fluctuating pressures was an adaptation of a quasi-steady procedure by McCarthy[32] for predicting fluctuating thrust and torque on a propeller. The procedure predicts the fluctuating propeller loads from the steady open-water propeller performance characteristics. The procedure is applied to predict unsteady pressures using the $\overline{C}_p$ versus J curves in Figure 13. The procedure is identical to the technique used earlier to approximate

the fluctuating load correction. Fluctuating pressure is produced by the variations in local advance coefficient, $J(\theta)$ and resultant inflow speed $V_R(\theta)$ as the propeller blade rotates through a spatially nonuniform wake.

In inclined flow, the quasi-steady procedure is relatively simple due to the simple nonuniform wake. The flow inclination, as seen in Figure 26, produces a uniform downward component of tangential velocity V_T. This tangential velocity component adds to the propeller's angular rotational speed when the blade is moving upward at θ = 270 deg, and subtracts from its rotational speed at θ = 90 deg as shown in Figure 26b. This variation in rotational speed produces a variation in local advance coefficient $J(\theta)$, with a maximum value at θ = 90 deg, and a minimum value at θ = 270 deg, as shown.

$$Jmax = J(90) = \frac{V_A}{D(n-V_T/2\pi r)} \quad Jmin = J(270) = \frac{V_A}{D(n+V_T/2\pi r)}$$

where V_T is V_c sin (7.5 deg), and $V_A \simeq V_c$

The sinusoidal variation in $J(\theta)$ produces a sinusoidal variation in pressure in the blade based on the $\overline{C}_p$ versus J curves in Figure 17 as shown in Figure 26c. Also, J_{min} and J_{max} produce corresponding pressure coefficients, C_{pJmin} and C_{pJmax}. The maximum and minimum pressures calculated from the pressure coefficients are,

$$(p-p_o)_{Jmax} = C_{pJmax} \cdot 1/2\rho V_R^2 \ (90)$$

$$(p-p_o)_{Jmin} = C_{pJmax} \cdot 1/2\rho V_R^2 \ (270)$$

where

$$V_R^2 \ (90) = V_c^2 + [2\pi r(n-V_T/2\pi r)]^2$$

$$V_R^2 \ (270) = V_c^2 + [2\pi r(n+V_T/2\pi r)]^2$$

The first harmonic pressure coefficient is approximated by,

$$\tilde{C}_{pl} = \frac{\frac{(p-p_o)_{Jmax}}{2} - \frac{(p-p_o)_{Jmin}}{2}}{1/2\rho[V_c^2+(2\pi rn)^2]}$$

This information produces a lagging cosine series phase angle ϕ_1, as defined by Equation (1), of 270 deg if C_{pl} is negative, and 90 deg if C_{pl} is positive. Substituting into the previous equations, C_{pl} can be represented as

$$\tilde{C}_{pl} = \frac{C_{pJmin}}{2}\left[\frac{V_c^2+(2\pi rn+V_T)^2}{V_c^2+(2\pi rn)^2}\right] - \frac{C_{pJmax}}{2}\left[\frac{V_c^2+(2\pi rn-V_T)^2}{V_c^2+(2\pi rn)^2}\right]$$

The first harmonic pressure coefficient $\tilde{C}_{pl}$, can be seen to depend upon two effects. One is the local variation in J producing the C_{pJmin} and C_{pJmax} terms. The other is the speed correction of those terms due to the local variation in speed V_R, represented by the ratios inside the brackets. Term C_{pJmin} will always be increased by the speed correction by a constant ratio, dependent upon radial position for a given operating condition. In a similar manner, C_{pJmin} will always be decreased.

From this result, trends can be observed in the predicted quasi-steady first harmonic pressure coefficients. Figure 27 demonstrates typical quasi-steady calculations on the suction and pressure sides of the propeller blade. Note that the magnitude of the slopes of the $\overline{C}_p$ versus J plots for the suction side and pressure side of the blade are roughly similar, but the pressure side has a negative slope while the suction side has a positive slope. This slope polarity difference will produce an opposite effect of the quasi-steady speed correction in calculating the first harmonic pressure coefficients. The speed correction will tend to decrease the first harmonic pressure coefficient on the pressure side of the blade, and increase it on the suction side. This trend is due to only the difference in local velocities at J_{max}, and J_{min}, and the signs of slopes of the $\overline{C}_p$ versus J curves.

The speed correction term produces a dependency of the first harmonic pressure coefficient on the magnitude of the mean pressure coefficient, $\bar{C}_p$. Since the velocity correction terms are constants multiplied by C_{pJmin}, and C_{pJmax}, increased values of C_{pJmin} and C_{pJmax} will produce an increased value of $\tilde{C}_{pl}$. This trend is important when observing $\tilde{C}_{pl}$ over a range of J, and when considering the accuracy of the first harmonic pressure coefficients, $\tilde{C}_{pl}$ generated from values of $\bar{C}_p$ with large speed effects.

The quasi-steady analysis represents an intuitive description of the fluctuating pressure, excluding any unsteady effects. It provides a good base for comparison of the measured data for the two propellers, and the unsteady theory by Tsakonas.[33,34] The correlation between the measured and quasi-steady results can also be compared to similar correlations of fluctuating blade loads performed by Boswell and Jessup.[5]

CORRELATION OF FIRST HARMONIC PRESSURE COEFFICIENTS WITH THEORY

The measured first harmonic pressure coefficient in Figures 22 and 23 generally tend to decrease in amplitude from leading to trailing edge. This trend was generally approximated by the quasi-steady approach, but with an amplitude 30 percent to 50 percent less than the measured result. This result matched similar correlations of quasi-steady and measured fluctuating blade loads by Boswell and Jessup.[5,6] Intuitively, the observed trend from leading edge to trailing edge was reasonable due to the higher sensitivity of the leading-edge pressures to angle-of-attack variation. Good correlation with the quasi-steady predictions was due partially to the shaft-rate frequency of the nonuniform tangential wake. Fluctuating effects will be small for low-frequency, shaft-rate variations in the wake. Therefore, with small fluctuating effects, a quasi-steady analysis should provide close agreement to the measured result. Also, good correlation may be due to the incorporation of measured mean results in the quasi-steady procedure, avoiding possible errors by the prediction of mean pressure variation with advance coefficient. The unsteady theory by Tsakonas et al.[33,34] produced a reduction in the first harmonic pressures in the first quarter chord at each radial station. The extreme nature of this trend as compared to both the measured and quasi-steady results produced little confidence in the accuracy of the method of Tsakonas et al.

The quasi-steady method and the experiment both indicate that the first harmonic amplitudes of the pressures are larger on the suction side of the blade than on the pressure side of the blade. This trend was consistent for both propellers except for the measurements nearest to the leading edge at the 0.5 and 0.7 radius stations, where the results on the pressure side were larger than the results on the suction side. This variation in fluctuating loading between the suction and pressure sides of the blades did not occur in the theoretical prediction method of Tsakonas et al., further supporting the hypothesis that this method does not adequately predict the distribution of pressures.

On the suction side of Propeller 4718 at the 0.5 and 0.7 radius positions, the quasi-steady analysis at certain chordwise positions over-predicted the measured first harmonic amplitudes. These over-predicted values were partially due to the strong dependence of the quasi-steady result on the magnitude of the mean pressure coefficient, $\overline{C}_p$. Some of the $\overline{C}_p$ measurements from the 40 to 70 percent chordwise locations exhibited a relatively strong speed dependence. The mean pressure coefficients were corrected upward for the speed effect, leaving $-\overline{C}_p$ values greater than average over the range of speeds conducted. This would artifically increase the quasi-steady results. A calculation of the quasi-steady results with reduced $\overline{C}_p$ values did not reduce the quasi-steady first harmonics enough to match the general trend completely, possibly implying inaccuracies or over-simplifications in the quasi-steady analysis.

CORRELATION OF FIRST HARMONIC PHASE ANGLE WITH THEORY

The measured first harmonic phase angles were generally in the range expected. On the suction side of the blade, most phase angles ranged from 60 deg to 120 deg, while on the pressure side of the blade, values ranged from 270 deg to 333 deg. There was no specific variation in phase angle over the chord. Cases of gradual phase angle increase, decrease, and consistency occurred over the chord, with some instances of sudden drops in phase angle near the trailing edge. No overall trend in phase angle occurred, but certain blade sections produced similarities between the two propellers tested.

On the suction side of the blade, at the 0.5 radius position, the phase angle of the first harmonic on the two propellers was strikingly similar. Values of 120 deg at the leading edge dropped slightly below the quasi-steady phase of 90 deg, remaining constant over most of the chord. In each case, the phase dropped substantially at the trailing edge, to approximately 100 deg. This drop in phase angle at the trailing edge was not predicted in the quasi-steady analysis, but justification for it existed in the $\overline{C}_p$ versus J curve slopes in Figures 21 and 22. The $\overline{C}_p$ versus J slopes on the suction side of the blade reversed polarity at the 0.5 and 0.7 radial positions on Propeller 4718 and at the 0.5 radial position on Propeller 4679. This polarity reversal could have caused a 180 deg phase angle shift at these gage locations, which was supported by the experimental results. This phase angle shift did not show up in the quasi-steady predictions due to the dominance of the speed correction terms coupled with small $\overline{C}_p$ versus J curve slopes and small first-harmonic amplitudes.

The first-harmonic phase angle on the blade pressure side at the 0.7 radius position (Figures 22d and 23d), was also similar for the two propellers with phase angles of approximately 300 deg, which was 30 deg greater than the quasi-steady prediction of 270 deg. There was an extreme speed dependence of the phase angle for Propeller 4718 at the chordwise positions from the midchord to the trailing edge. This variance in phase angle is attributed to the small measured amplitudes at the corresponding locations causing inaccuracies in the measured phase angles.

At the 0.9 radius position (Figures 22e, 22f, 23e, and 23f), the four conditions, representing the two propellers and two sides of the blades, each show measured phase angles 30 deg to 60 deg greater than the quasi-steady results of 90 deg and 270 deg on the suction and pressure sides, respectively. Also, in three of the four cases, the phase angles increased from leading edge to trailing edge along the chord. These trends could be related to effects of the tip-vortex rollup process.

On the pressure side of Propeller 4718 at the 50 percent chord, 0.5 radius position, the first harmonic pressure was 180 deg out of phase from the expected value. Figure 22b demonstrates this unusual variation from the general trends. This behavior implies a phase shift in the first harmonic amplitudes along the chord at the 50 percent position. At this particular gage location, there was no loading effect, as shown in Figure 9b. Therefore, no uncertainty was introduced due to the

quasi-steady loading correction. Also there was a negligible variation in $\overline{C}_p$ with speed. This implies good credibility in measurement at this gage location.

The quasi-steady prediction at this gage location (0.5R, 0.5x/c) supported the measured result by agreeing with both the first harmonic phase angle and amplitude. The good quasi-steady correlation relates to the reversed slope of the $\overline{C}_p$ versus J curve in Figure 17. As J decreases, the pressure coefficient $\overline{C}_p$ decreases rather than increasing as with the other gages on the pressure side at the 0.5 radius.

This anomaly in the fluctuating pressure was supported by the steady measurements conducted over a range of advance coefficients. An obvious polarity error at this gage location would not explain this anomaly due to the correct sign of the mean pressure coefficient, $\overline{C}_p$. The evidence indicates that a real-flow phenomenon produced the unexpected behavior at this location. Separation is not an obvious hypothesis due to its location on the pressure side of the blade, but is a possibility due to the adverse pressure gradient starting at the 50 percent chord position. Physically, in uniform flow, the inclined flow, increased loading increases the pressures on the pressure side of the blade and thereby decreases the local velocity. At this gage location (0.5R, 0.5x/c), the local velocity increased instead of decreasing. The anomaly could be due to a severe local effect of various induced velocities in the flow regime, possibly causing large cross flows.

UNSTEADY PRESSURE MEASUREMENTS OVER A RANGE OF J

The first harmonic pressure coefficients and phases were measured over a range of advance coefficients for both propellers, and are shown in Figures 28 and 29. Quasi-steady predictions of the first harmonic amplitudes were calculated over similar J ranges and plotted in Figures 30, 31, and 32.

A general trend on the suction side of the blades indicated a decrease in the measured first harmonic amplitudes in the midchord region, with decreasing values of J. The 0.9 radius position did not follow this trend. Propeller 4679, at 0.9 radius, produced a sharp increase in the first-harmonic amplitude at the leading edge with decrease in J, while on Propeller 4718 the same trend occurred to a lesser degree. This trend at the tip could be due to the separation of the tip vortex as J decreases.

The variation of first harmonic amplitudes with J on the pressure side of the blades appeared to be less than on the suction side. A general trend occurred at the 0.5 and 0.7 radius positions where the leading-edge values dropped with decreasing J, while the midchord values slightly increased. Dissimilar trends occurred at the 0.9 radius position for both propellers, again possibly caused by tip-vortex effects.

The first harmonic phase angles on either propeller did not produce any consistent trend with variation in J. The phase angles in various cases increased, decreased, or remained constant. Some evidence indicates that the variations in phase angle with J were coupled to trends in amplitudes that deviated from the previously stated general trends. The suction side of Propeller 4718 at the 0.5 and 0.7 radius positions showed large variations in phase in the mid- to aft-chord region. These could be coupled to larger-than-expected amplitudes in the same region at low J.

Quasi-steady predictions of first-harmonic amplitudes were calculated, producing good correlation with the measured trends on the suction and pressure sides of the blade. As with the design J correlations, the quasi-steady analysis underpredicted the measured amplitudes by 30 to 50 percent. On the blade suction side, the quasi-steady result produced decreasing amplitudes with J in the midchord region, similar to the measured result. On the blade pressure side, the quasi-steady calculation produces a similar consistent trend of first harmonic amplitude with J over most of the chord with a similar decrease in amplitude at the leading edge.

The quasi-steady analysis was performed on Propeller 4718 using both the first and second order $\overline{C}_p$ versus J curves. On gages where a noticeable nonlinearity occurred, variations in the quasi-steady predictions occurred, as seen by comparing Figures 30 and 31 in the leading-edge regions. It appears that the second-order curves more closely resemble the measured results implying dependence of the fluctuating pressures on the nonlinear variation of $\overline{C}_p$ with J observed in uniform flow.

The quasi-steady procedure generally predicted a constant first-harmonic phase angle with J of $\phi_1 = 90$ deg on the blade suction side, and $\phi_1 = 270$ deg on the blade pressure side. This consistency of phase angle weakly supports the concept that phase angle variations with J are related to variations in the trends observed in

both the measured and predicted amplitudes. These variations could be produced by effects not considered in the quasi-steady procedure, such as unsteady flows of the tip vortex, hub, and fairwater.

SUMMARY

Experiments were described in which blade-surface pressures were measured on two model-side controllable-pitch propellers. Pressures were measured at 40 locations on the blade surface in uniform and inclined flow, over a range of Reynolds number and advance coefficients. The discussion of experimental technique included descriptions of the hardware and data analysis systems. The results are summarized as follows:

1. Pressure measurement instrumentation

a. At best, pressures were measured on propeller blades with accuracies comparable to laboratory calibrations of ± 0.07 psi.

b. The thin blade gage installation configur tion (Figure 5b) displayed negligible loading effects, while the thick blade gage installation configuration (Figure 5a) showed substantial loading effects of varying magnitude.

2. The mean pressure distributions produced fair correlation with the equivalent two-dimensional theory with the following deviations observed.

a. The $\overline{C}_p$ distribution at the 0.5 radius showed a marked deviation from the theoretical prediction on the suction side of the blade, resulting in an unexpected suction peak at the 50 to 70 percent chord position.

b. Propeller 4679, characterized by wide blades with large swept tips, at the 0.7 radius on the suct n side, produced a leading-edge suction peak attributed to local blade shape. Also, a reduction occurred in suction pressure through the midchord with increased suction pressures towards the trailing edge. At the 0.9 radius on the suction side, suction pressures were greater than predicted, hence C_{pmin} was less than predicted.

3. At constant J, substantial variations in $\overline{C}_p$ occurred at certain gage locations over a Reynolds number range of 2 to 5×10^6. The following results are noted:

a. The variation of $\overline{C}_p$ with R_n appeared independent of J.

b. At the 0.5 and 0.7 radii, variation of $\overline{C}_p$ with R_n occurred at numerous gage locations with the largest variation occurring at the 0.5 radius on the suction side for Propeller 4718.

c. At the 0.9 radius, suction side, the $\overline{C}_p$ variation on Propeller 4679 occurred toward the leading edge while the C_p variation on Propeller 4718 occurred toward the trailing edge.

d. Roughening the leading edge with sand produced no noticeable change in the $\overline{C}_p$ distribution.

4. The variation of $\overline{C}_p$ with J led to the following observations:

a. At most blade locations, $\overline{C}_p$ varied linearly with J. Slight second-order nonlinearity occurred on Propeller 4718 at the leading edges and 0.9 radius. On Propeller 4679, nonlinearity occurred at various, more numerous locations on the blade.

b. Generally, over the chord, $\overline{C}_p$ values on the pressure side of the blade were more sensitive to J than on the suction side at the 0.5 and 0.7 radius, while the reverse was true at the 0.9 radius.

c. On the suction side of the blades at the 0.5 and 0.7 radii the chord position of insensitivity to J occurred not at the trailing edge as expected, but around the 80 percent chord position.

d. The sensitivity of C_p to J, increased toward the leading edge, as expected.

5. Unsteady pressure measurements were performed with the propellers operating in 7.5 degree inclined flow at design J. Quasi-steady and unsteady theoretical comparisons were made, resulting in the following:

a. Measured first harmonic pressure coefficient amplitude $\tilde{C}_{p1}$ and phase angle ϕ_1 were independent of Reynolds number.

b. The quasi-steady predictions of $\tilde{C}_{p1}$ underestimated the measured values by 30 percent to 50 percent, but generally followed the measured $\tilde{C}_{p1}$ distribution along the chord.

c. The quasi-steady first harmonic phase angle prediction of $\phi_1 = 90$ deg on the suction side and $\phi_1 = 270$ deg on the pressure side of the blade was only approximately matched by the measured results. Variations in these predictions occurred at the various radial and chord positions with no obvious trends observed. In some cases, sharp phase changes occurred near the trailing edge.

d. The prediction of $\tilde{C}_{p_1}$ from the unsteady theory of Tsakonas et al.,[31] produced an unrealistic drop in $\tilde{C}_{p1}$ near the leading edge. Also, the $\tilde{C}_{p1}$ distribution was identical for the suction and pressure sides of the blade at a given blade section, contrary to measured results. The validity of the unsteady procedure of Tsakonas et al., appears to be questionable based on consistently poor correlation with measured results in inclined flow.

CONCLUSIONS

The following conclusions were made based on the summarized results:

1. The pressure measurement system performed satisfactorily, providing sufficient measurement accuracy for the present state of theoretical correlations. Of the pressure distributions that were measured, the most reliable data are considered to be those showing low speed and loading effects.

2. The measured mean pressure distributions provided fair correlation with equivalent two-dimensional theoretical pressure distributions. Some large discrepancies were hypothesized as followed:

a. At the 0.5 radius on the suction side, unexpected measured suction peaks are thought to be caused by flow interference at the hub and include three-dimensional effects.

b. The irregularities of the measured pressures on the suction side of Propeller 4679 at the 0.7 and 0.9 radii are felt to be due to the influence of three-dimensional effects and tip-vortex formation from the leading edge.

3. Variation in the pressure distribution with Reynolds number is believed to be caused by real flow effects, and not instrumentation errors. Reynolds-number effects influenced by three-dimensional separation and tip-vortex formation are possible causes. Relatively thick blade sections, and highly-swept leading edges are the primary factors producing the above effects.

4. Based on the results of the leading-edge roughness tests, it is concluded that both propellers operated with turbulent boundary layers throughout the Reynolds number range tested.

5. At the 0.9 radius, the unexpectedly large sensitivity of $\overline{C}_p$ to J on the suction side of Propeller 4679 is attributed to tip-vortex separation.

6. Good correlation with the quasi-steady predictions is attributed to the low frequency of the nonuniform wake, and the use of measured mean pressures in the quasi-steady procedure. The general underestimation by the quasi-steady technique was similar to quasi-steady correlations with measured fluctuating blade loads by Boswell and Jessup.[5,6]

7. Sharp increases in $\tilde{C}_p$, at the 0.9 radius of Propeller 4679 are attributed to tip-vortex separation.

8. Insufficient data were obtained to compute lift coefficients for individual radii.

9. Calculations of pressure distribution for measured sections showed large deviations from those computed for the design shape, caused by local irregularities on the surface. It is believed that in viscous flow, a more conventional pressure distribution would occur. (See the Appendix)

RECOMMENDATIONS

Work should be done in the near future to complete the effort that has been described. Many of the unresolved questions should be resolved by performing the following:

1. The experimental results should be compared to the results of the latest propeller lifting surface theories, such as the theory of Kerwin and Lee.[35] This will provide a more exact representation of the mean and unsteady pressure distributions than the methods used in this report.

2. Water-tunnel tests should be conducted on Propellers 4679 and 4718. Cavitation tests would verify the minimum-pressure areas on the blades. Thrust and torque measurements could be used to correlate integrated pressures for the two propellers. Finally, flow visualization techniques should be used to identify possible areas of transition and separation over a range of Reynolds number.

3. New gage mounting techniques should be developed that minimize the influence of blade loading and maintain a smooth blade surface in the region of pressure measurement on the blade. Also, a technique should be devised so that a greater number of points along the blade chord could be measured. This would permit calculations of integrated load for thrust and torque correlations.

ACKNOWLEDGMENTS

The author is indebted to many members of the staff at the David W. Taylor Naval Ship Research and Development Center. Without the combined effort of these individuals, the task could not have been performed. Special appreciation is extended to Ben Wisler for maintaining the 1000 hp dynamometer and the blade pressure measurement systems, to Mike Jeffers for developing and maintaining the computer data collection and analysis procedures, to John Webb for maintaining the pressure gage electronics, to Douglas Dahmer for assisting with test procedures, and data reduction, and to Dona Nigro for much of the final data reduction and plotting. Special thanks go to Robert Boswell for his guidance and support provided during all stages of the experiments.

APPENDIX

COMPARISON OF MEASURED AND DESIGN GEOMETRY OF PROPELLER 4718

In an attempt to explain the discrepancies between the measured and design pressure distributions, the model blade section geometry was investigated. Detailed measurements of Propeller 4718 were made and compared with design section geometry at the 0.5, 0.7, and 0.9 radial positions. Pressure distributions were calculated using the measured geometry and were compared to design predictions.

Measurements were taken while each blade was supported in a fixture positioning the blade at the design pitch. No measurement of pitch was obtained, because the blades were not attached to the hub. The increased complication of measuring actual pitch was not considered necessary, because of the good agreement between measured and predicted pressures near the blade leading edges at design conditions. The primary concern was the effect of the general variations from design in the geometry of the sections.

Measurements were obtained using a Validator coordinate measuring machine coupled to a PDP 11 minicomputer. The computer was programmed to automatically measure vertical distances to the blade surface along the 0.5, 0.7, and 0.9 radii positions at 0.5-degree angular increments across the blade surface. Figure 33 shows the measuring arrangement. Upon completion of measurements on the suction side, the blade was rotated 180 deg in the fixture for measurements on the pressure side of the blade. Approximately 120 points were measured at the 0.5 and 0.7 radii, and 90 points at the 0.9 radius on each side of the two blades on which the surface pressures were measured. The measurements of Cartesian Coordinates (x,y,z) were stored on a 10 megabyte disk pack interfaced to the minicomputer. Later, the data were transferred to magnetic tape, and stored on file on a CDC 6700 computer for further analysis.

The measured results were transferred from Cartesian Coordinates as measured, to section offsets for comparison to design values. The corrdinate transformation program, REVERSE,* was used to convert the measured blade-surface points to section offsets. To make the transformation, the position of the nose-tail line was needed. To define the nose-tail line the extreme leading and trailing edge points must be

*Reported informally by M.J. Chambers and T.E. Brockett in NSRDC TN 282, "Computer Programs for Calculating Propeller Geometry," (November 1973).

measured. These measurements are very difficult to perform and are subject to error. In this case, the nose-tail line was specified by calculating it from design values of chordlength, pitch, skew, and rake. Actual values of pitch, skew, and rake occurring during the pressure measurement test could not be measured. Therefore, design values were used and varied slightly to place the measured offsets close to the design values. The relative position of each measured offset remained constant, while the section was displaced to match the design section. This was performed by calculating two common points near the ends of each section, and adjusting the measured section to minimize the difference in the location of the points between the two sections.

MEASURED RESULTS

Figure 34 shows the comparison between the measured and design blade sections at the 0.5, 0.7, and 0.9 radial positions. Table 9 lists the offsets of Blade C at the 0.7 radius. Each figure shows the section properly proportioned, and expanded to allow a more detailed comparison. In all cases, the general measured section shape matches the design shape quite well. The expanded section views indicate a tendency for the measured section to be thicker than design over most of the section except at the leading edge where the measured section is thinner. This could be indicative of the manufacturing process, where extensive hand finishing at the leading edge is necessary. The largest measured deviation in offset was approximately 0.006 in. on the suction side of Blade B at the 0.7 radius, as shown in Figure 34d.

A possible error could have occurred, influencing the offset measurement uniformly across the chord. An error in the measurement of the reference axis of the blades would have increased the offsets on both sides of the blade, thus explaining the extra thickness measured. A thicker leading edge would result, perhaps obscuring a critical problem with leading-edge shape. It is doubtful that this error occurred.

A variety of localized irregularities in blade shape were also measured over most of the sections. Where surface pressures were measured, roughness was caused by gage cover plates protruding above the surrounding blade surface. This was most prevalent at the 0.9 radius where the coverplate gage configuration was used

exclusively. On the opposite side of the blades, roughness was measured due to the resin filled gage wire channels. In most cases, the resin potting material was not satisfactorily faired into the blade surface. This was not viewed as a serious problem because pressures were not measured in these areas. Pressure distribution calculations were performed replacing the rough side of the blade with smooth design offsets. Results showed that the irregularities on one side of the blade did not influence the pressure distribution on the other side of the blade.

CALCULATION OF PRESSURE DISTRIBUTIONS FROM MEASURED SECTIONS

Pressure distributions were calculated from measured offsets using the procedure of Brockett.[30] The measured sections were assumed to be at the two-dimensional ideal angle of attack (see Table 2), representing the design J condition. To perform the pressure distribution computations, the measured offsets were modified and supplemented as described below.

1. A cosine function distribution of offsets was required for the calculation, therefore, 120 offsets were interpolated across the chord of each section. The cosine distribution produces a progressively finer increment of points towards the ends of the section.

2. The leading edge point was not measured, so a reasonable leading edge shape was extrapolated by fitting a second order curve of the form:

$$y = A_o \sqrt{x} + A_1 x$$

where A_o and A_1 = constants.
The curve passed through the leading edge with an infinite slope, and through the first reasonable measured offset, with the same slope as the interpolated offsets. In some cases the first measured offset was too close to the section centerline, possibly indicating that the section chordlength was shorter than the assumed design value. Figure 35 shows these results.

3. Details of the trailing edge appeared to be very critical for producing reasonable pressure distributions. The calculation procedure assumed the trailing-edge point to be symmetrically located about the zero offset position for the suction and pressure sides of the section. The procedure used to aline the measured offsets with design did not force the trailing-edge points to symmetrical locations. This procedure resulted in sharp kinks in the pressure-side offsets at the trailing edge, which completely altered the pressure distribution. By fairing out the kink at the trailing edge, reasonable pressure distributions were obtained. The modifications to the sections are shown in Figure 36. The pressure distributions varied only slightly with the extent of fairing, provided the sharp kink was eliminated.

4. The pressure distributions were calculated from equivalent two-dimensional measured section shapes. Since the measured sections were true three-dimensional shapes, the measured meanline had to be reduced to its equivalent two-dimensional value. Assuming the design meanline distribution of a NACA 66 airfoil section of a = 0.8 meanline, the offsets were adjusted to have the camber producing the required lift coefficient in two-dimensional flow. The coordinates on the suction and pressure side were reduced as follows:

$$Y_{2D} = Y - (f_M - f_{M2D}) \ (E_c/f_M)$$

After the above modifications were made, potential flow pressure distributions were calculated for each of the measured sections. Figure 37 shows the comparison predicted from measured and design offsets. Also shown is the difference between the measured and design offsets, expanded by a factor of ten. The pressure distributions predicted from measured offsets generally matched the design curves over most of the chord. Extreme fluctuations in the pressure distribution occurred over most of the sections caused by the local irregularities in the section shape. The magnitude of the pressure fluctuations appeared to be dependent upon the change in slope surrounding the irregularity. The measured offsets produced extreme variations in pressure from design at the leading edge, partially due to the approximated leading-edge shape resulting from insufficient measured offsets at the leading edge.

LIMITATIONS OF THE PRESSURE DISTRIBUTION CALCULATION

The major limitation of the method used to calculate the pressure distribution was the inability to account for the local irregularities in the section shape in a manner compatible with real-fluid effects. The extreme fluctuations in the pressure distributions appeared to overpredict the influence of the section irregularities. This problem may be partially due to the numerical representation of the section shape used during the pressure distribution computation. The technique of Brockett[30] is a conformal mapping procedure using trigonometric interpolation polynomials to describe the section shape. A trigonometric series is fitted analytically to the offsets at the prescribed chordwise points. By requiring the series to pass through the given points, unfair offsets will produce sinusoidal variations in the section shape between points. The conformal mapping procedure then calculates the potential pressure distribution of the series-described section shape. Sharp pressure fluctuations may result from the relatively large variations in geometry between prescribed offset points.

Figure 38 shows a comparison between the section geometry created from the trigonometric series representation and the measured offsets interpolated to a cosine distribution from the measured geometry. Correlation can be seen between the pressure fluctuations and the irregularities in the section shape. In Figure 38c, the series representation of the offsets are quite close to the measured values, while Figures 38a and 38b produce distinct deviations causing changes in section slope at the points where pressure is calculated. The variations produced by the series representation in these cases is considered small compared to the size of the irregularity of the section. Therefore, it is believed that the potential flow pressure distribution calculation is reasonable from a mathematical standpoint. The details of the pressure distribution about each irregularity, in some cases, is only approximated by the series representation of the geometry, but since the measured irregularity is not sufficiently defined, a more exact pressure distribution is inappropriate.

The boundary layer must also be considered when interpreting the calculated pressure distributions of the measured sections. Small irregularities in section geometry, producing fluctuations in the potential-flow pressure distribution, will

be smoothed out by the boundary layer depending upon its thickness. Therefore, the potential-flow solution will exaggerate the variations in pressure when predicting the flow over the sections. Generally, the section irregularities are within the boundary layer over most of the section, except at the leading edge where the boundary layer is very thin. In this area, surface irregularities would cause serious pressure fluctuations, strongly influencing leading-edge cavitation. Localized flow separation tripped by surface irregularities could also occur. The effect on the pressure distribution could be very complex and unpredictable. Unfortunately, procedures for coupling the influence of the boundary layer to irregular surface pressure predictions are unavailable, so the effect can be considered only qualitatively.

SUMMARY AND CONCLUSIONS

The section offsets of Propeller 4718 were measured at 0.5, 0.7, and 0.9 radii. Using a computer interfaced to a coordinate measuring machine, one could automatically measure offsets at 0.5-deg increments across the blade sections. From the measured geometry, pressure distributions were calculated and compared to design values. The following results and conclusions were obtained:

1. The measured geometry matched the design geometry in general shape. The measured blade sections were generally slightly thicker than design over most of the chord except at the leading edge, where the measured sections were thinner possibly due to hand finishing.

2. Local irregularities in the blade shape were measured, produced by uneven potting resin, and pressure gage coverplates in the blade surface.

3. Calculated pressure distributions from the measured offsets matched the pressure distributions for the design geometry in the general shape; therefore, variations in constructed section geometry did not explain the discrepancies in the measured surface pressures. Irregularities in the blade surface produced sharp variations in the pressure distributions, but are not thought to be related to abnormalities in the measured pressure distributions.

4. The trigonometric series used to describe the blade section for the pressure distribution calculation matched the measured offsets exactly and may have represented

the actual surface reasonably well over most of the section. At the local irregularities, the fluctuations in the calculated pressure distribution approximately represented the potential flow pressure distribution of the measured blade section.

5. The pressure fluctuations predicted by the potential flow model are probably smoothed out in the real flow by the viscous boundary layer. At the leading edge, where the boundary layer is thin, pressure fluctuations due to section irregularities probably occur, and would greatly influence cavitation inception at the leading edge. This effect emphasizes the importance of improving the detail geometry of model- and full-scale propellers, especially at the leading edges.

Fi-ure 1 - Drawings of DTNSRDC Model Propellers 4679 and 4718

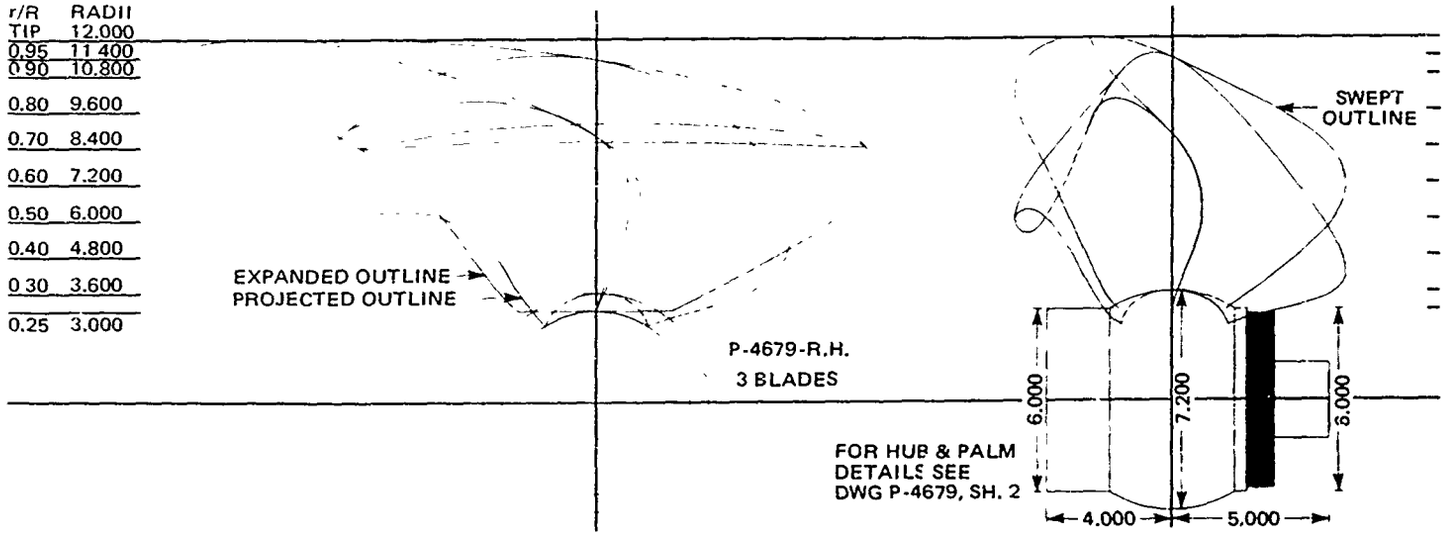

Figure 1a - Propeller 4679

Figure 1 (Continued)

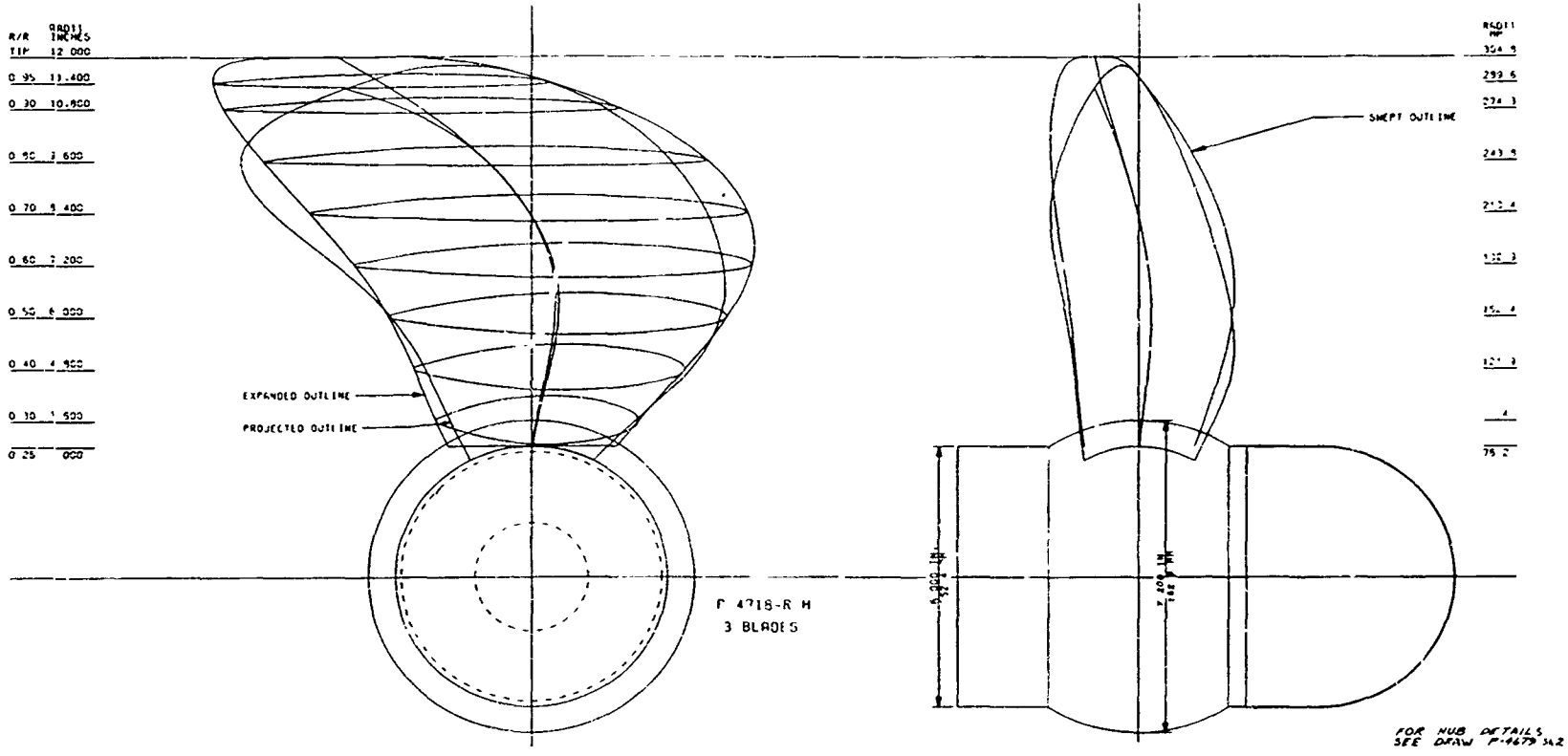

Figure 1b - Propeller 4718

Figure 2a - Propeller 4679

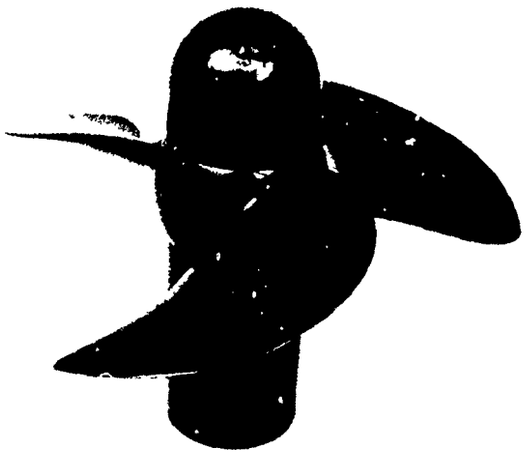

Figure 2b - Propeller 4718

Figure 2 - Photographs of DTNSRDC Model Propellers 4679 and 4718

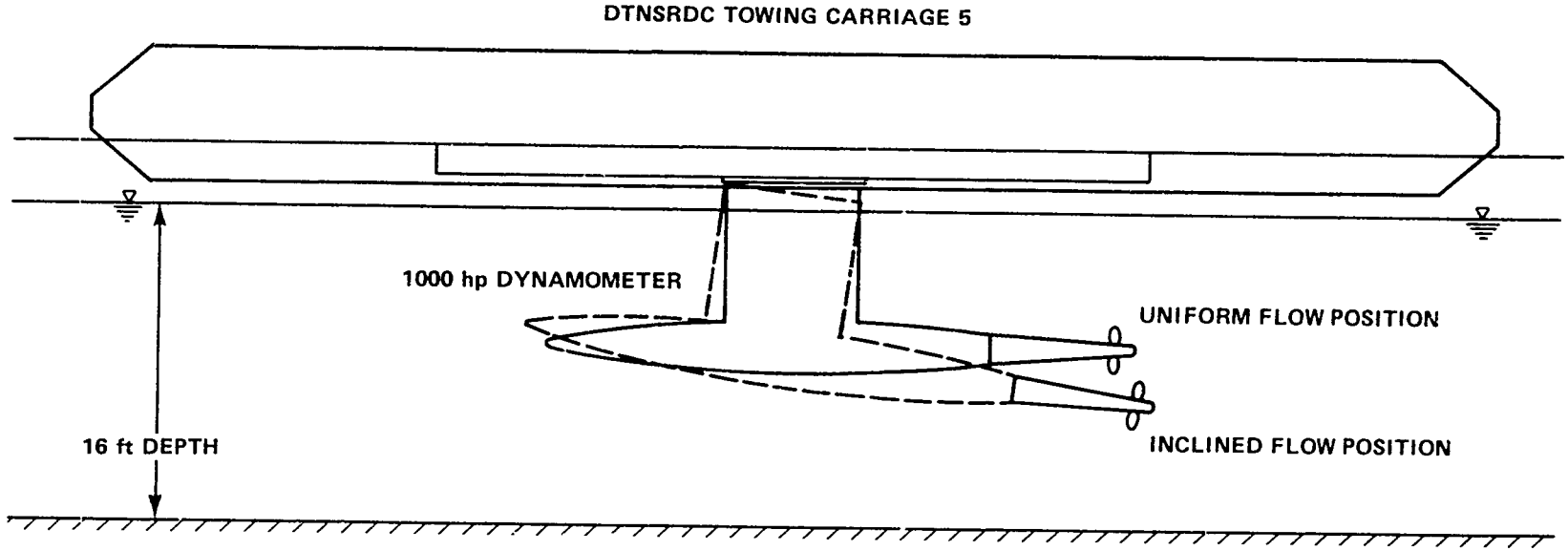

Figure 3 - Schematic of Test Arrangement Showing 1000 Horsepower Dynamometer

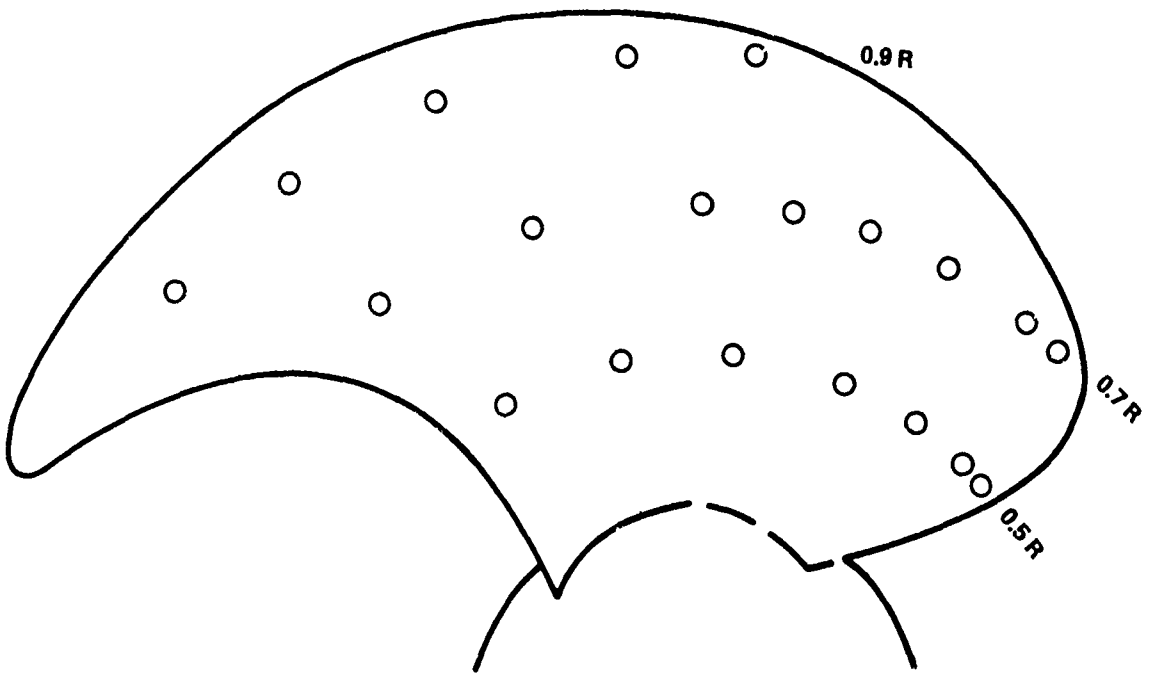

Figure 4 - Approximate Location of Pressure Transducers

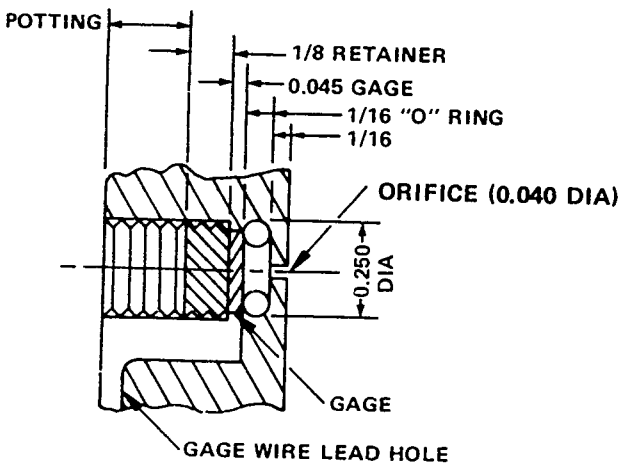

Figure 5a - Configuration on Thick Portion of Blade

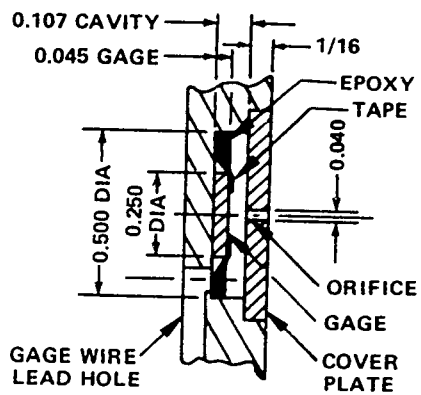

NOTE: ALL DIMENSIONS ARE IN INCHES

Figure 5b - Configuration on Thin Portion of Blade

Figure 5 - Configurations for Mounting Transducers in Helmholtz Cavities

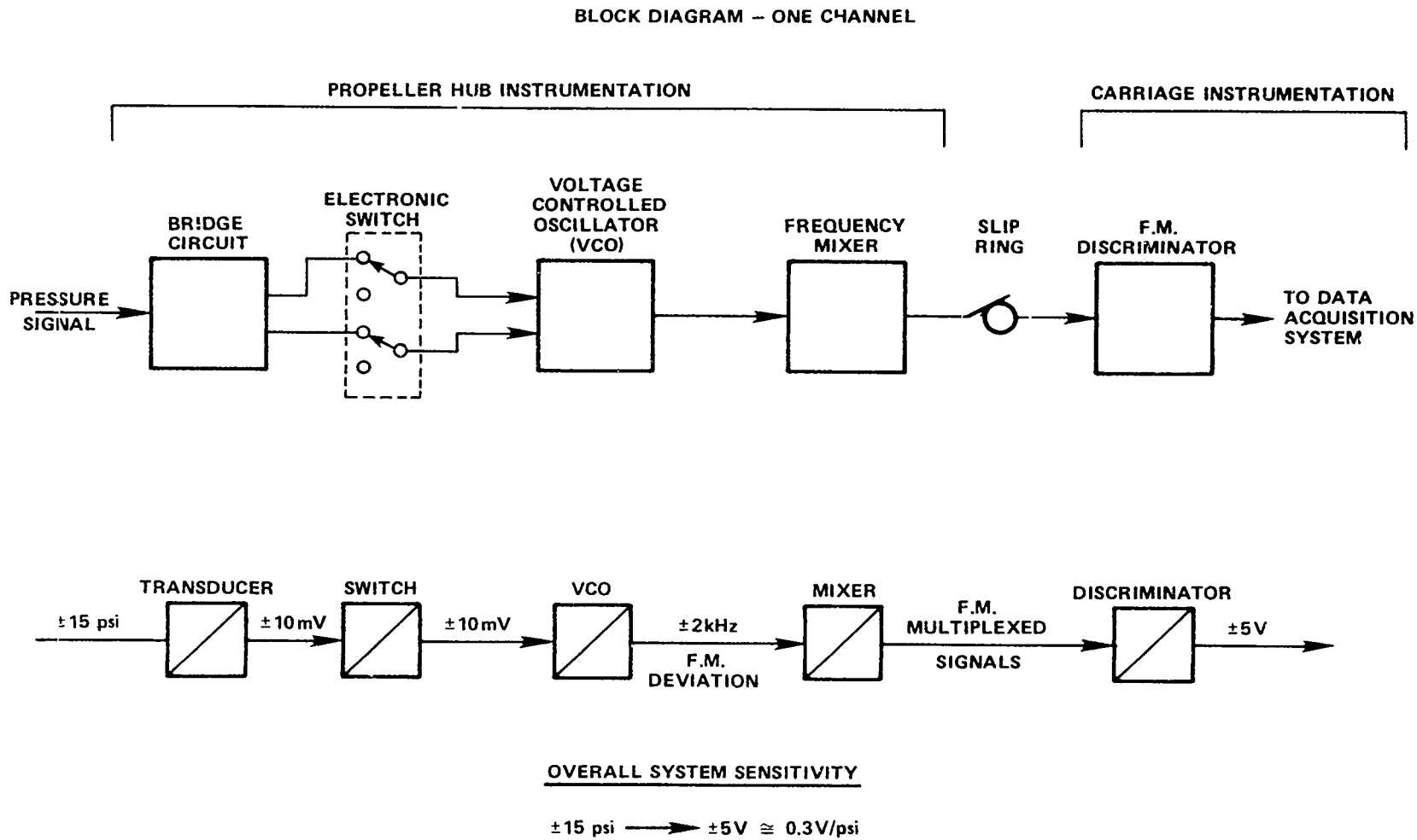

Figure 6 – Schematic of Instrumentation for Typical Pressure Transducer Channel

Figure 7 - Variation of Mean Loading Pressure Coefficient with Advance Coefficient for Propeller 4718

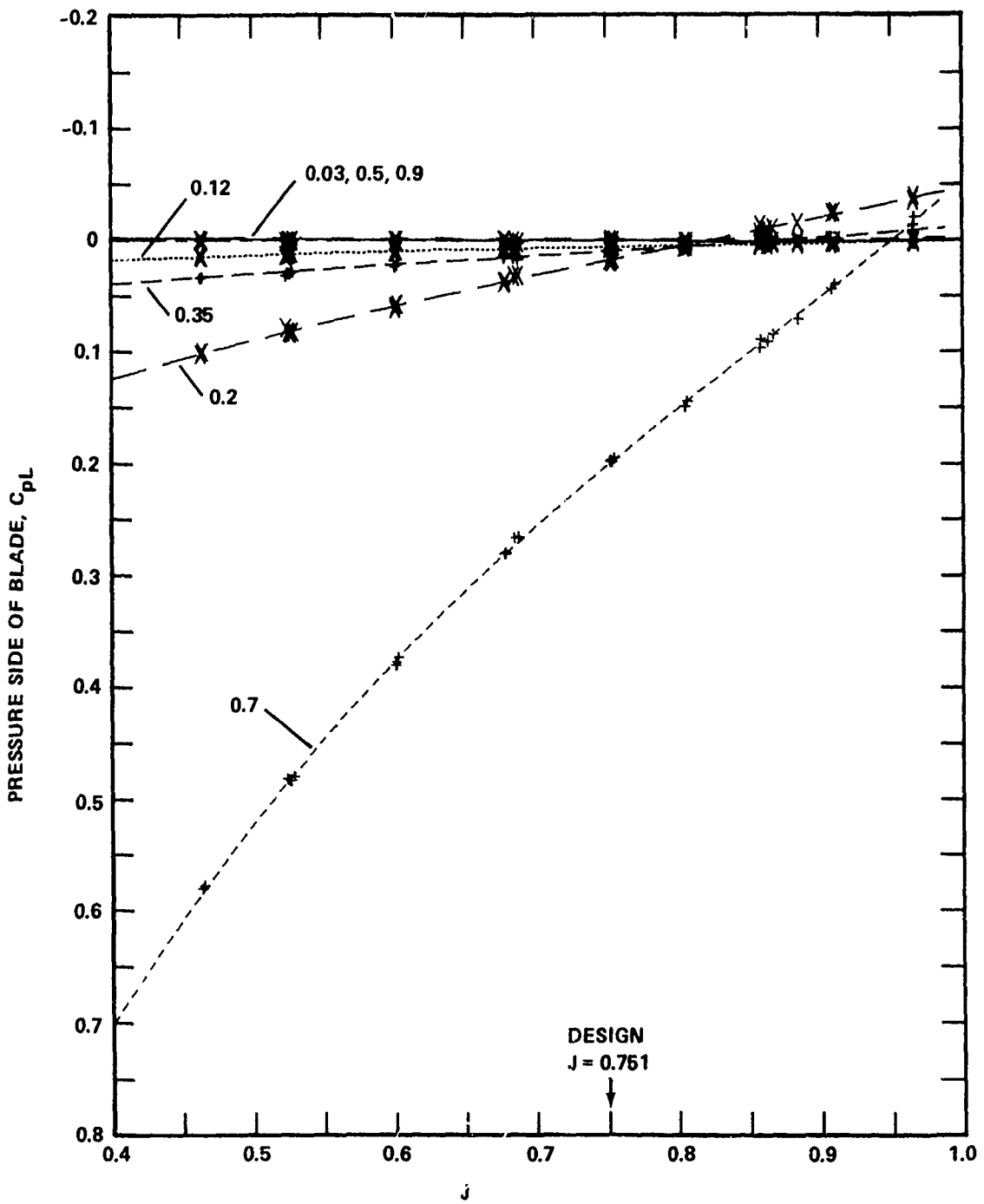

Figure 7a - r/R = 0.5, at Measured x/c Positions, V_{Ro} - 27.4 Feet per Second

Figure 7 (Continued)

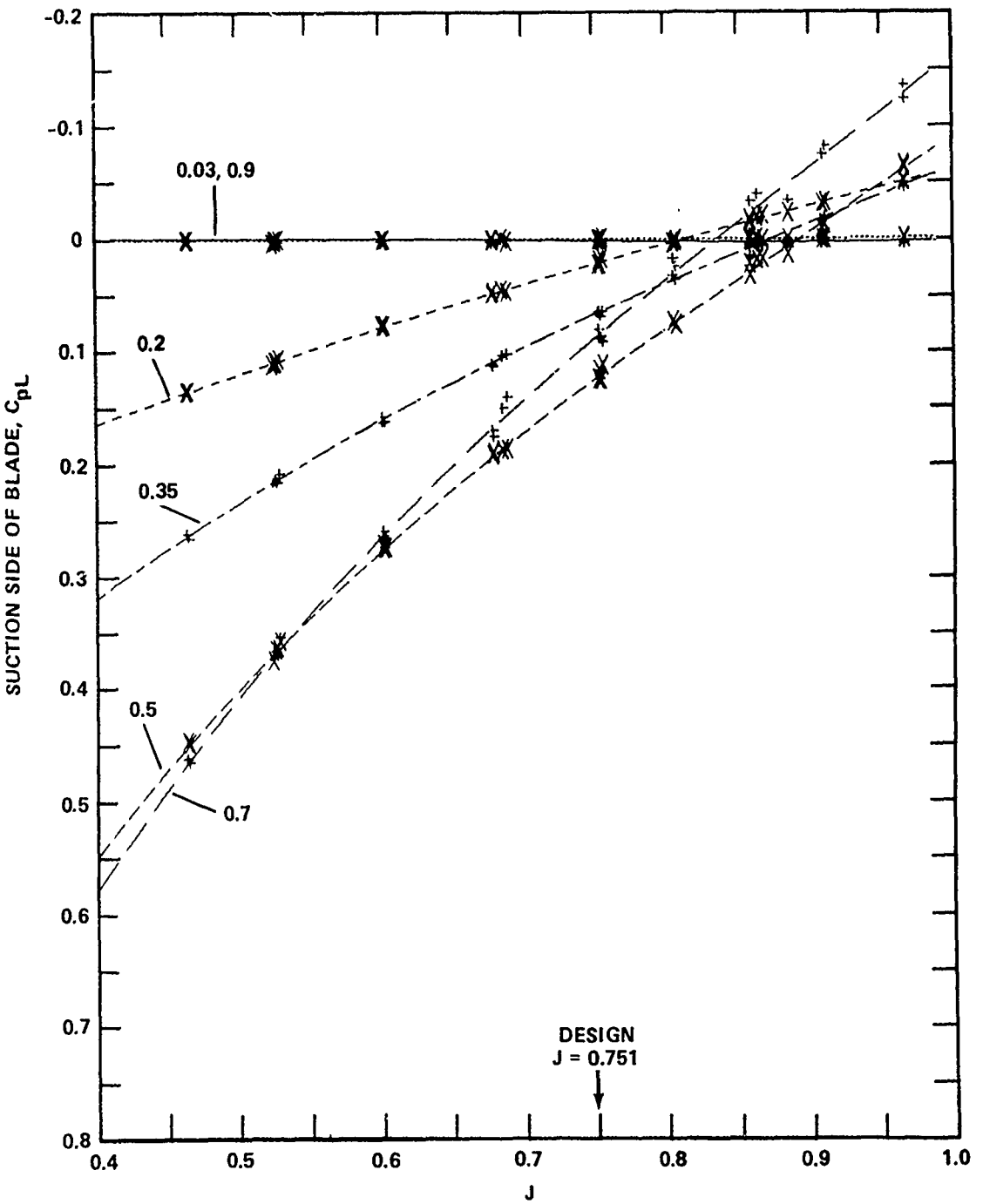

Figure 7 (Continued)

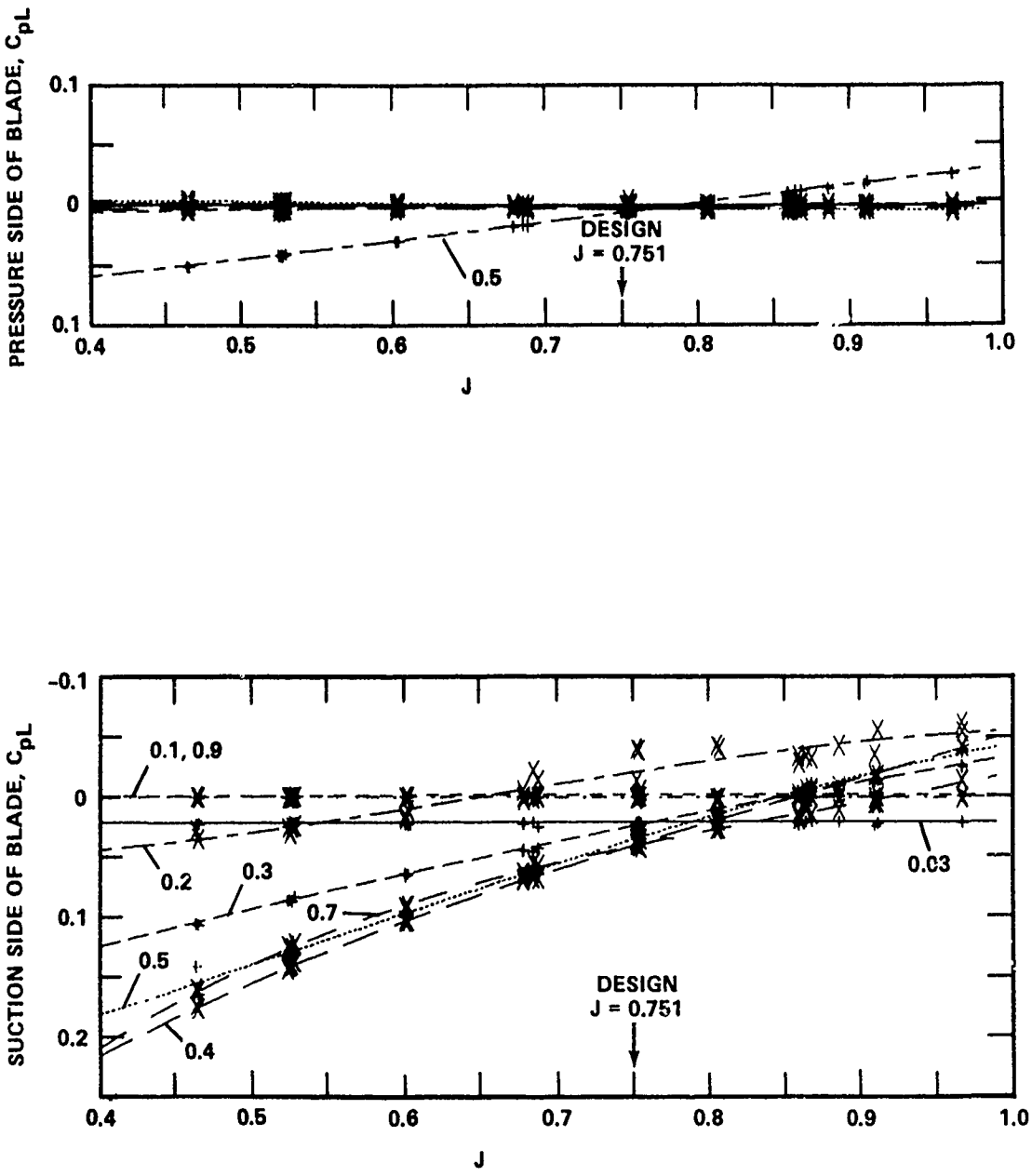

Figure 7b - r/R = 0.7, at Measured x/c Positions, V_{Ro} = 36.6 Feet per Second

Figure 7 (Continued)

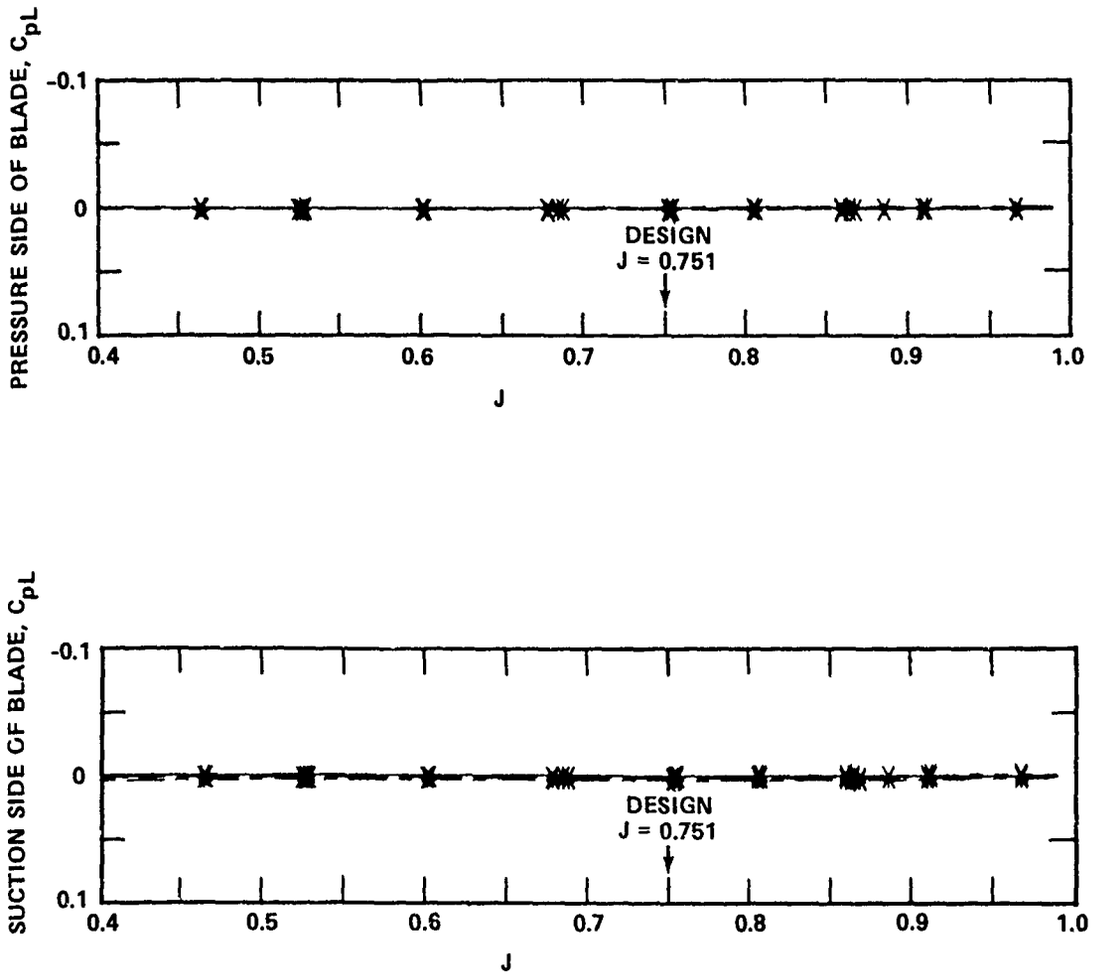

Figure 7c - r/R = 0.9, at Measured x/c Positions, V_{Ro} = 46.1 Feet per Second

Figure 8 - Variation of Mean Loading Pressure Coefficient with Inflow Speed for Propeller 4718 at Design J

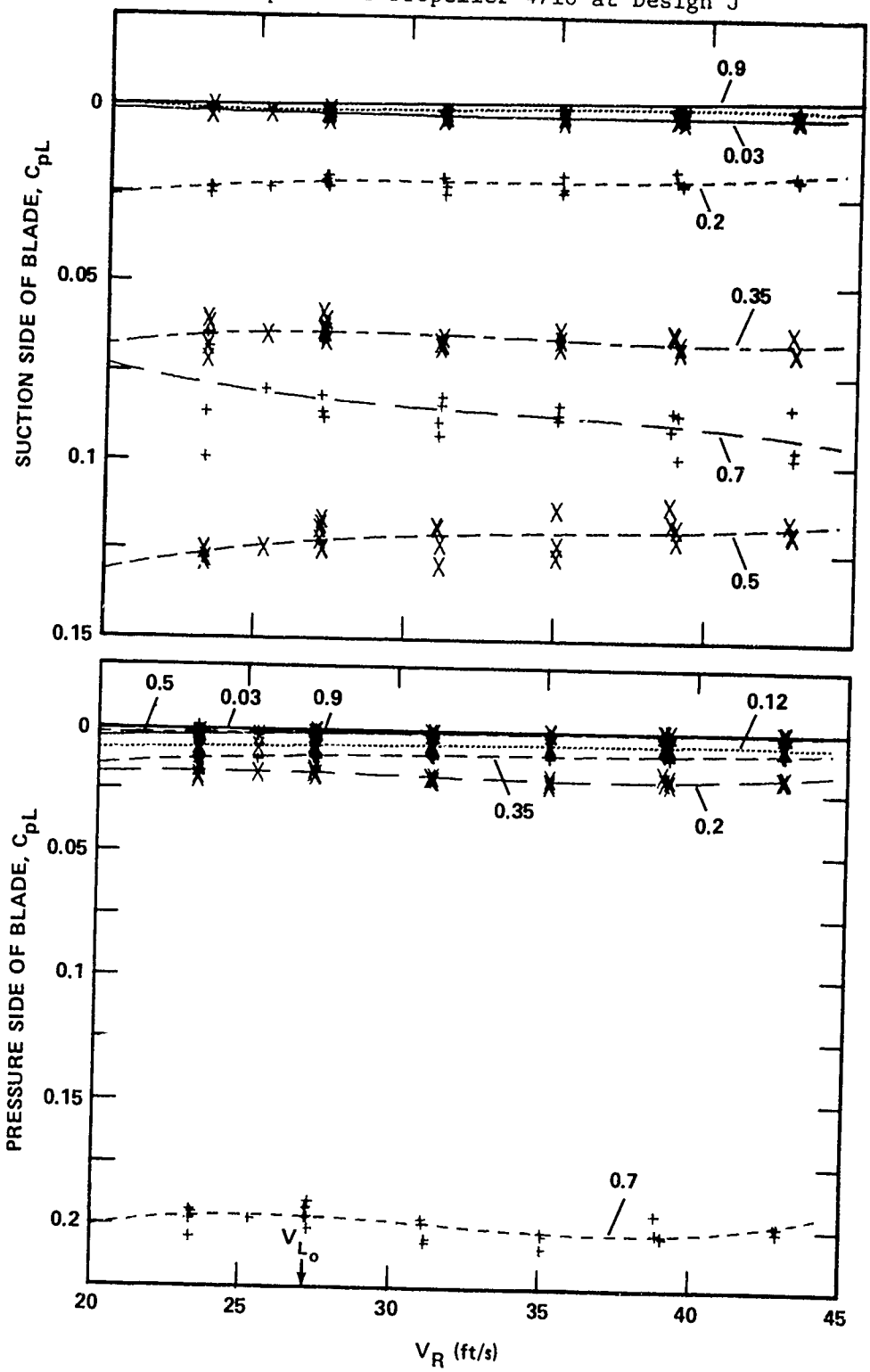

Figure 8a - r/R = 0.5, at Measured x/c Positions

Figure 8 (Continued)

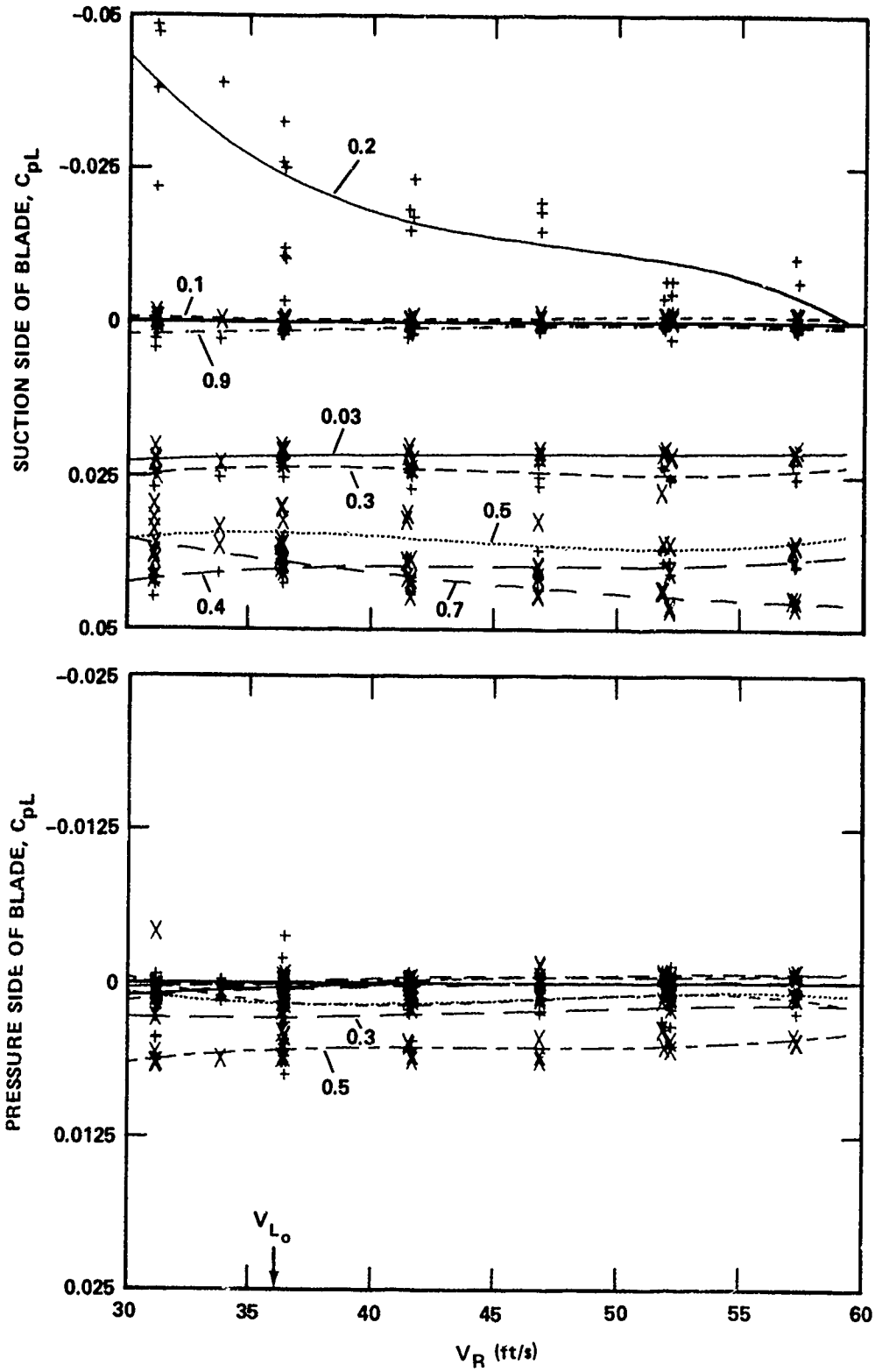

Figure 8b - r/R = 0.7, at Measured x/c Positions

Figure 8 (Continued)

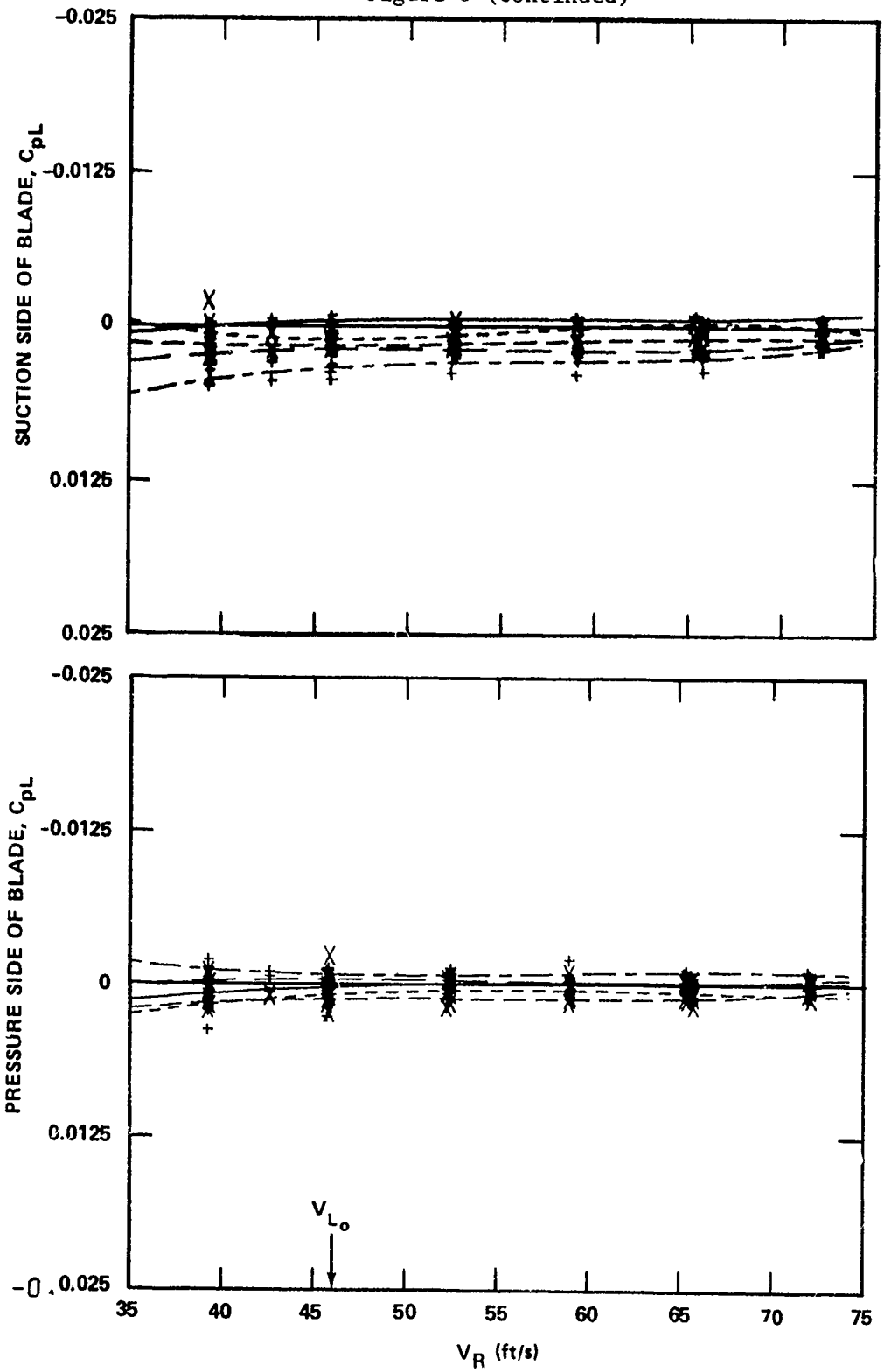

Figure 8c - r/R = 0.9, at Measured x/c Positions

Figure 9 - First Harmonic Pressure Coefficients with Propeller 4718 Inclined 7.5 Degrees at Design J; Comparison of Uncorrected with Approximate Loading Corrected Results

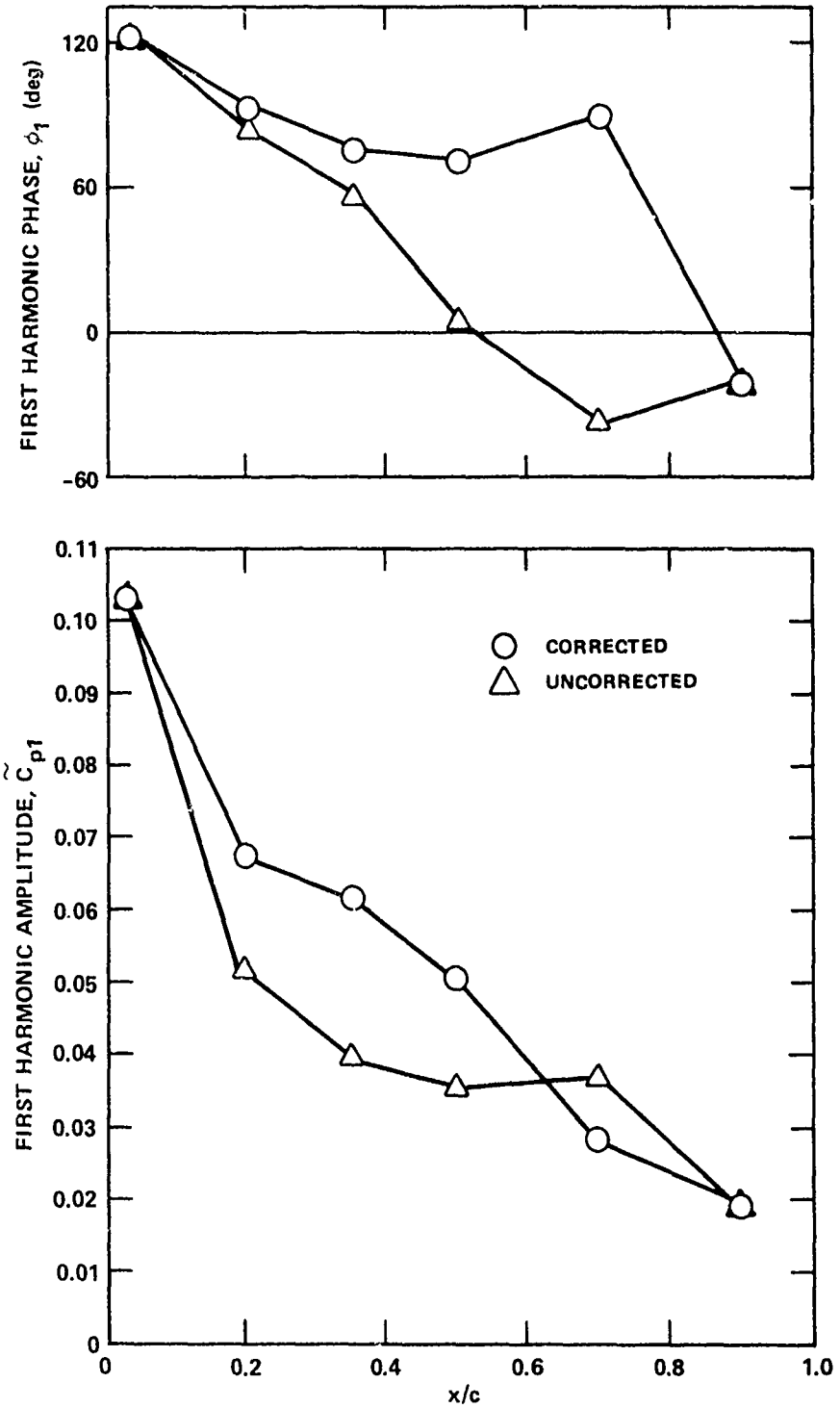

Figure 9a - Suction Side of Blade at r/R = 0.5

Figure 9 (Continued)

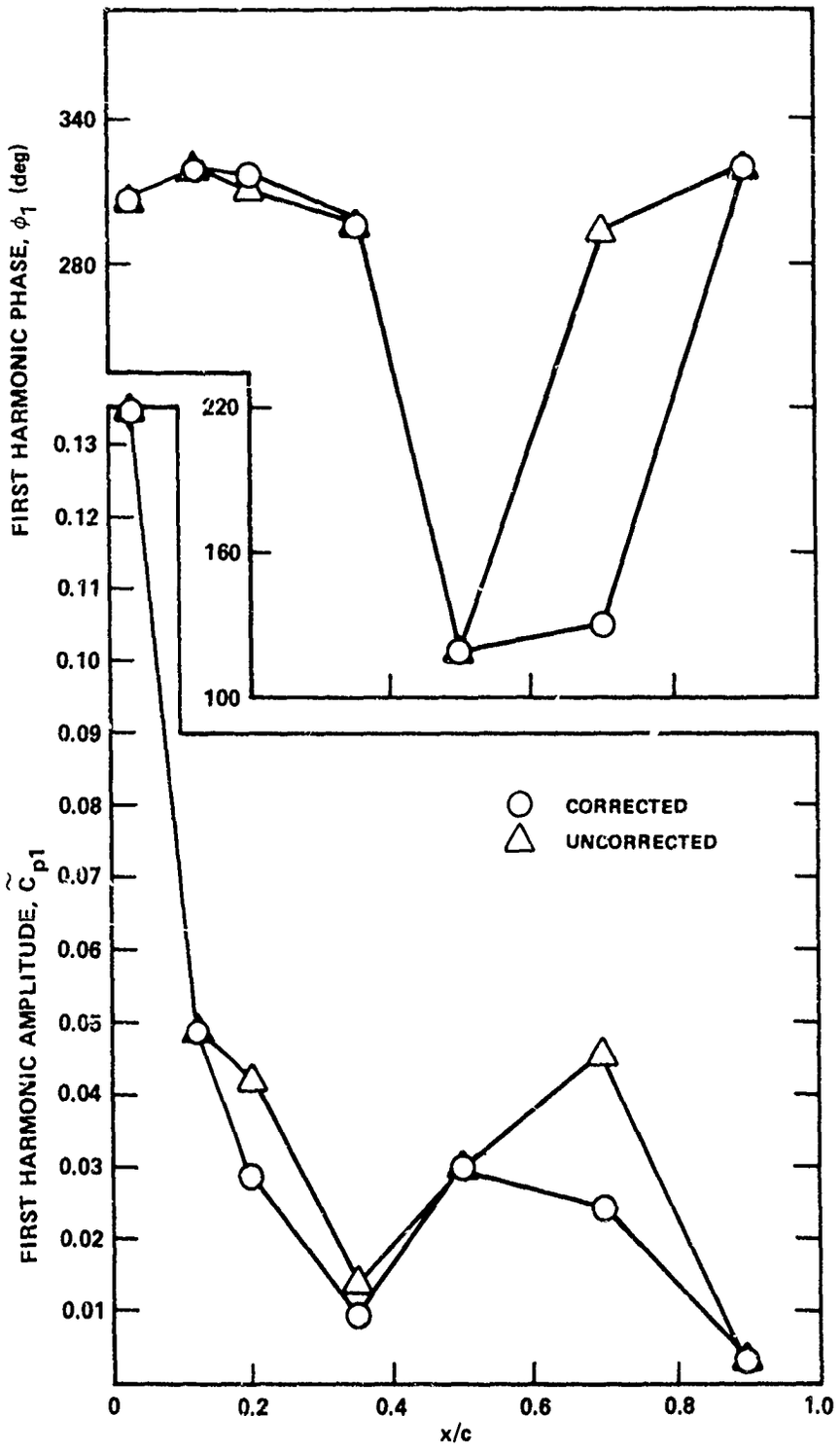

Figure 9b - Pressure Side of Blade at r/R = 0.5

Figure 9 (Continued)

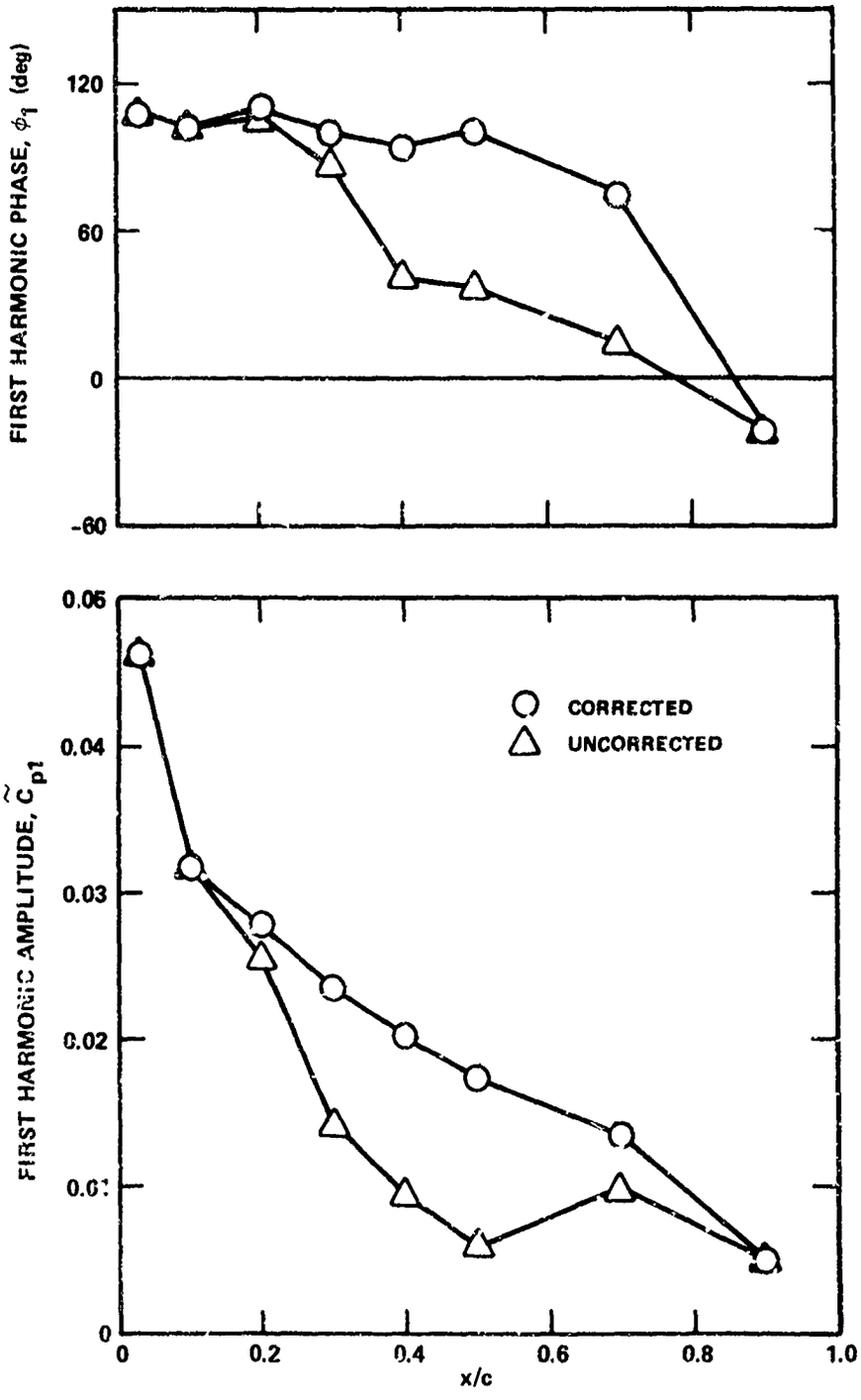

Figure 9c - Suction Side of Blade at r/R = 0.7

Figure 9 (Continued)

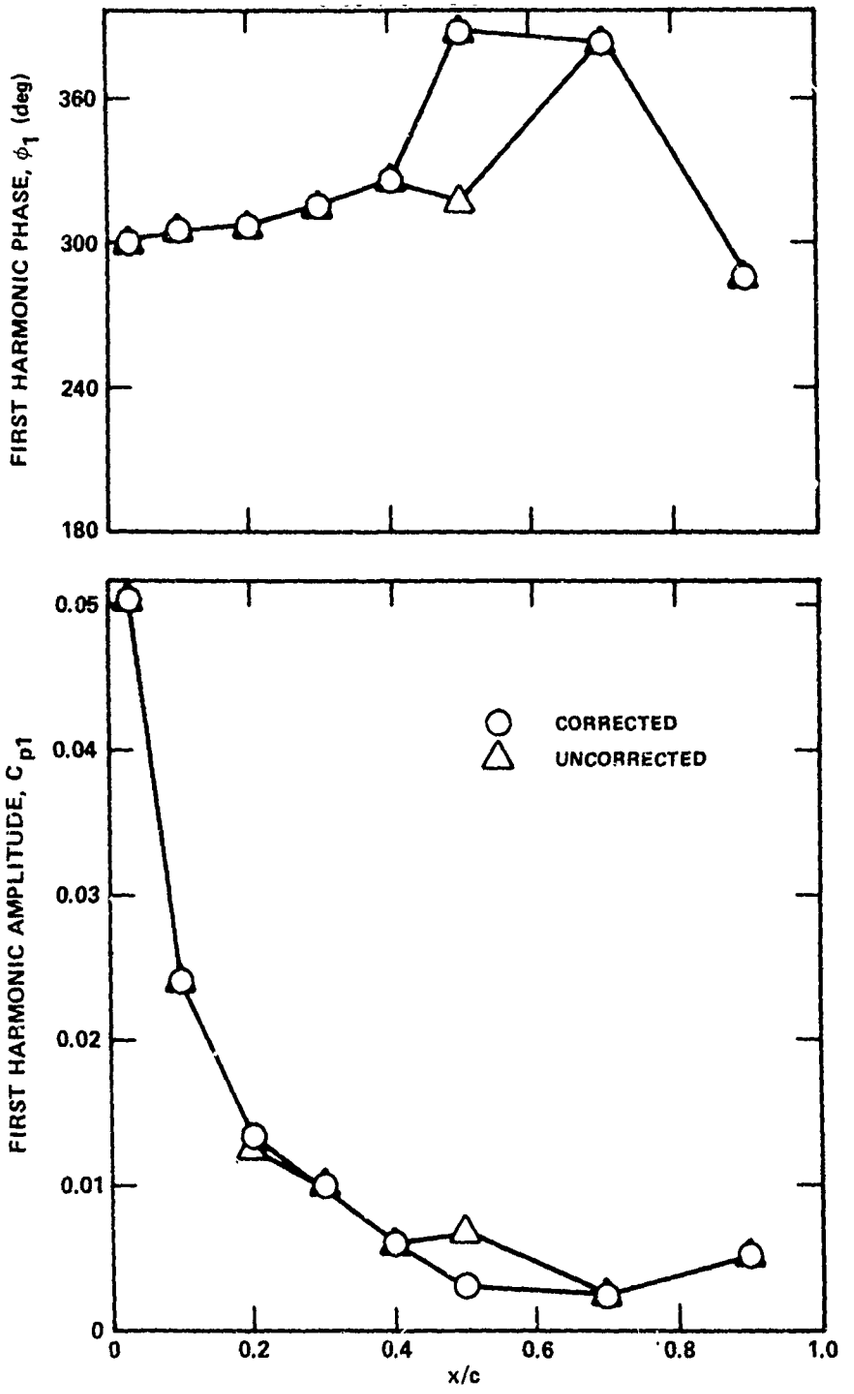

Figure 9d - Pressure Side of Blade at r/R = 0.7

Figure 10 - First Harmonic Pressure Coefficients with Propeller 4679 Inclined 7.5 Degrees at Design J; Comparison of Uncorrected with Approximate Loading Corrected Results

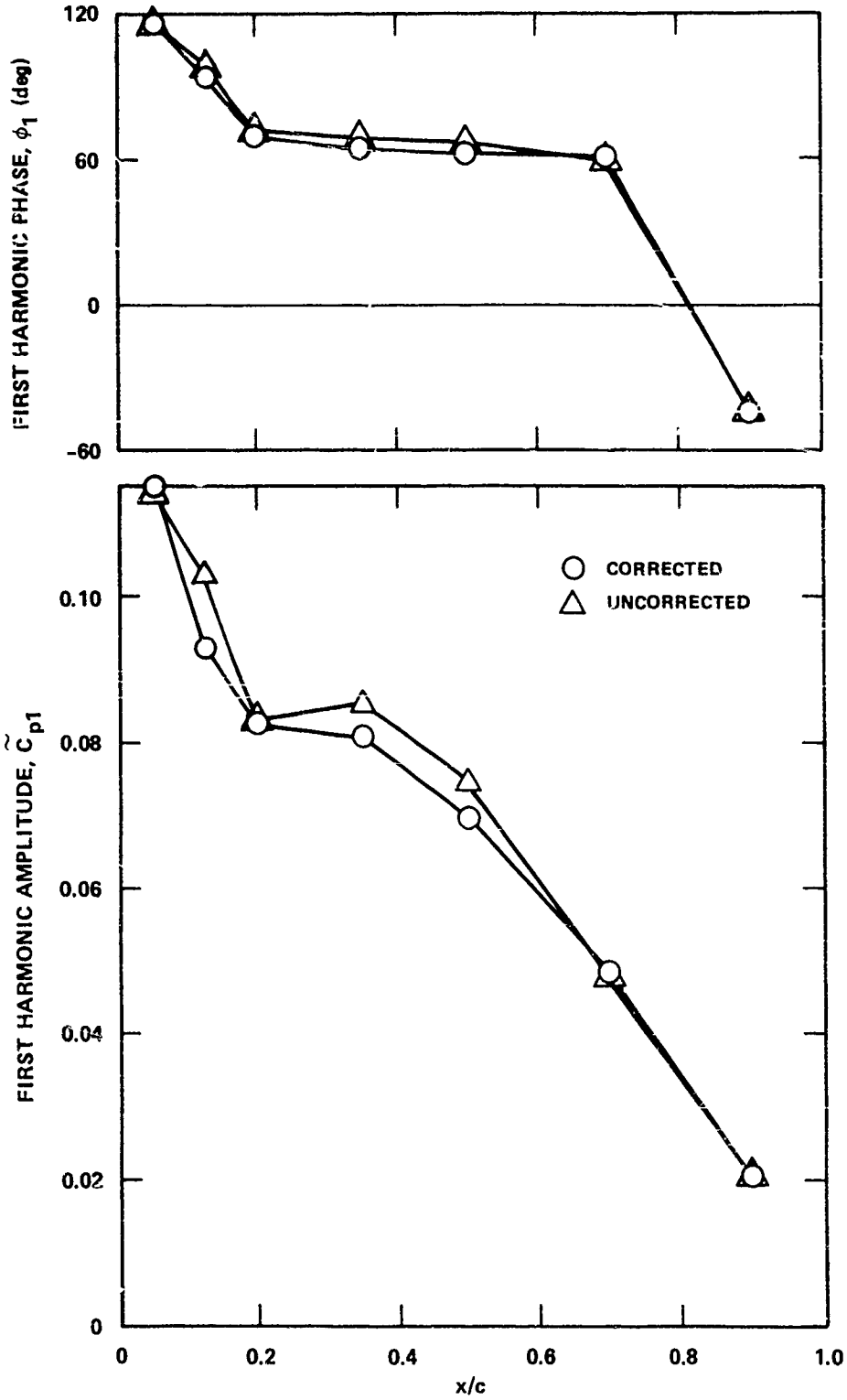

Figure 10a - Suction Side of Blade at r/R = 0.5

Figure 10 (Continued)

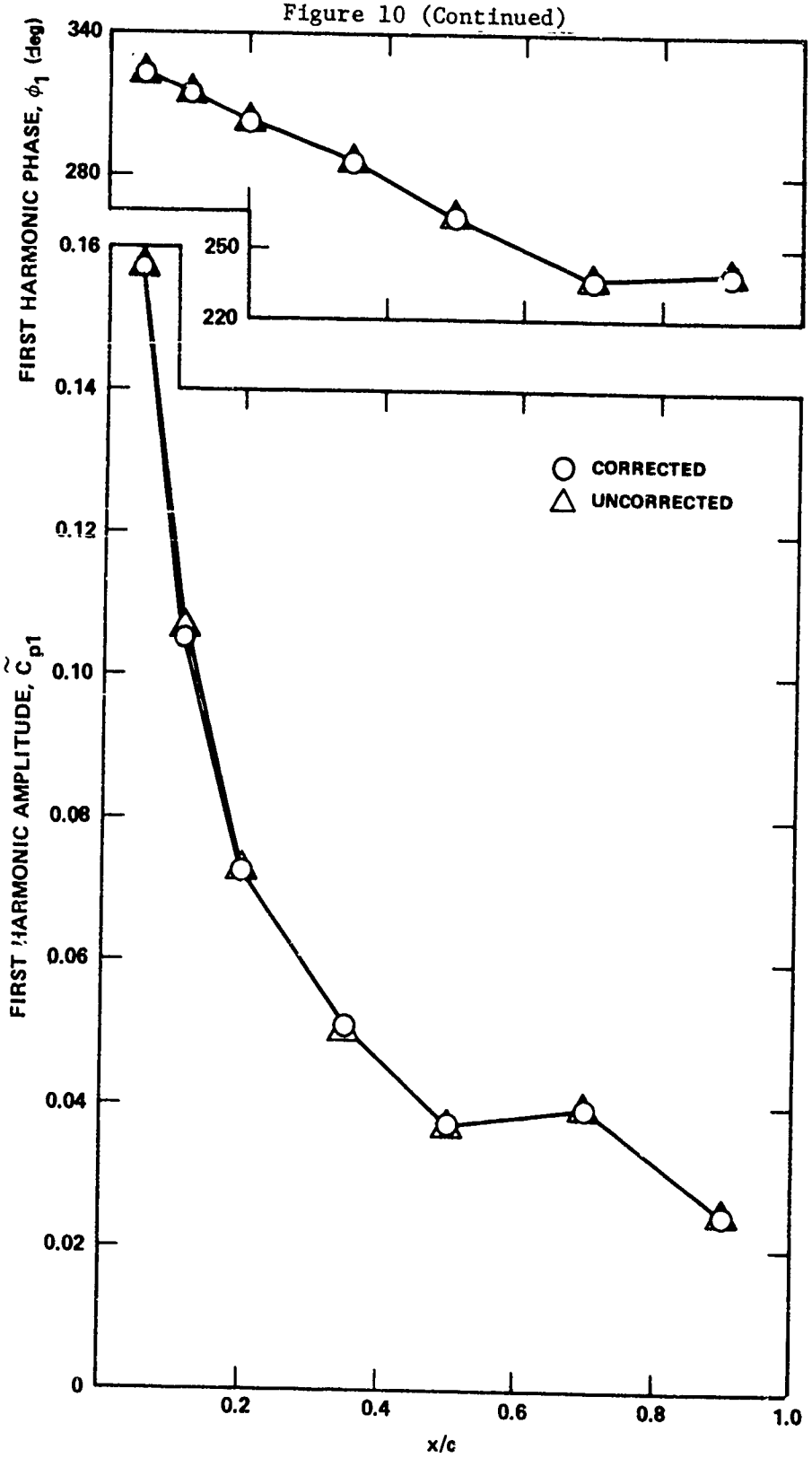

Figure 10b - Pressure Side of Blade at r/R = 0.5

Figure 10 (Continued)

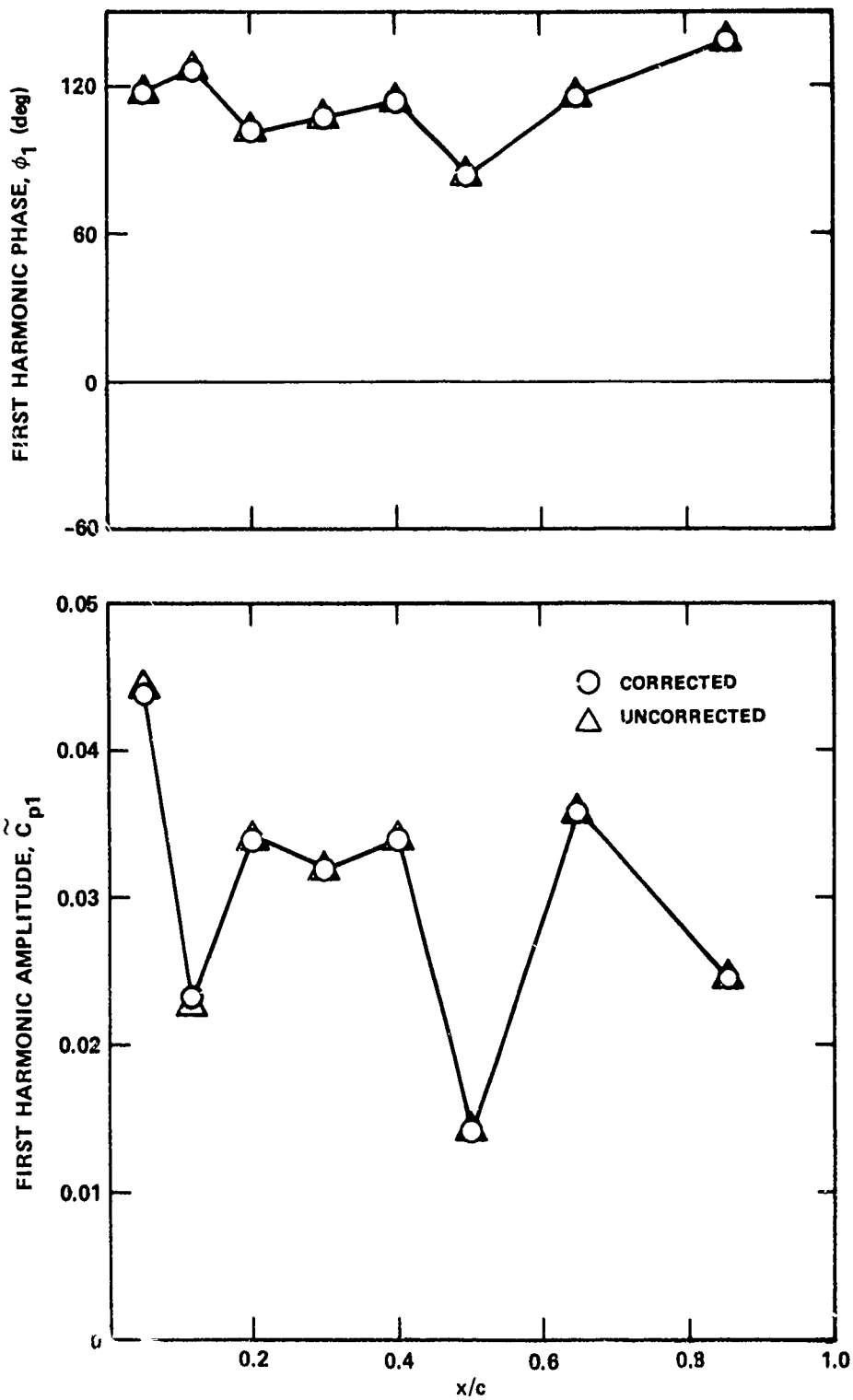

Figure 10c - Suction Side of Blade at r/R = 0.7

Figure 10 (Continued)

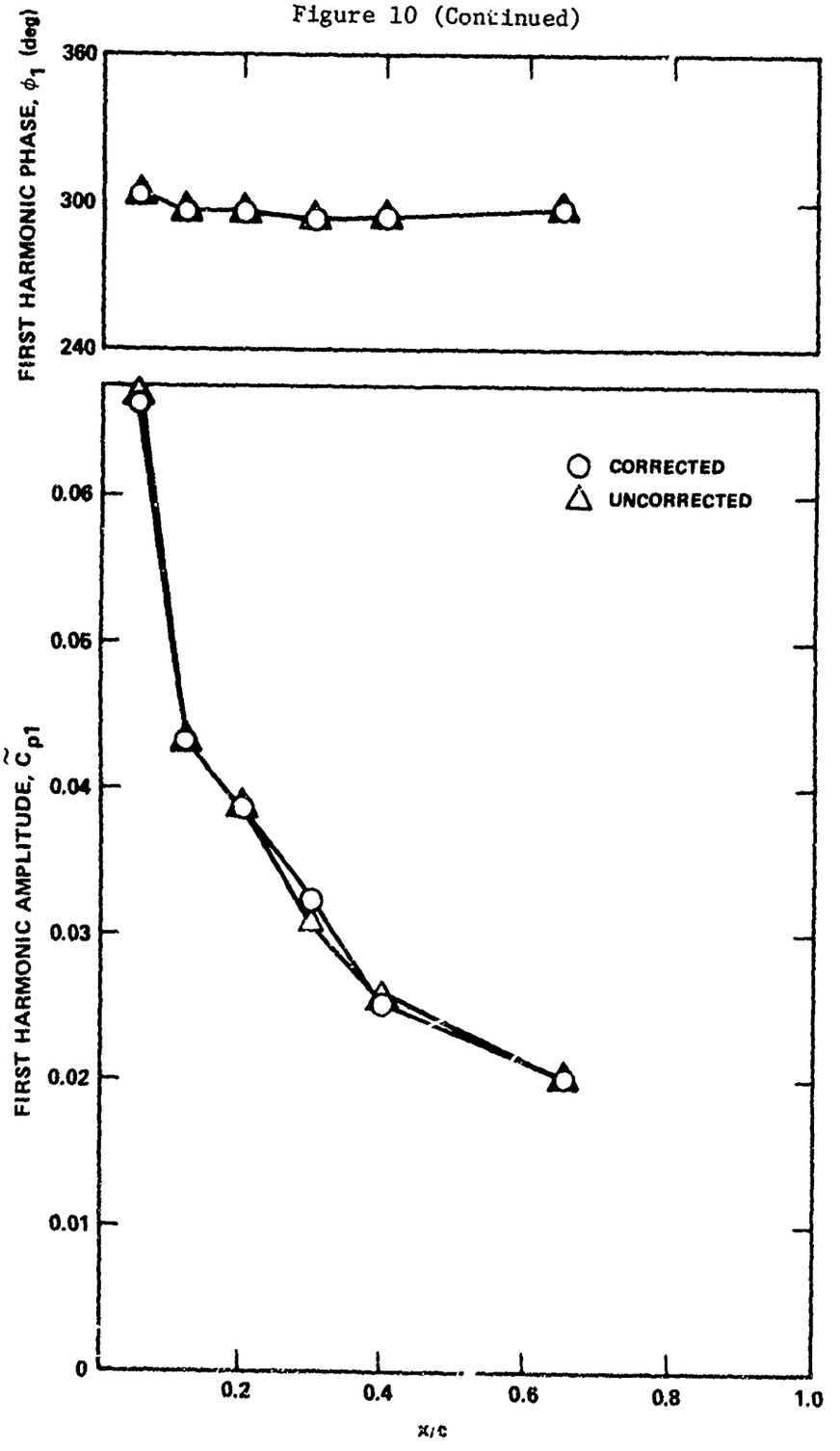

Figure 10d - Pressure Side of Blade at r/R = 0.7

Figure 11 - Average Distribution of $\overline{C}_p$ at Design J for Propellers 4718 and 4679 Over a Range of Reynolds Numbers

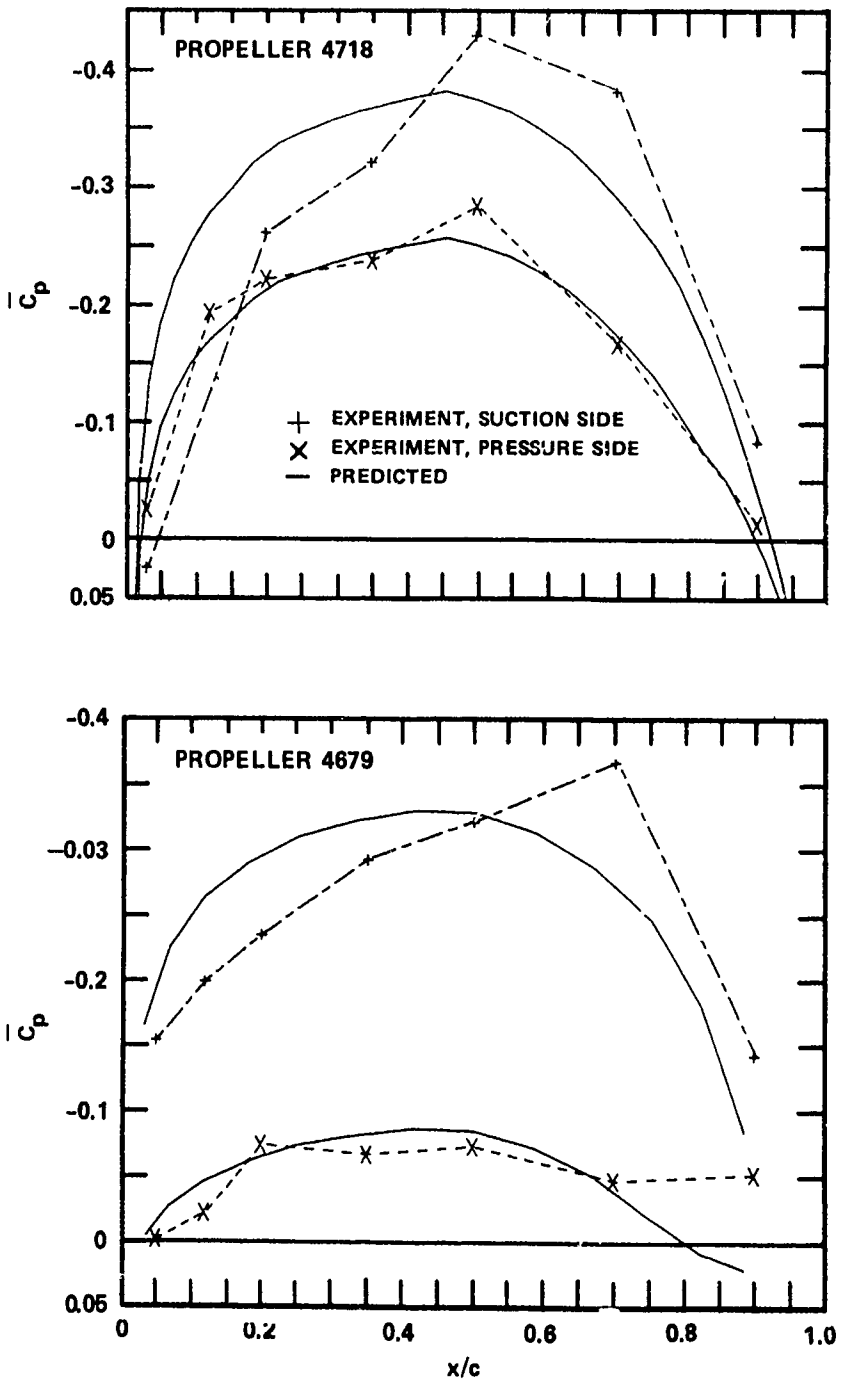

Figure 11a - r/R = 0.5

Figure 11 (Continued)

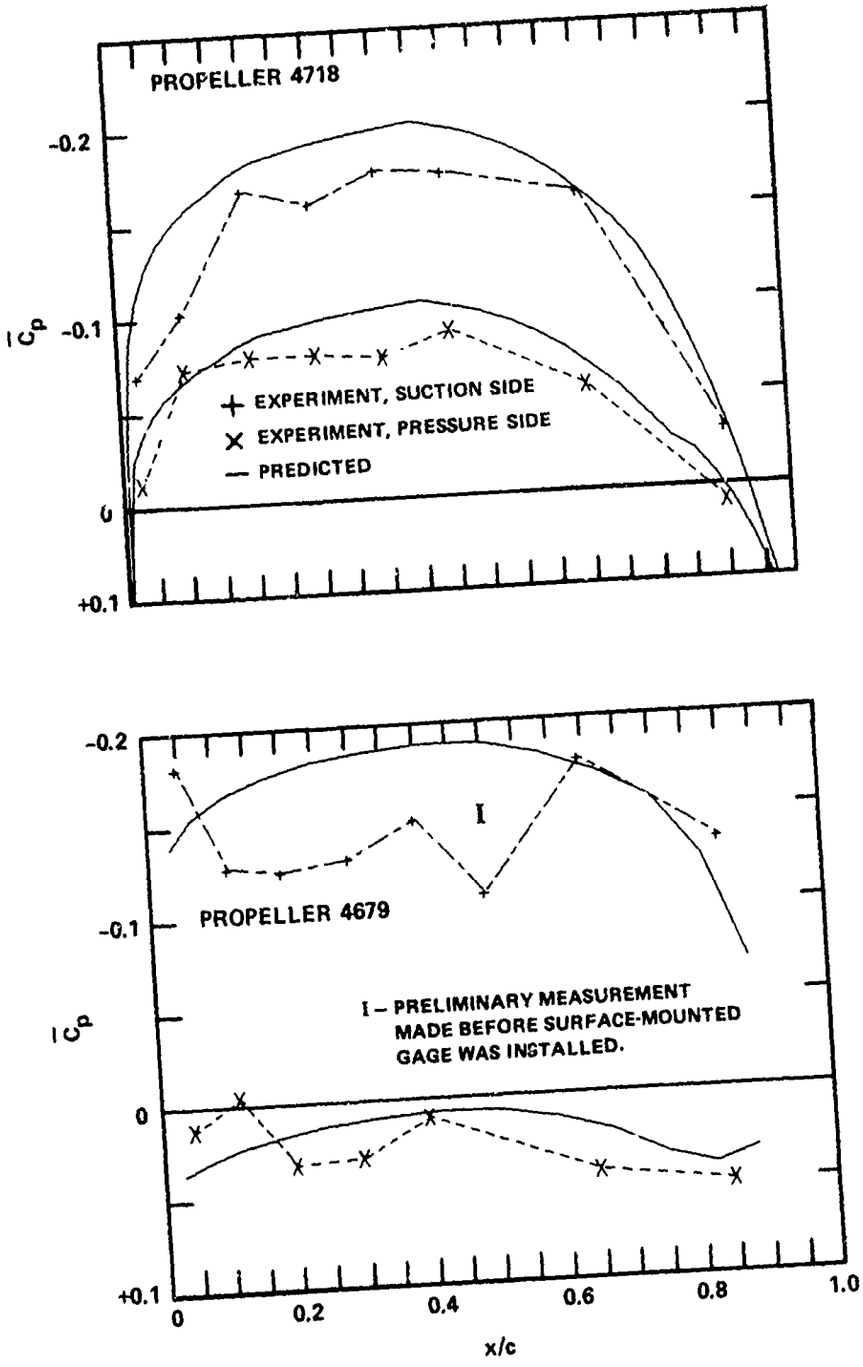

Figure 11b – r/R = 0.7

Figure 11 (Continued)

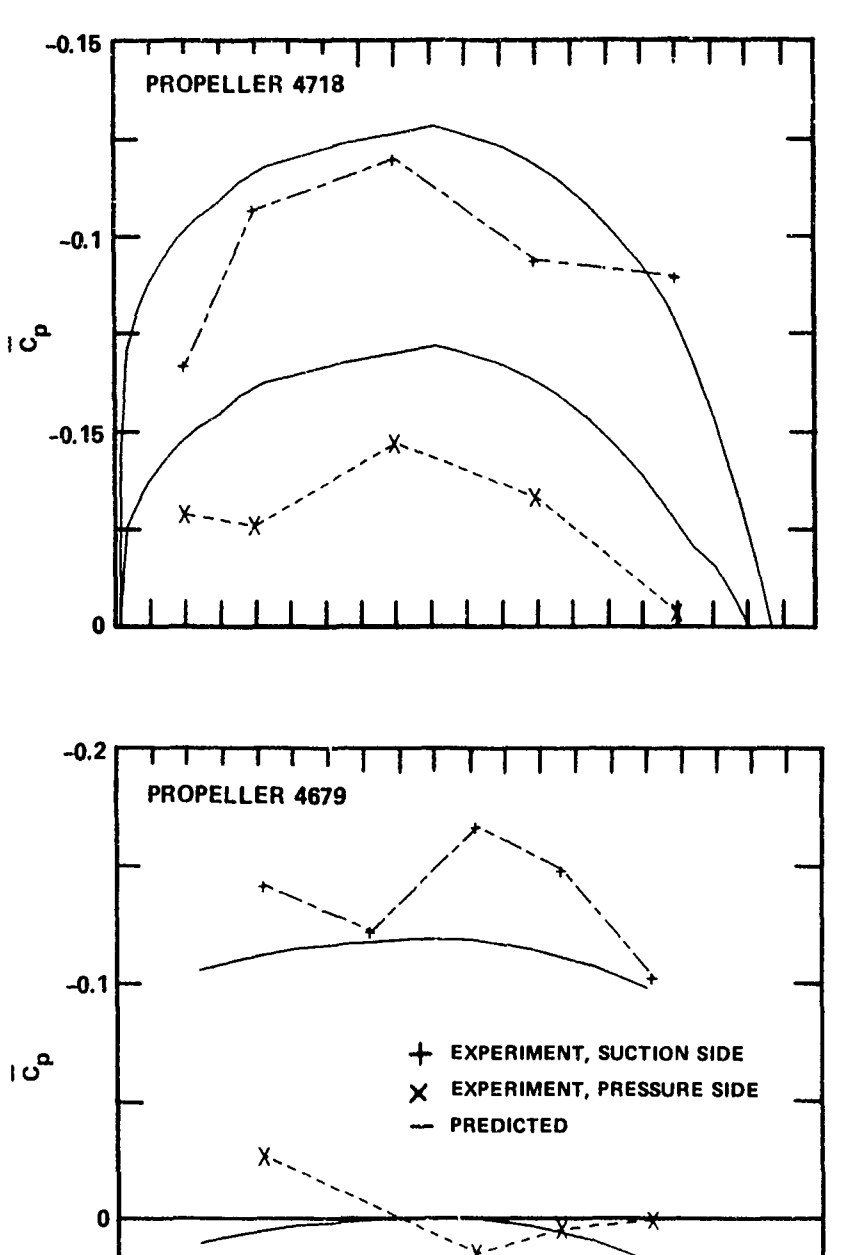

Figure 11c - r/R = 0.9

Figure 12 - Variation of $\bar{C}_p$ Distribution with Reynolds Number for Propeller 4718 Operating at Design J

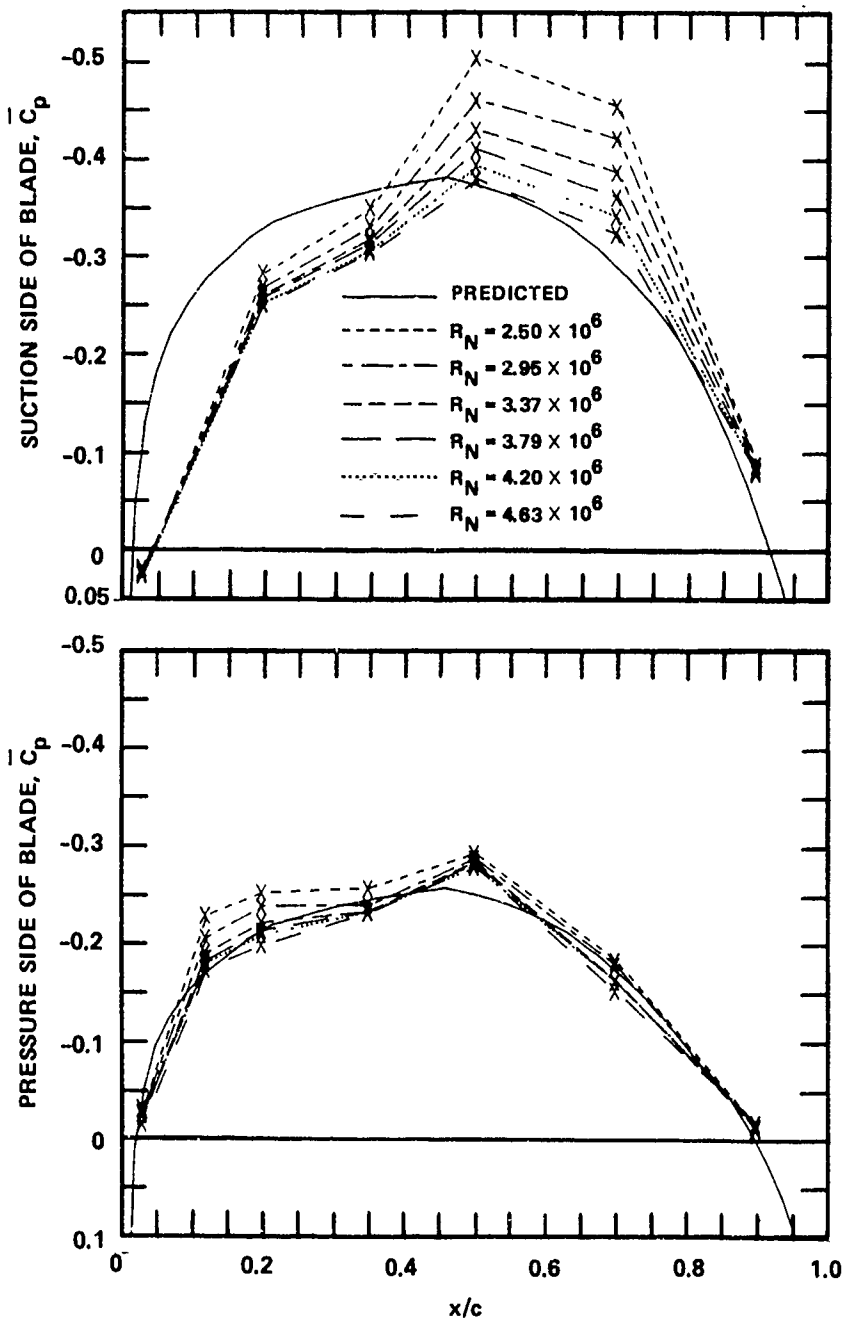

Figure 12a - r/R = 0.5

Figure 12 (Continued)

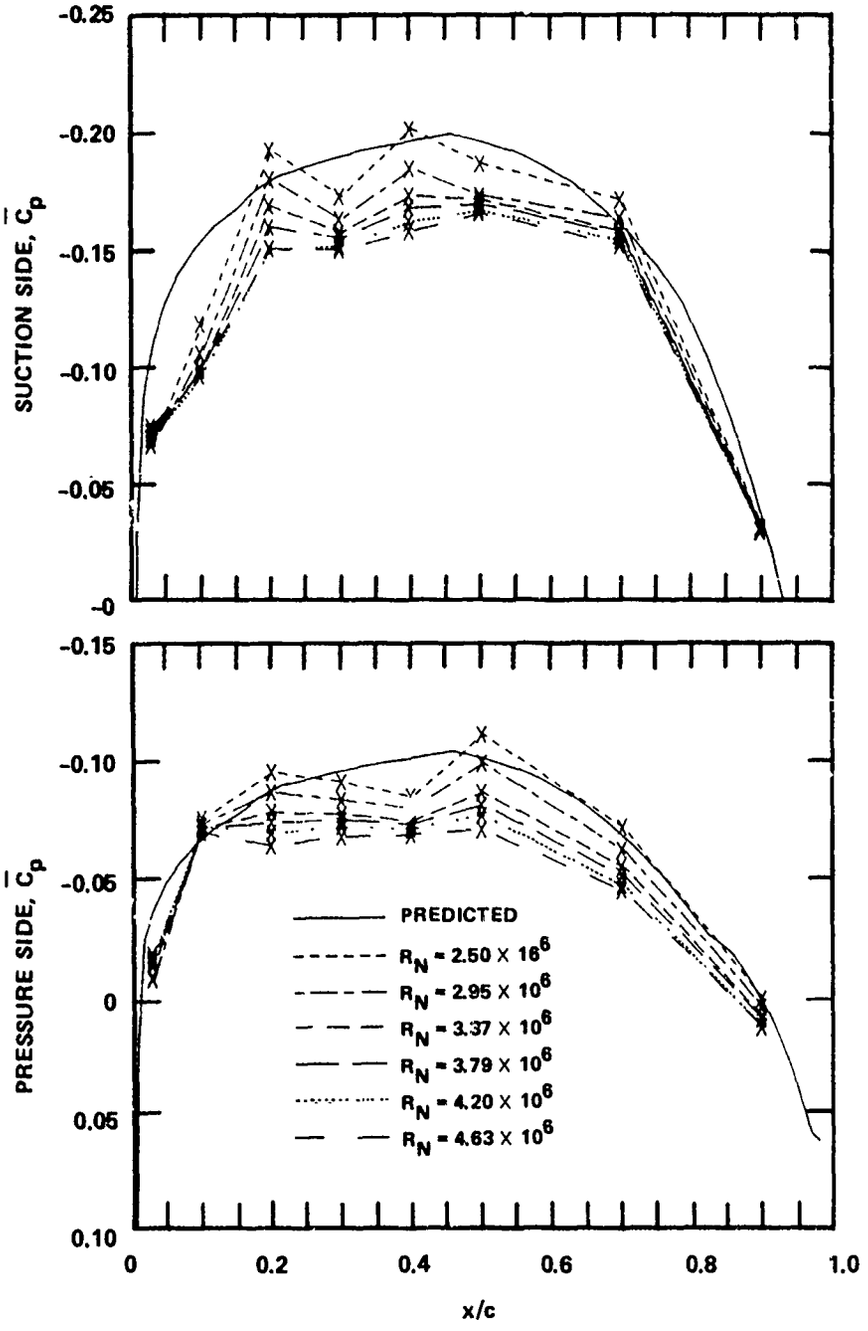

Figure 12b - r/R = 0.7

Figure 12 (Continued)

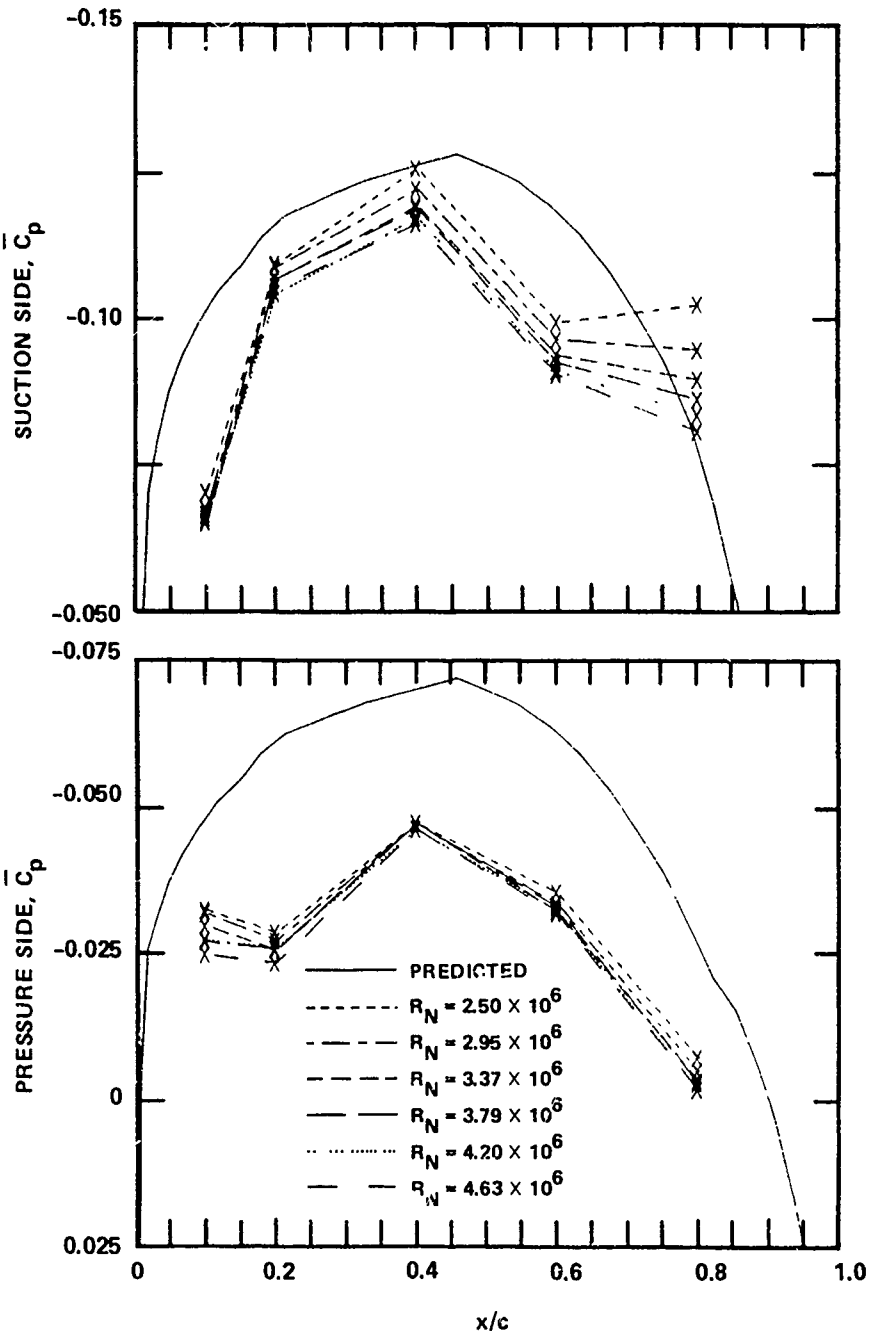

Figure 12c - r/R = 0.9

Figure 13 - Variation of $\overline{C}_p$ Distribution with Reynolds Number for Propeller 4679 Operating at Design J

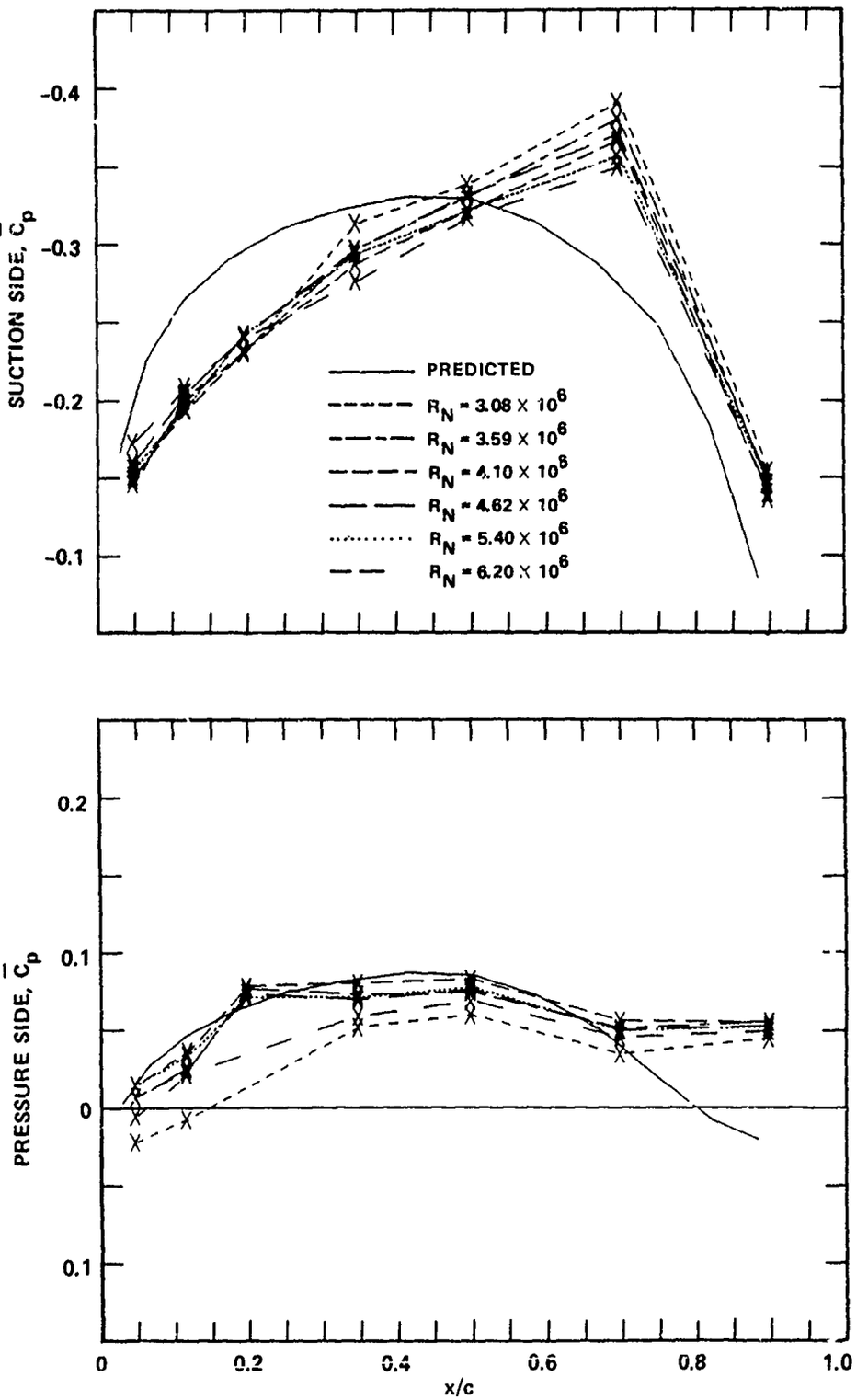

Figure 13a - r/R = 0.5

Figure 13 (Continued)

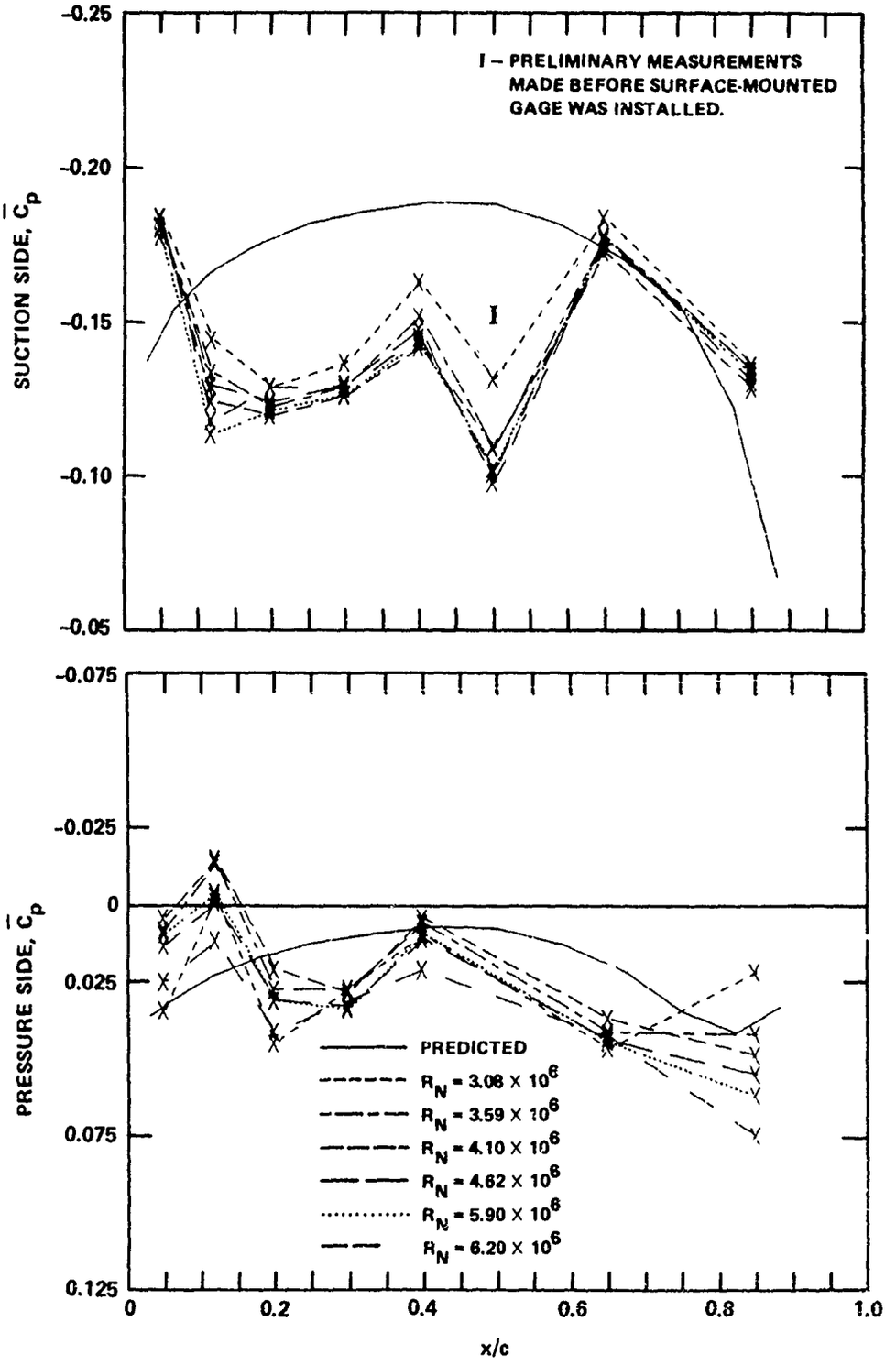

Figure 13b - r/R = 0.7

Figure 13 (Continued)

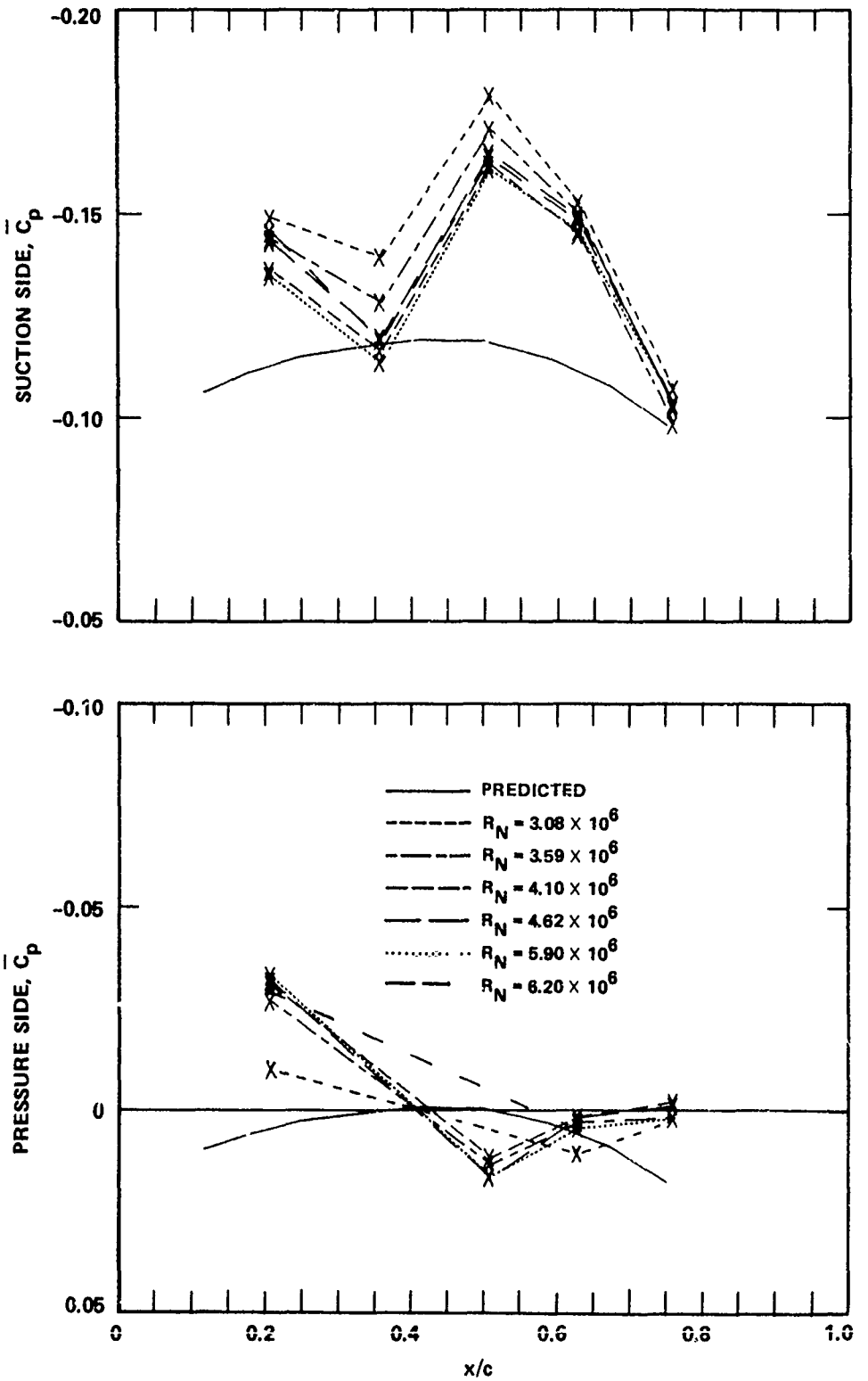

Figure 13c - r/R = 0.9

Figure 14 - Variation of $\overline{C}_p$ with Inflow Speed at Design J for Propeller 4718

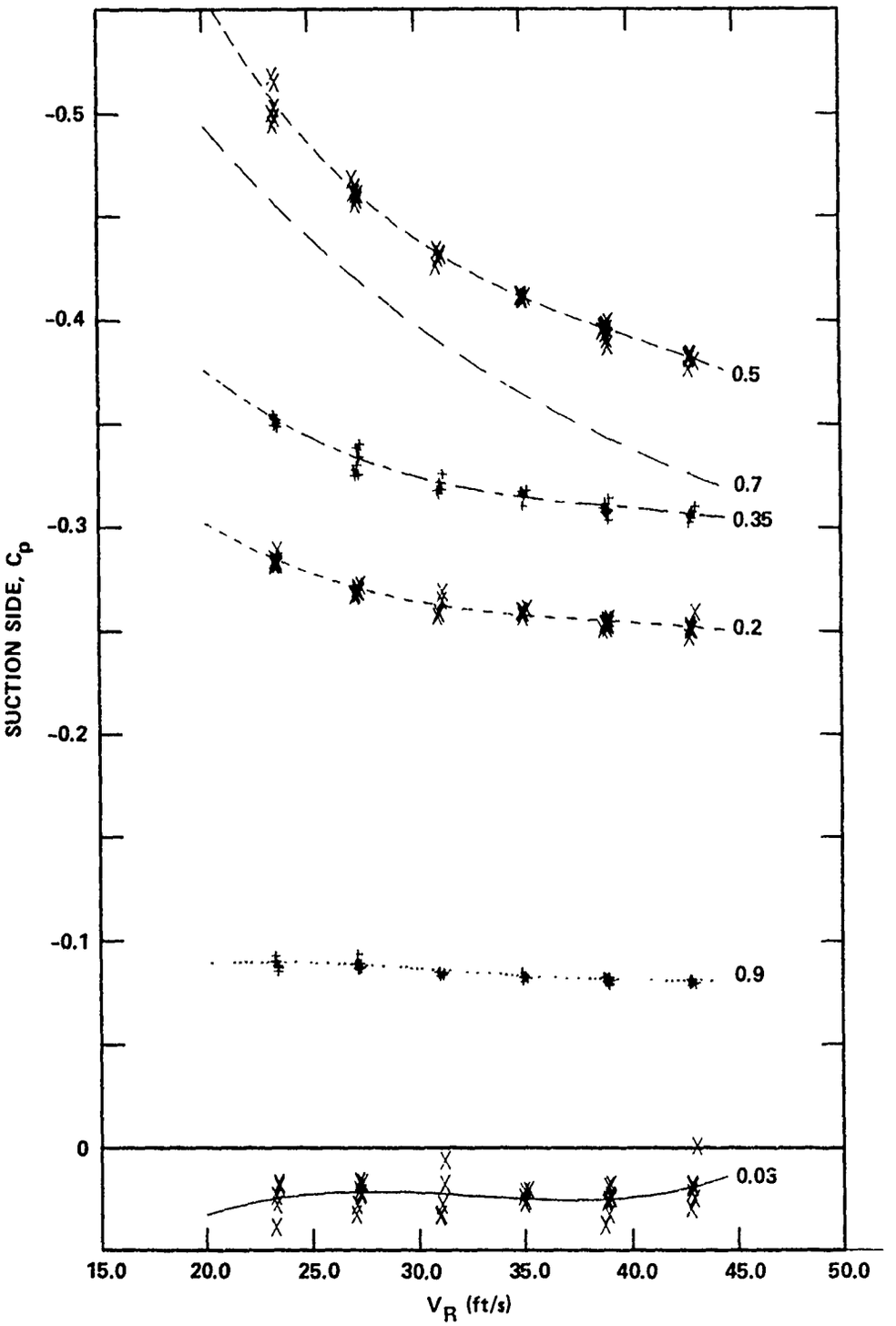

Figure 14a - r/R = 0.5, at Measured x/c Positions

Figure 14 (Continued)

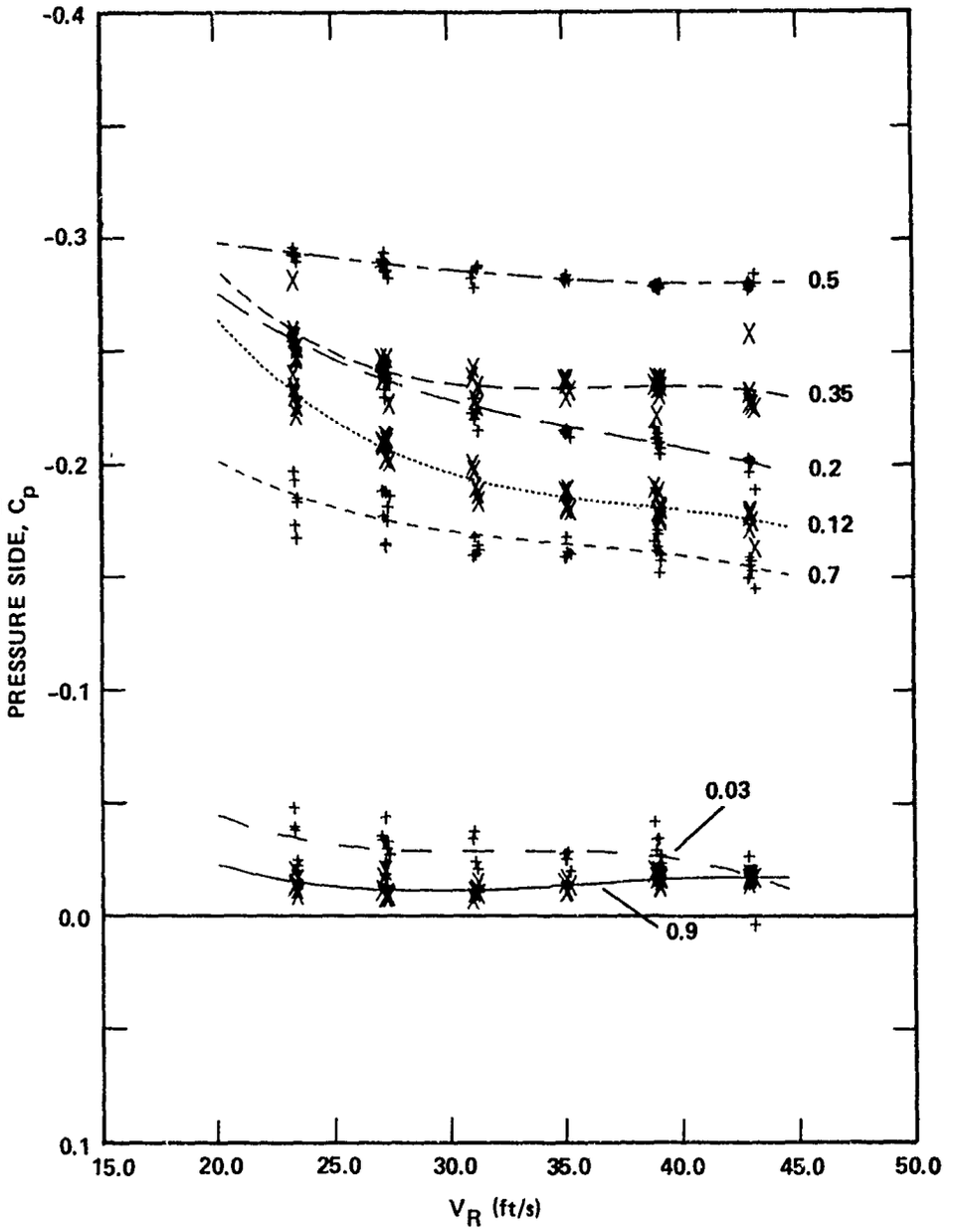

Figure 14a (Continued)

Figure 14 (Continued)

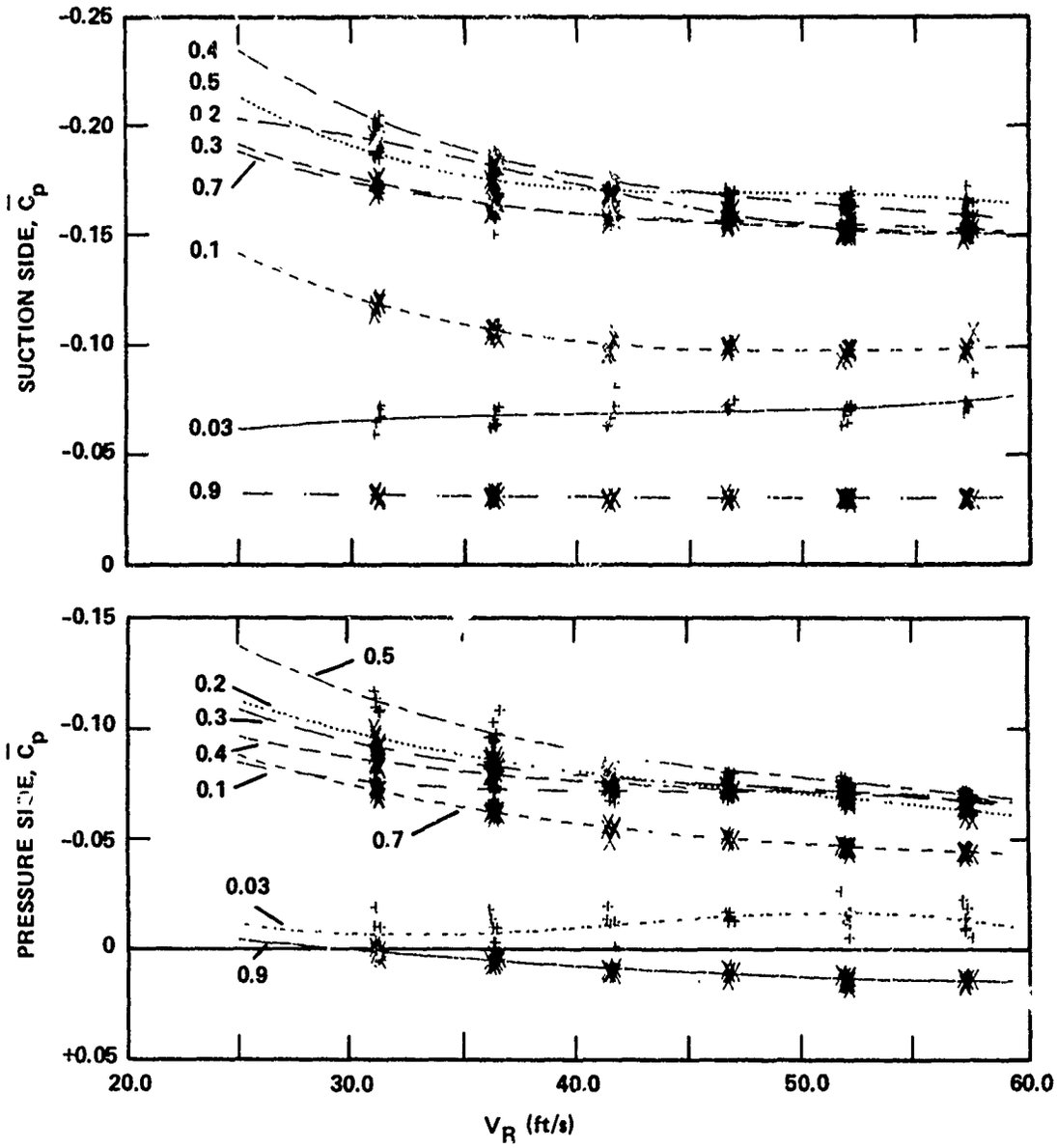

Figure 14b - r/R = 0.7, at Measured x/c Positions

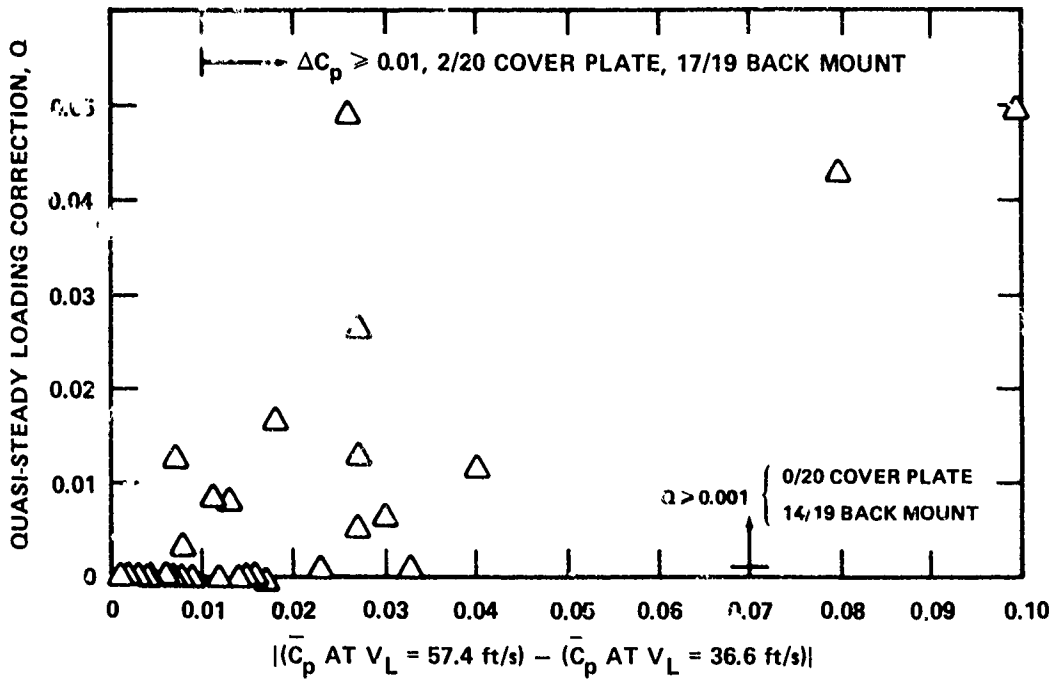

Figure 15a - Propeller 4718

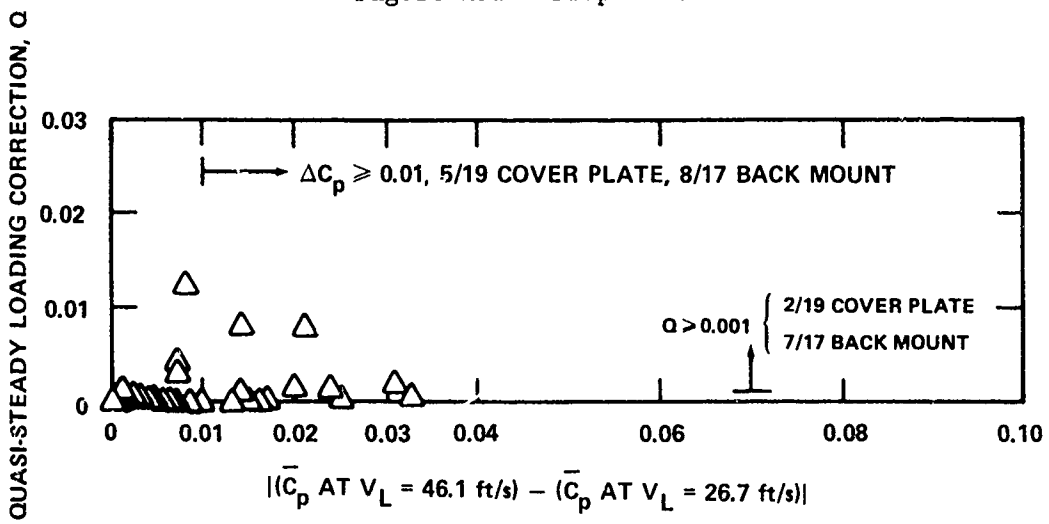

Figure 15b - Propeller 4679

Figure 15 - Correlation Between Speed Effect and Loading Effect

Figure 16 - Variation of $\overline{C}_p$ with J, with and without Speed Correction for Propeller 4718

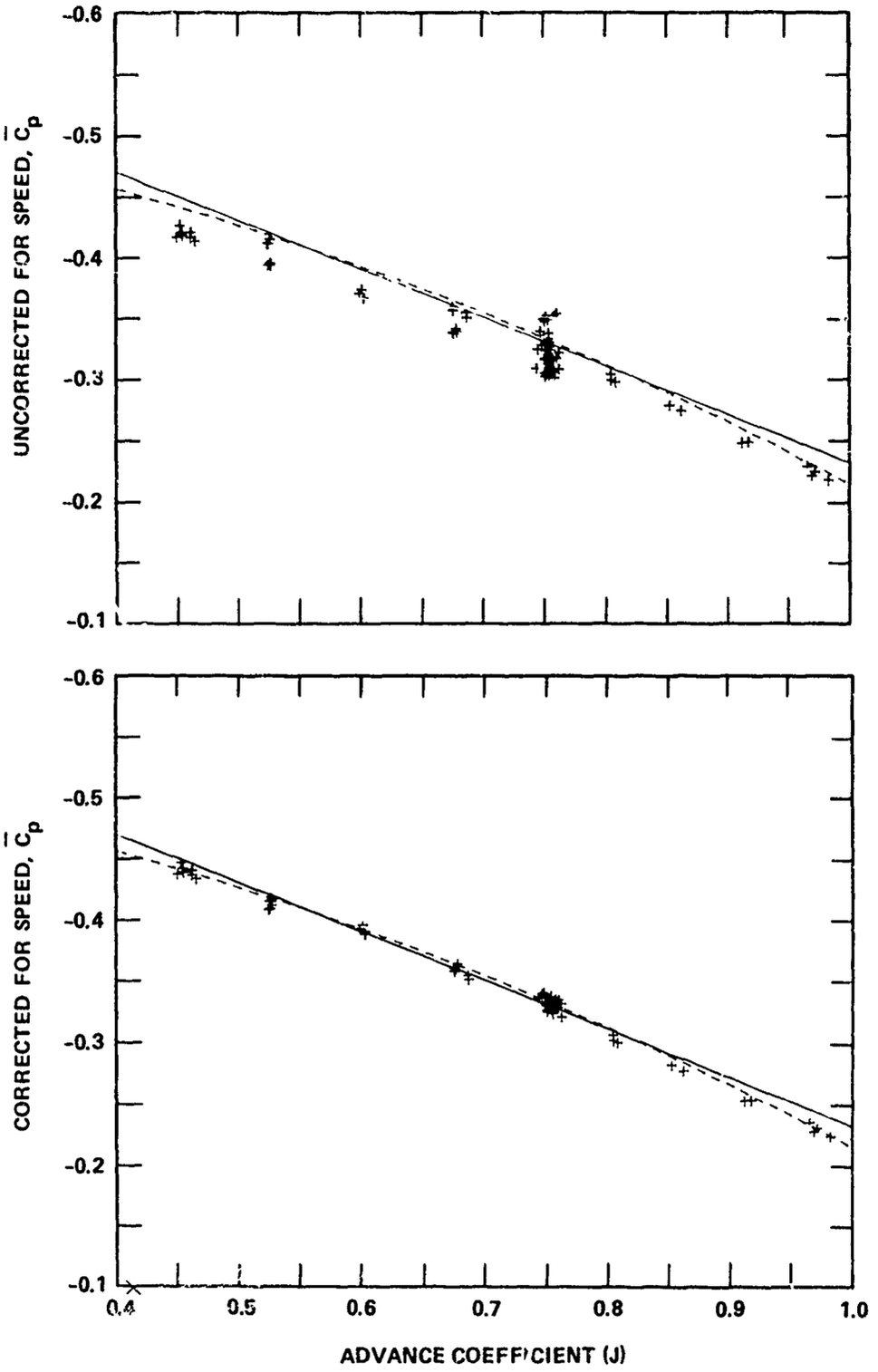

Figure 16a - Gage 24, x/c = 0.35, r/R = 0.5, Suction Side of Blade

Figure 16 (Continued)

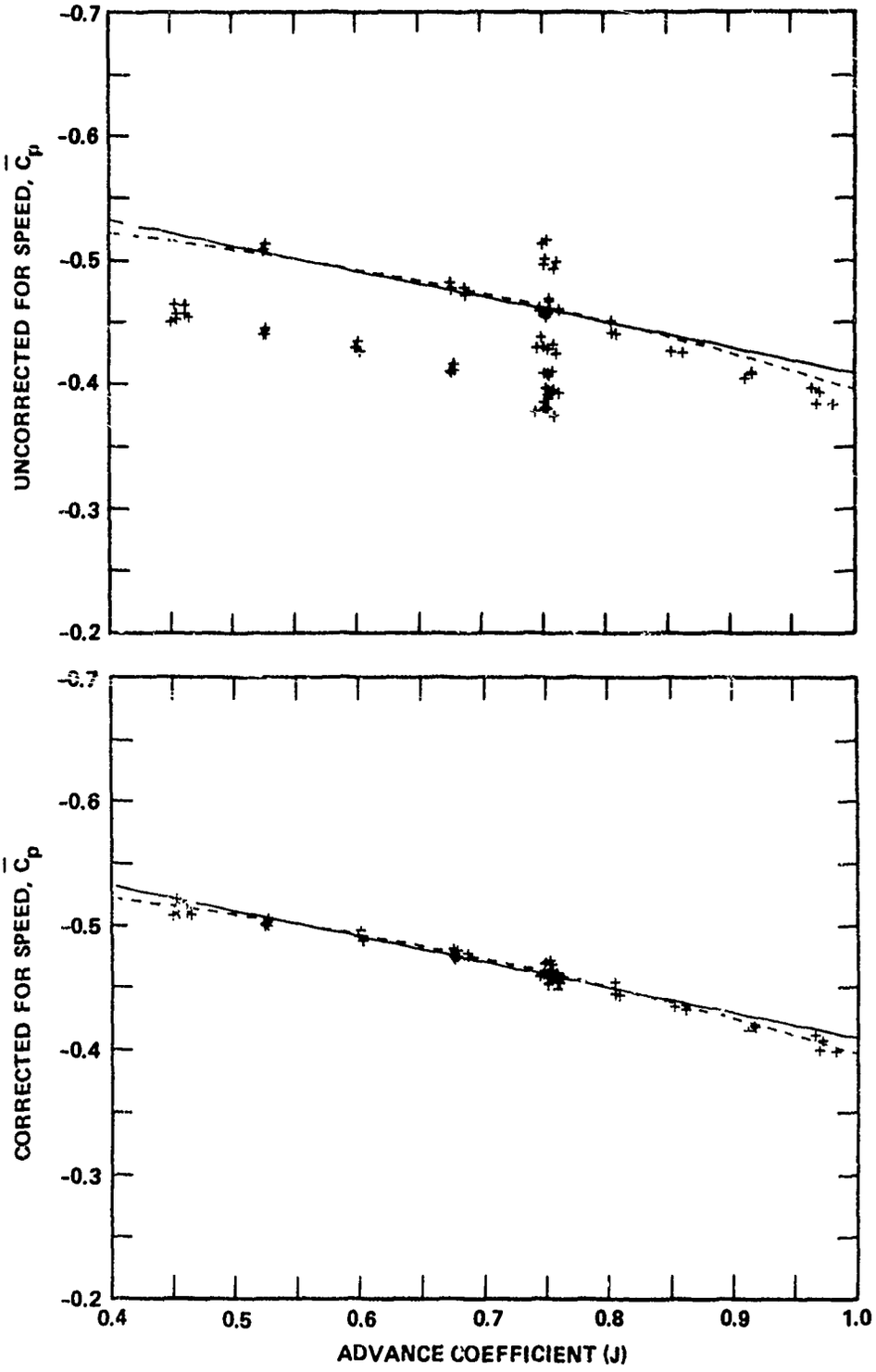

Figure 16b - Gage 25, x/c = 0.5, r/R = 0.5, Suction Side of Blade

Figure 16 (Continued)

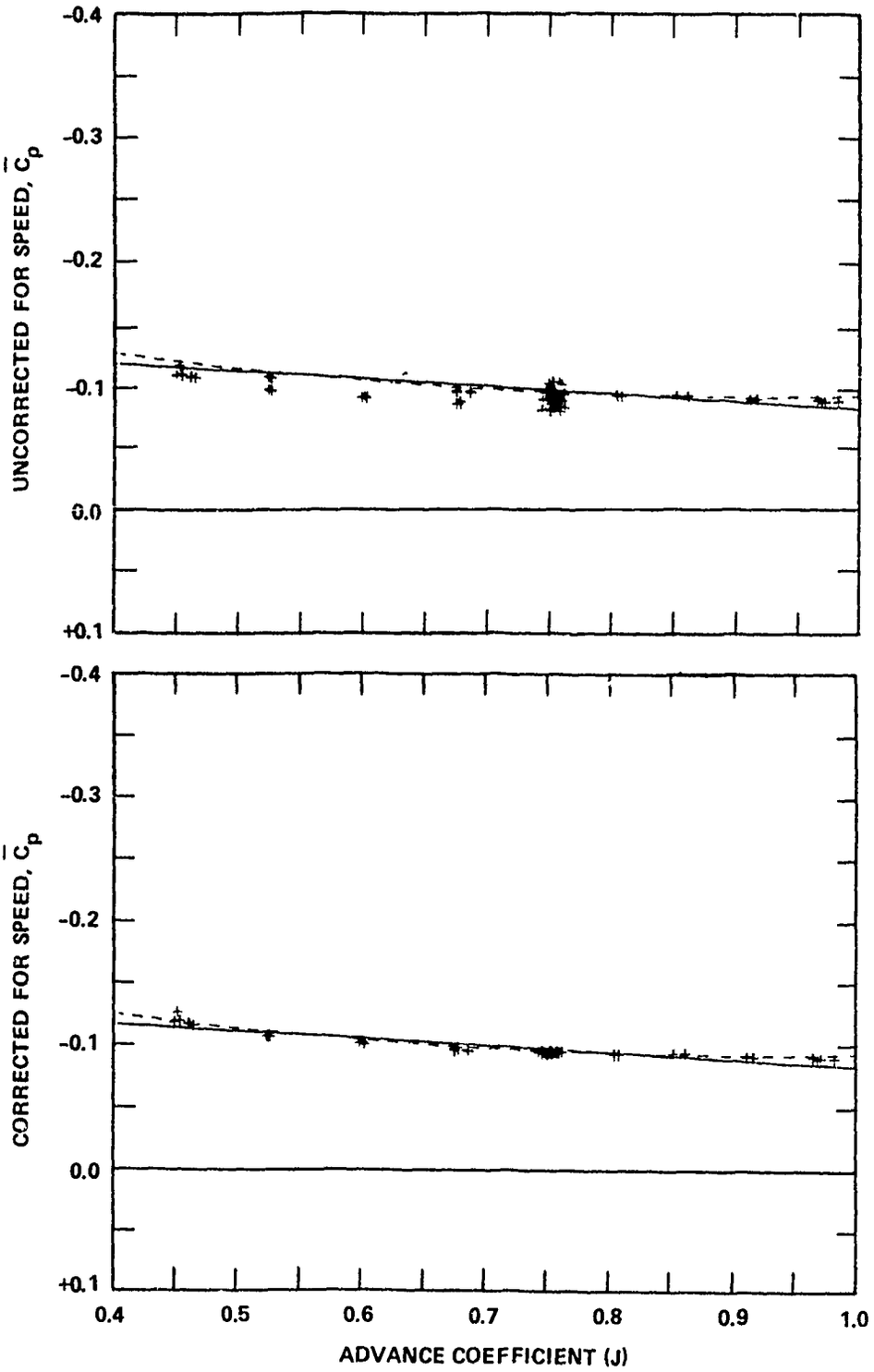

Figure 16c - Gage 40, x/c = 0.8, r/R = 0.9, Suction Side of Blade

Figure 16 (Continued)

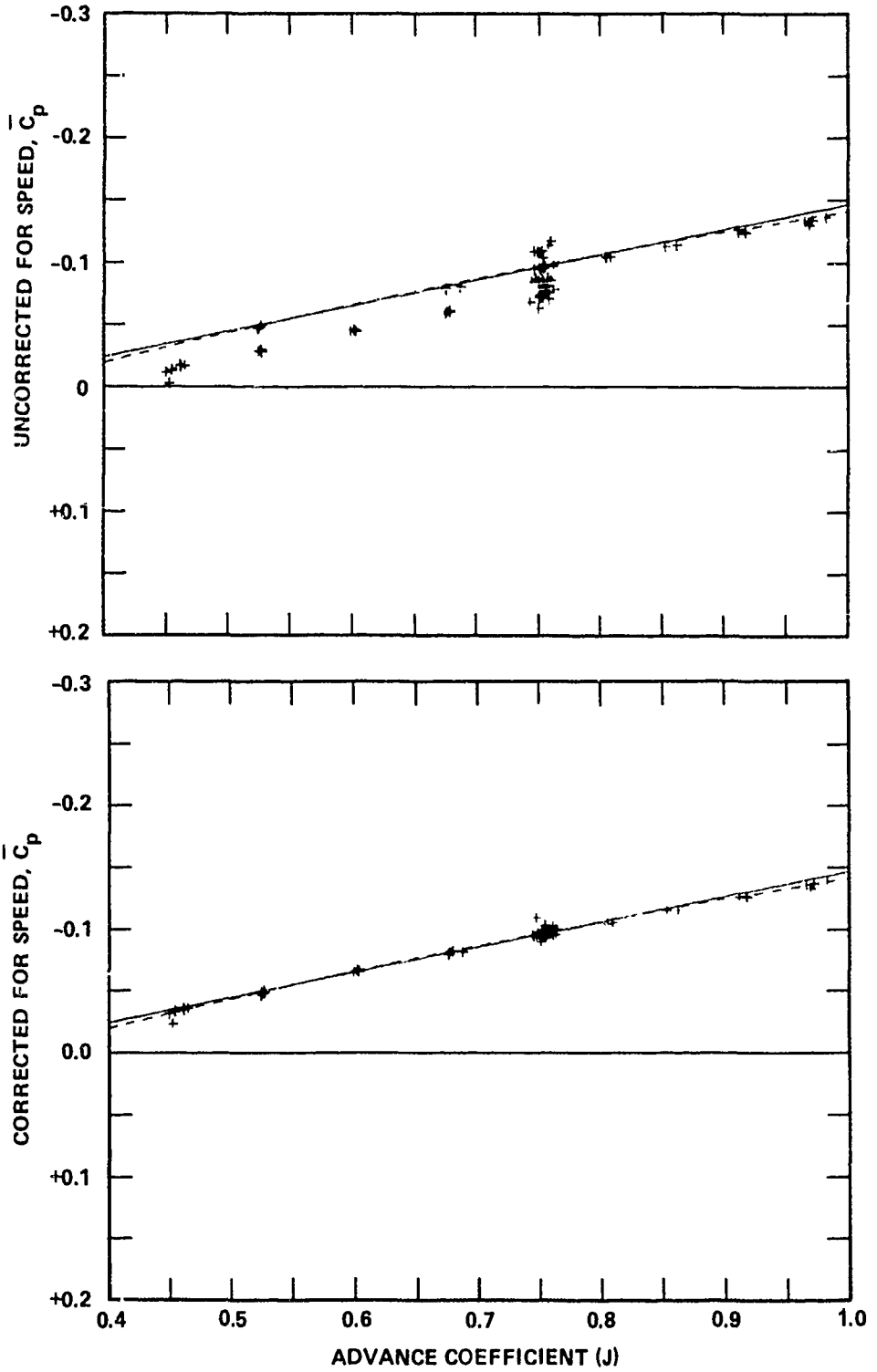

Figure 16d - Gage 10, x/c = 0.5, r/R = 0.7, Pressure Side of Blade

Figure 17 - Variation of $\overline{C}_p$ with J, with Speed Correction

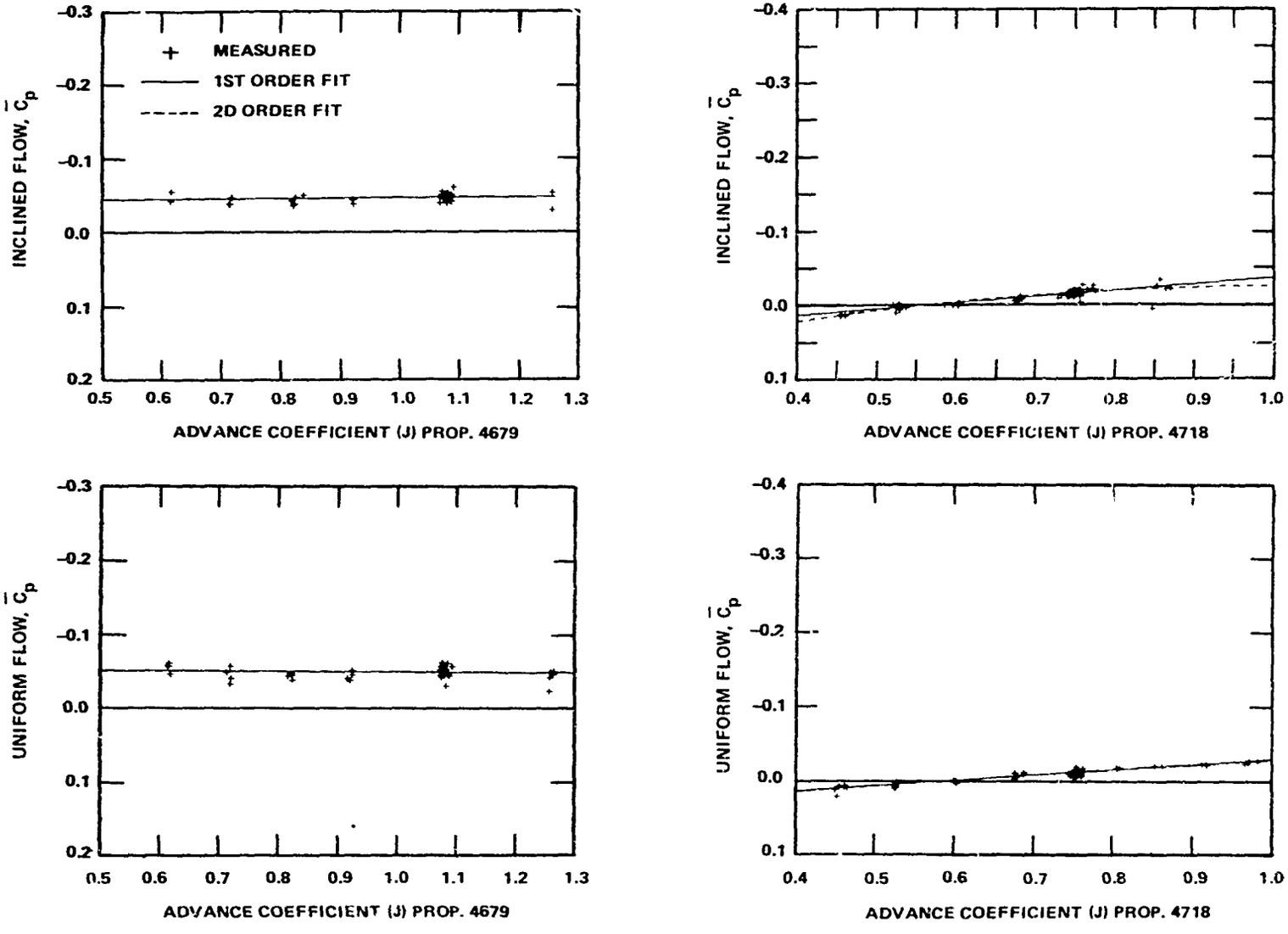

Figure 17a - Gage 1, x/c = 0.9, r/R = 0.5, Pressure Side

Figure 17 (Continued)

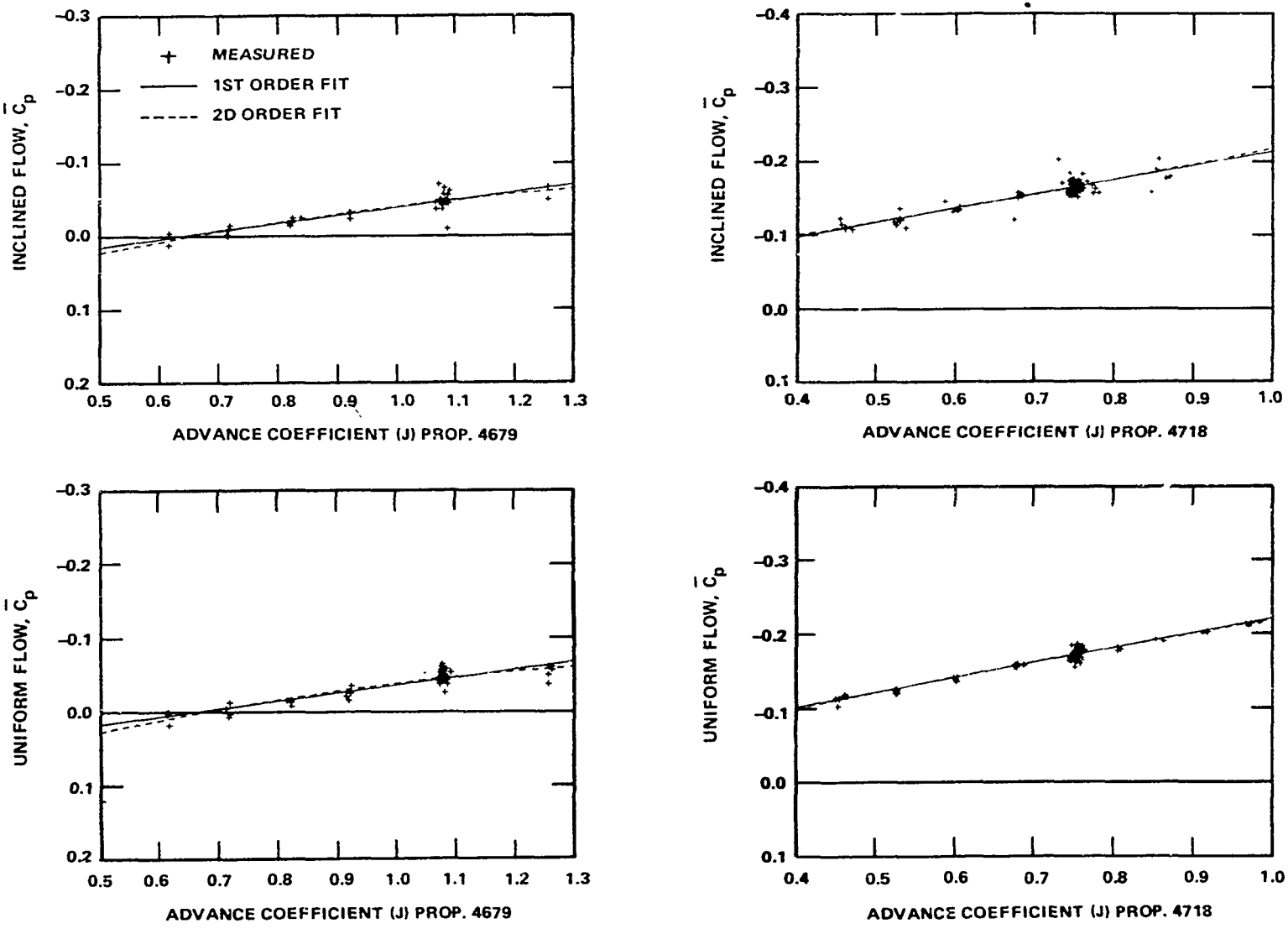

Figure 17b - Gage 2, x/c = 0.7, r/R = 0.5, Pressure Side

Figure 17 (Continued)

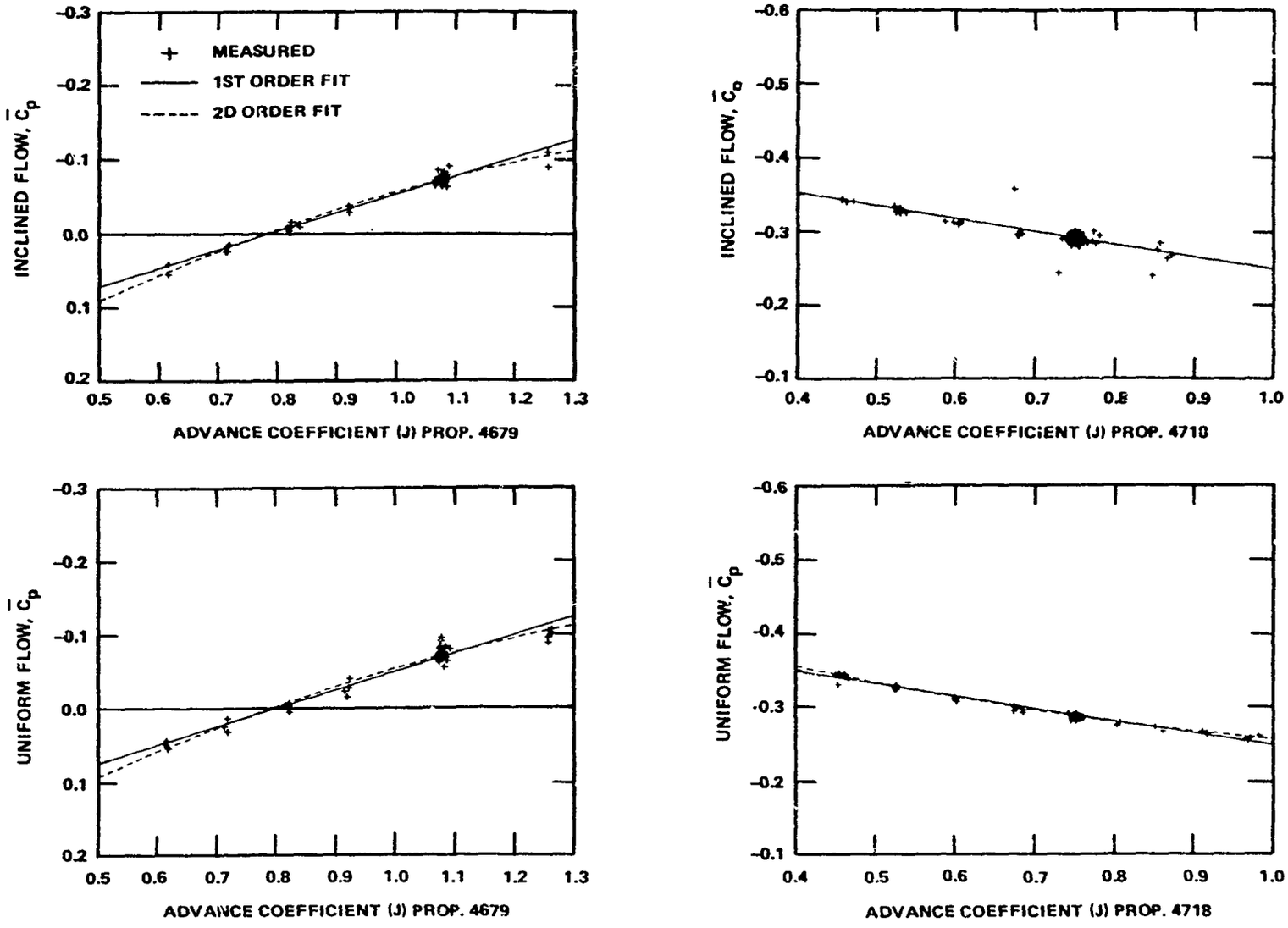

Figure 17c - Gage 3, x/c = 0.5, r/R = 0.5, Pressure Side

Figure 17 (Continued)

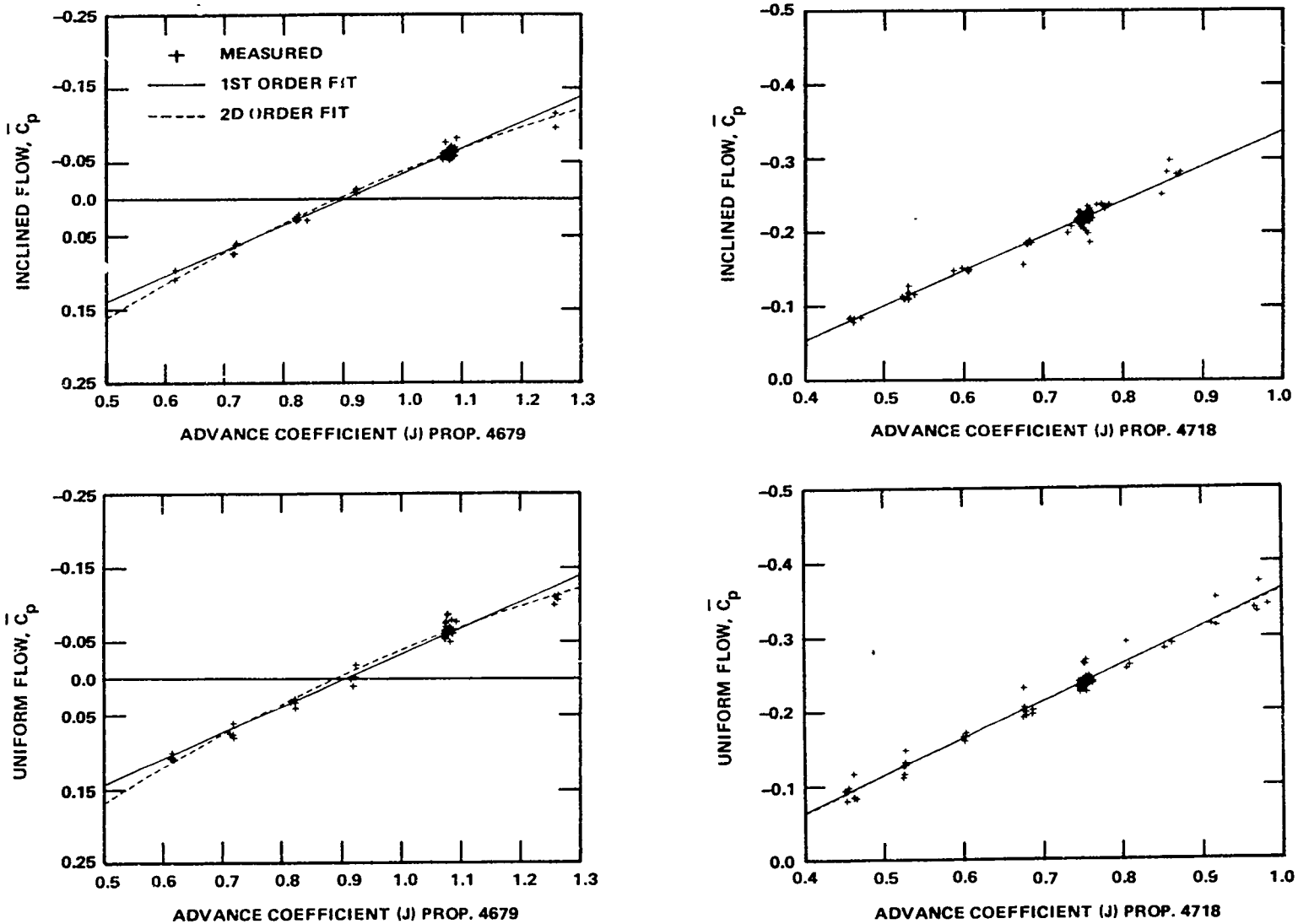

Figure 17d - Gage 4, x/c = 0.35, r/R = 0.5, Pressure Side

Figure 17 (Continued)

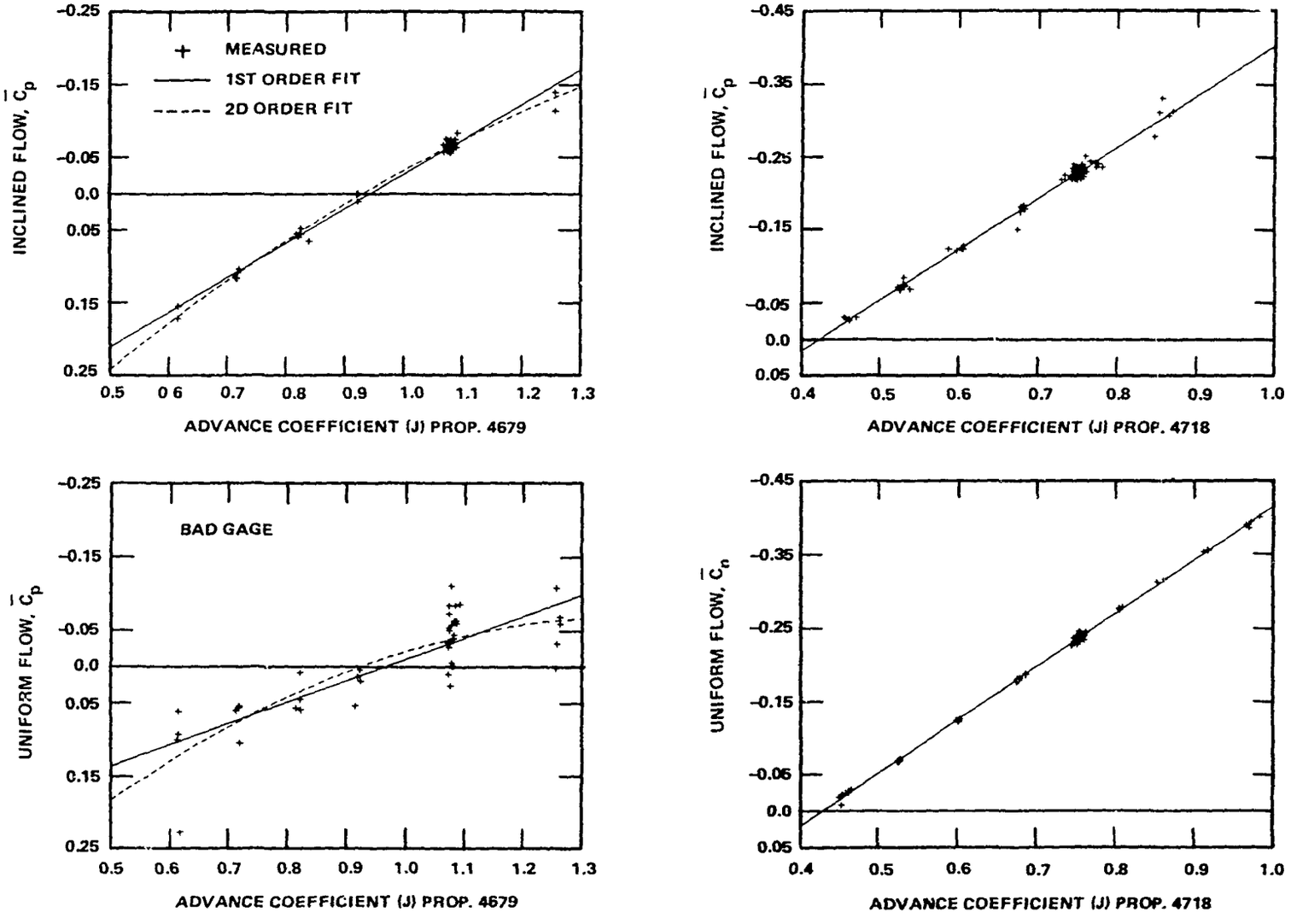

Figure 17e - Gage 5, x/c = 0.2, r/R = 0.5, Pressure Side

Figure 17 (Continued)

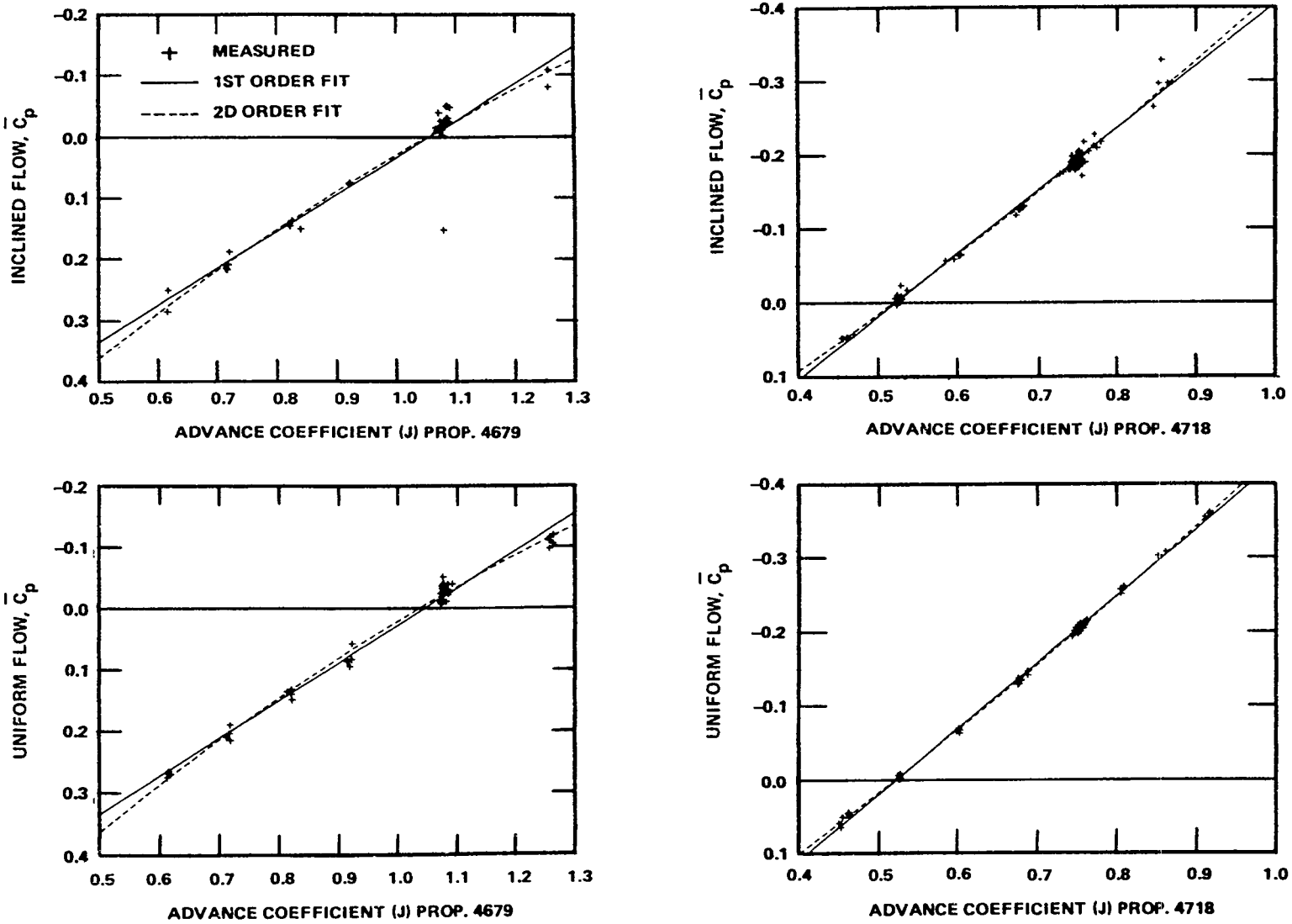

Figure 17f - Gage 6, x/c = 0.12, r/R = 0.5, Pressure Side

Figure 17 (Continued)

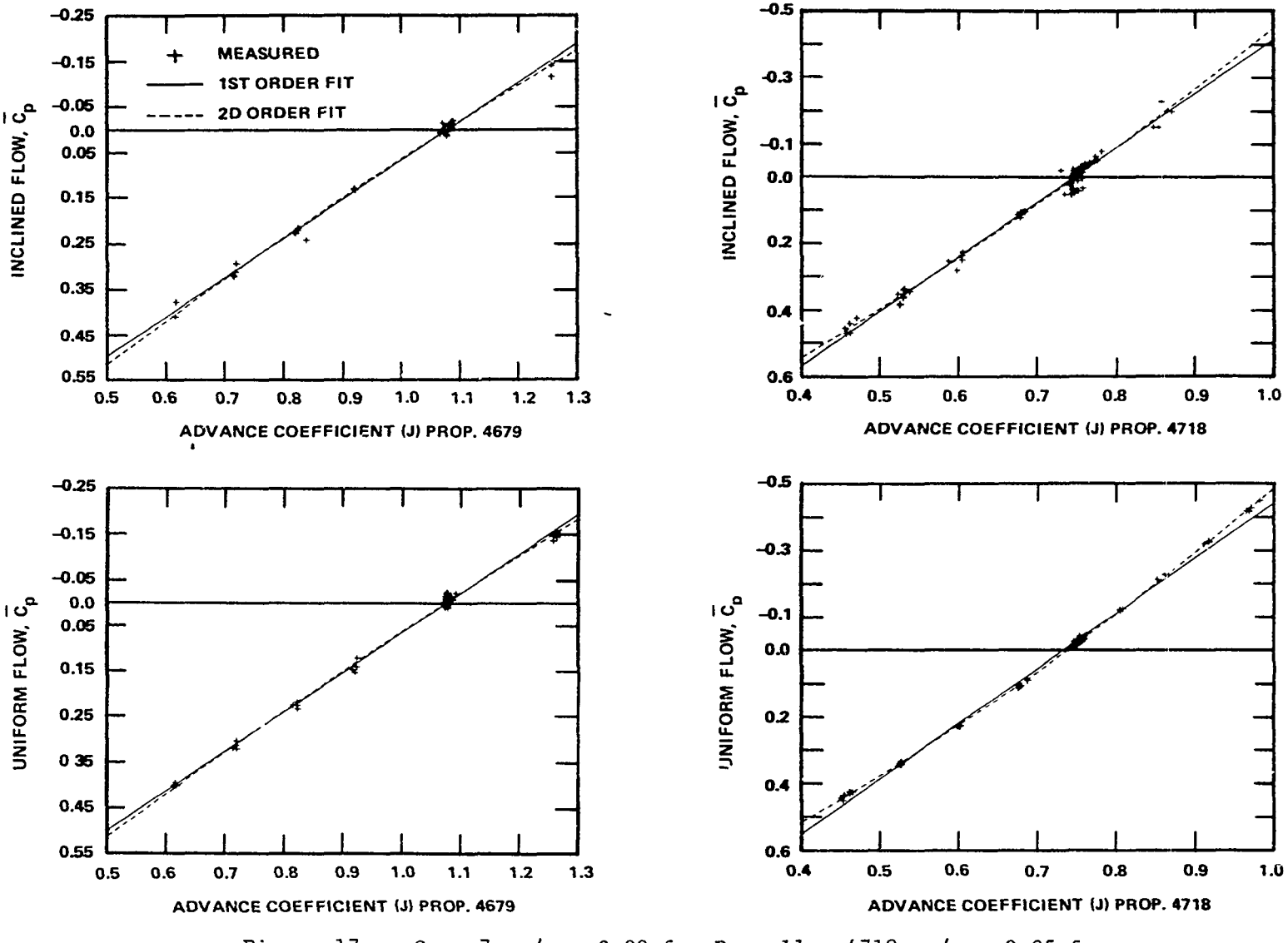

Figure 17g - Gage 7, x/c = 0.03 for Propeller 4718, x/c = 0.05 for Propeller 4679, r/R = 0.5, Pressure Side of Blade

Figure 17 (Continued)

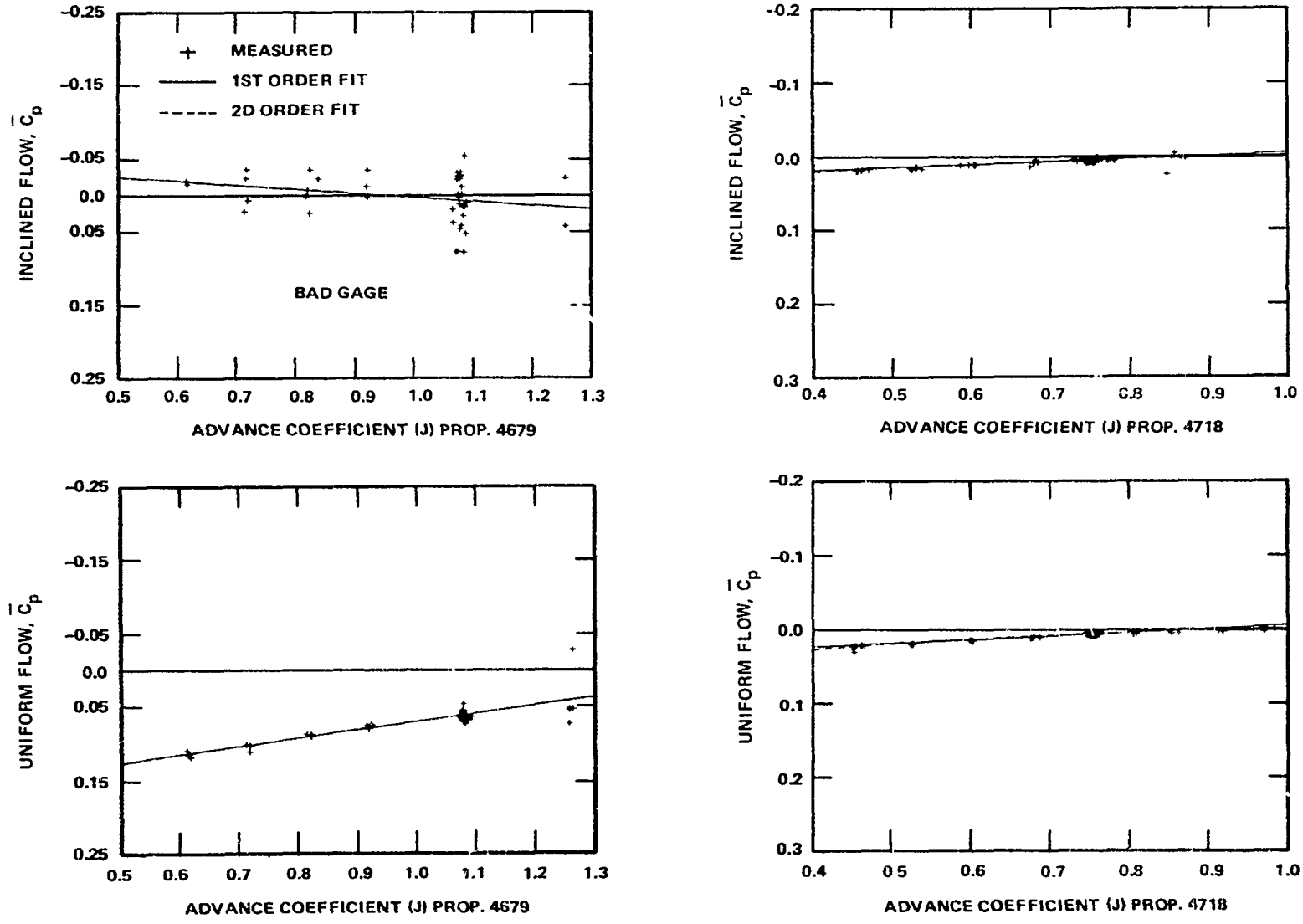

Figure 17h - Gage 8, x/c = 0.9 for Propeller 4718, x/c = 0.85 for Propeller 4679, r/R = 0.7, Pressure Side of Blade

Figure 17 (Continued)

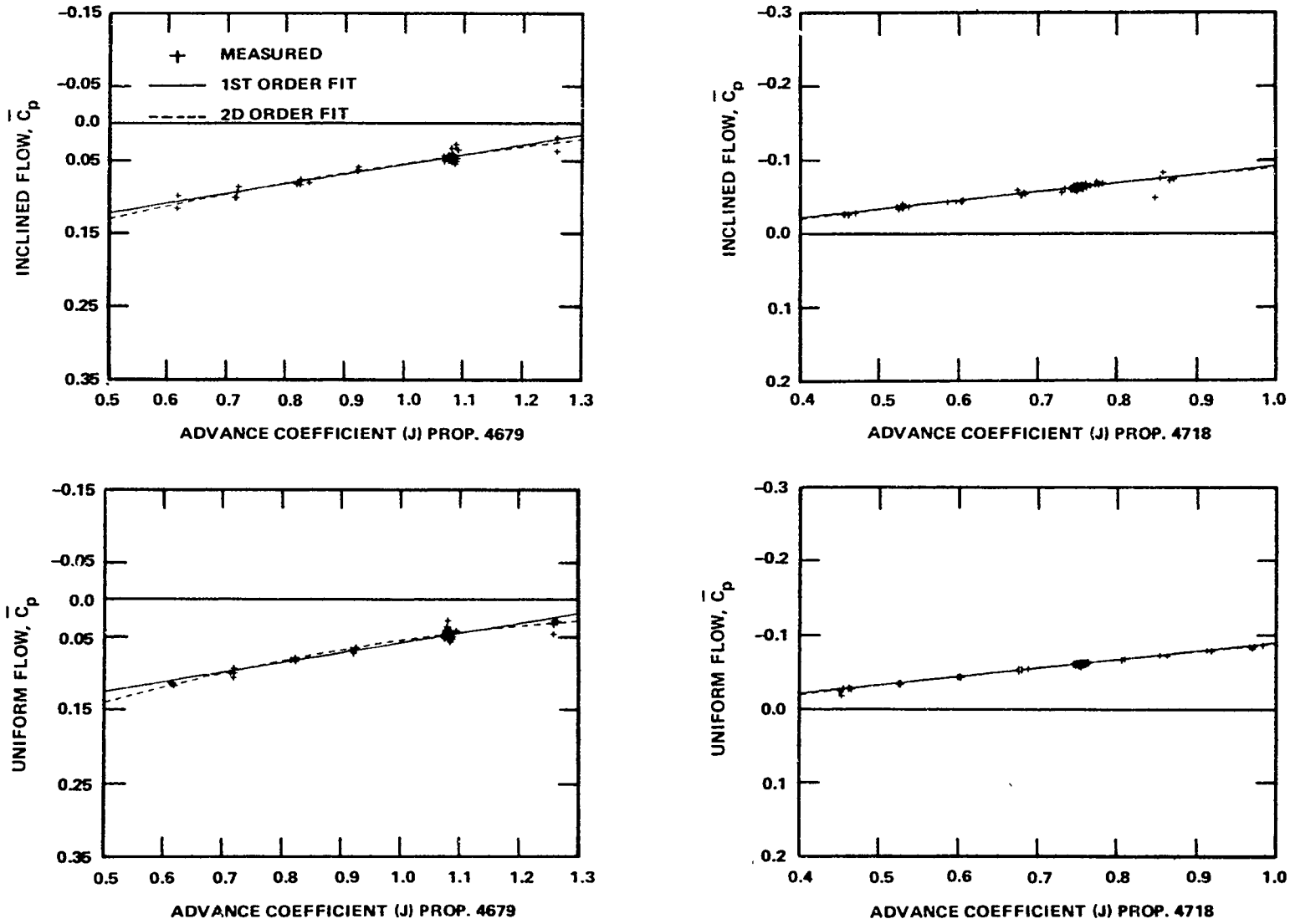

Figure 17i - Gage 9, x/c = 0.7 for Propeller 4718, x/c = 0.65 for Propeller 4679, r/R = 0.7, Pressure Side of Blade

Figure 17 (Continued)

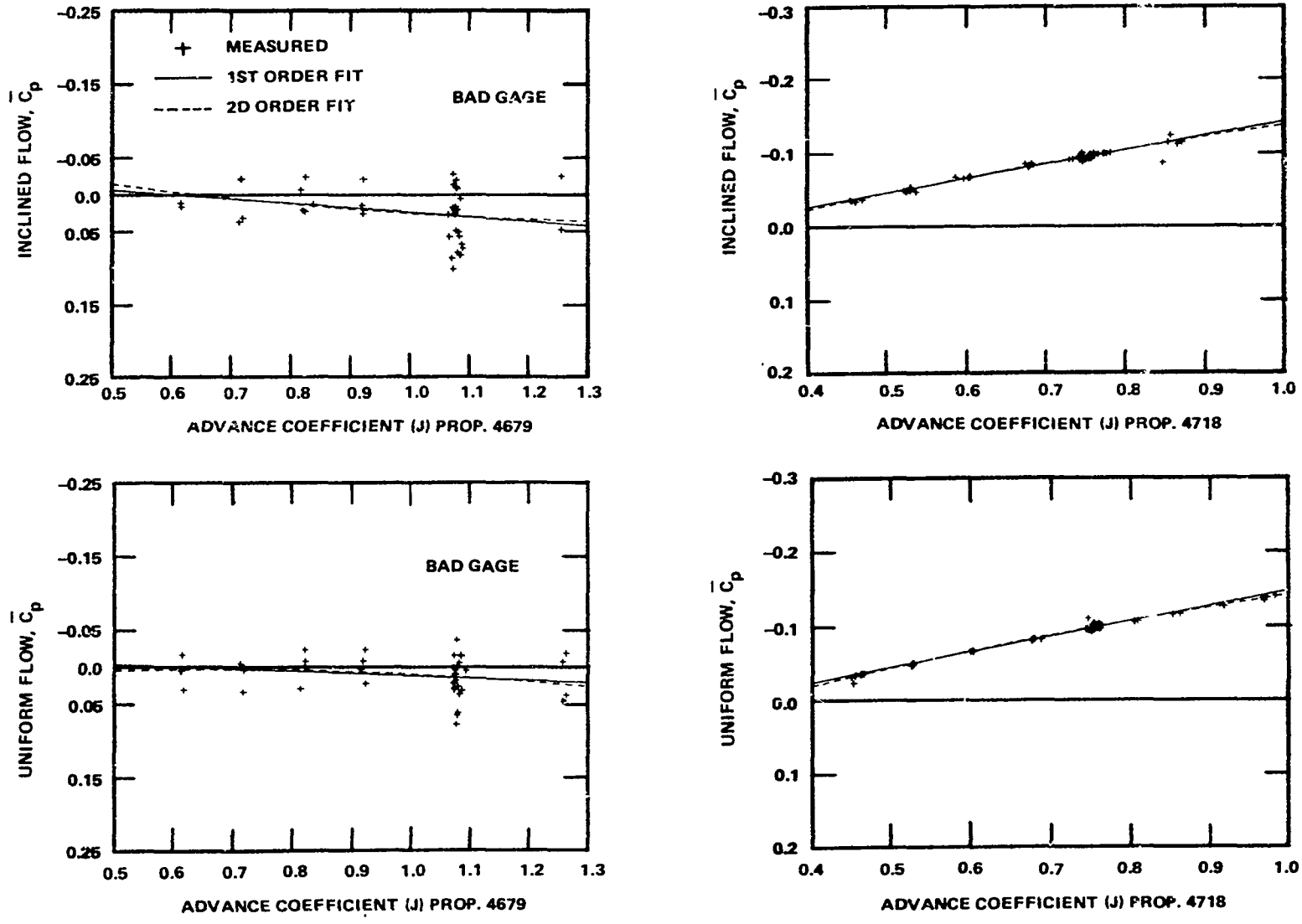

Figure 17j - Gage 10, x/c = 0.5, r/R = 0.7, Pressure Side of Blade

Figure 17 (Continued)

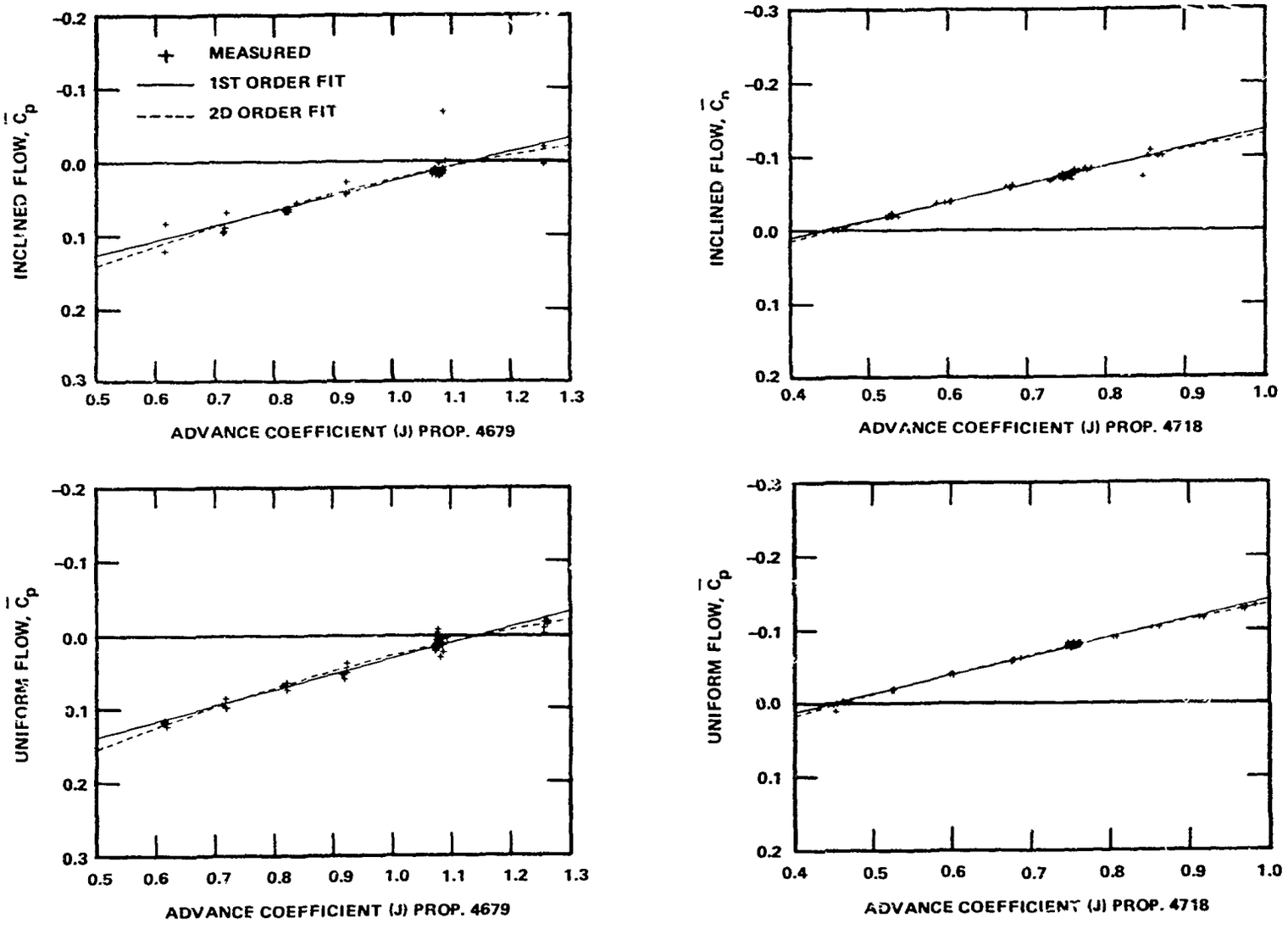

Figure 17k - Gage 11, x/c = 0.4, r/R = 0.7, Pressure Side of Blade

Figure 17 (Continued)

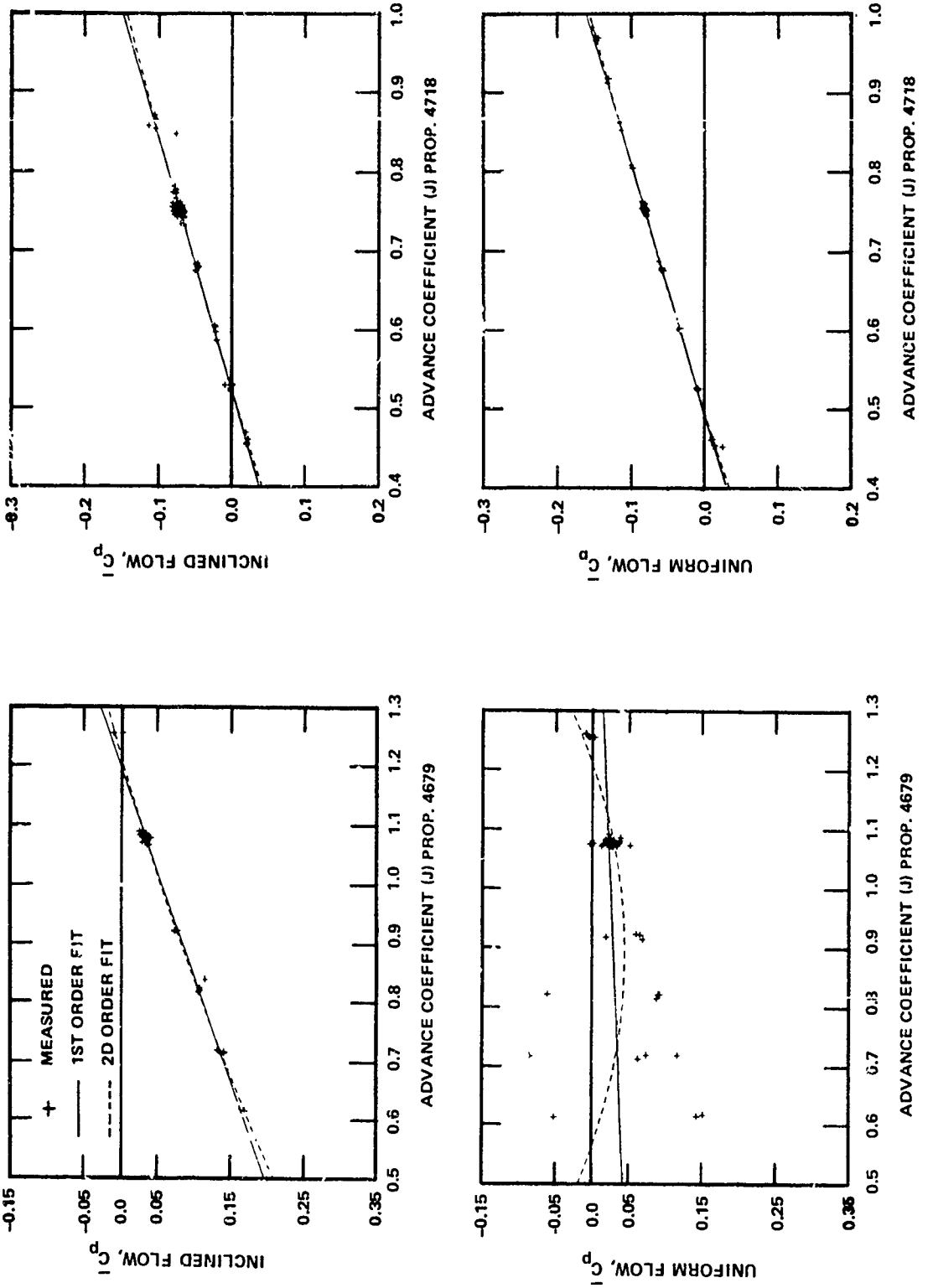

Figure 171 - Gage 12, x/c = 0.3, r/R = 0.7, Pressure Side of Blade

Figure 17 (Continued)

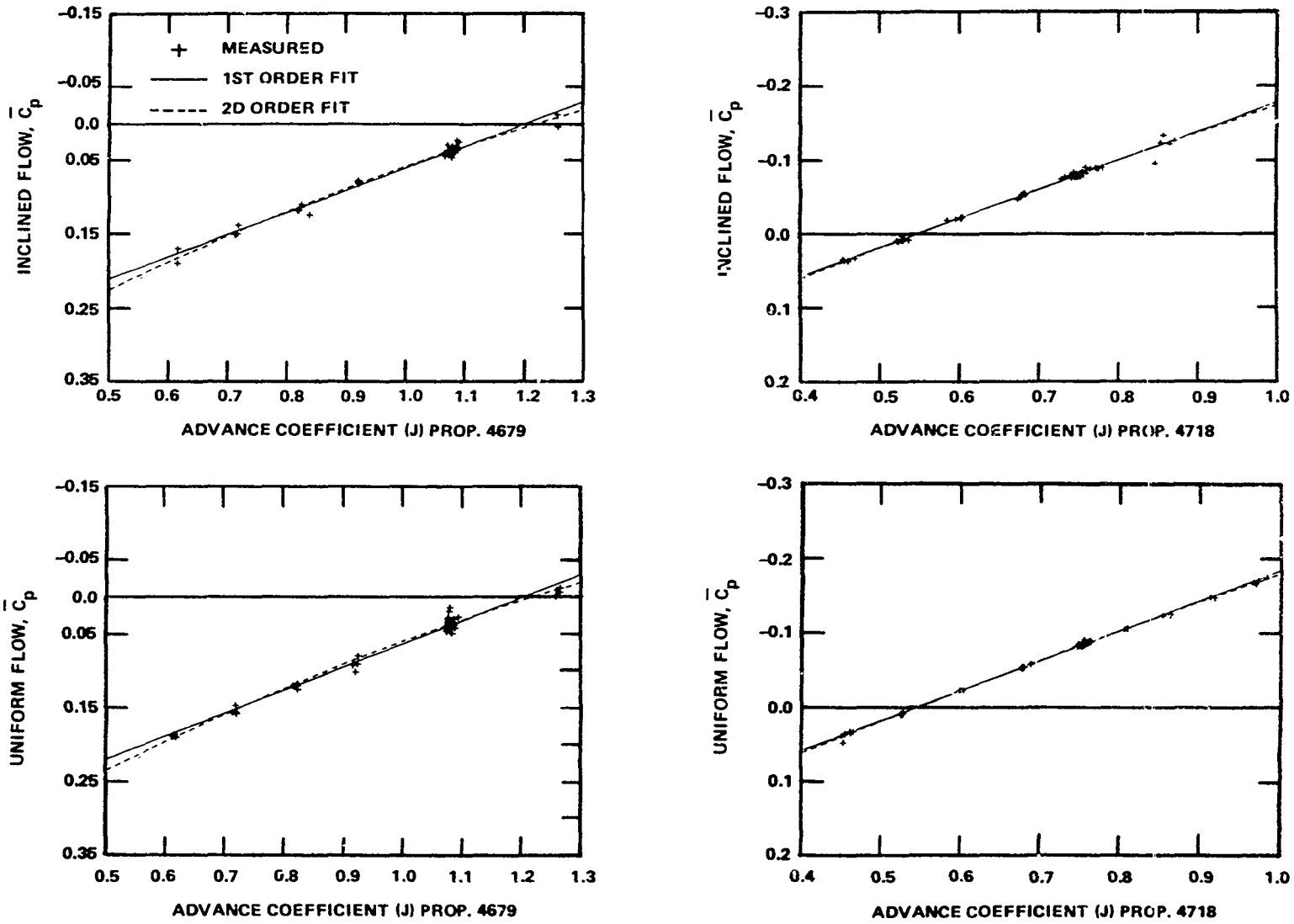

Figure 17n - Gage 13, x/c = 0.2, r/R = 0.7, Pressure Side of Blade

Figure 17 (Continued)

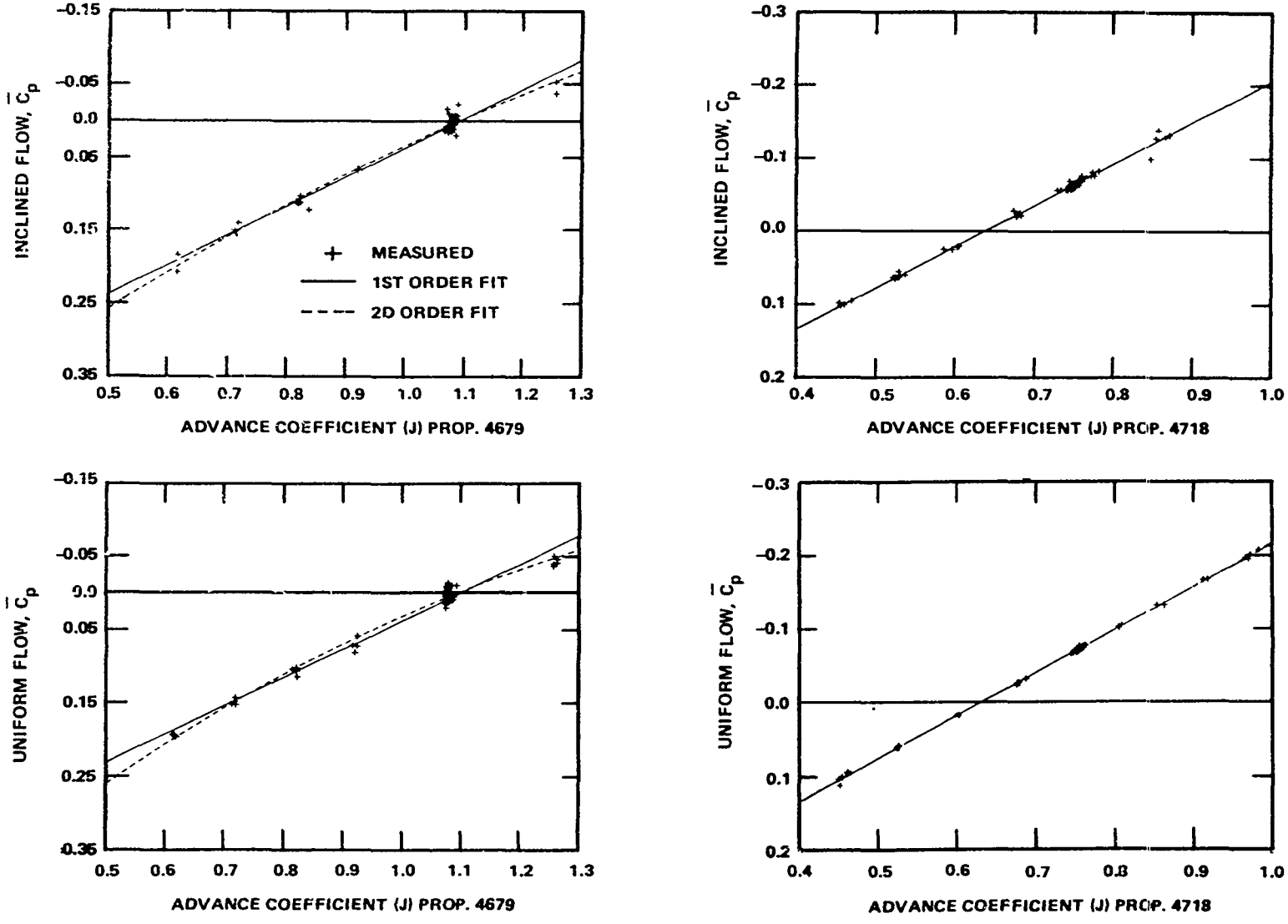

Figure 17n - Gage 14, x/c = 0.1 for Propeller 4718, x/c = 0.12 for Propeller 4679, r/R = 0.7, Pressure Side of Blade

Figure 17 (Continued)

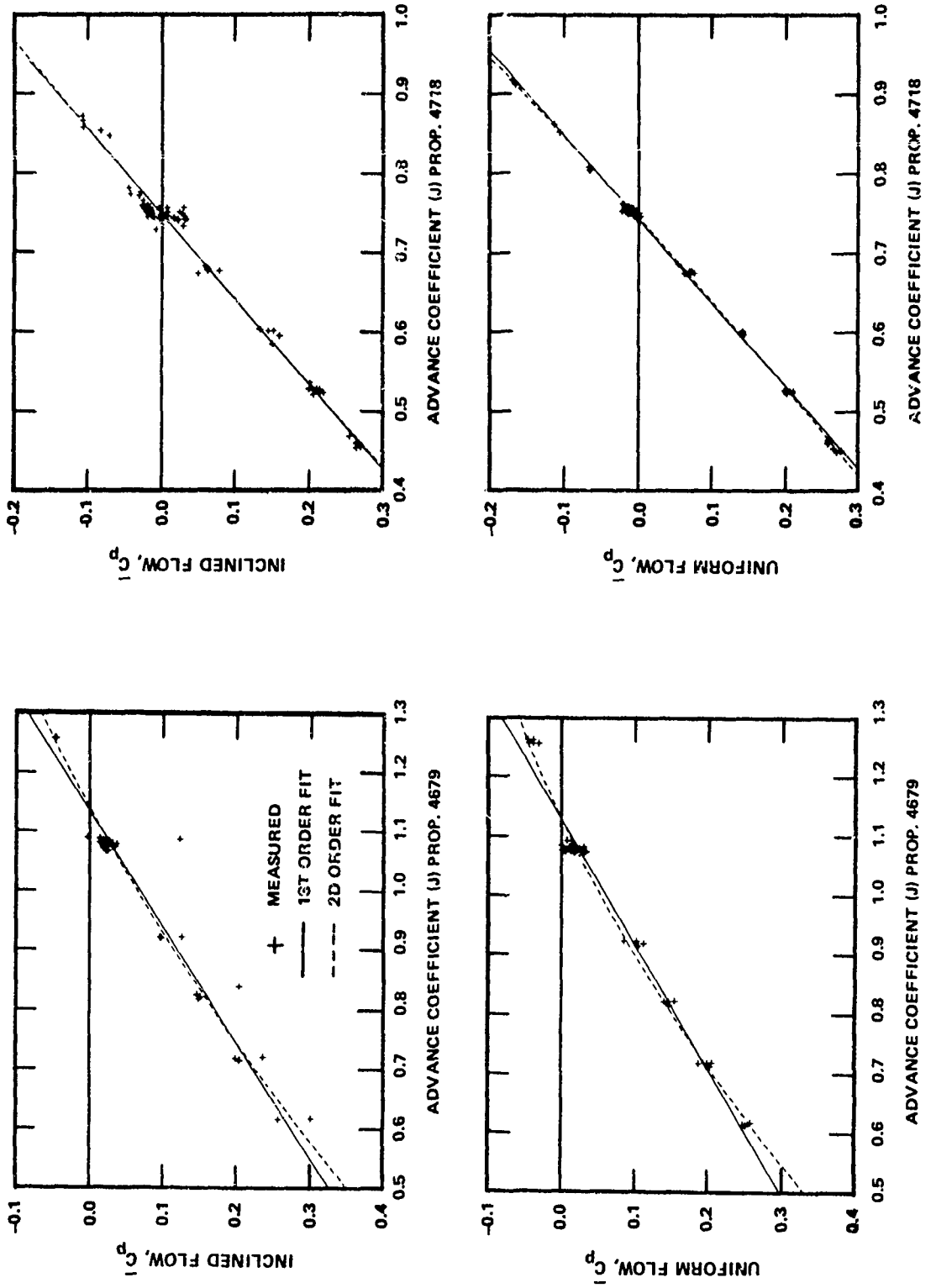

Figure 17o - Gage 15, x/c = 0.03 for Propeller 4718, x/c = 0.05 for Propeller 4679, r/R = 0.7, Pressure Side of Blade

Figure 17 (Continued)

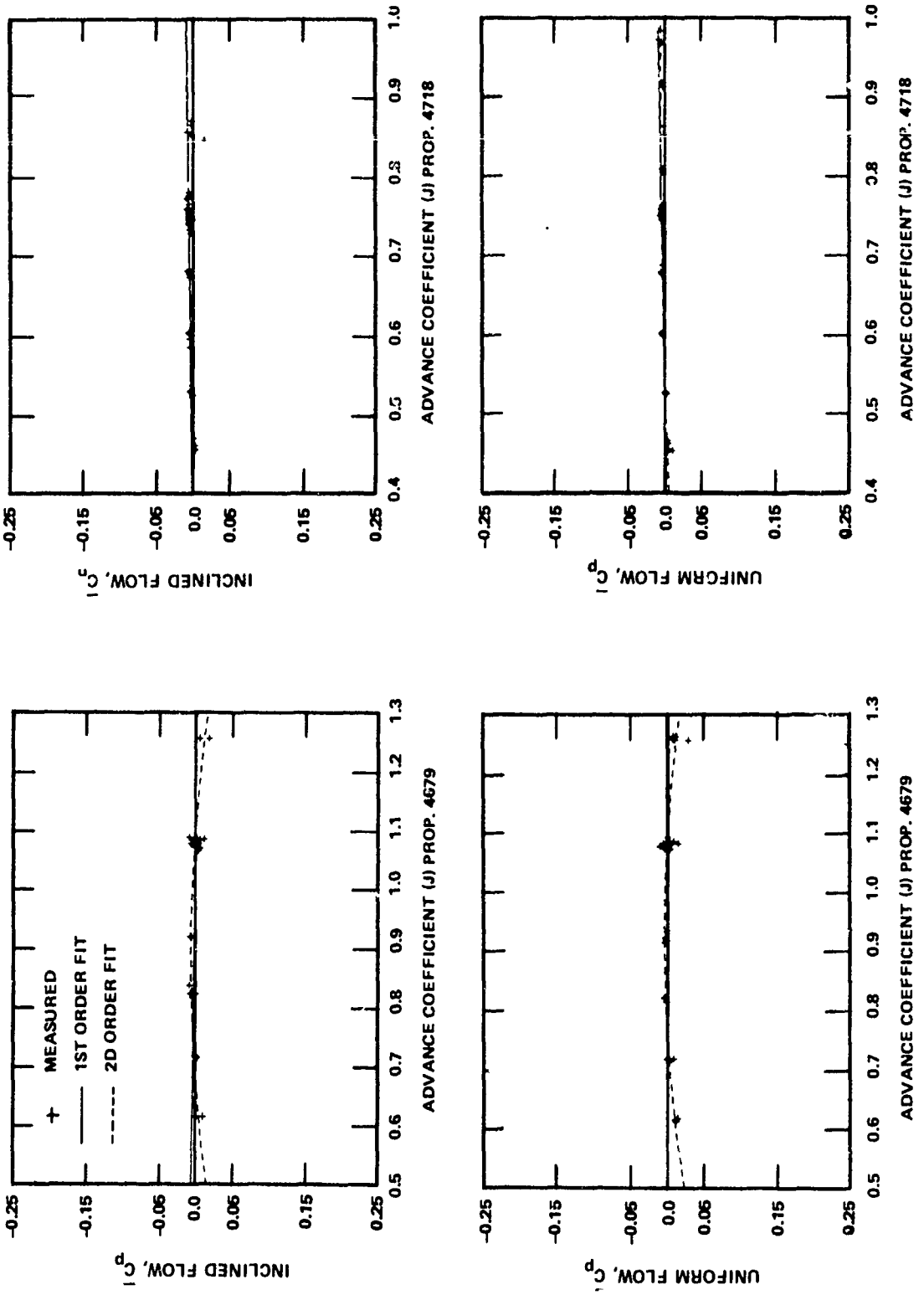

Figure 17p - Gage 16, x/c = 0.8 for Propeller 4718, x/c = 0.9 for Propeller 4679, r/R = 0.9, Pressure Side of Blade

Figure 17 (Continued)

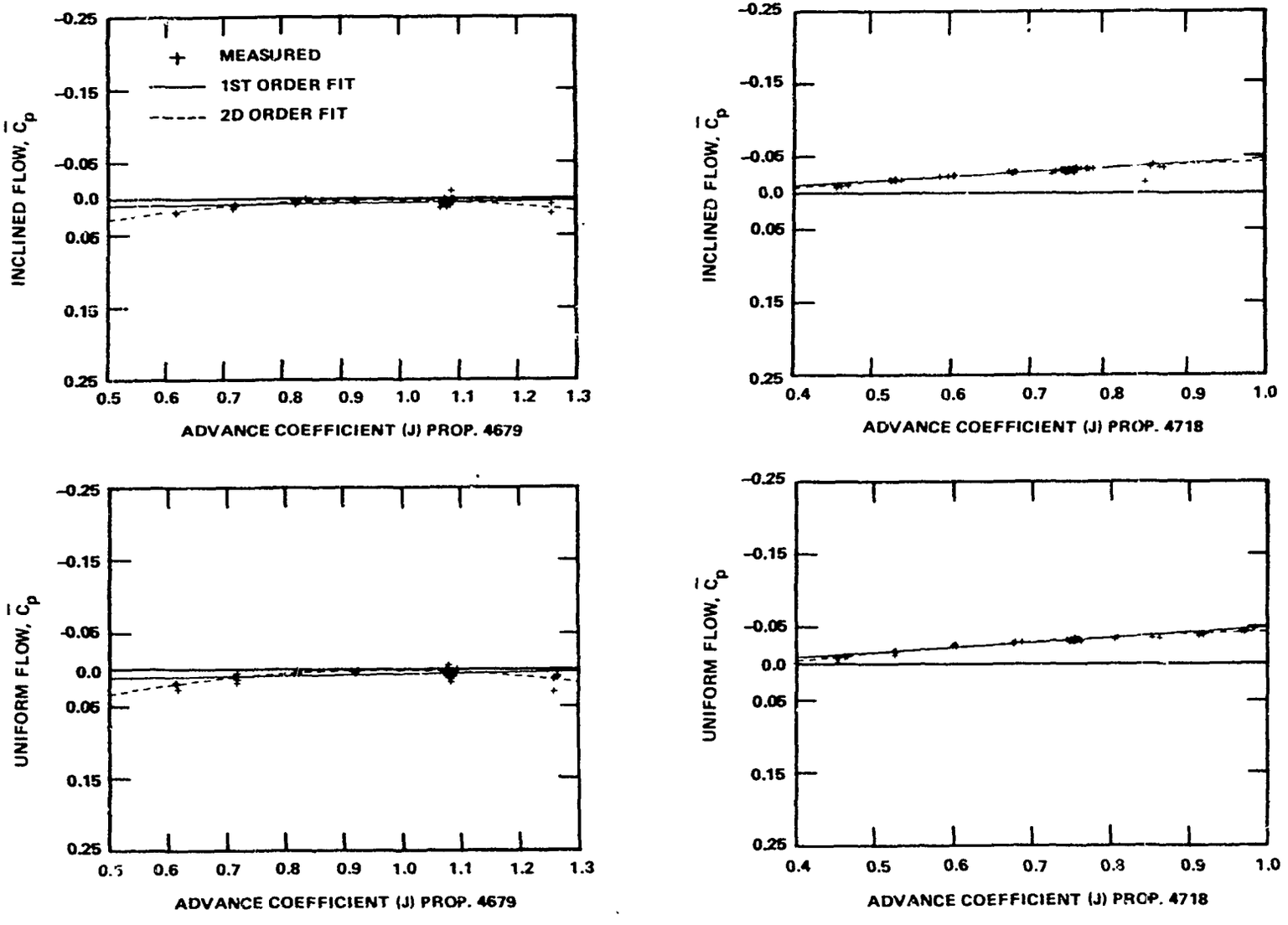

Figure 17q - Gage 17, x/c = 0.6 for Propeller 4718, x/c = 0.63 for Propeller 4679, r/R = 0.9, Pressure Side of Blade

Figure 17 (Continued)

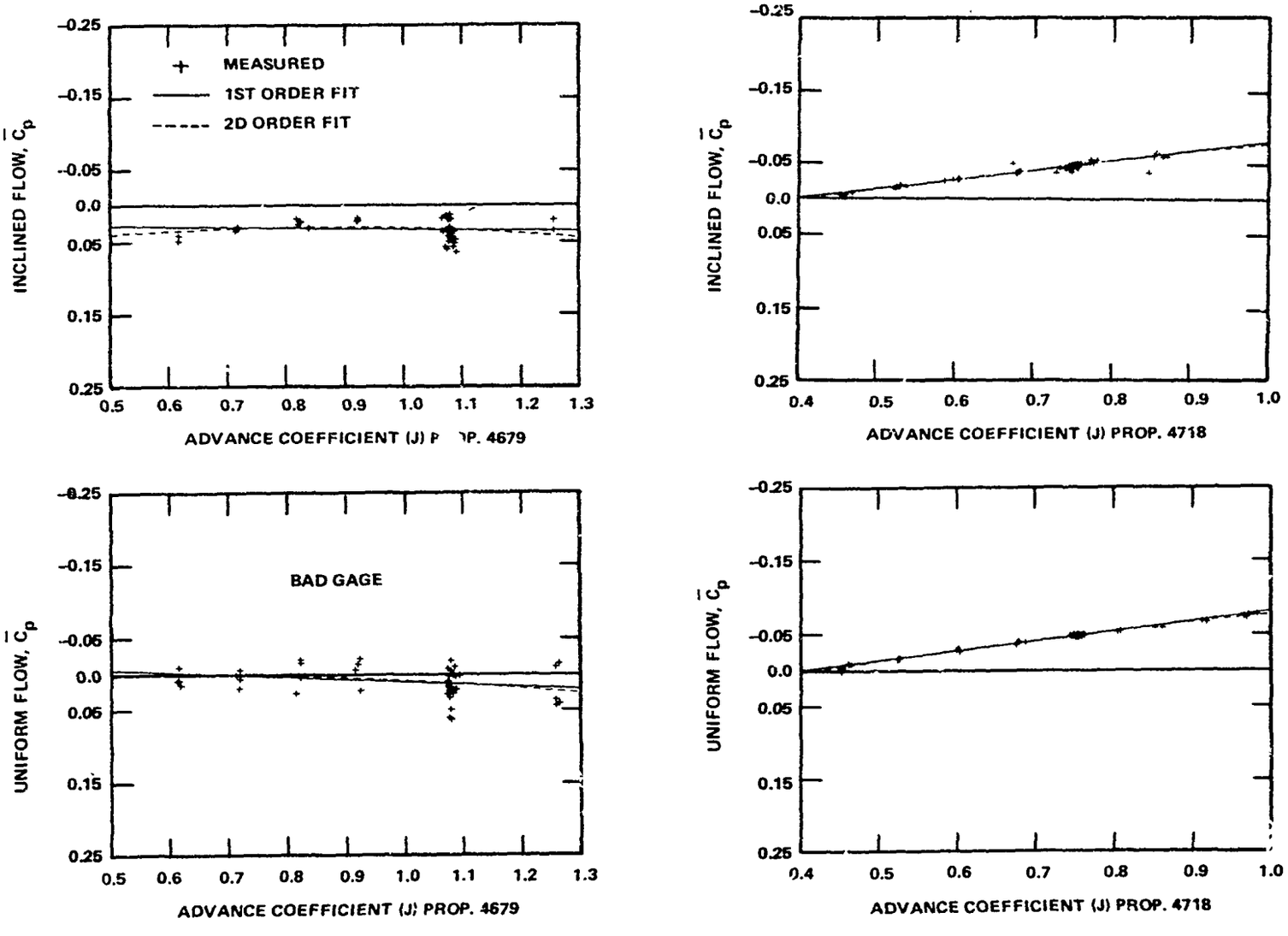

Figure 17r - Gage 18, x/c = 0.4 for Propeller 4718, x/c = 0.51 for Propeller 4679, r/R = 0.9, Pressure Side of Blade

Figure 17 (Continued)

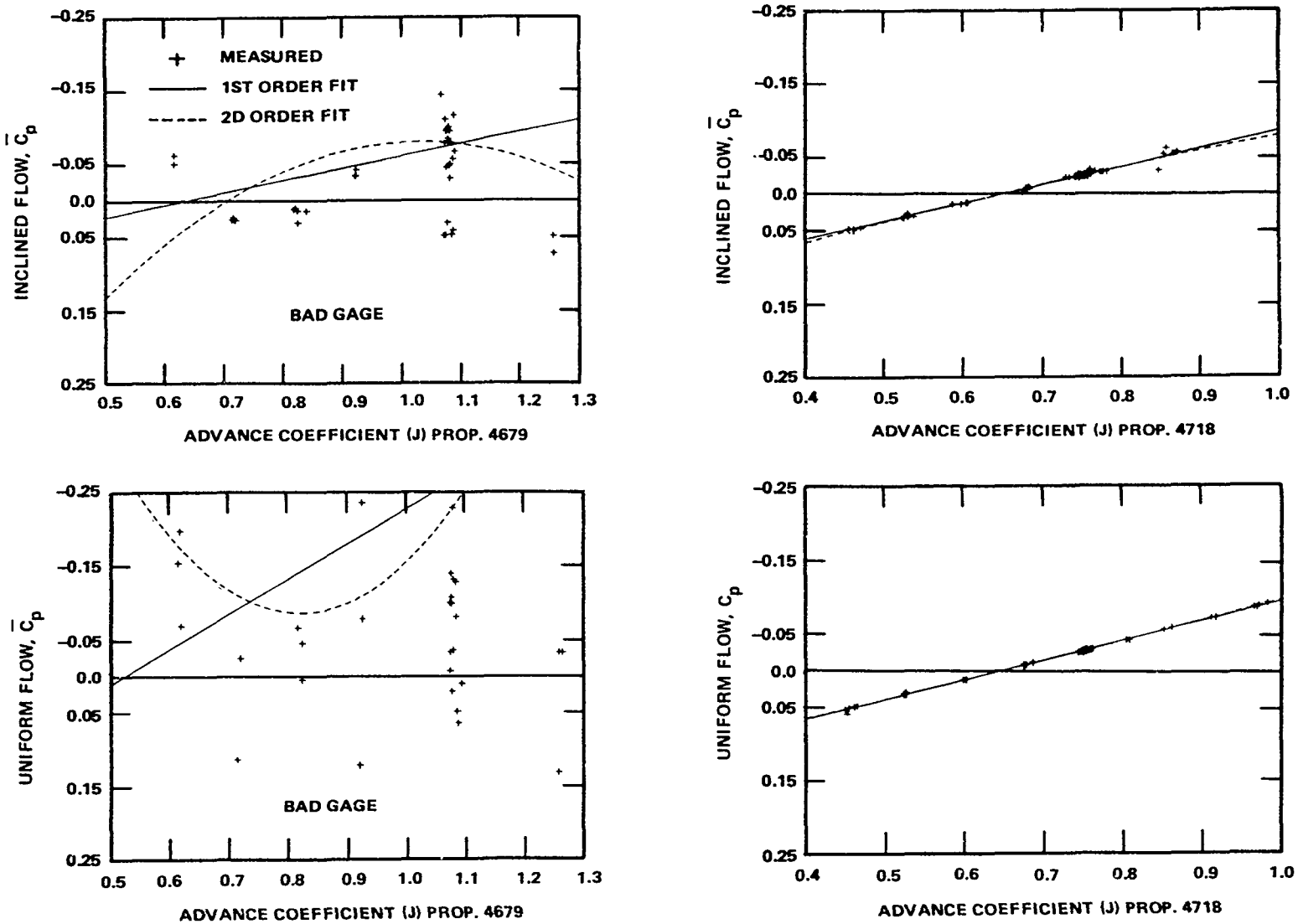

Figure 17s - Gage 19, x/c = 0.2 for Propeller 4718, x/c = 0.36 for Propeller 4679, r/R = 0.9, Pressure Side of Blade

Figure 17 (Continued)

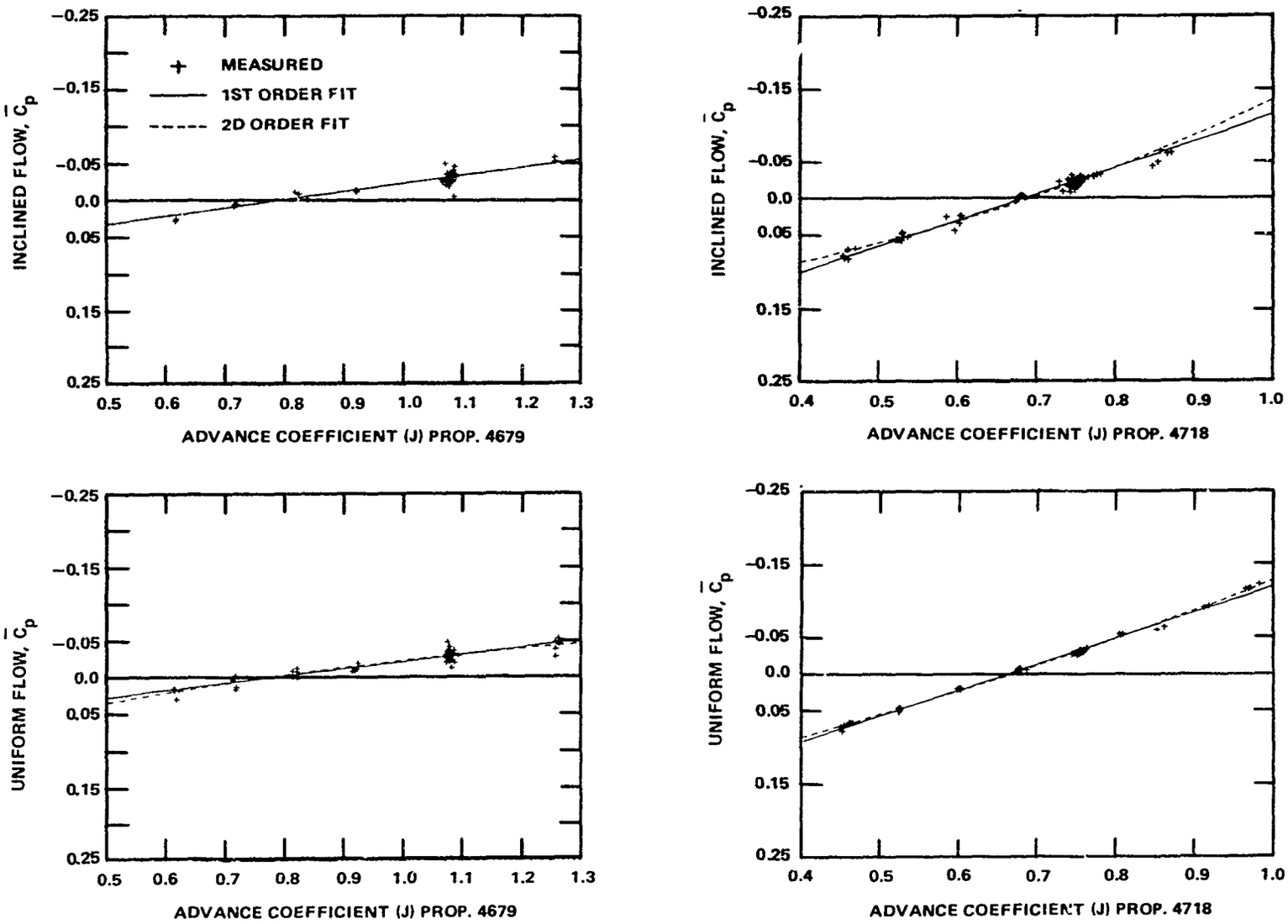

Figure 17t - Gage 20, x/c = 0.1 for Propeller 4718, x/c = 0.21 for Propeller 4679, r/R = 0.9, Pressure Side of Blade

Figure 17 (Continued)

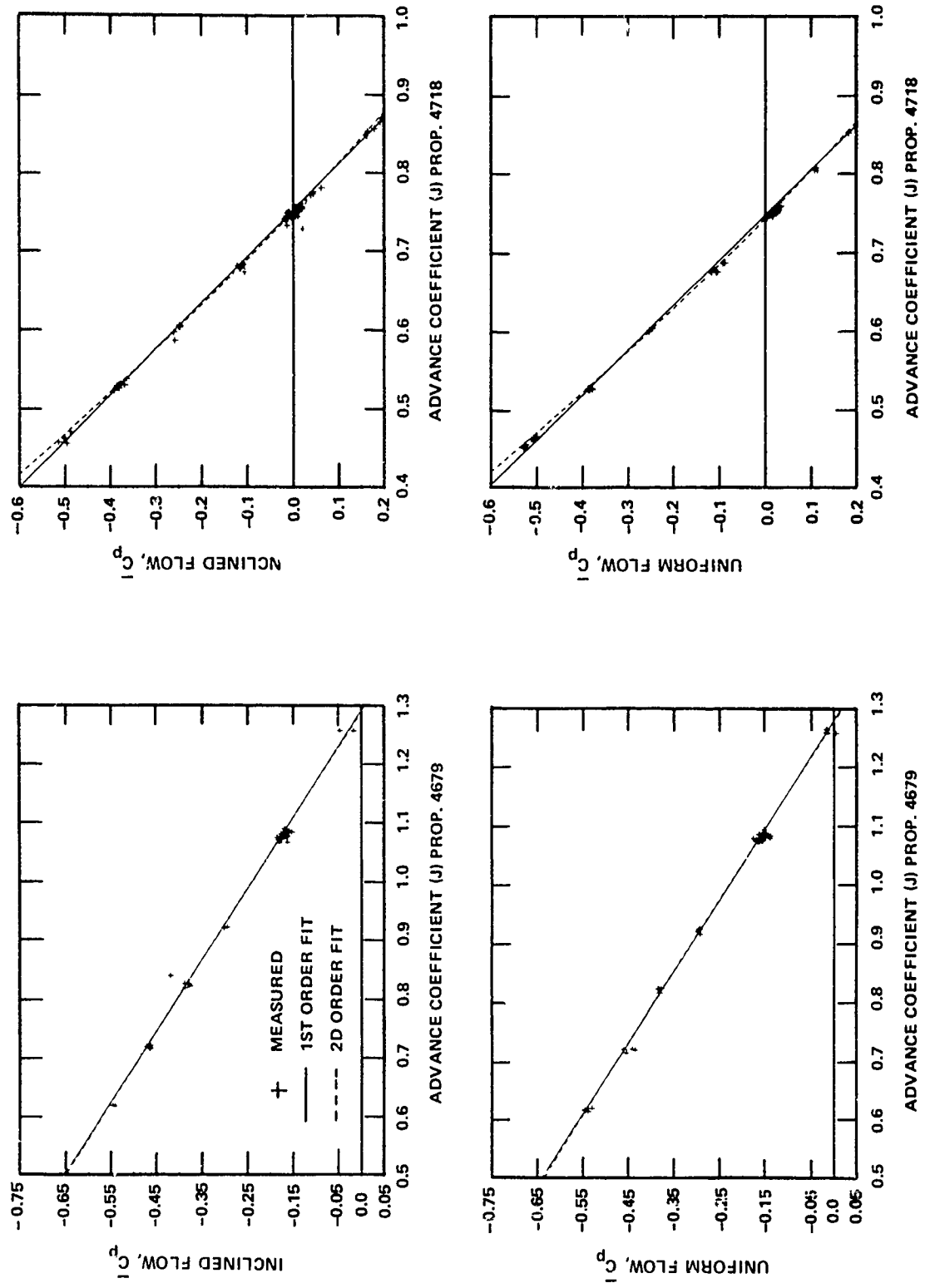

Figure 17u - Gage 21, x/c = 0.03 for Propeller 4718, x/c = 0.05 for Propeller 4679, r/R = 0.5, Suction Side of Blade

Figure 17 (Continued)

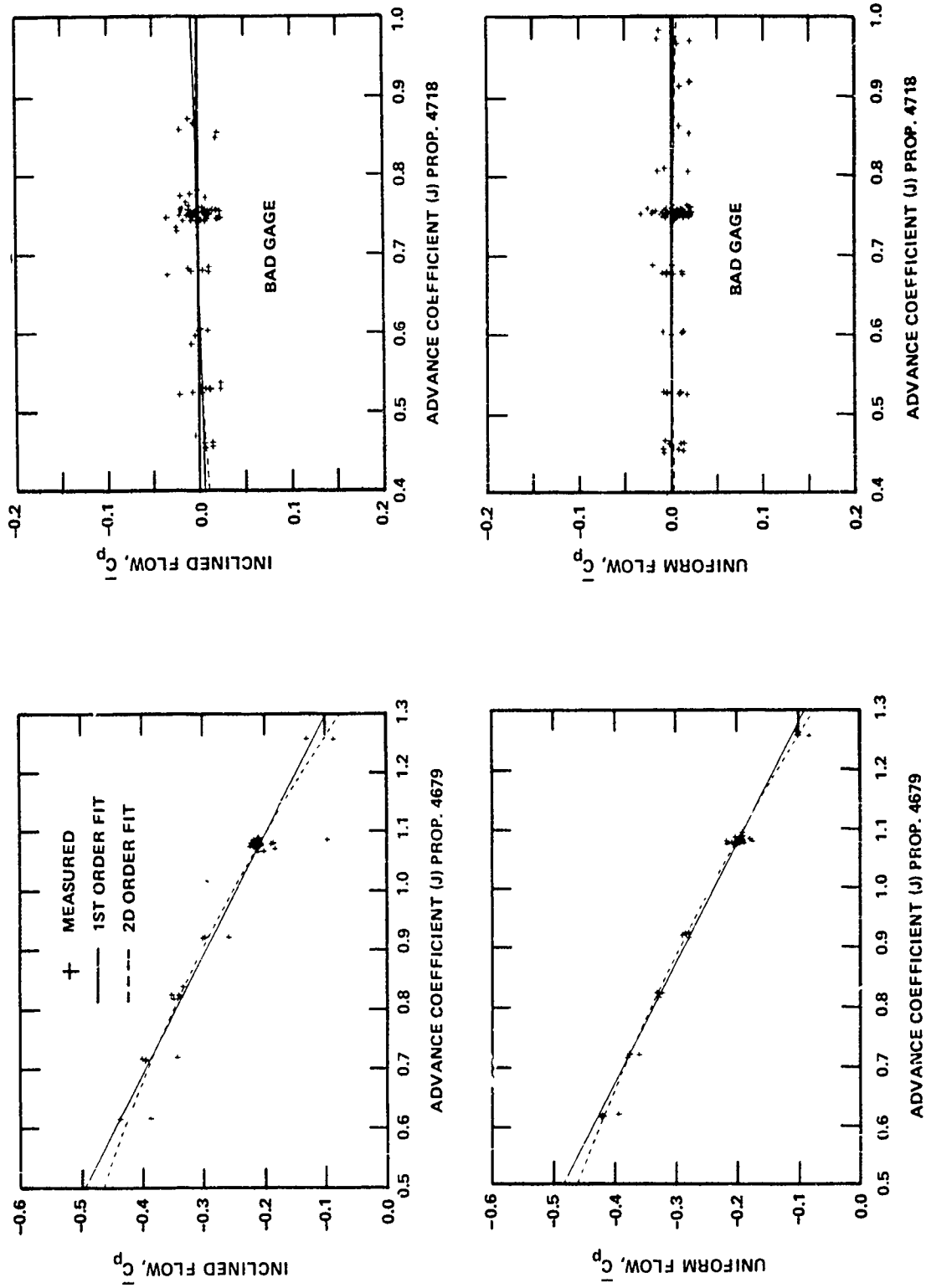

Figure 17v - Gage 22, x/c = 0.12, r/R = 0.5, Suction Side of Blade

Figure 17 (Continued)

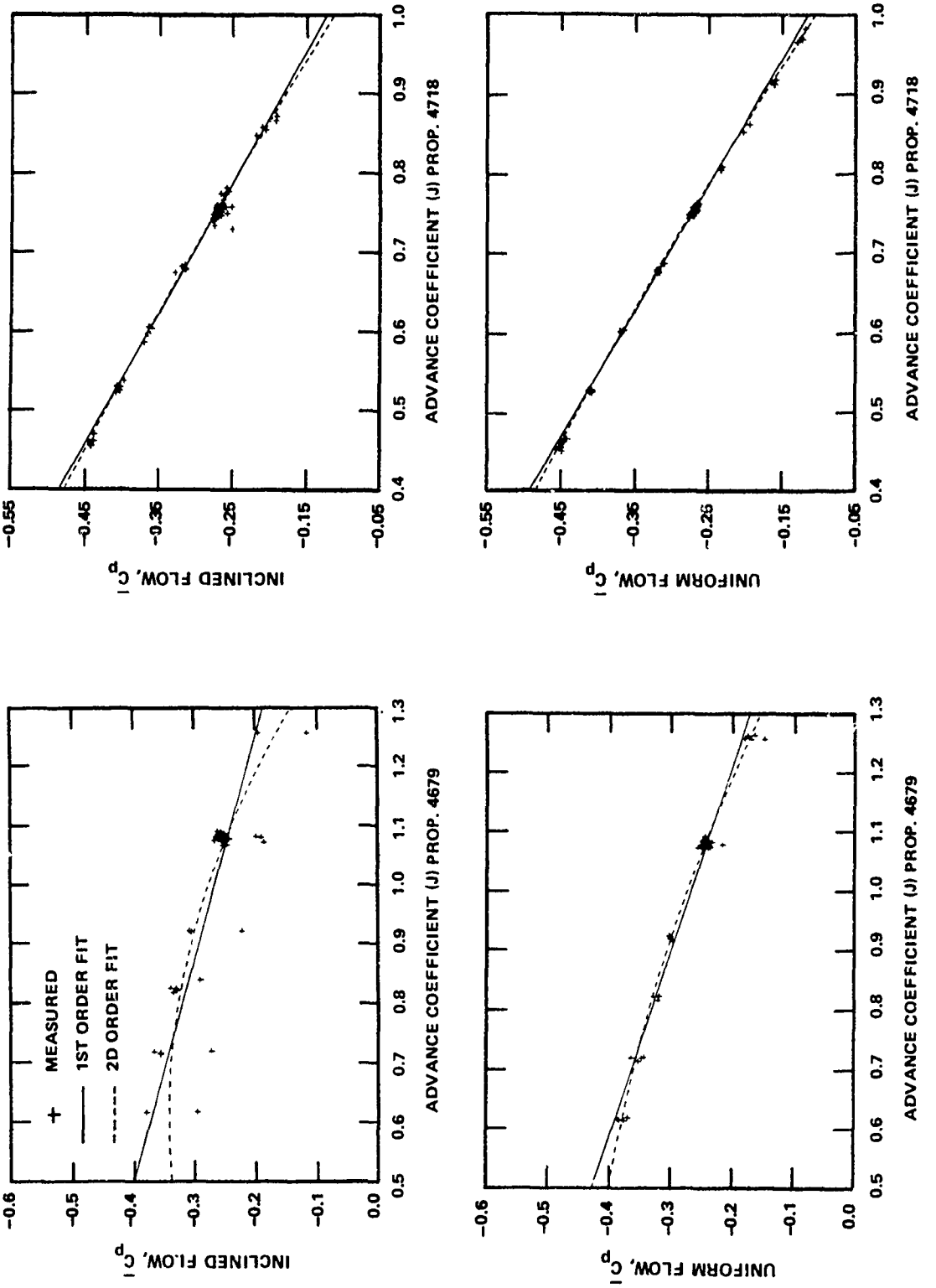

Figure 17w - Gage 23, x/c = 0.2, r/R = 0.5, Suction Side of Blade

Figure 17 (Continued)

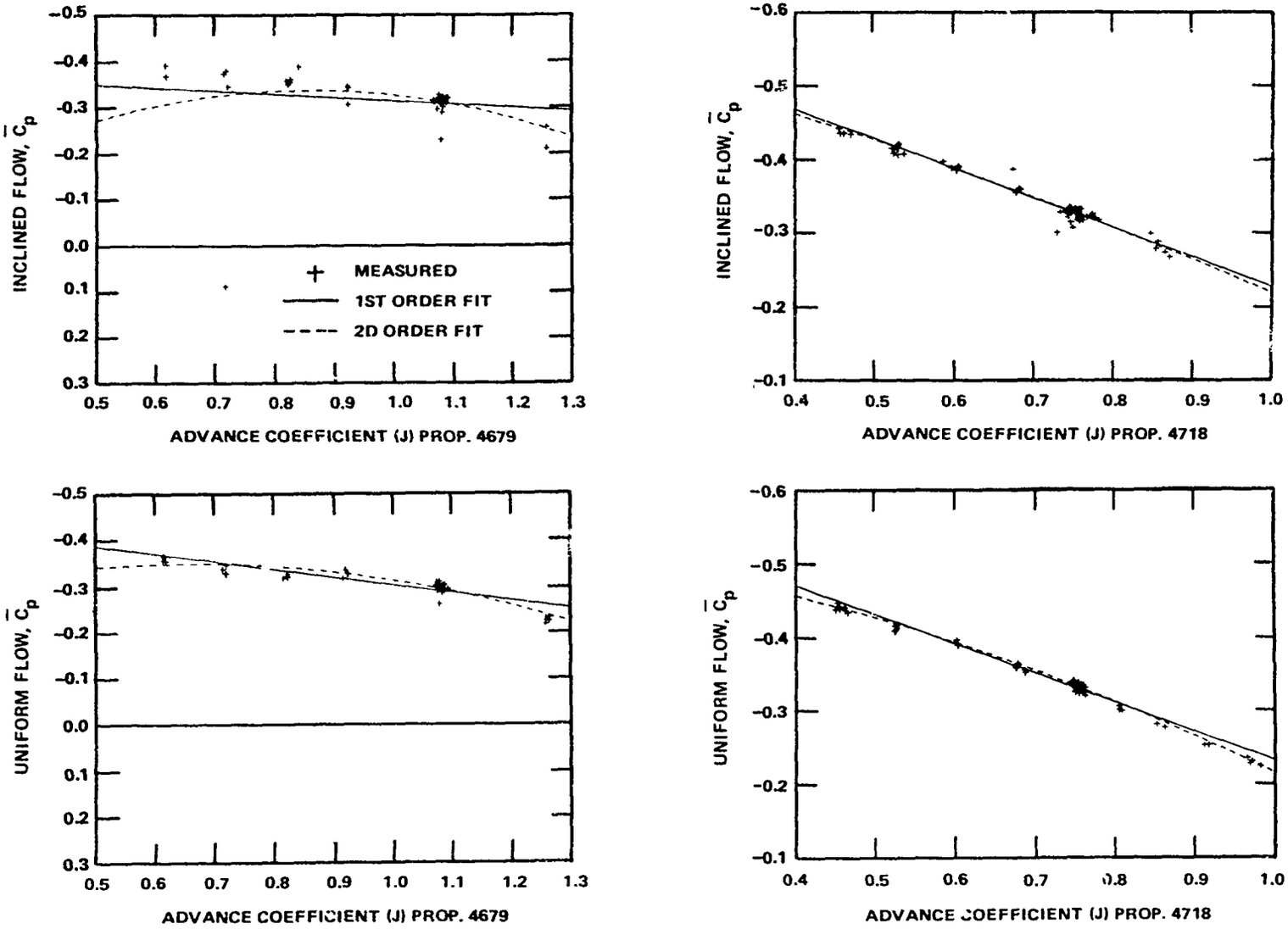

Figure 17x - Gage 24, x/c = 0.35, r/R = 0.5, Suction Side of Blade

Figure 17 (Continued)

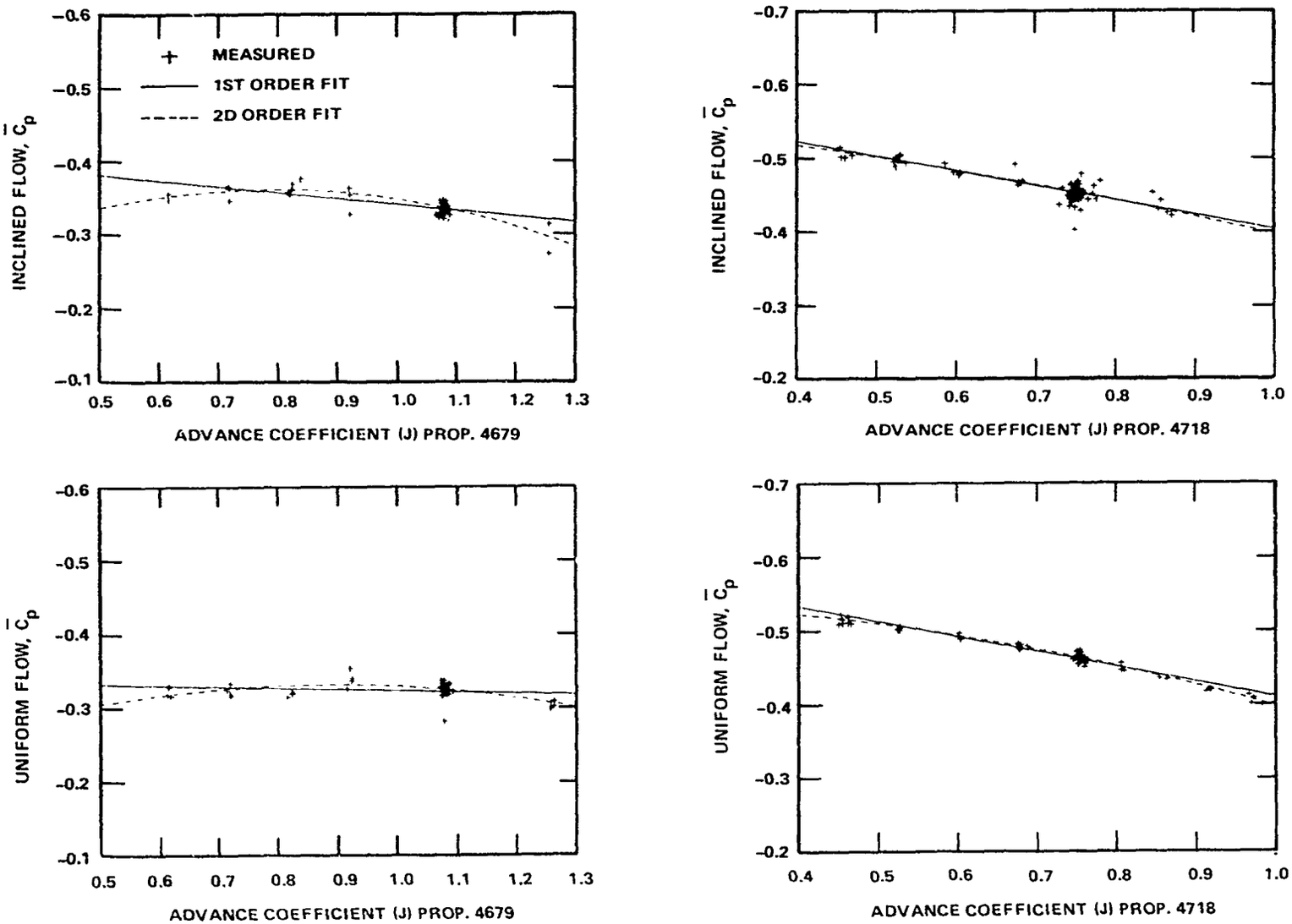

Figure 17y - Gage 25, x/c = 0.5, r/R = 0.5, Suction Side of Blade

Figure 17 (Continued)

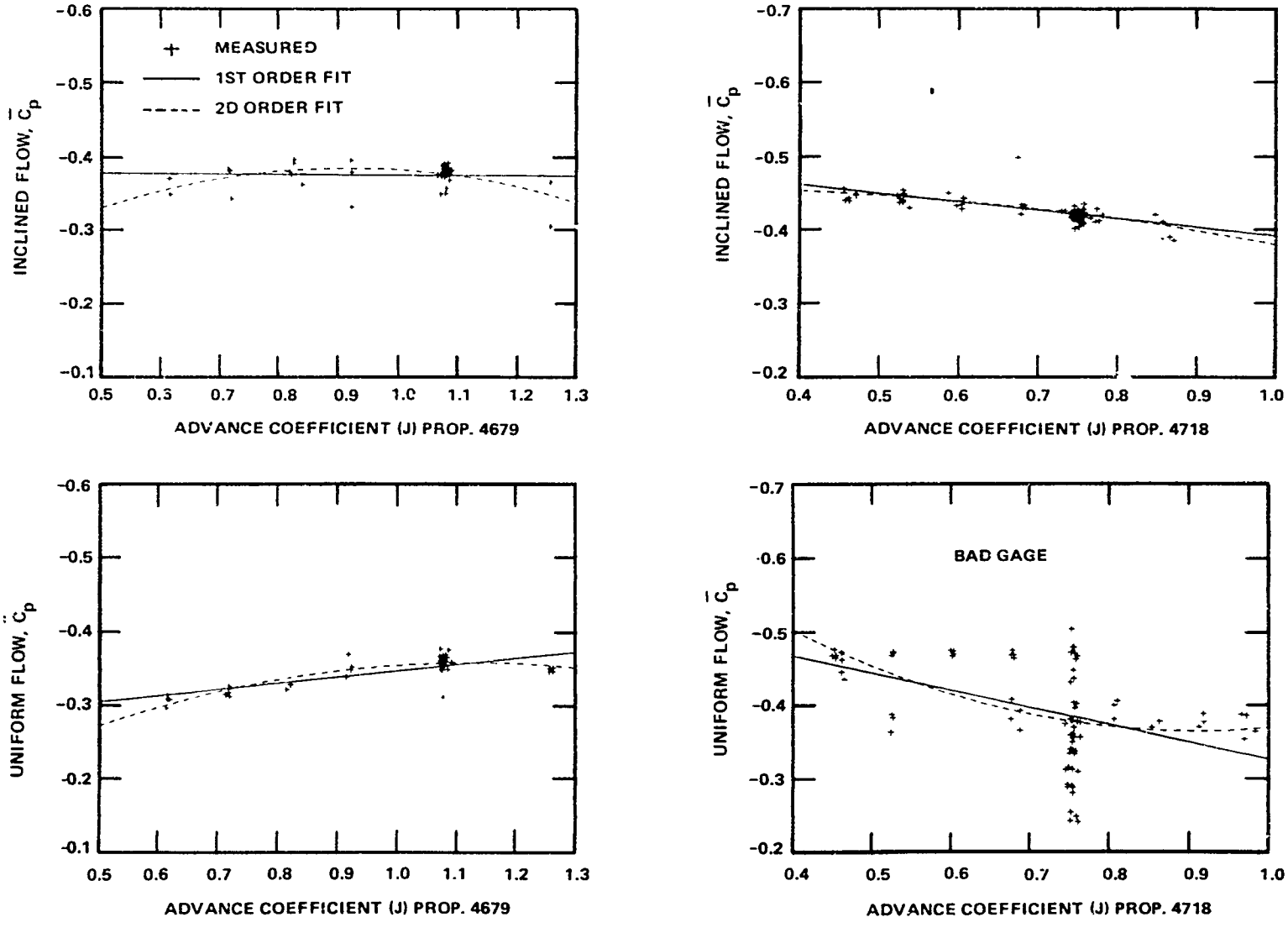

Figure 17z - Gage 26, x/c = 0.7, r/R = 0.5, Suction Side of Blade

Figure 17 (Continued)

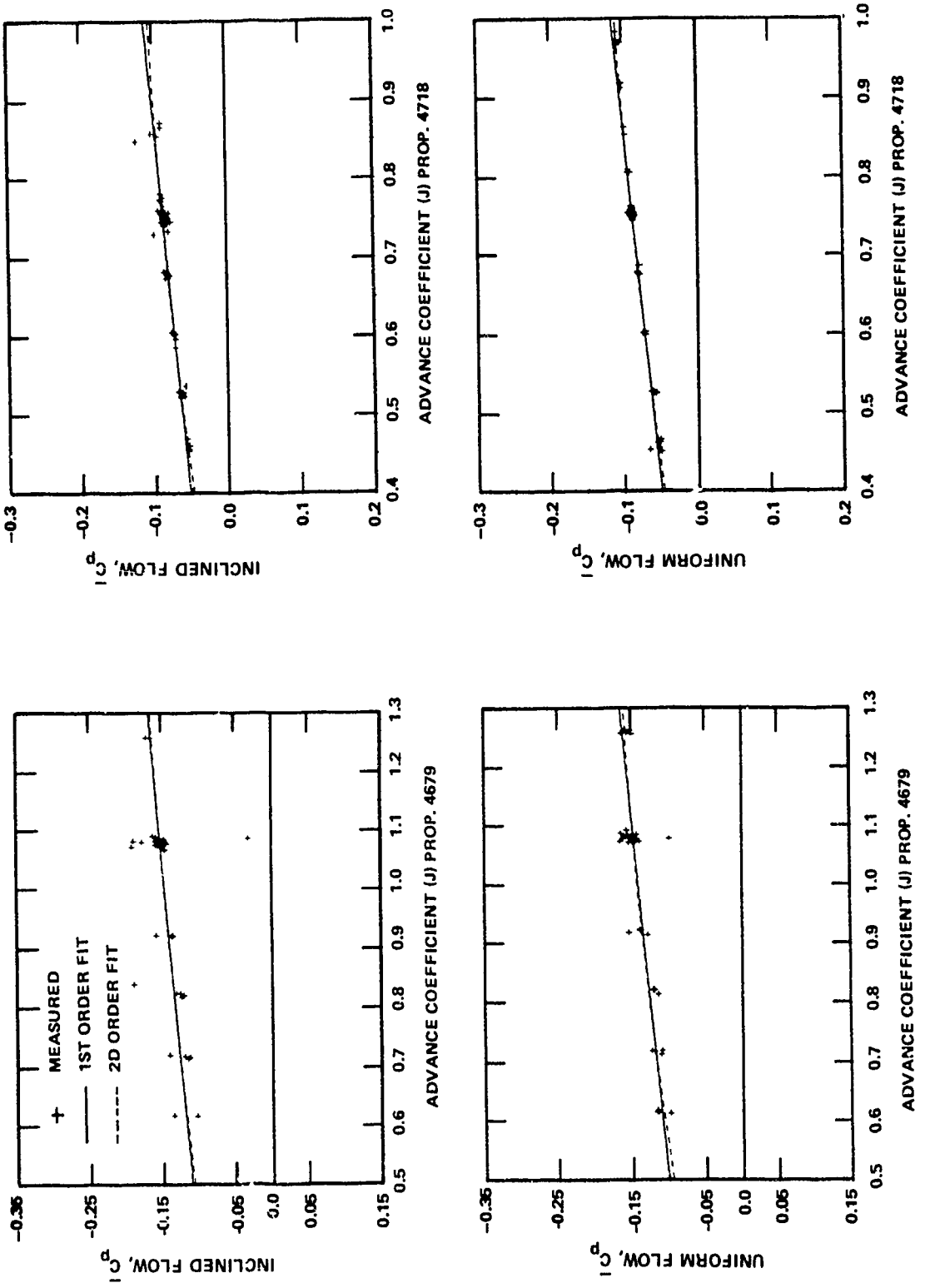

Figure 17aa - Gage 27, x/c = 0.9, r/R = 0.5, Suction Side of Blade

Figure 17 (Continued)

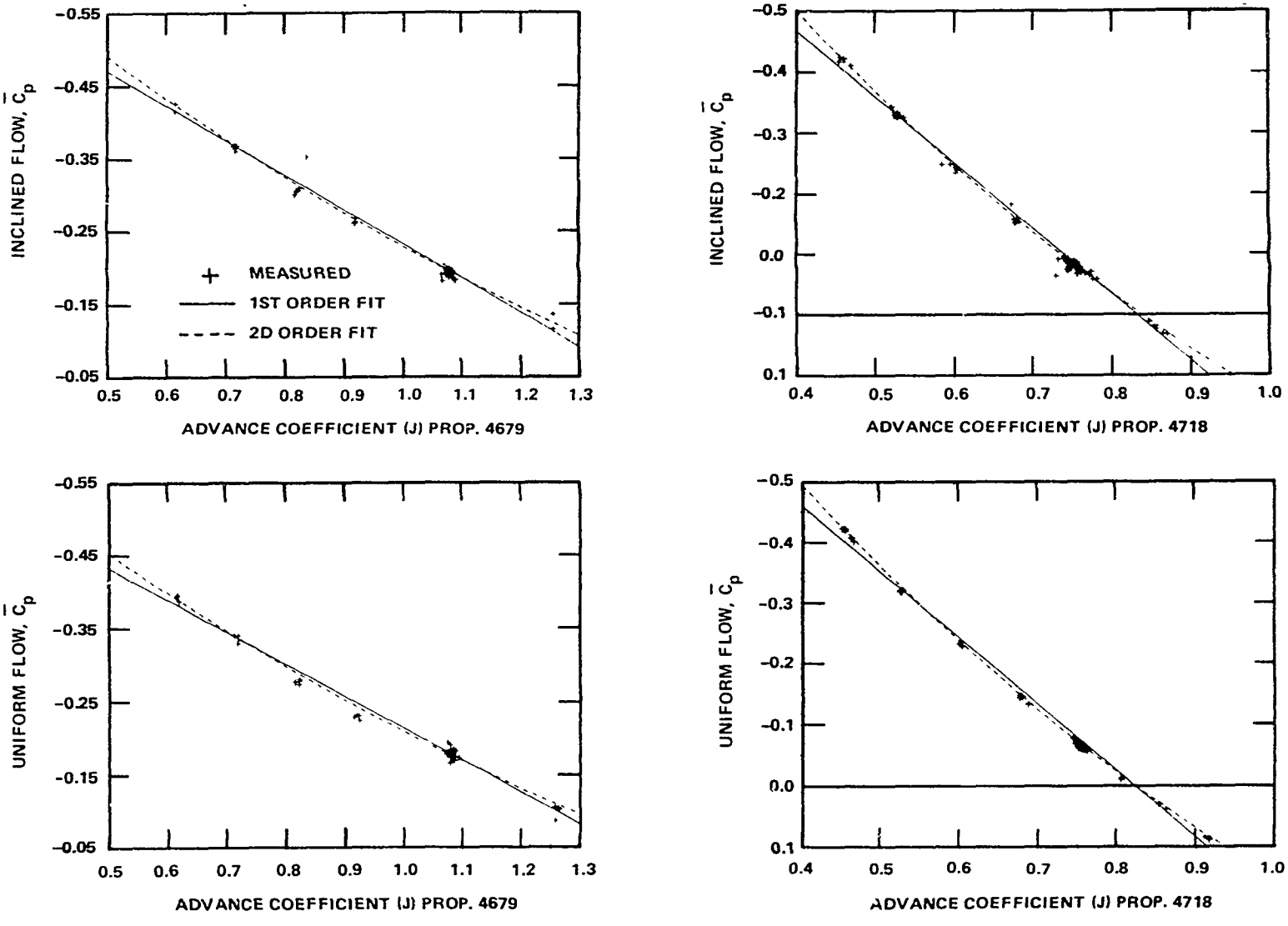

Figure 17bb - Gage 28, x/c = 0.03 for Propeller 4718, x/c = 0.05 for Propeller 4679, r/R = 0.7, Suction Side of Blade

Figure 17 (Continued)

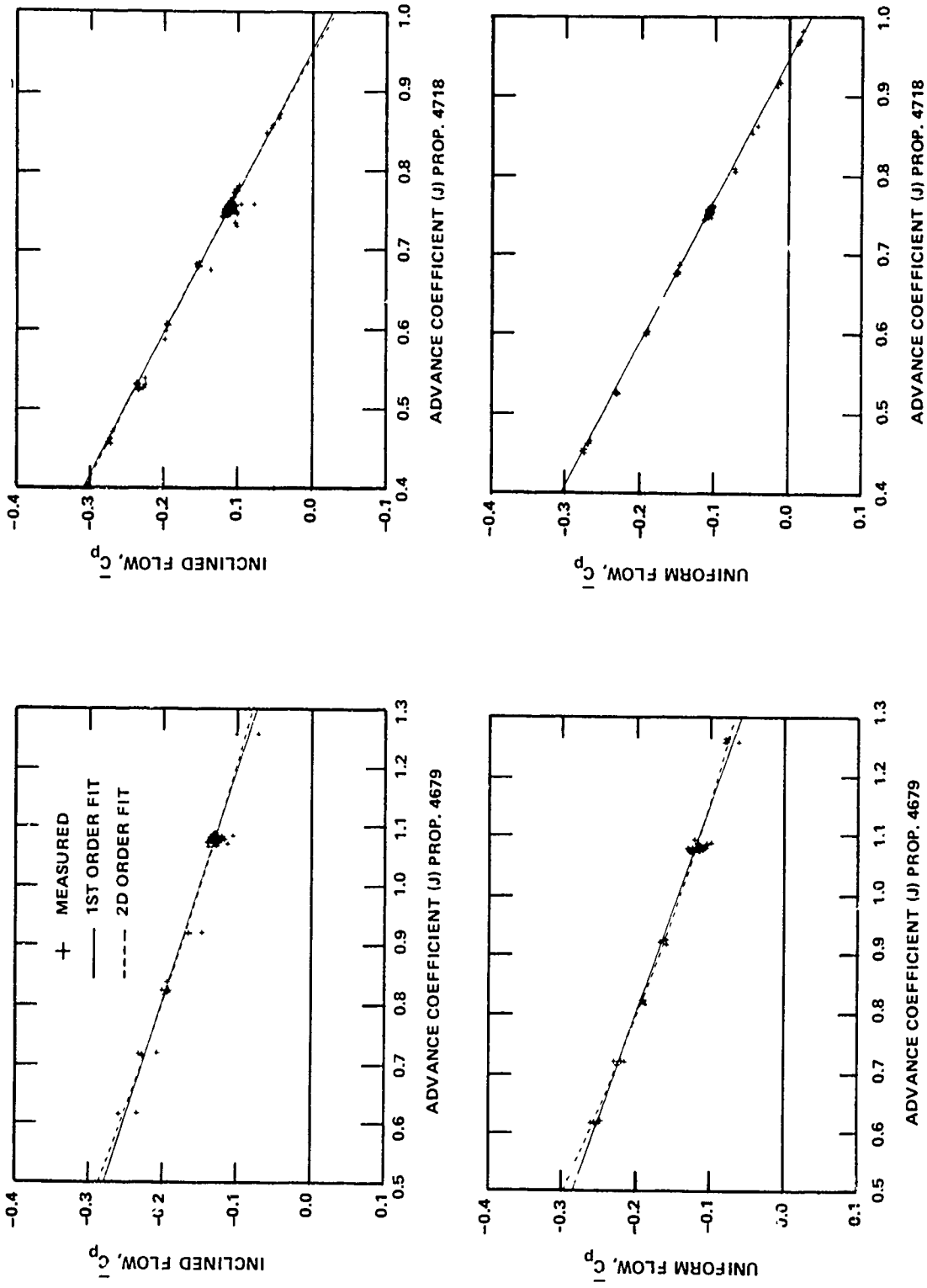

Figure 17cc - Gage 29, x/c = 0.1 for Propeller 4718, x/c = 0.12 for Propeller 4679, r/R = 0.7, Suction Side of Blade

Figure 17 (Continued)

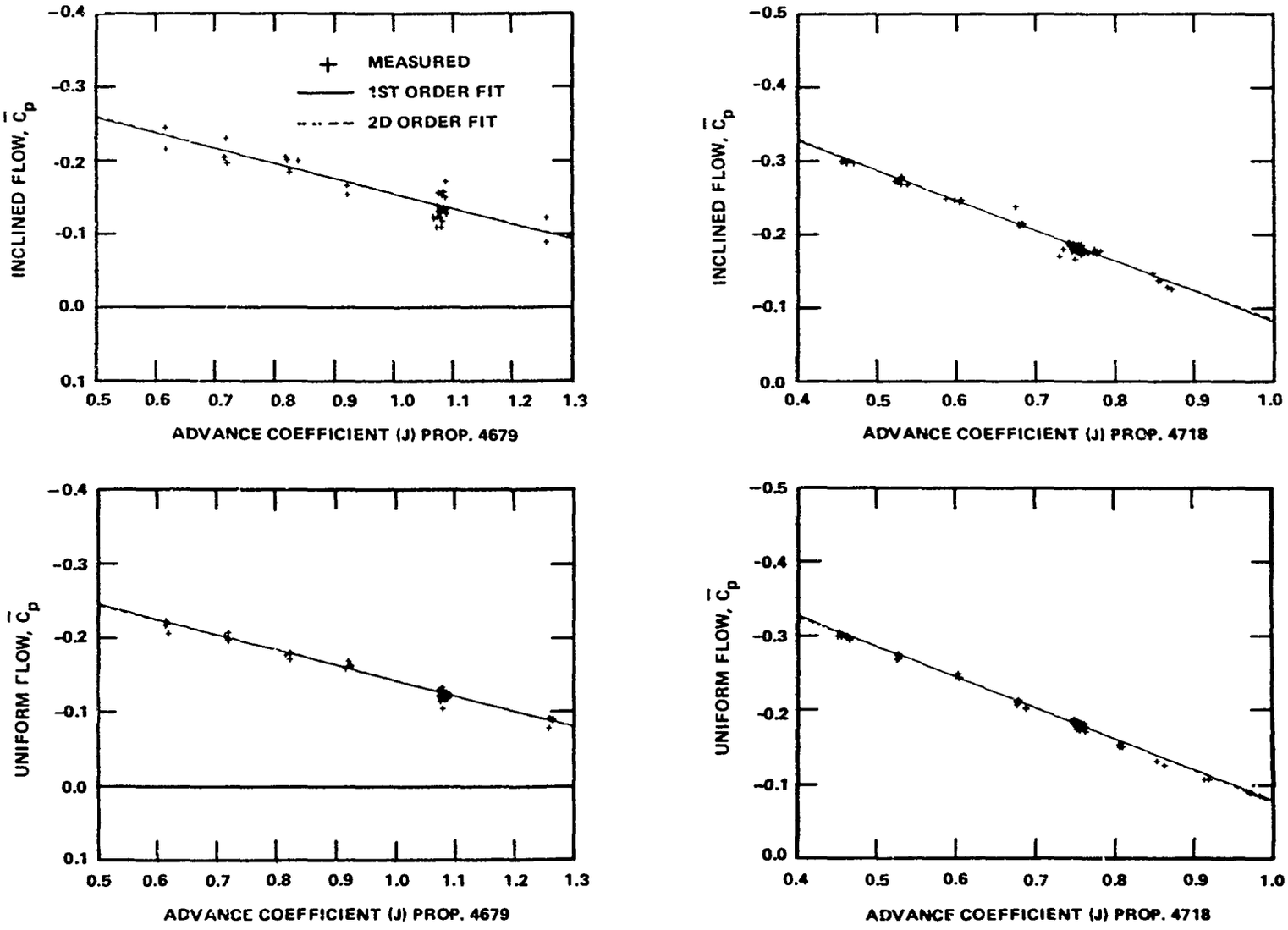

Figure 17dd - Gage 30, x/c = 0.2, r/R = 0.7, Suction Side of Blade

Figure 17 (Continued)

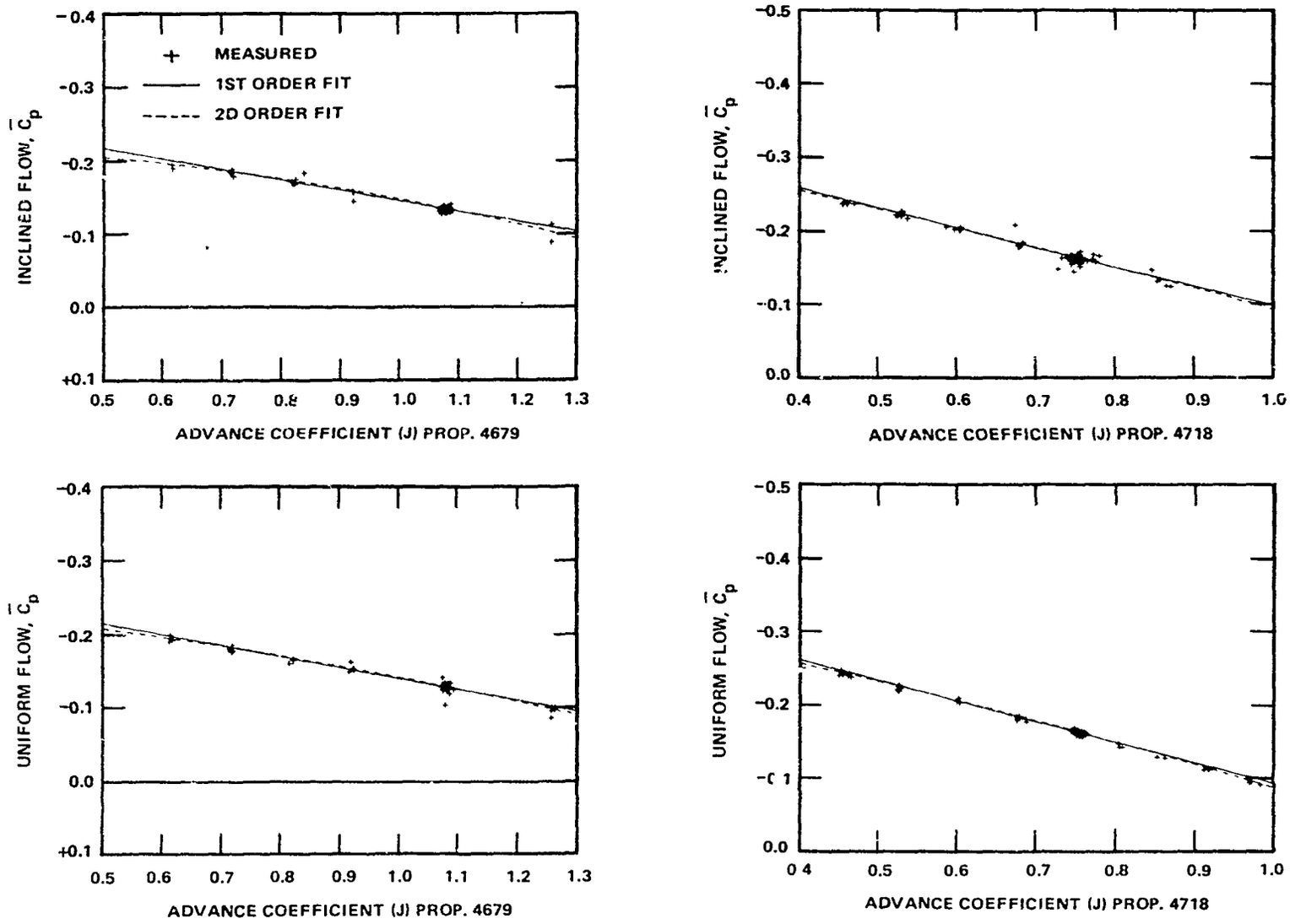

Figure 17ee - Gage 31, x/c = 0.3, r/R = 0.7, Suction Side of Blade

Figure 17 (Continued)

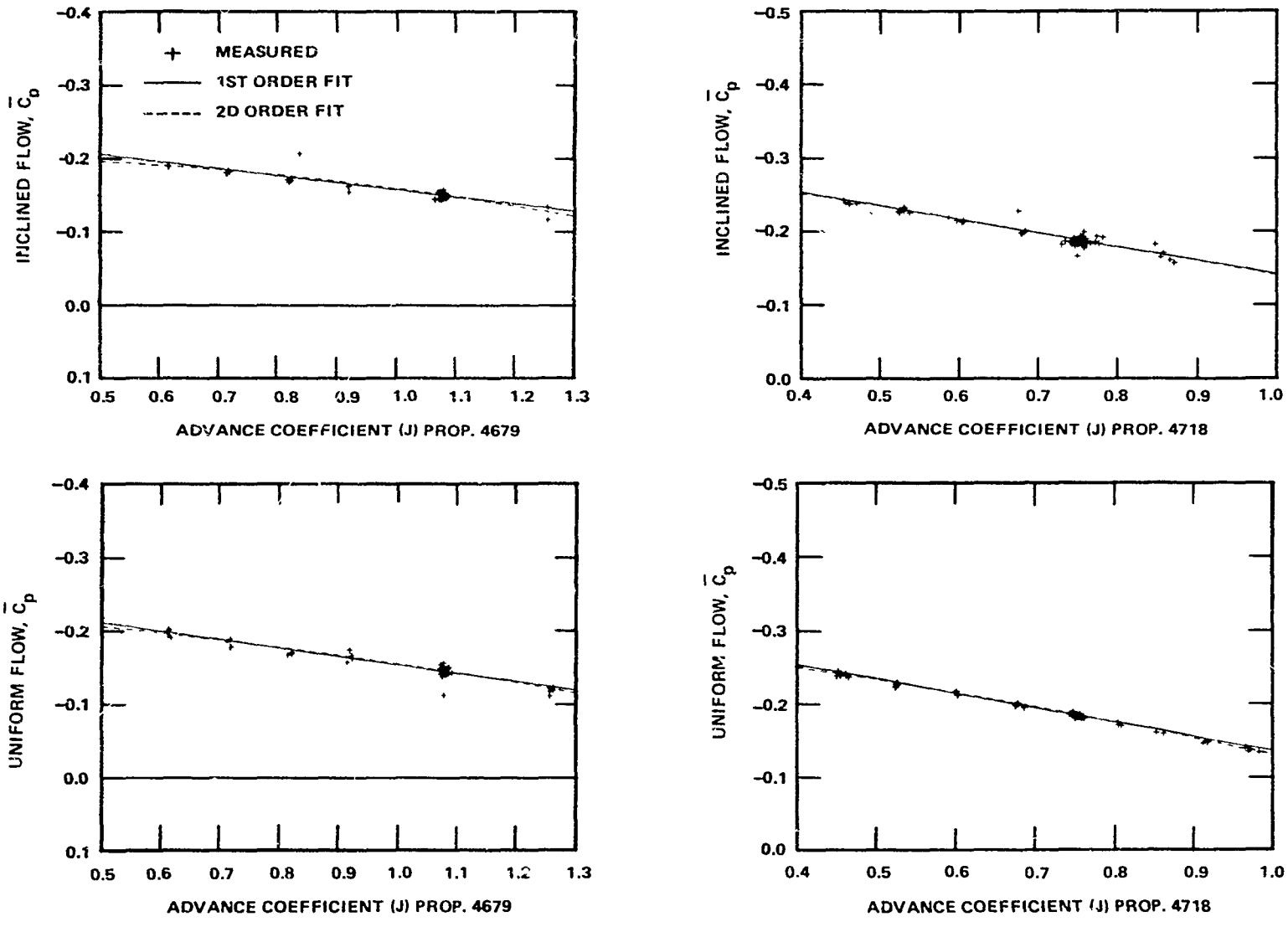

Figure 17ff - Gage 32, x/c = 0.4, r/R = 0.7, Suction Side of Blade

Figure 17 (Continued)

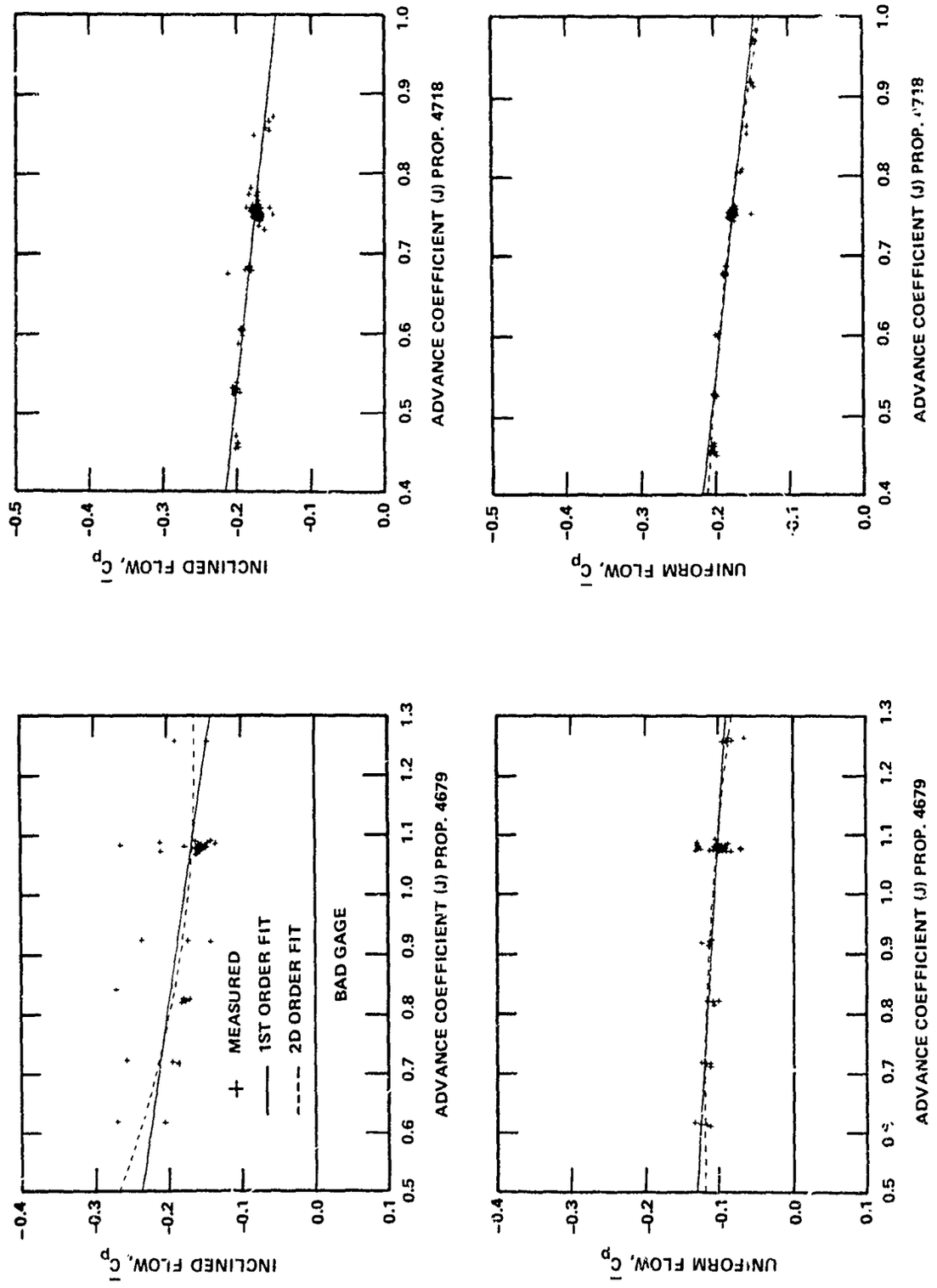

Figure 17gg - Gage 33, x/c = 0.5, r/R = 0.7, Suction Side of Blade

Figure 17 (Continued)

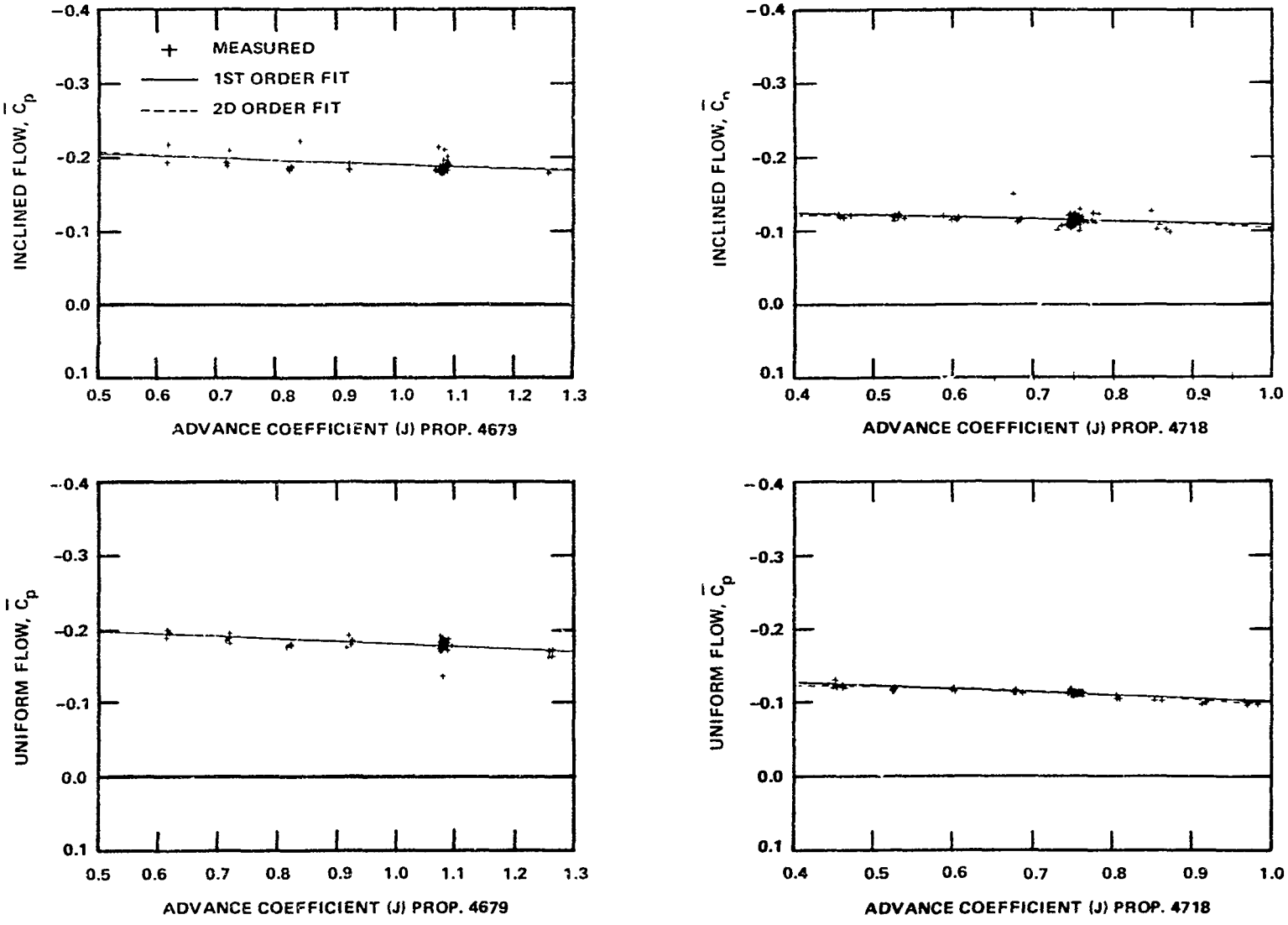

Figure 17hh - Gage 34, x/c = 0.7 for Propeller 4718, x/c = 0.65 for Propeller 4679, r/R = 0.7, Suction Side of Blade

Figure 17 (Continued)

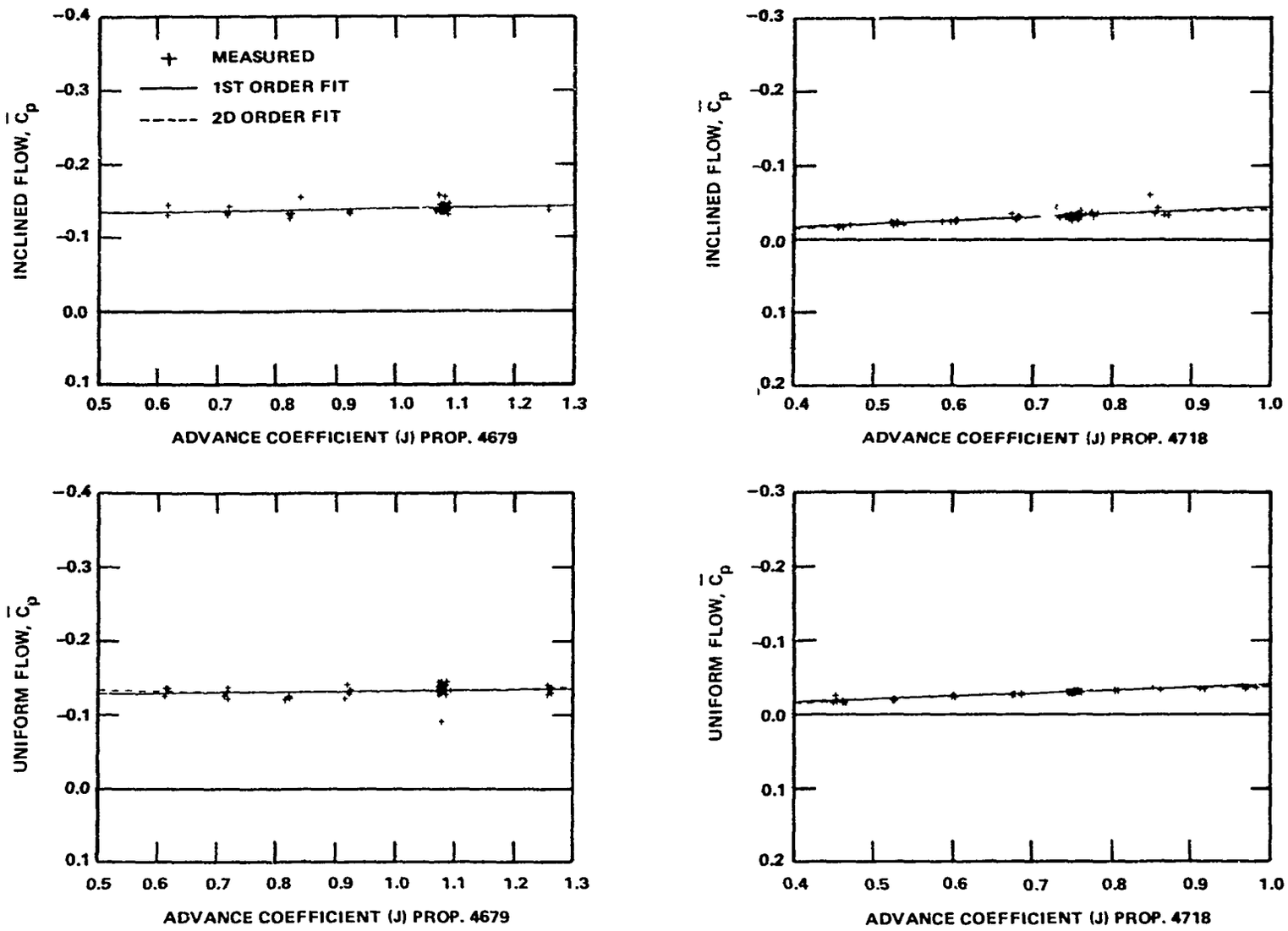

Figure 17ii - Gage 35, x/c = 0.9 for Propeller 4718, x/c = 0.85 for Propeller 4679, r/R = 0.7, Suction Side of Blade

Figure 17 (Continued)

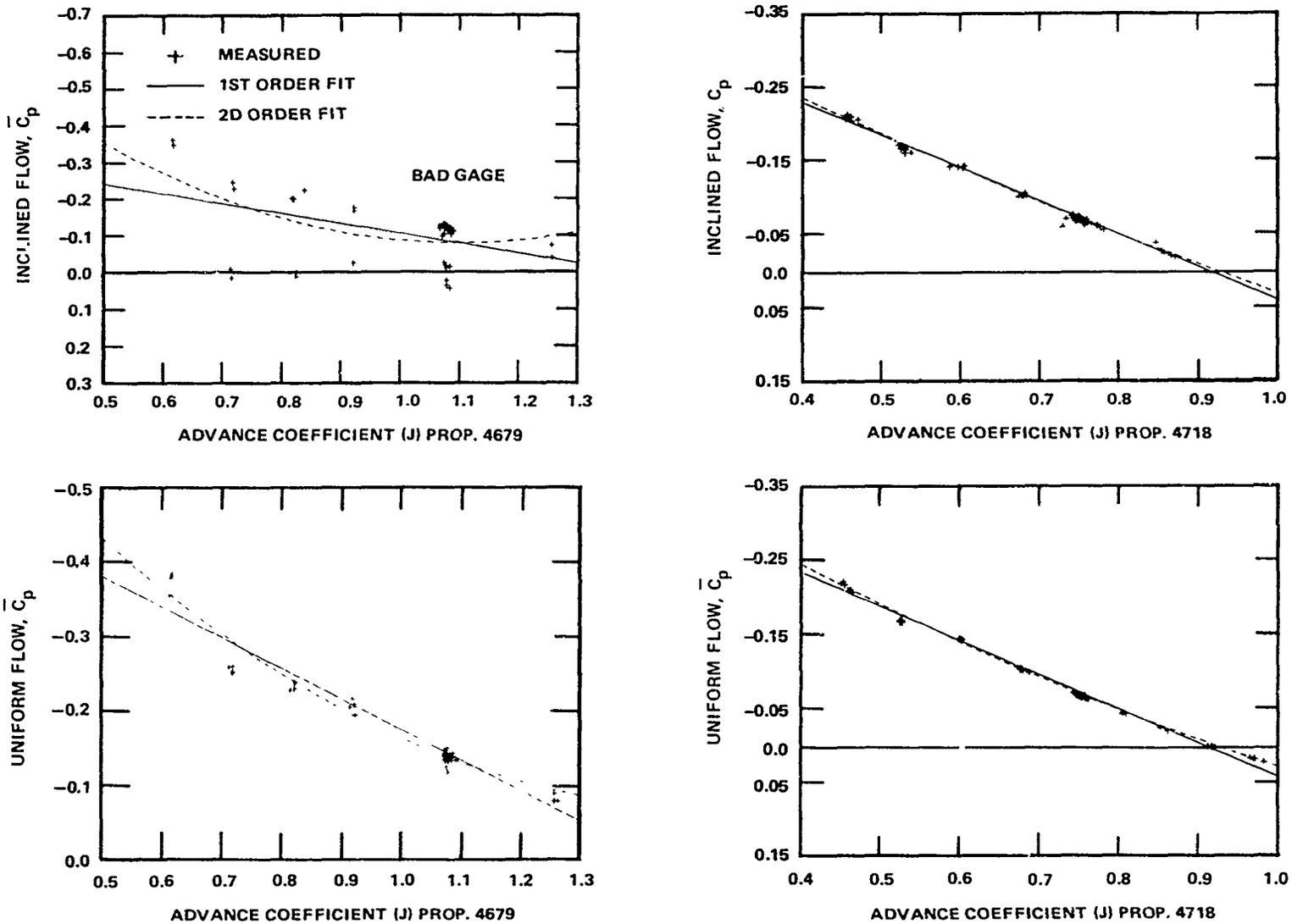

Figure 17jj - Gage 36, x/c = 0.1 for Propeller 4718, x/c = 0.21 for Propeller 4679, r/R = 0.9, Suction Side of Blade

Figure 17 (Continued)

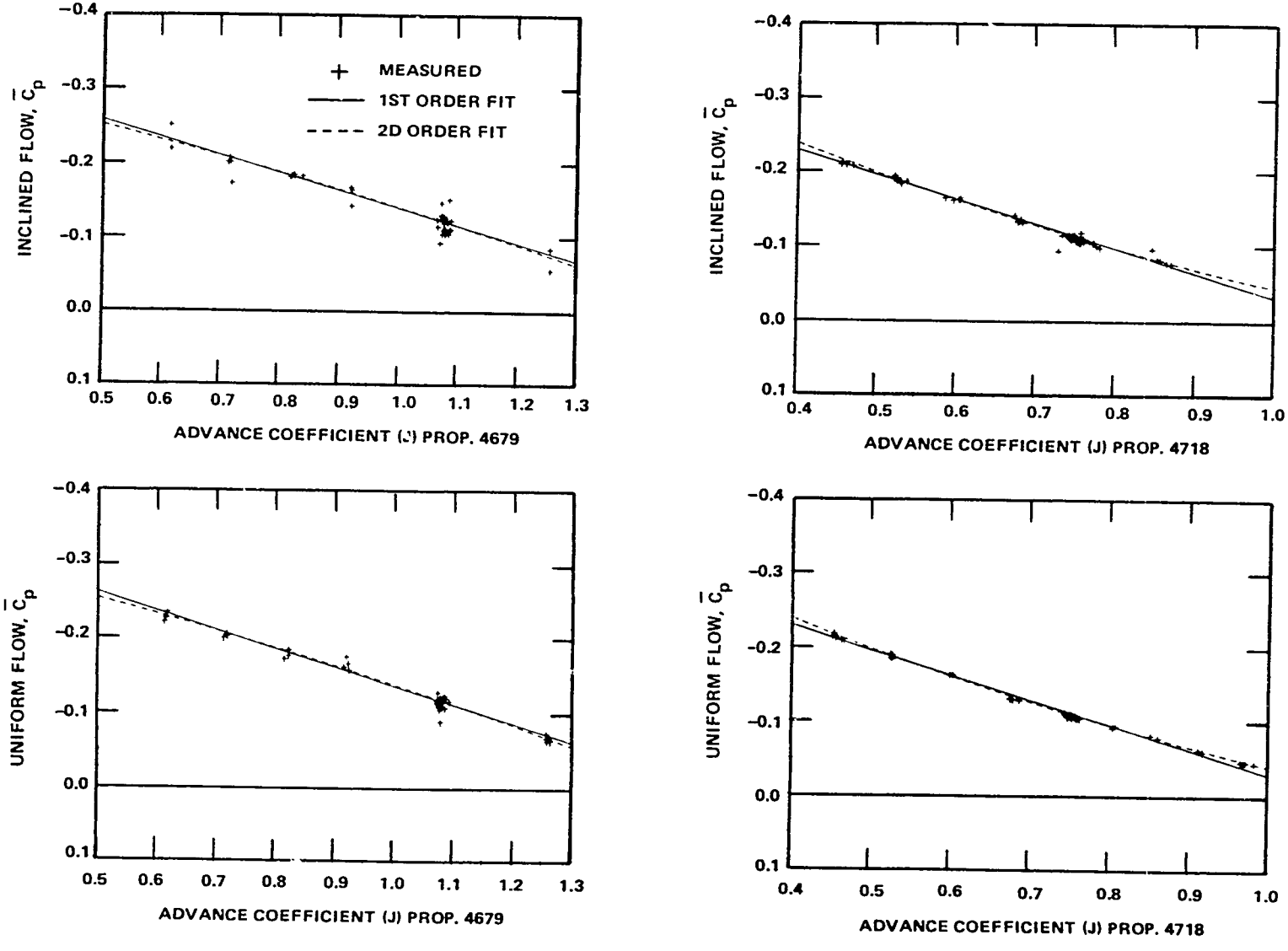

Figure 17kk - Gage 37, x/c = 0.2 for Propeller 4718, x/c = 0.36 for Propeller 4679, r/R = 0.9, Suction Side of Blade

Figure 17 (Continued)

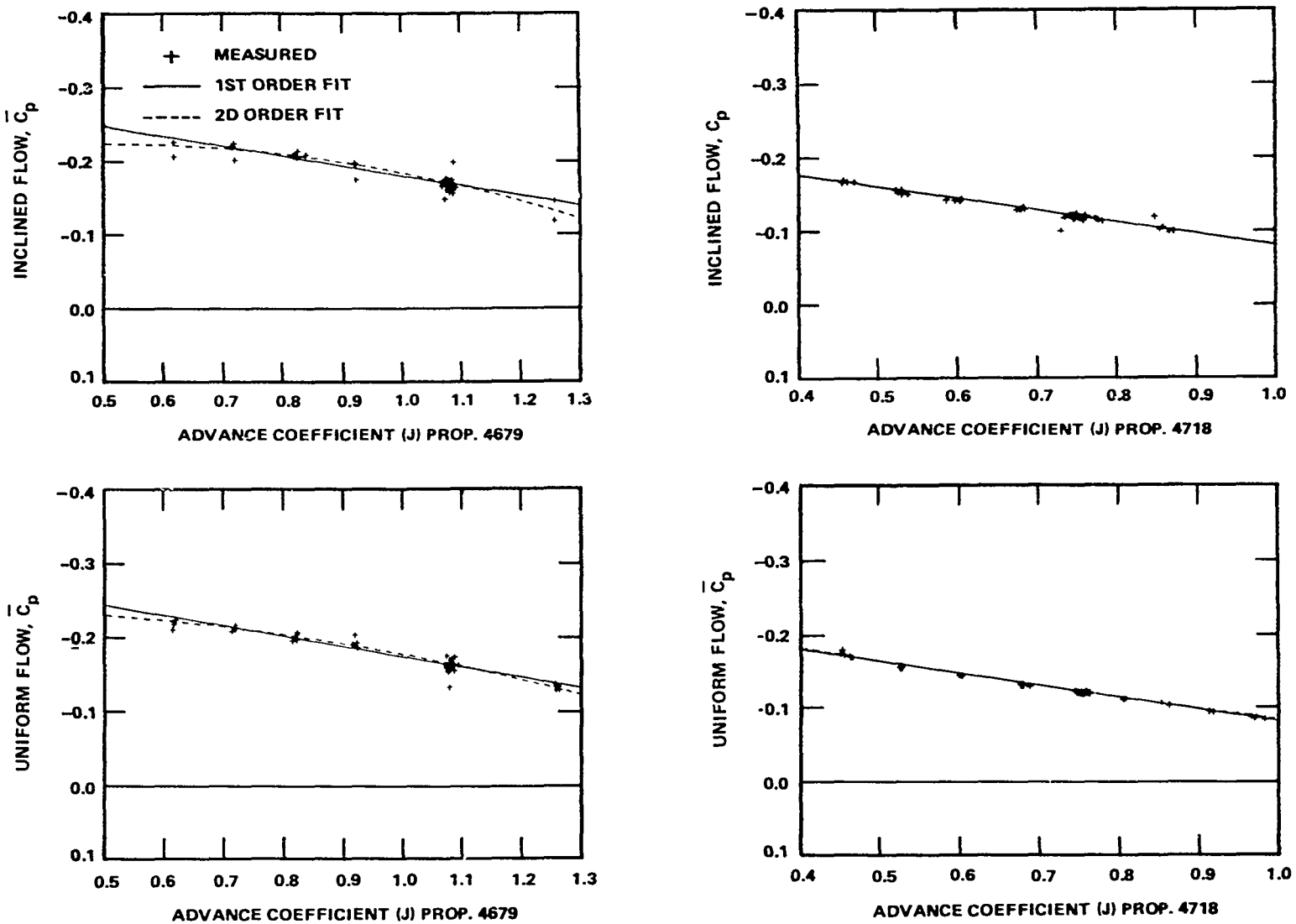

Figure 1711 - Gage 38, x/c = 0.4 for Propeller 4718, x/c = 0.51 for Propeller 4679, r/R = 0.9, Suction Side of Blade

Figure 17 (Continued)

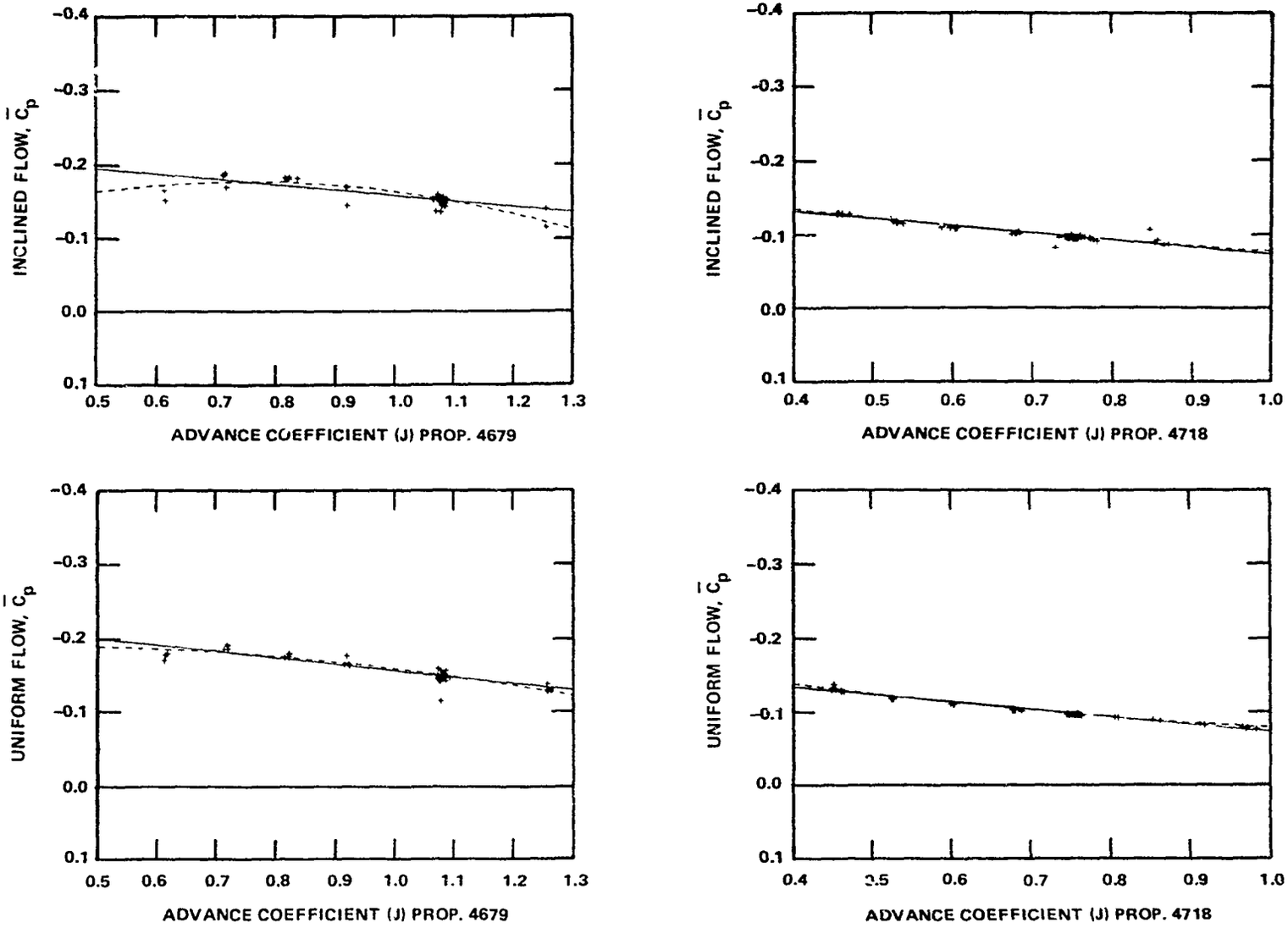

Figure 17mm - Gage 39, x/c = 0.6 for Propeller 4718, x/c = 0.63 for Propeller 4679, r/R = 0.9, Suction Side of Blade

Figure 17 (Continued)

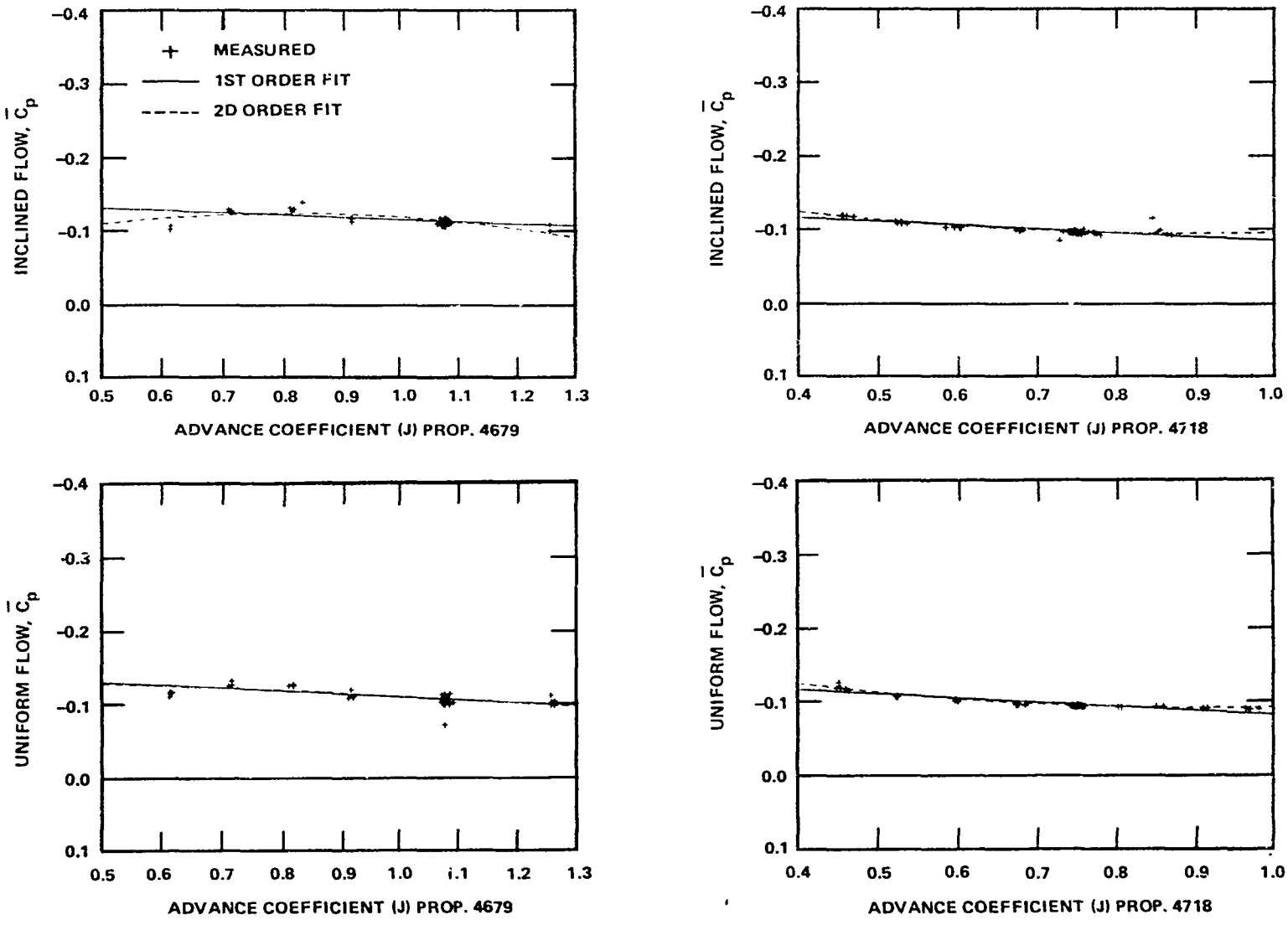

Figure 17nn - Gage 40, x/c = 0.8 for Propeller 4718, x/c = 0.76 for Propeller 4679, r/R = 0.9, Suction Side of Blade

Figure 18 - Variation of $\overline{C}_p$ Distribution with J, with Speed Correction, for Propeller 4679

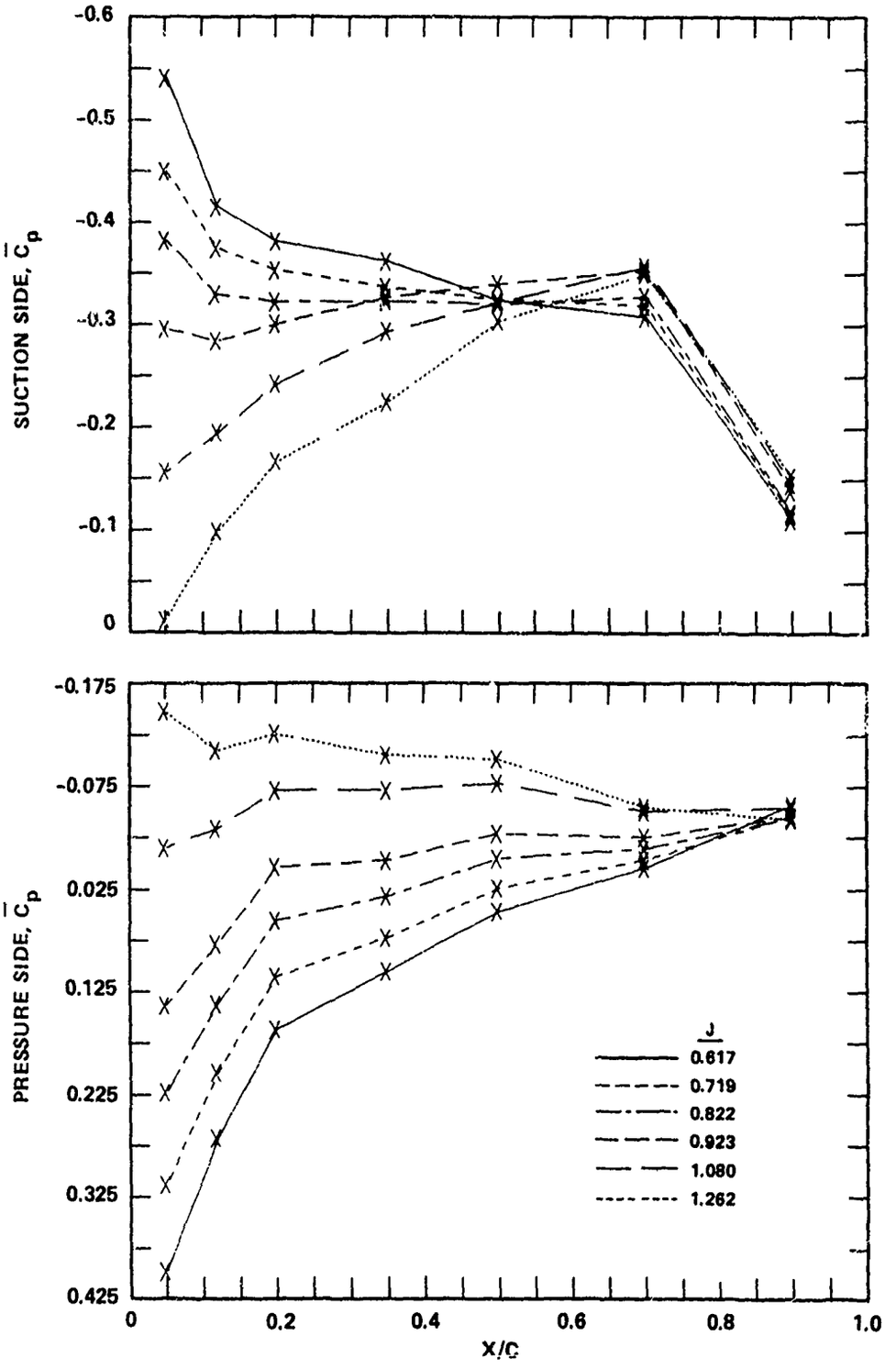

Figure 18a - r/R = 0.5

Figure 18 (Continued)

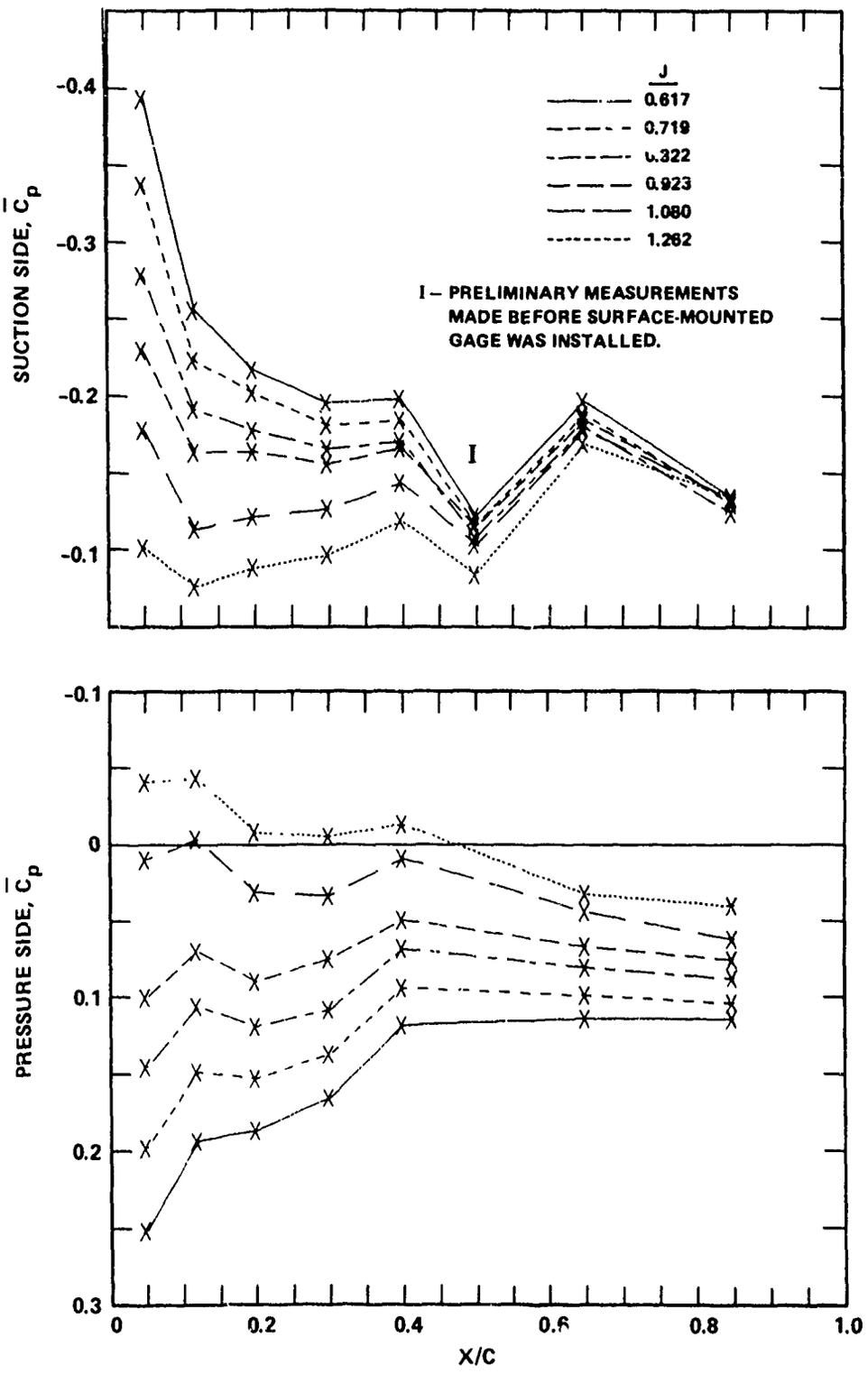

Figure 18b - r/R = 0.7

Figure 18 (Continued)

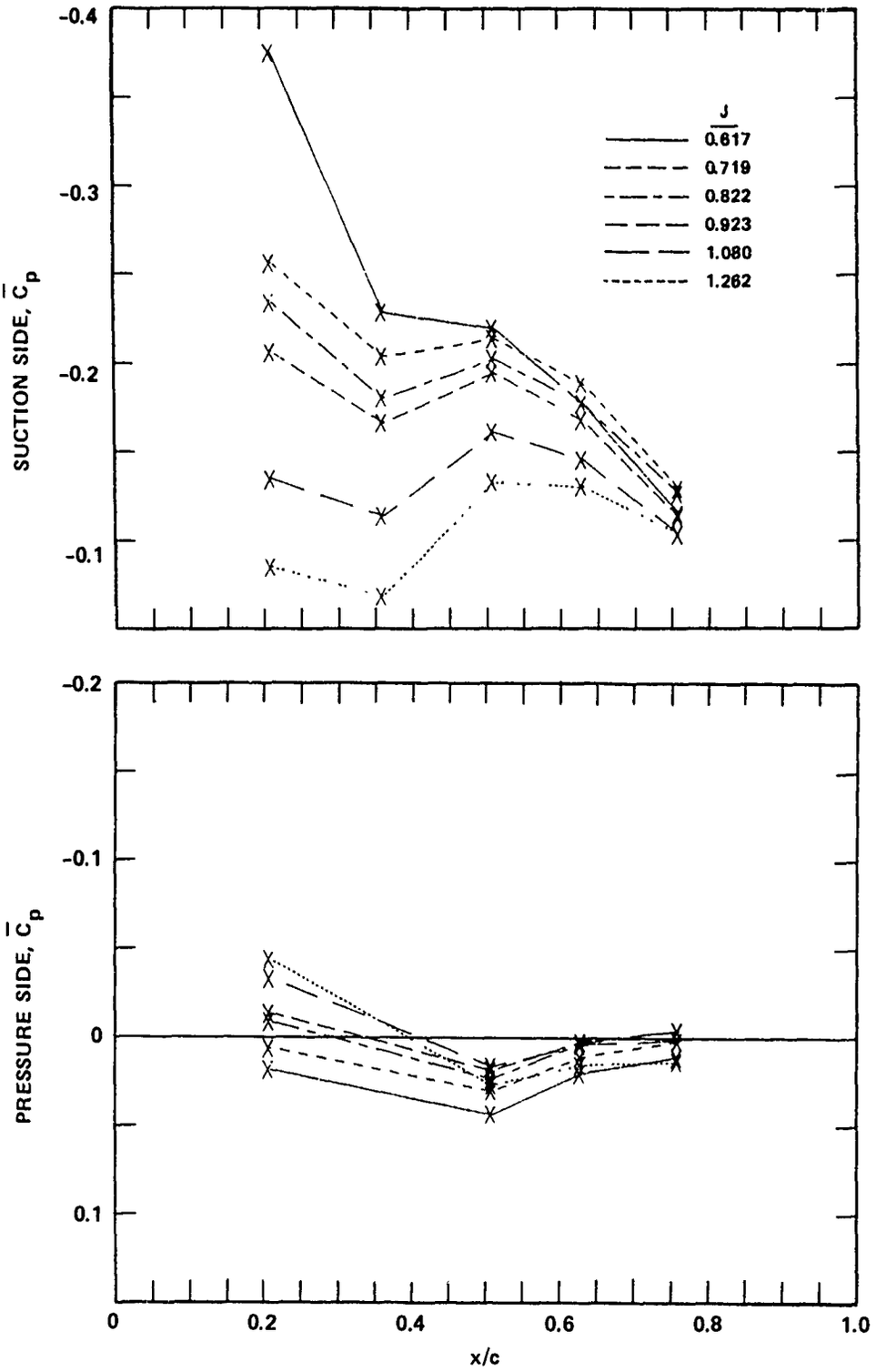

Figure 18c - r/R = 0.9

Figure 19 - Variation of $\overline{C}_p$ Distribution with J, with Speed Correction, for Propeller 4718

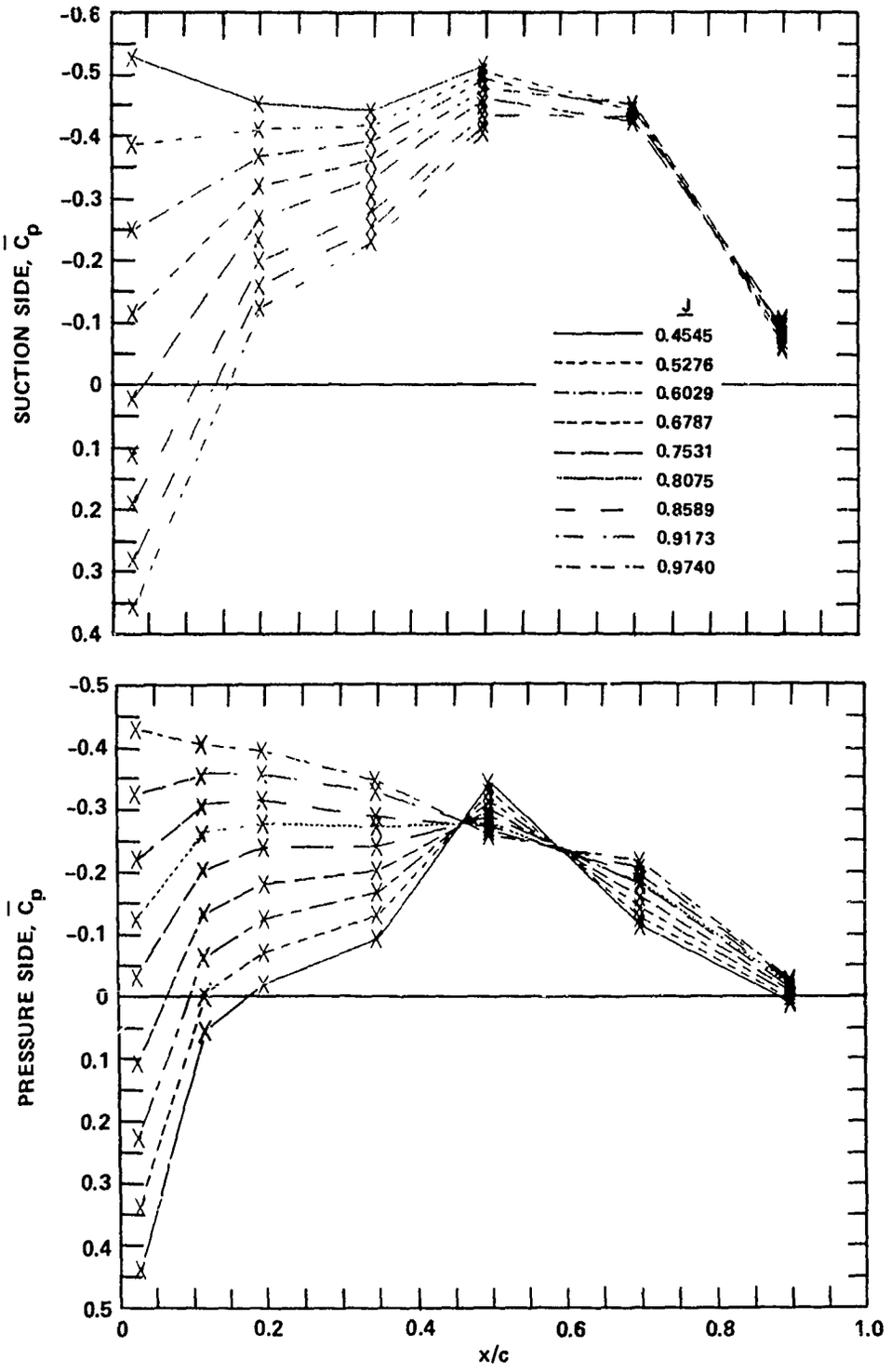

Figure 19a - r/R = 0.5

Figure 19 (Continued)

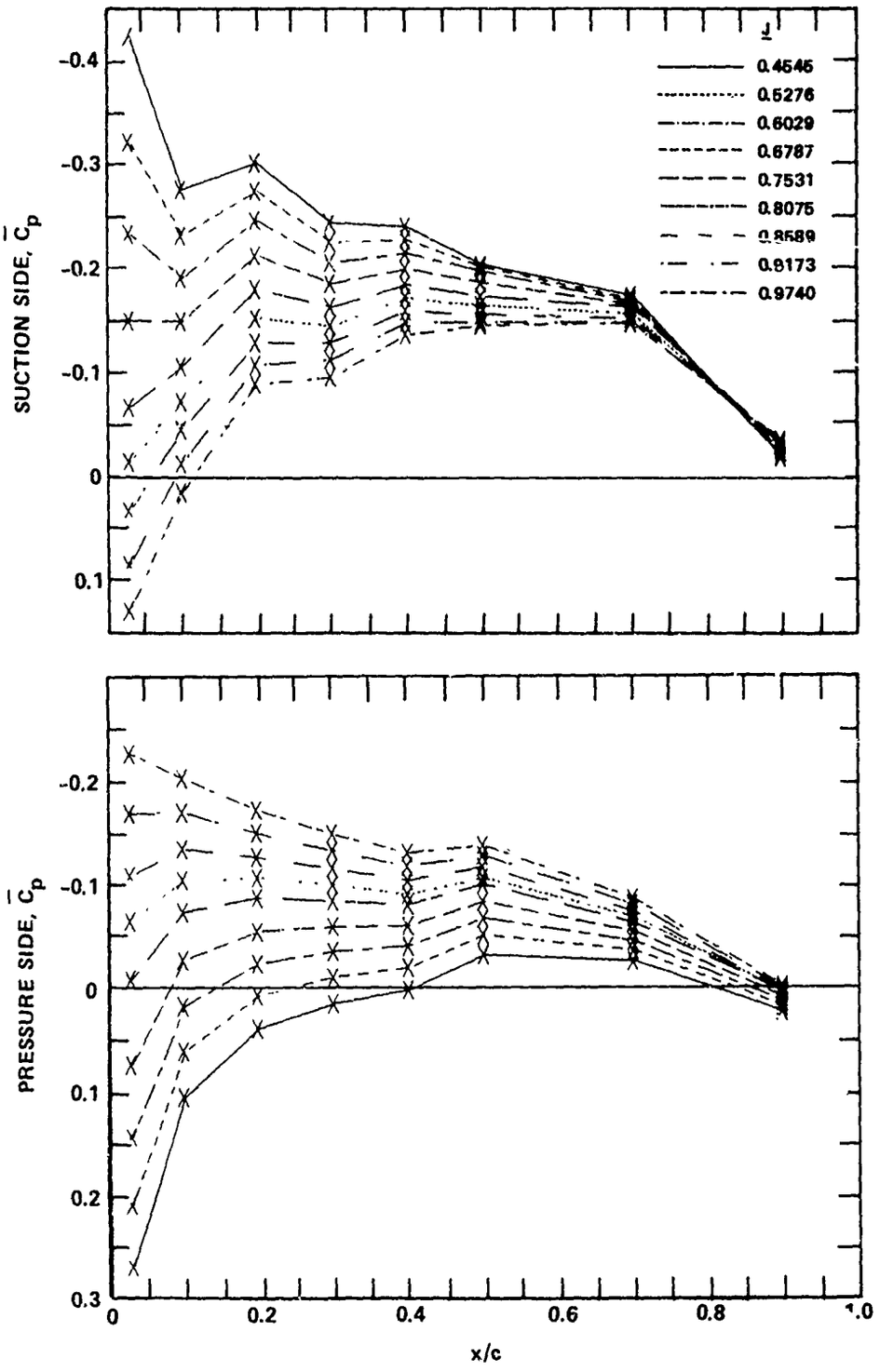

Figure 19b - r/R = 0.7

Figure 19 (Continued)

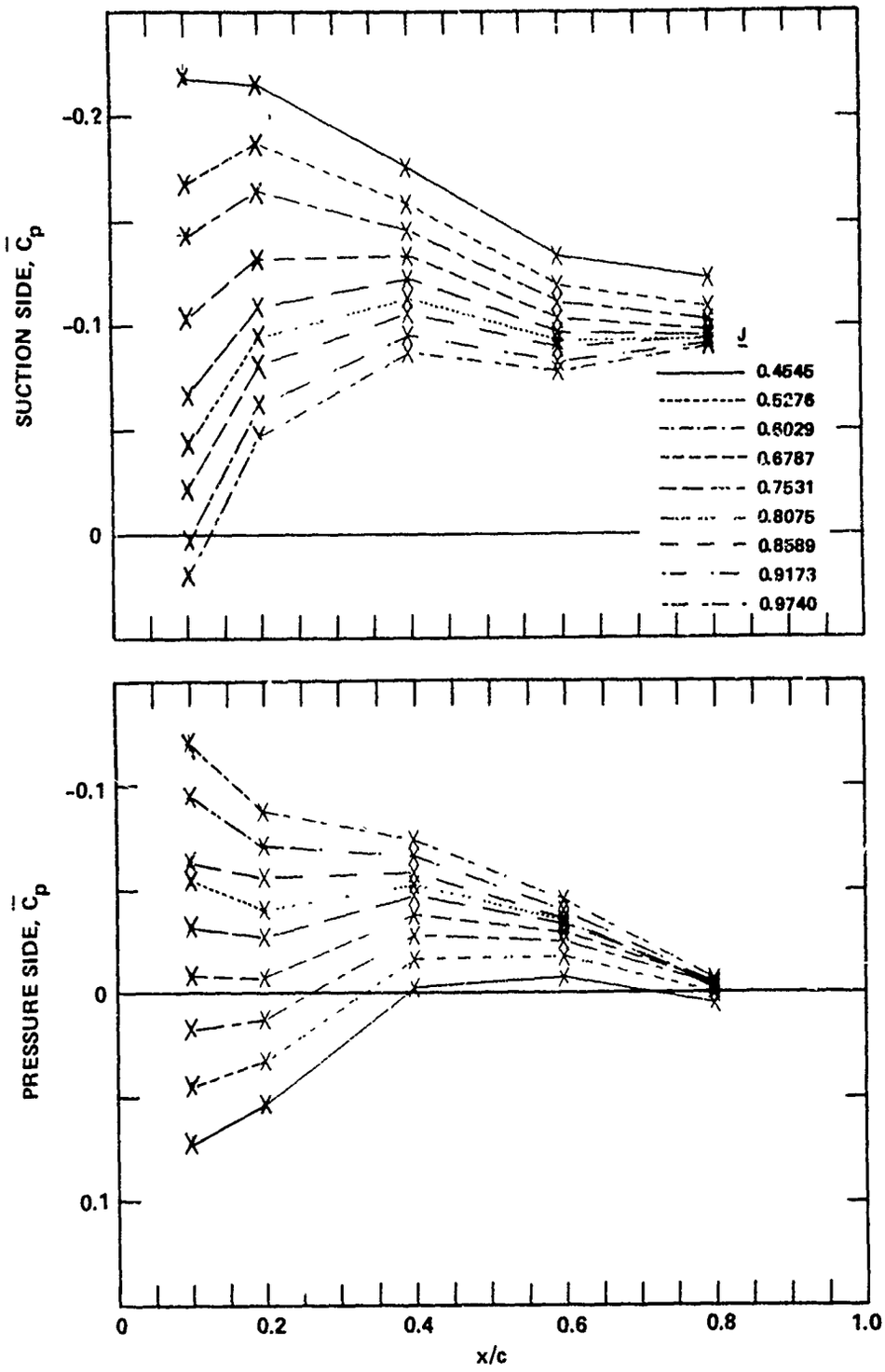

Figure 19c - r/R = 0.9

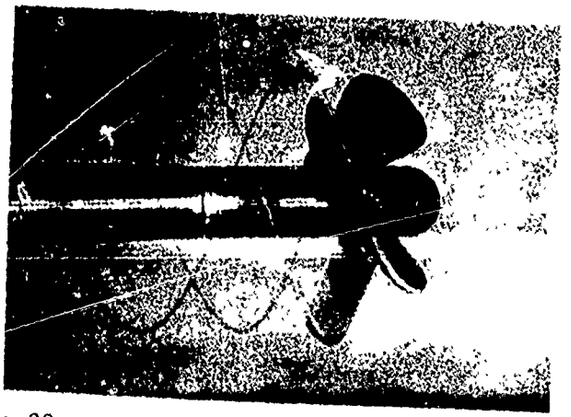

Figure 20a - J = 0.6, $V_{R_{0.7}}$ = 51.4 Feet per Second

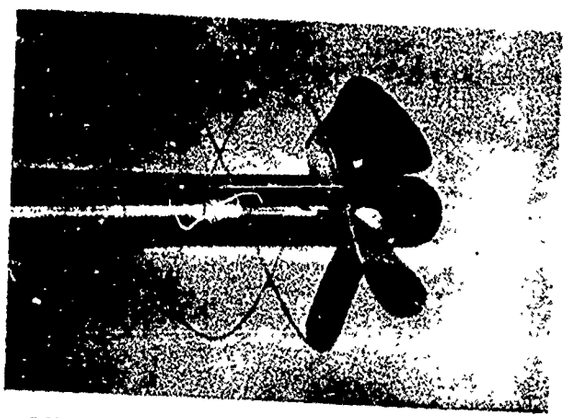

Figure 20b - J = 0.8, $V_{R_{0.7}}$ = 51.8 Feet per Second

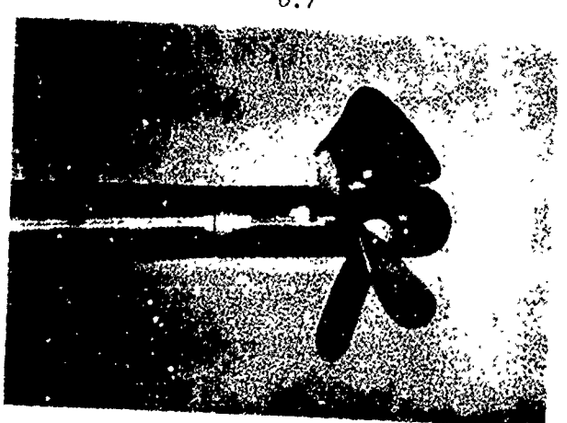

Figure 20c - J = 1.077, $V_{R_{0.7}}$ = 49.82 Feet per Second

Figure 20 - Tip Vortex Formation on Propeller 4679 at Varying Advance Coefficients

Figure 21 - Slope of $\overline{C}_p$ versus J Curve for Propeller 4718

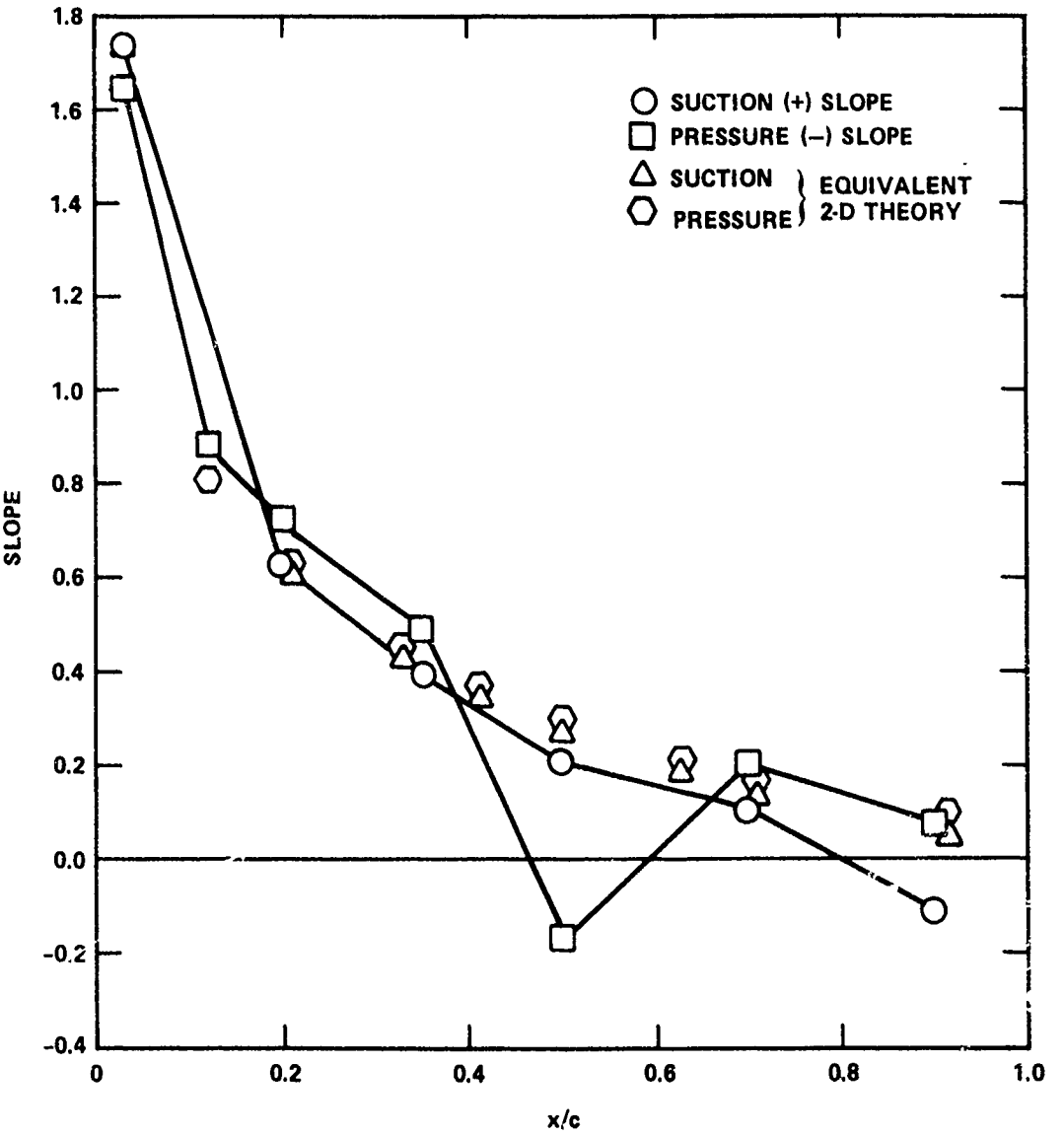

Figure 21a - r/R = 0.5

Figure 21 (Continued)

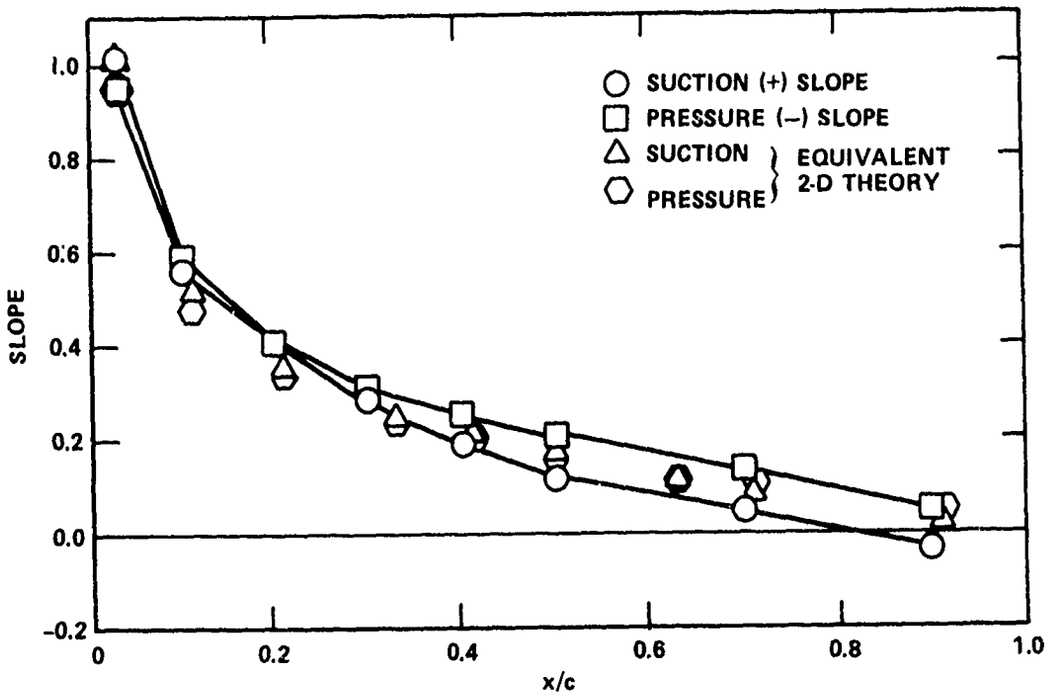

Figure 21b - r/R = 0.7

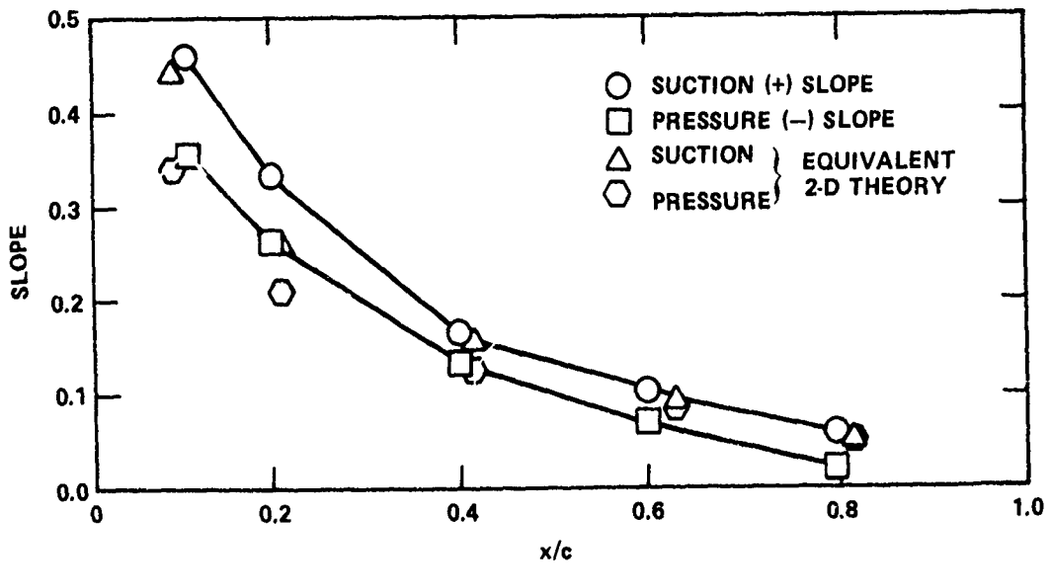

Figure 21c - r/R = 0.9

Figure 22 - Slope of $\overline{C}_p$ versus J Curve for Propeller 4679

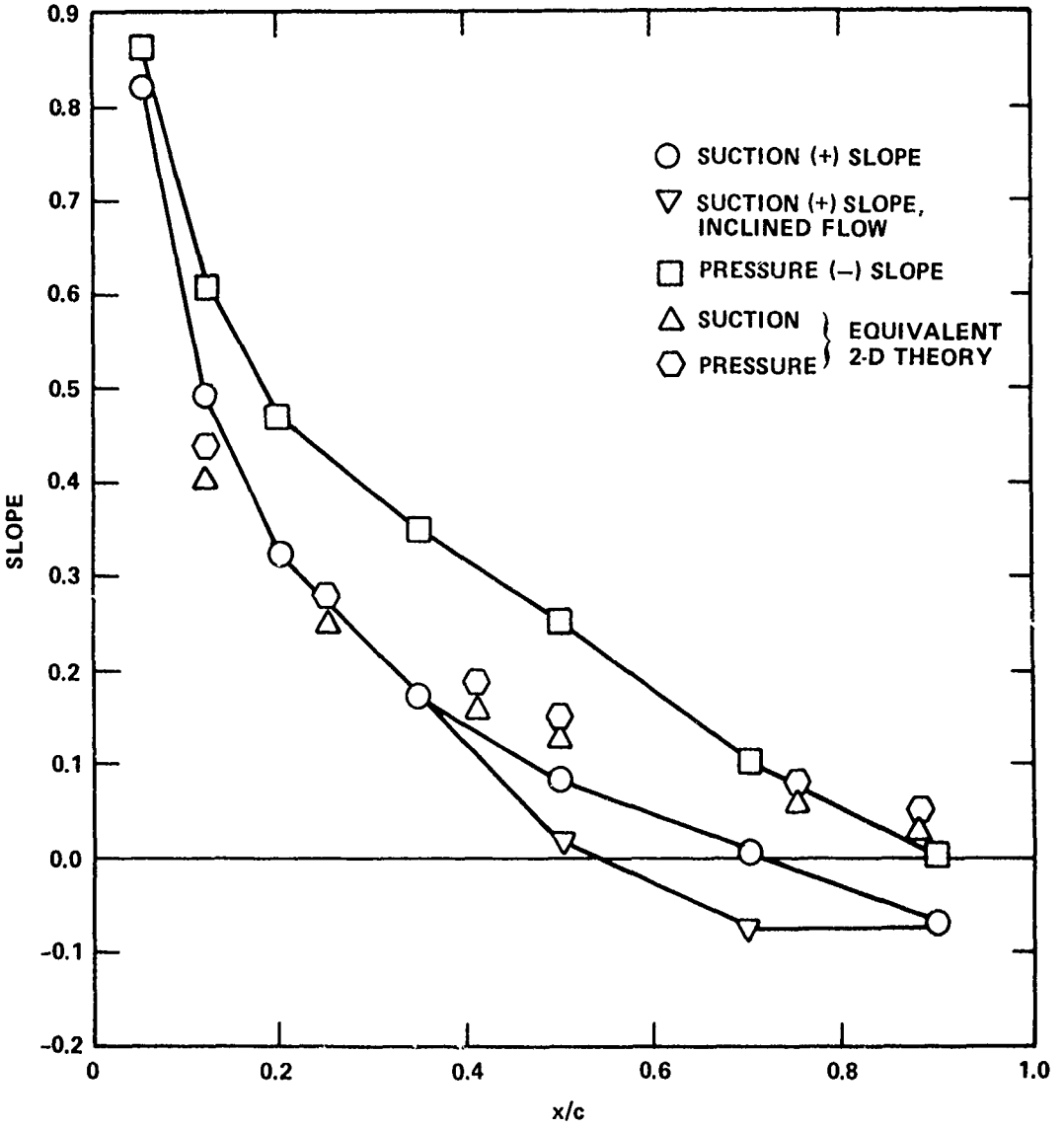

Figure 22a - r/R = 0.5 (Inclined flow result shown when differing from uniform flow result)

Figure 22 (Continued)

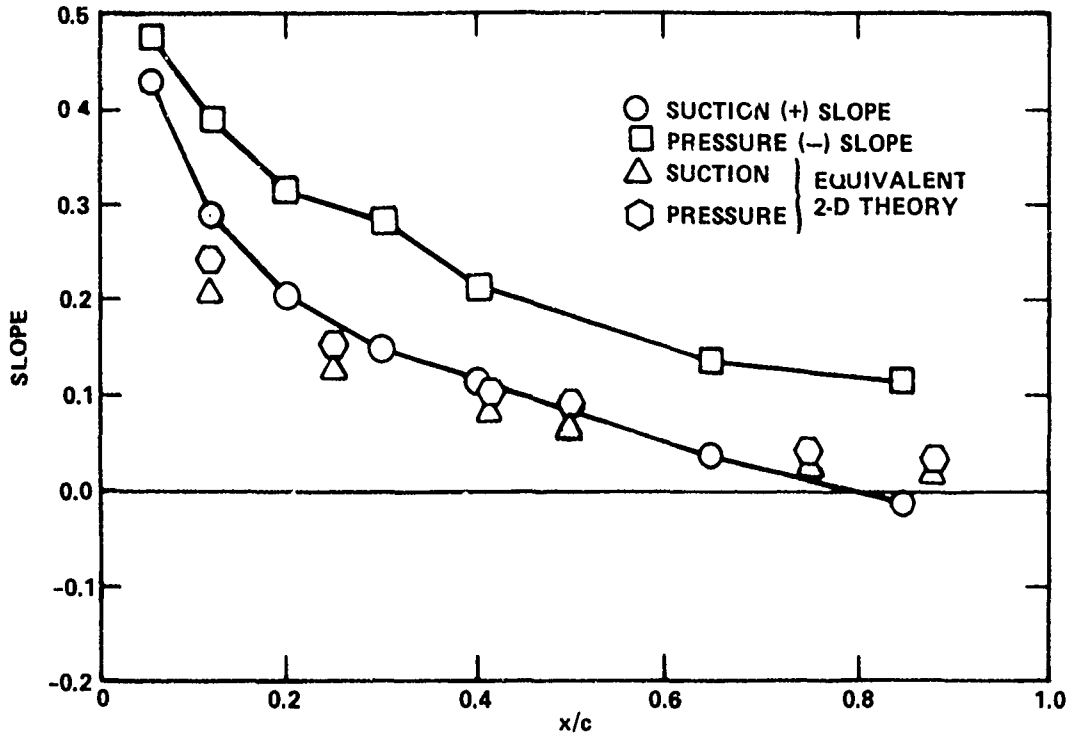

Figure 22b - r/R = 0.7

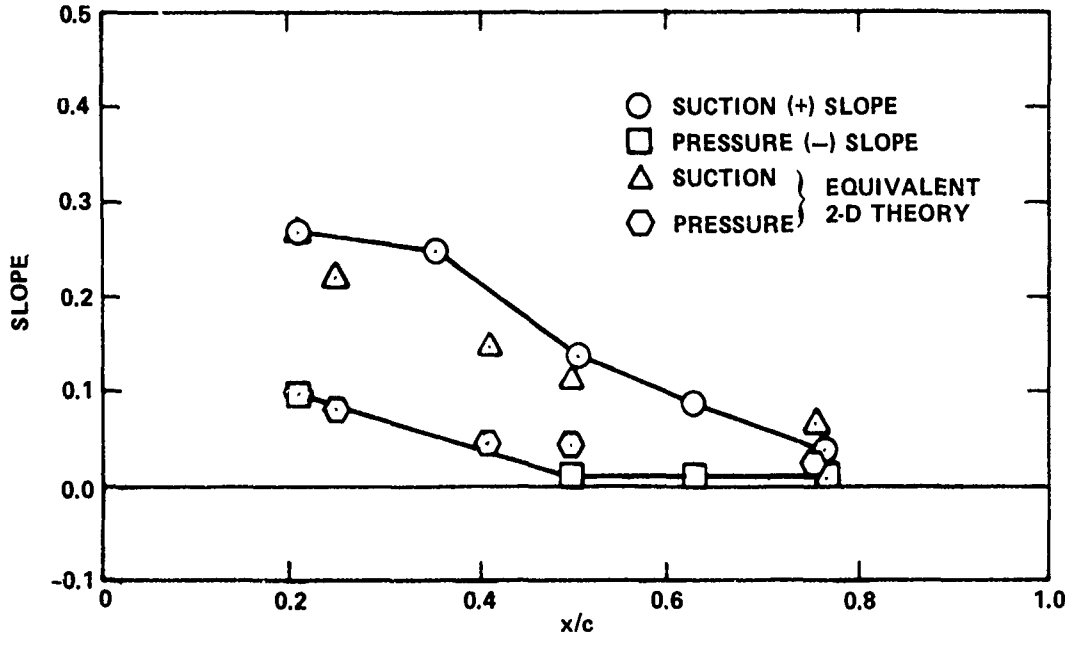

Figure 22c - r/R = 0.9

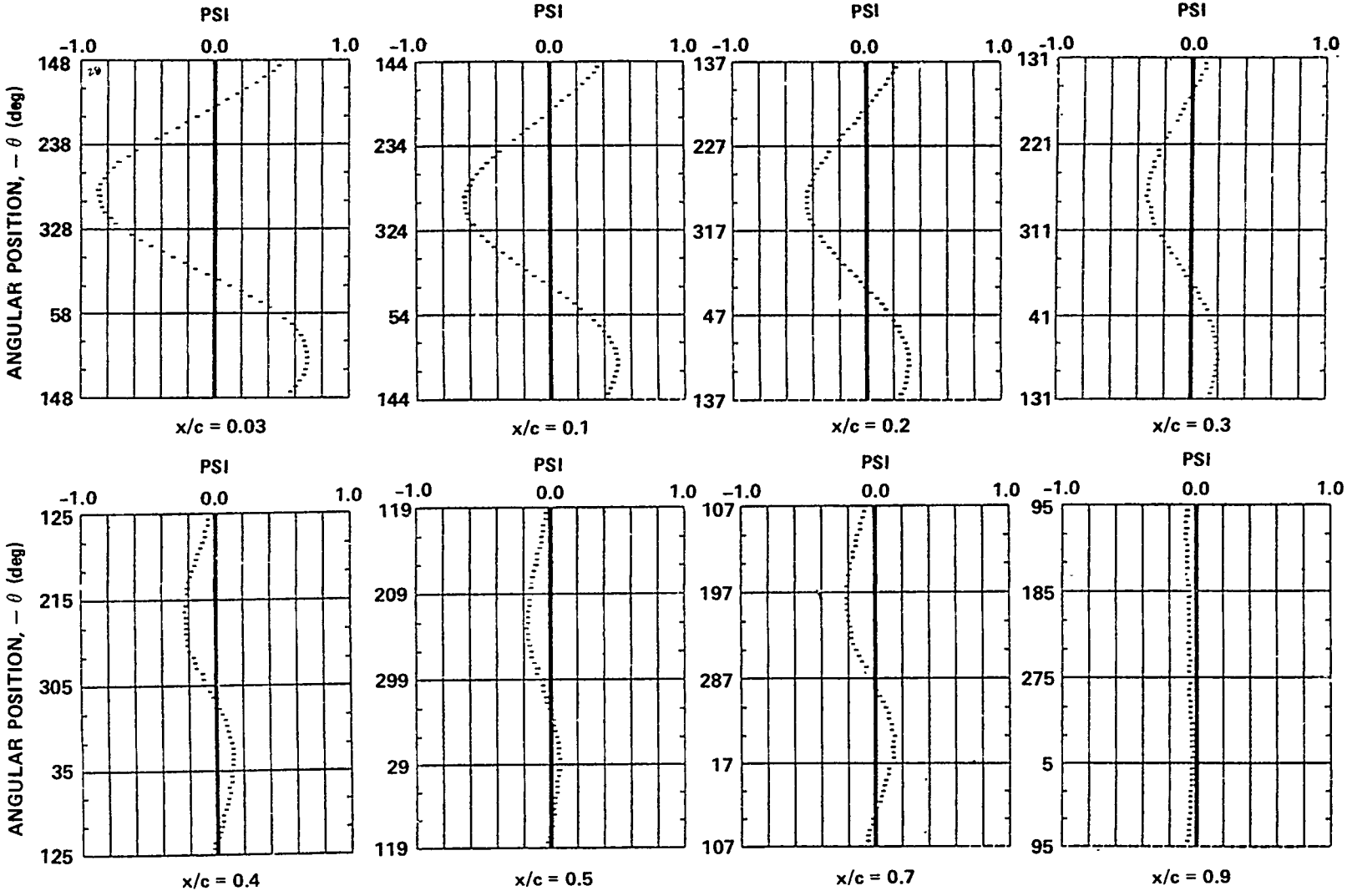

Figure 23 - Variation of Pressure with Gage Angular Position, Propeller 4718, 0.7R, Suction Side, J = 0.756, V_c = 16.91 Feet per Second

Figure 24 - First Harmonic Pressure Coefficient with Propeller 4679 Inclined 7.5 Degrees at Design J; Correlations of Experimental Results with Analytical Procedures

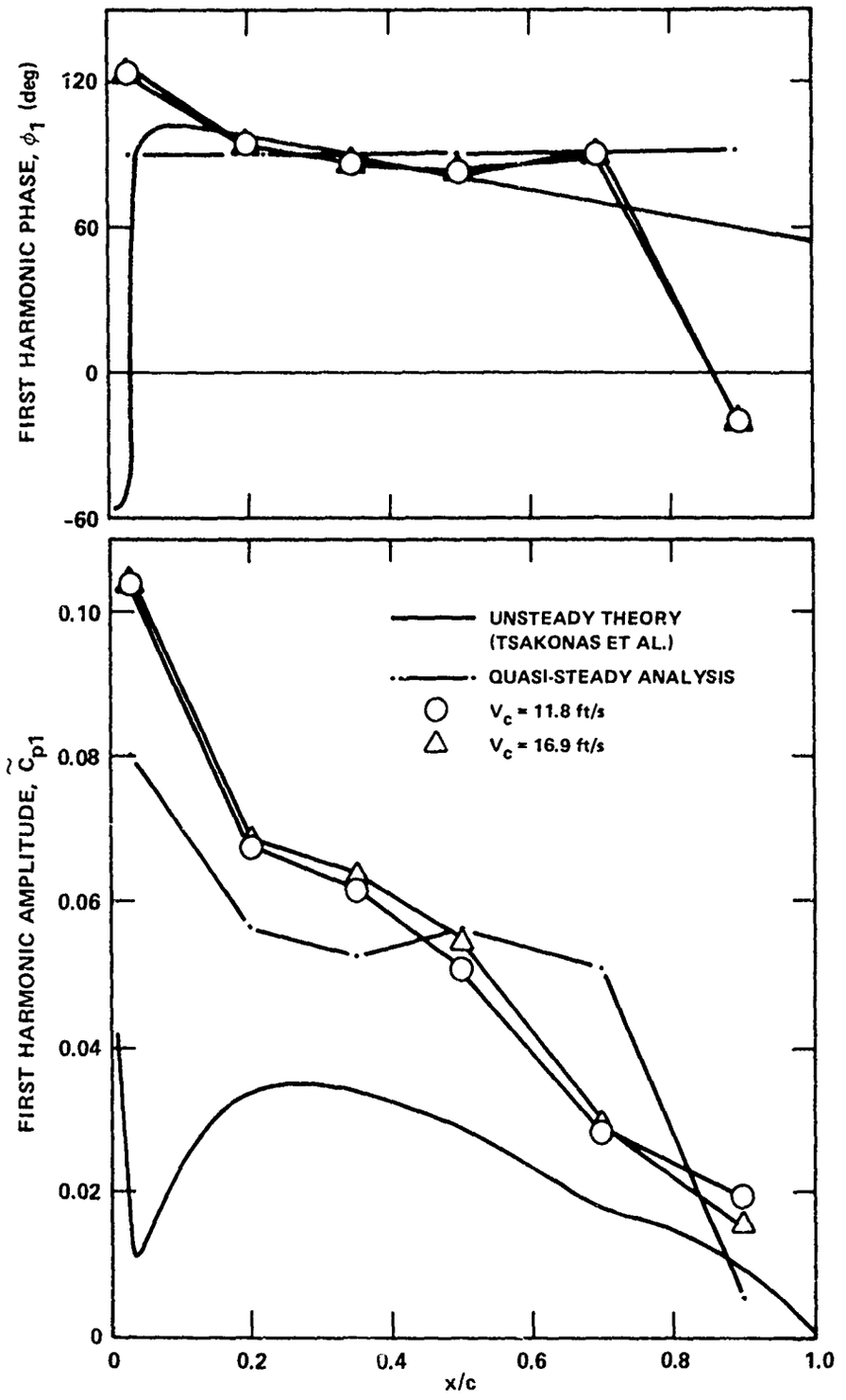

Figure 24a - r/R = 0.5, Suction Side

Figure 24 (Continued)

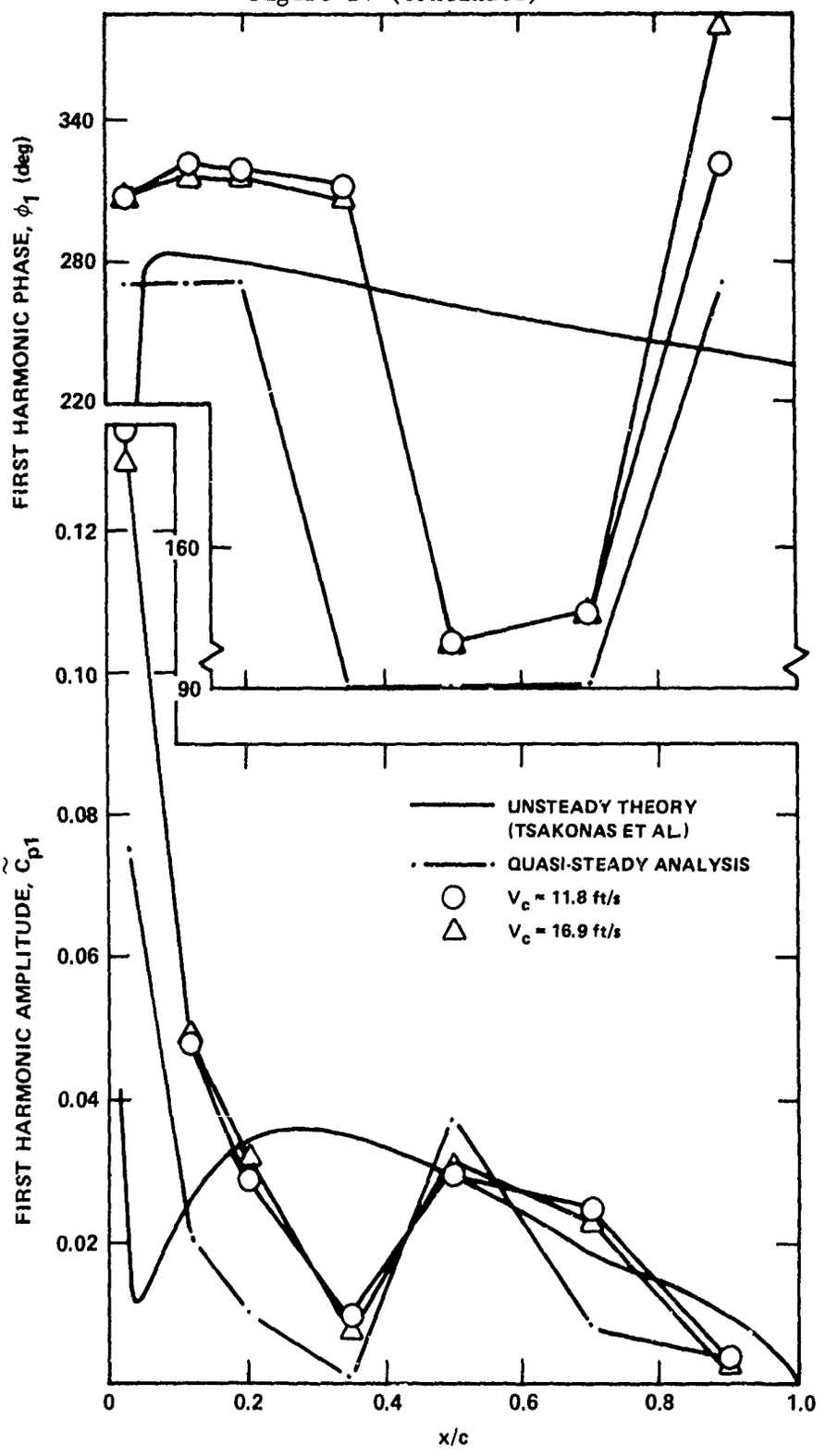

Figure 24b - r/R = 0.5, Pressure Side

Figure 24 (Continued)

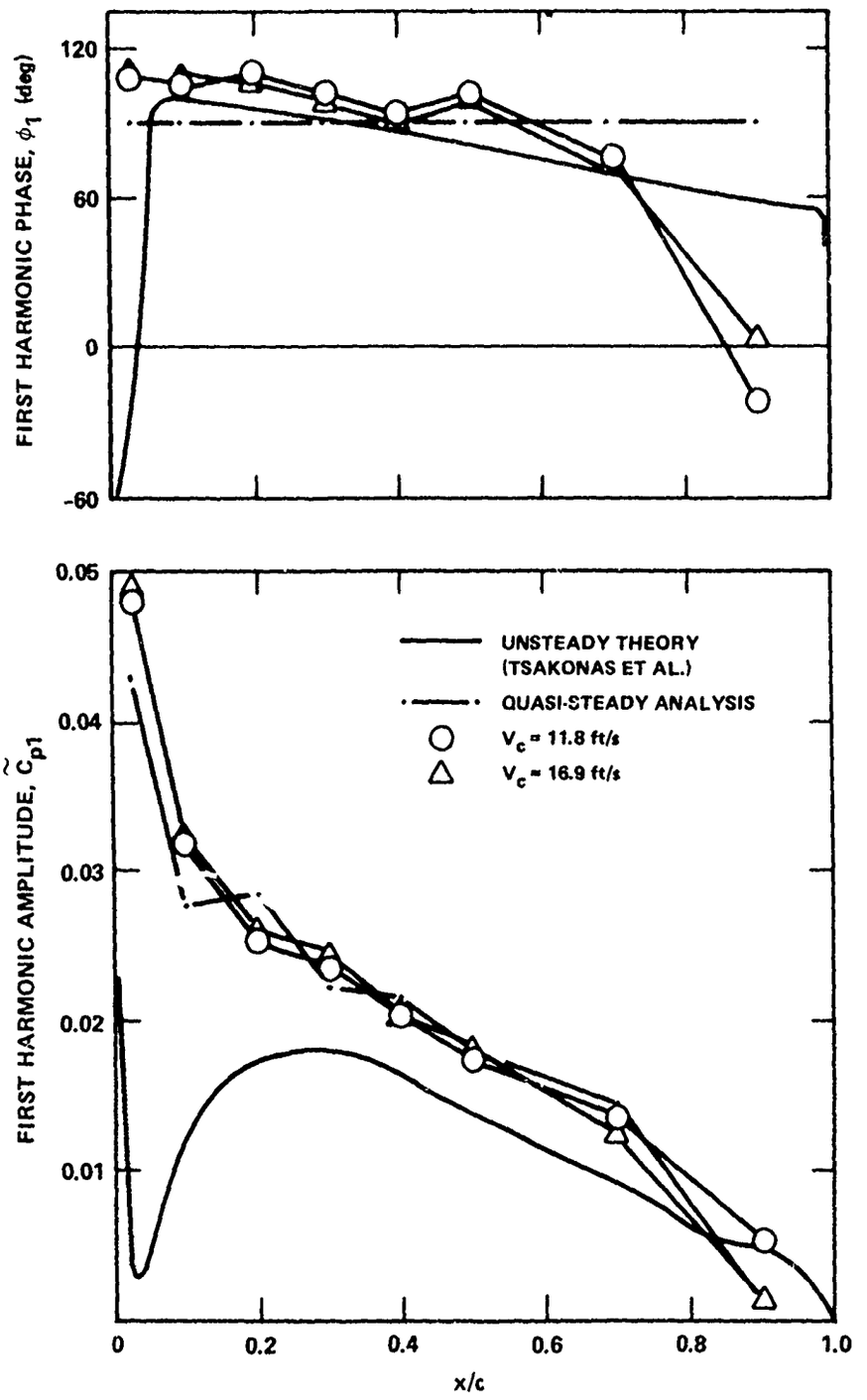

Figure 24c - r/R = 0.7, Suction Side

Figure 24 (Continued)

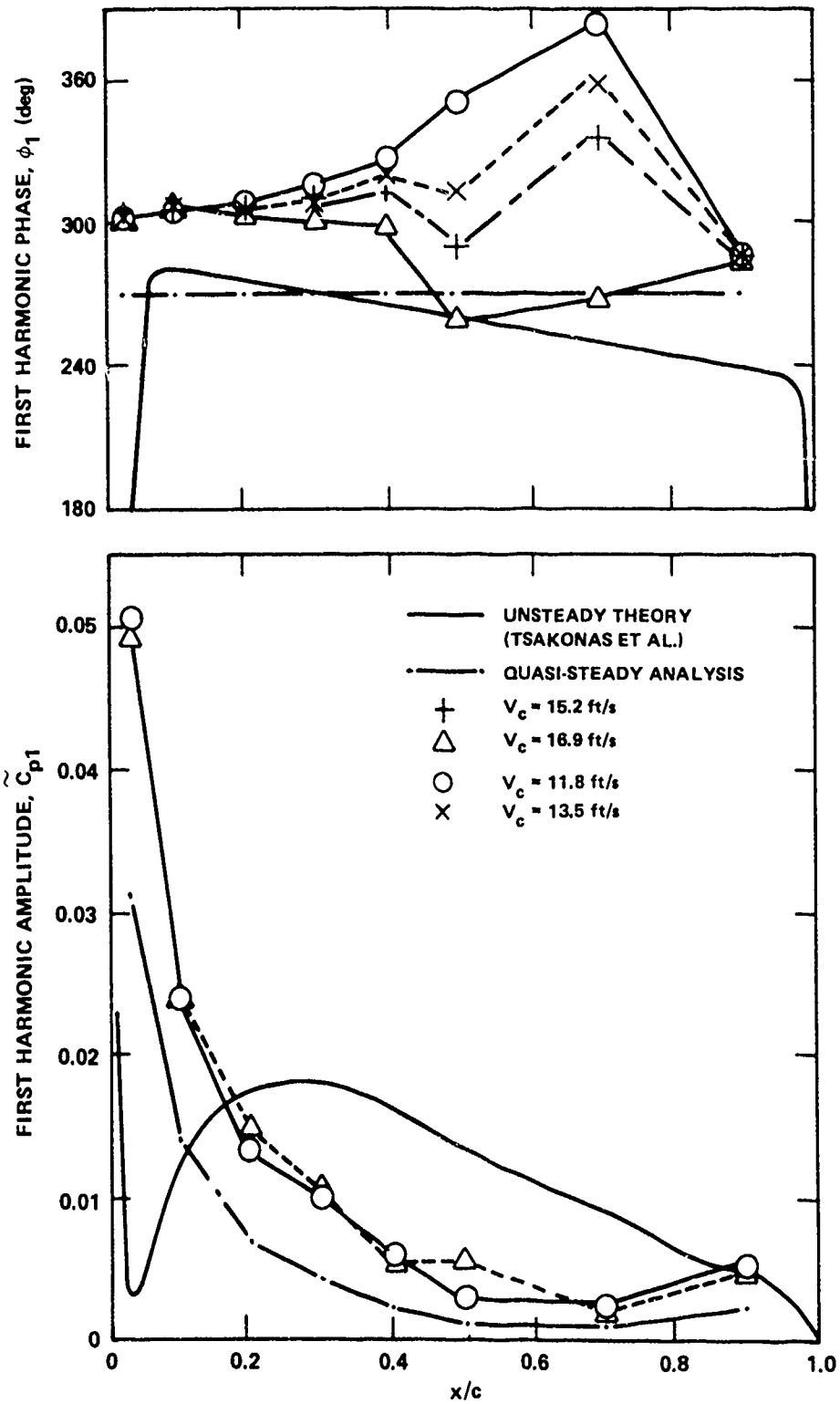

Figure 24d - r/R = 0.7, Pressure Side

Figure 24 (Continued)

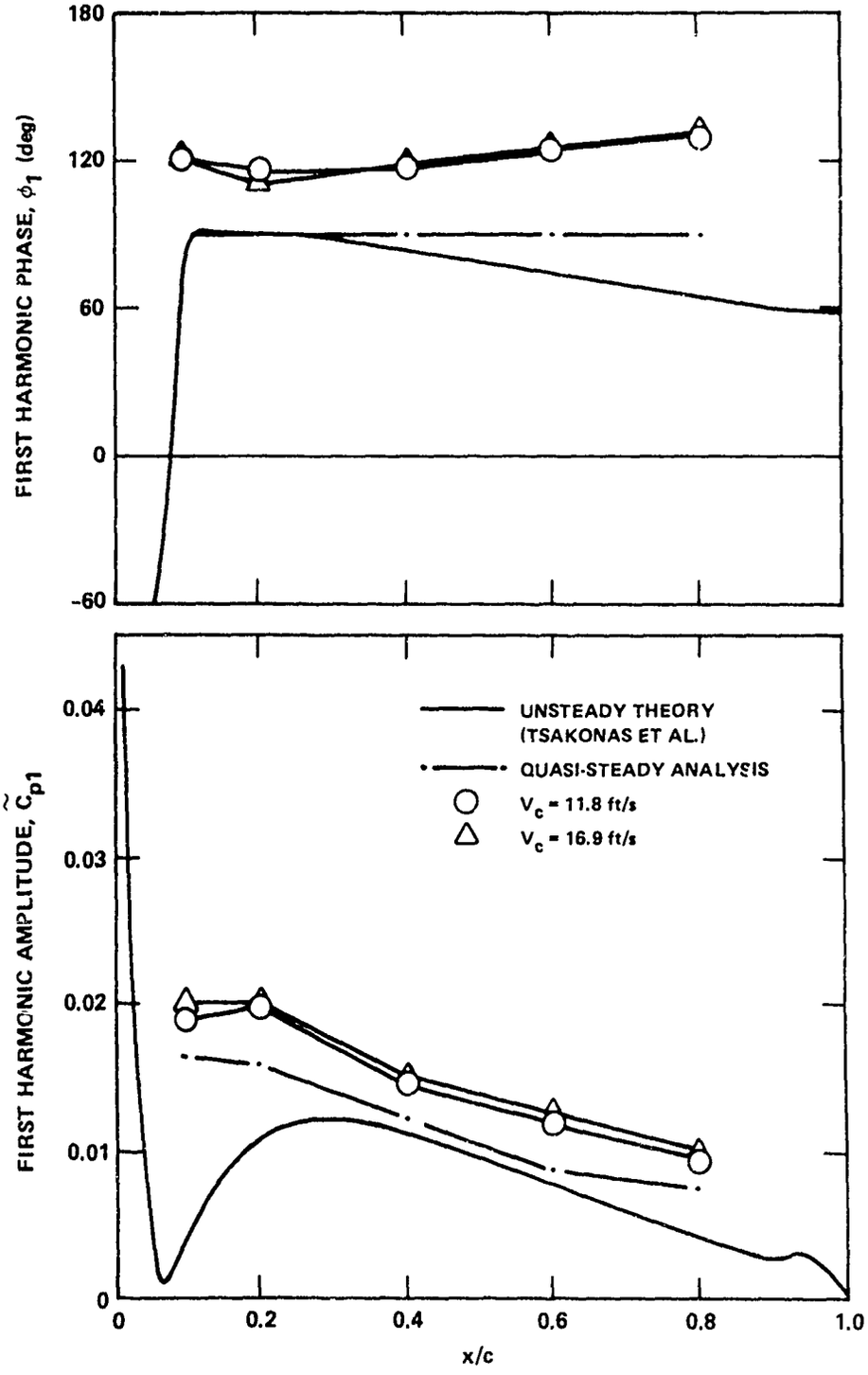

Figure 24e - r/R = 0.9, Suction Side

Figure 24 (Continued)

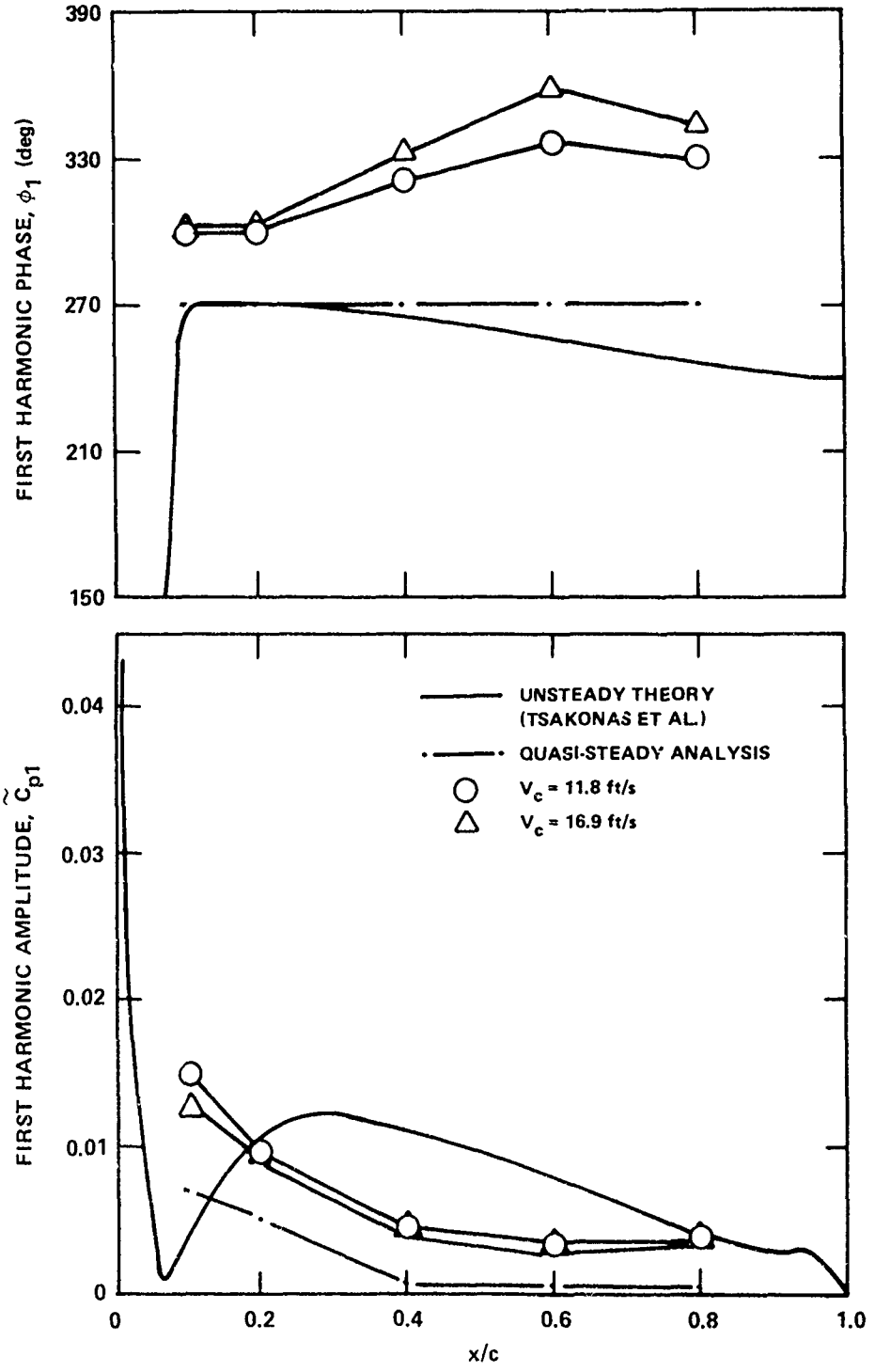

Figure 24f - r/R = 0.9, Pressure Side

Figure 25 - First Harmonic Pressure Coefficients with Propeller 4679 Inclined 7.5 Degrees at Design J; Correlation of Experimental Results with Analytical Procedures

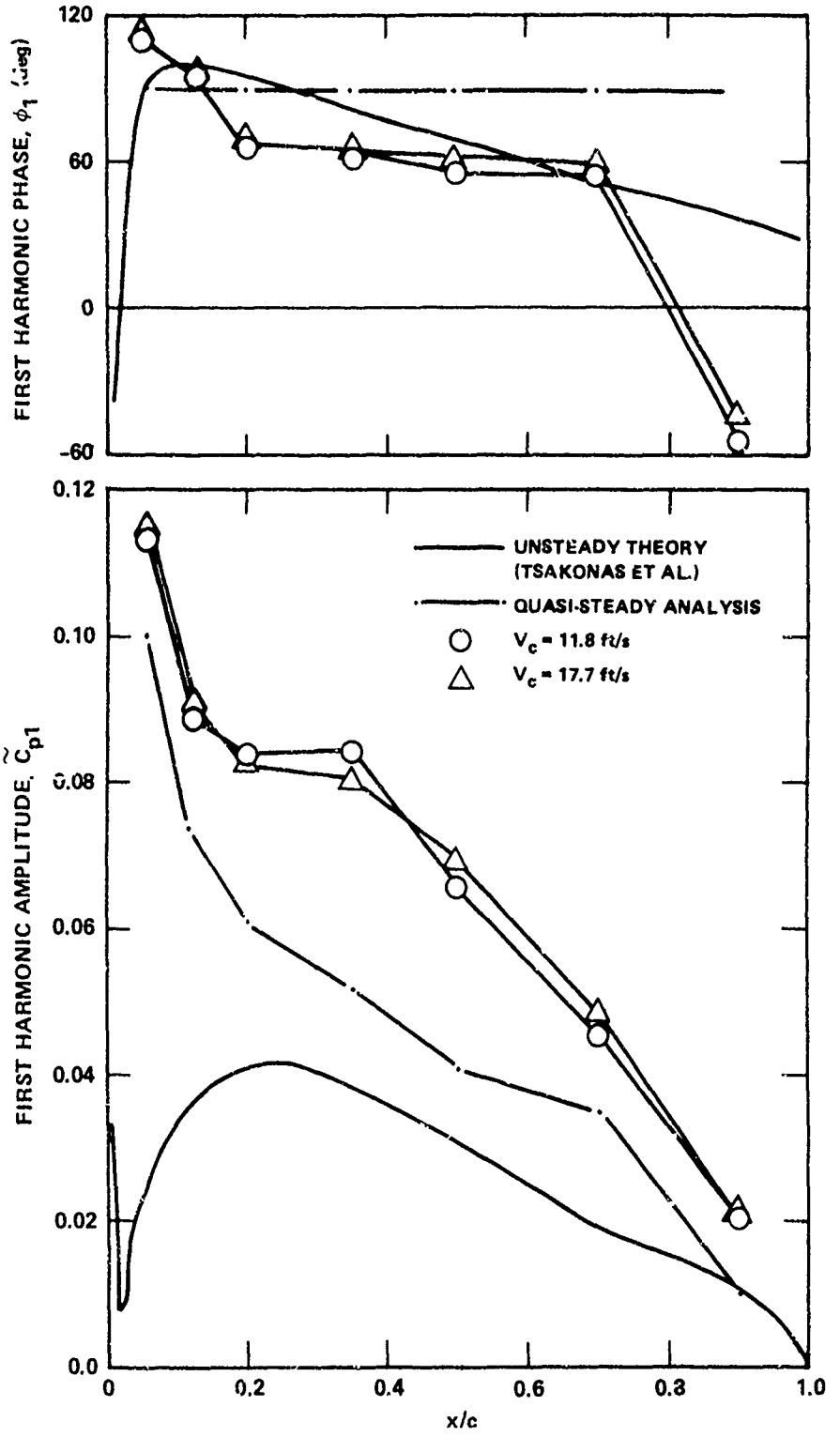

Figure 25a - r/R = 0.5, Suction Side

Figure 25 (Continued)

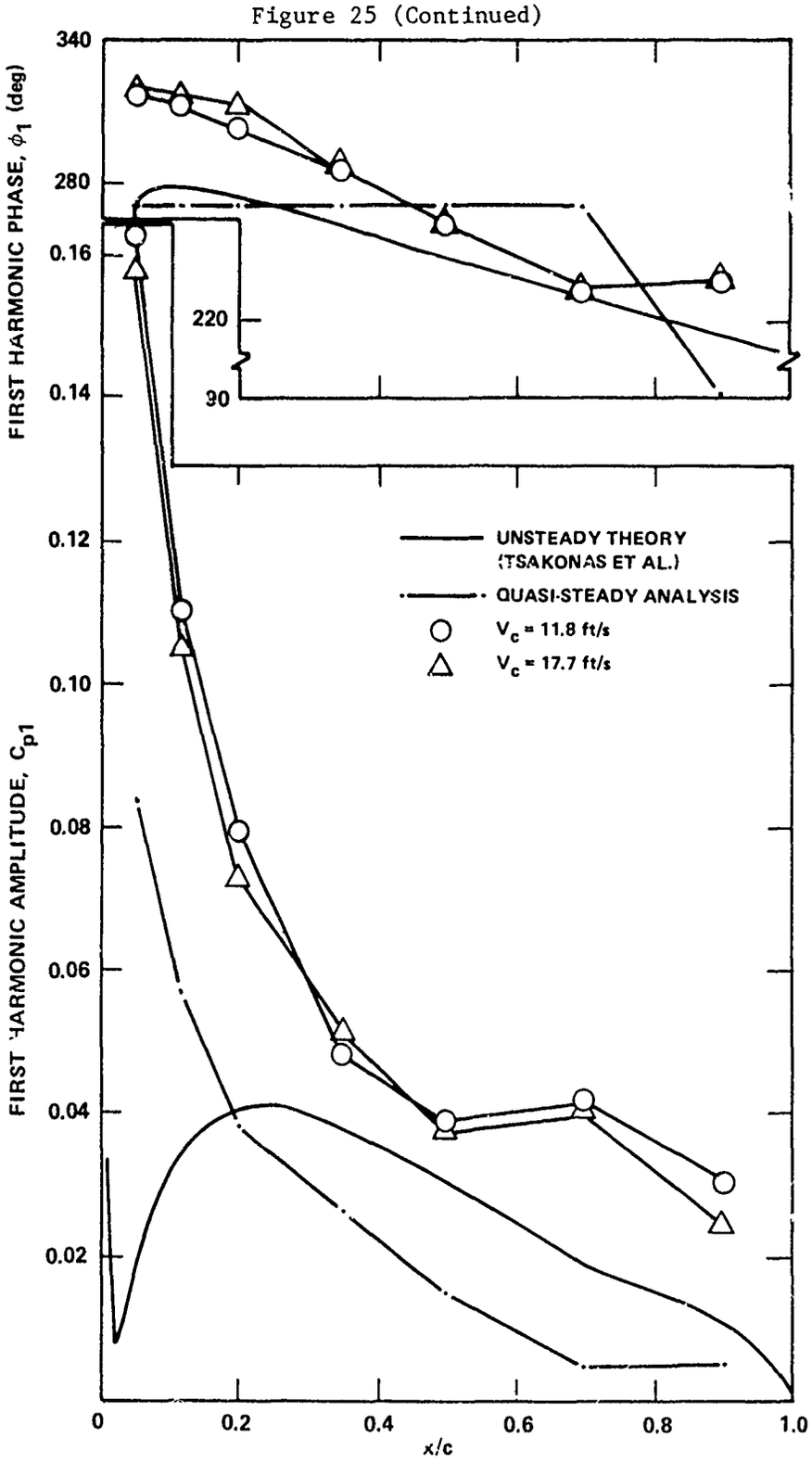

Figure 25b - r/R = 0.5, Pressure Side

Figure 25 (Continued)

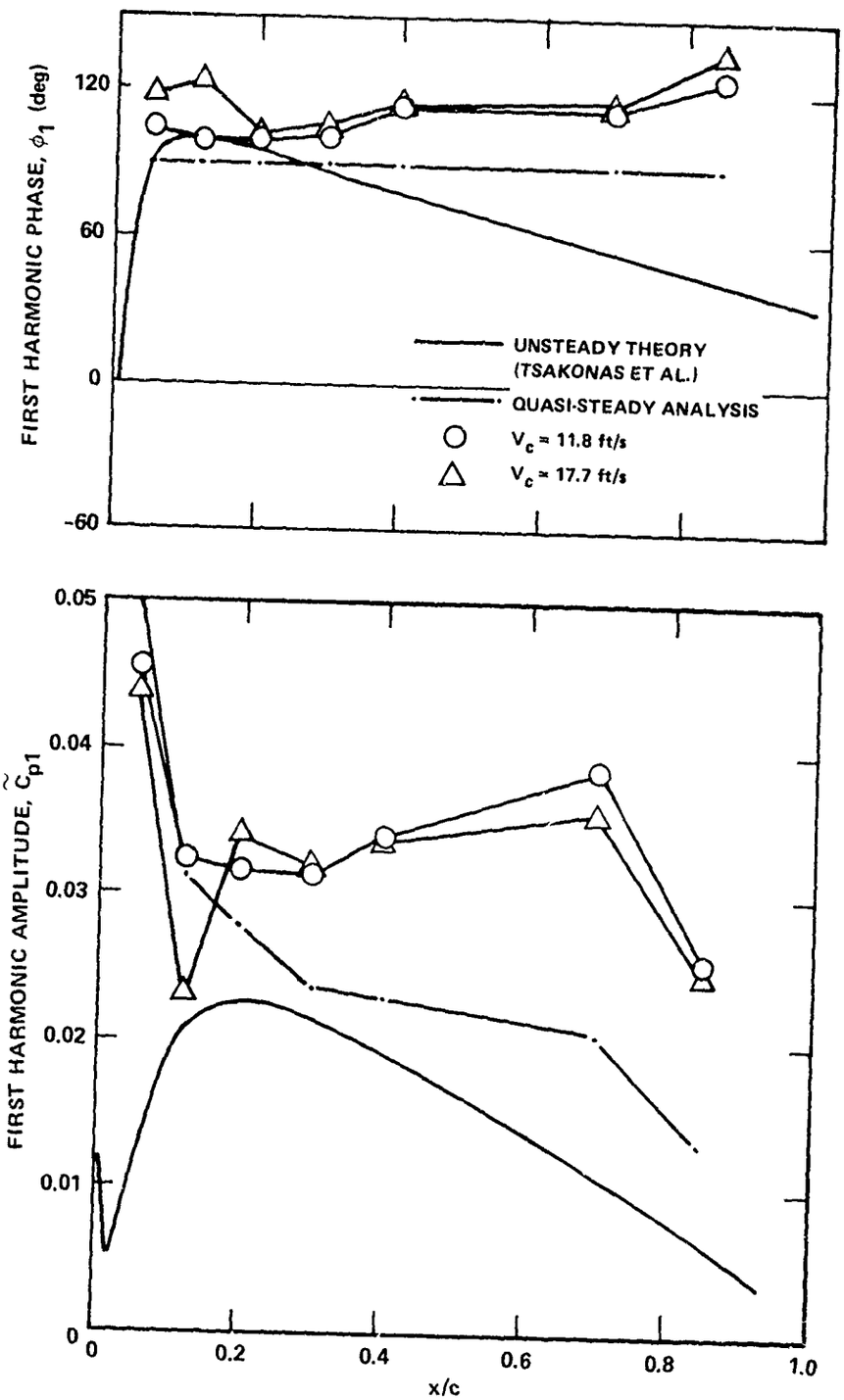

Figure 25c - r/R = 0.7, Suction Sid

Figure 25 (Continued)

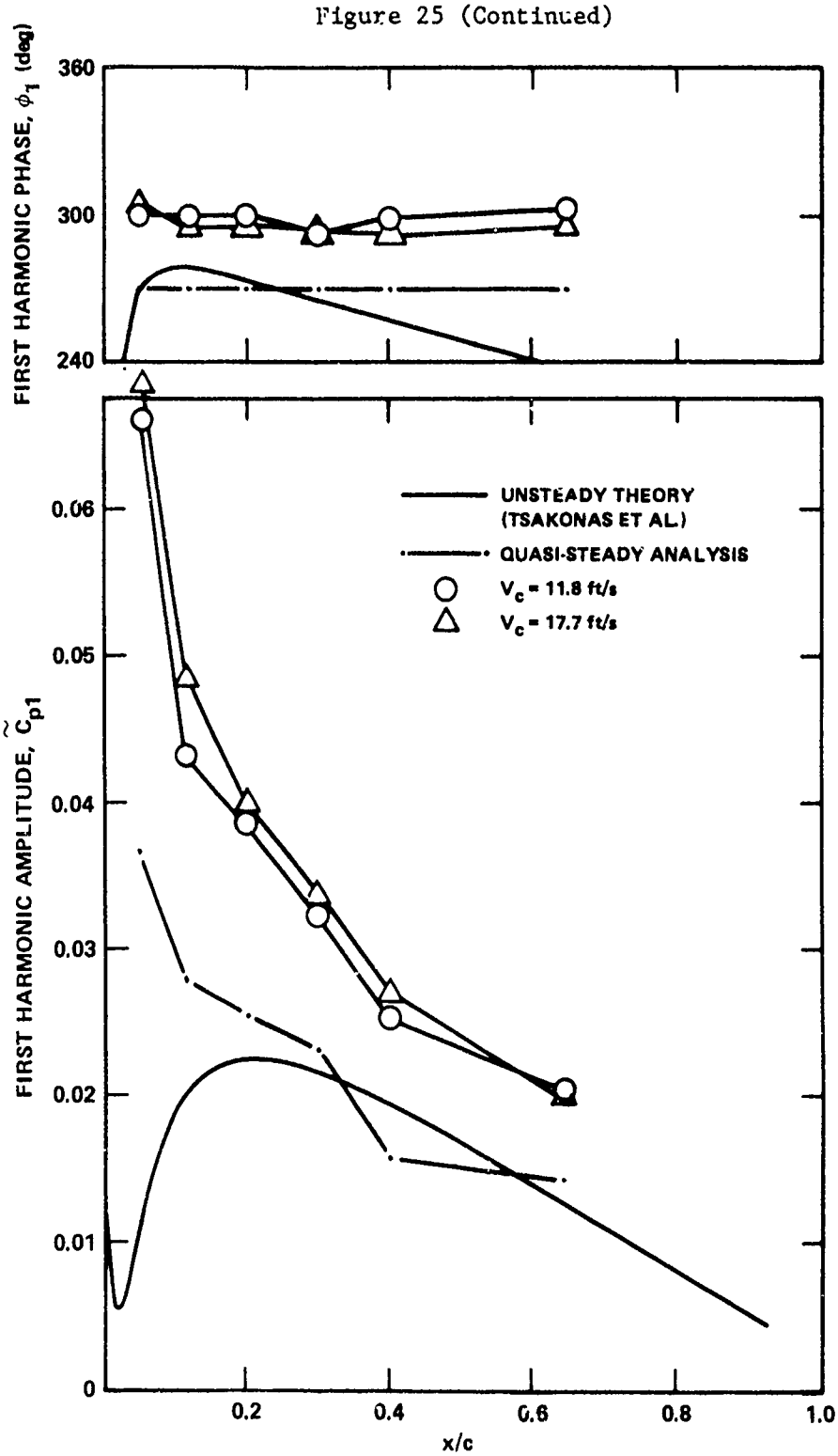

Figure 25d - r/R = 0.7, Pressure Side

Figure 25 (Continued)

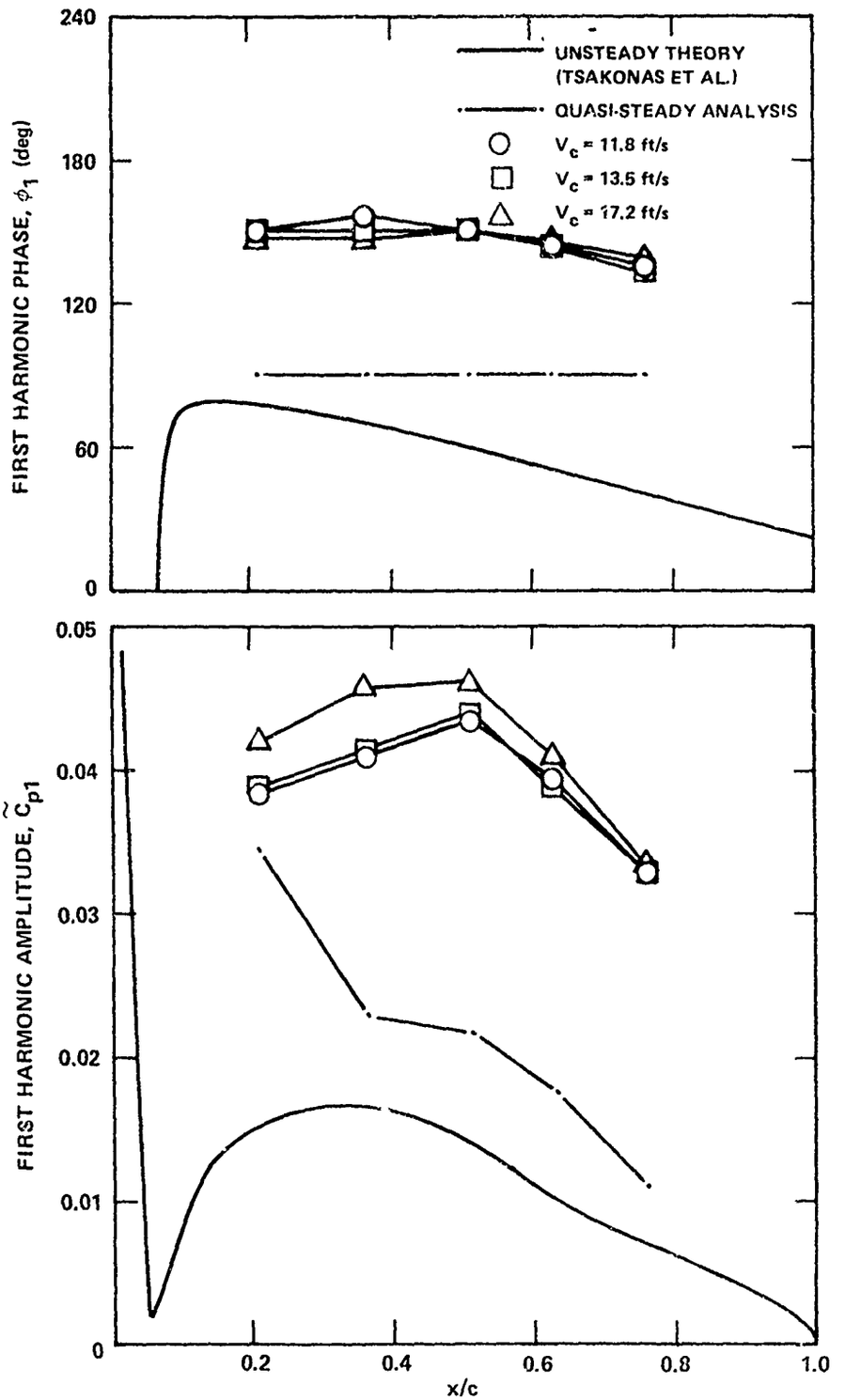

Figure 25e - r/R = 0.9, Suction Side

Figure 25 (Continued)

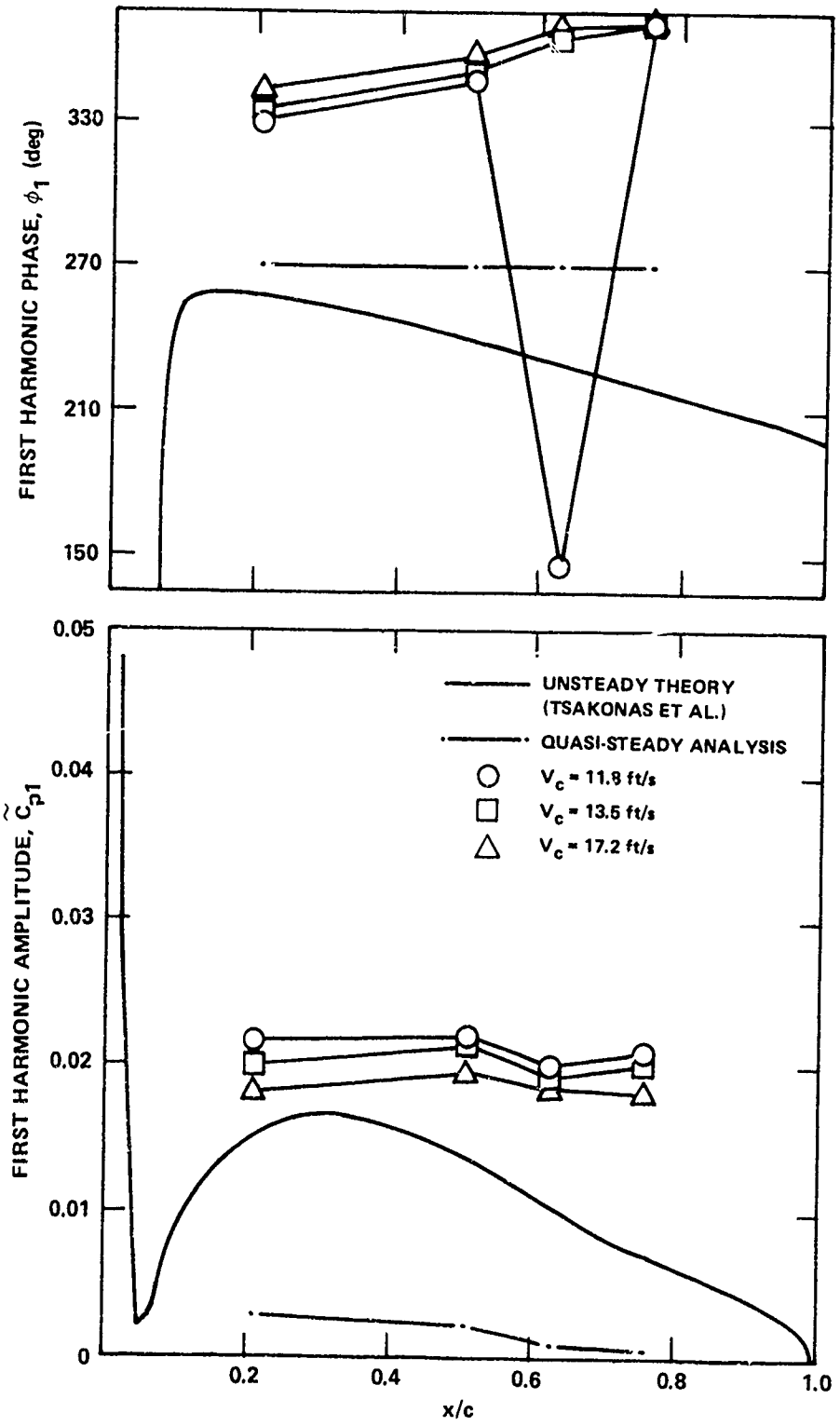

Figure 25f - r/R = 0.9, Pressure Side

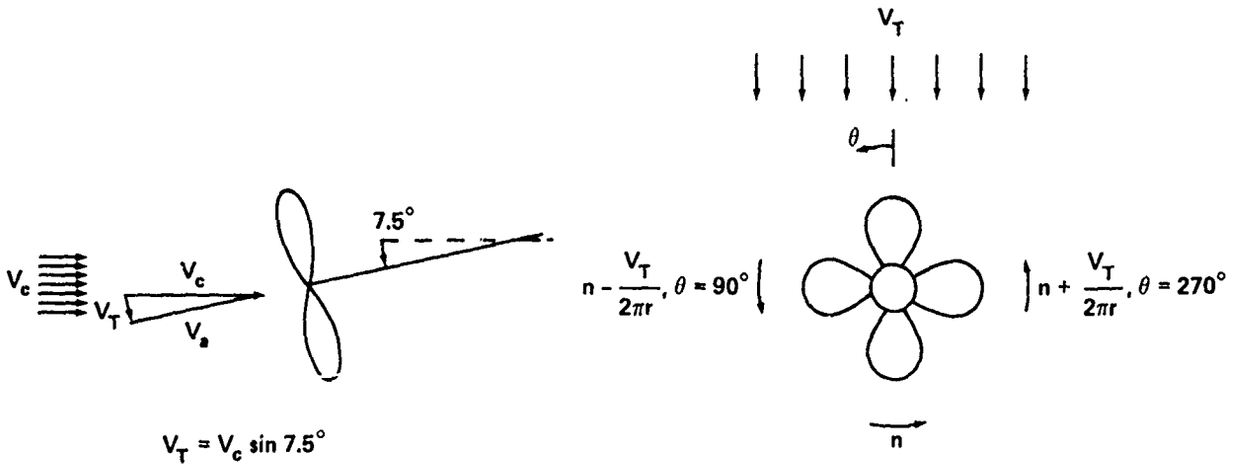

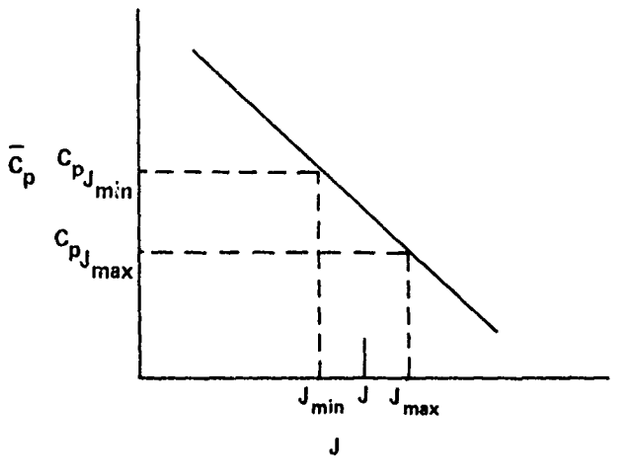

(From Figure 17)

Figure 26 - Quasi-Steady Analysis of Fluctuating Pressure Coefficients in Inclined Flow

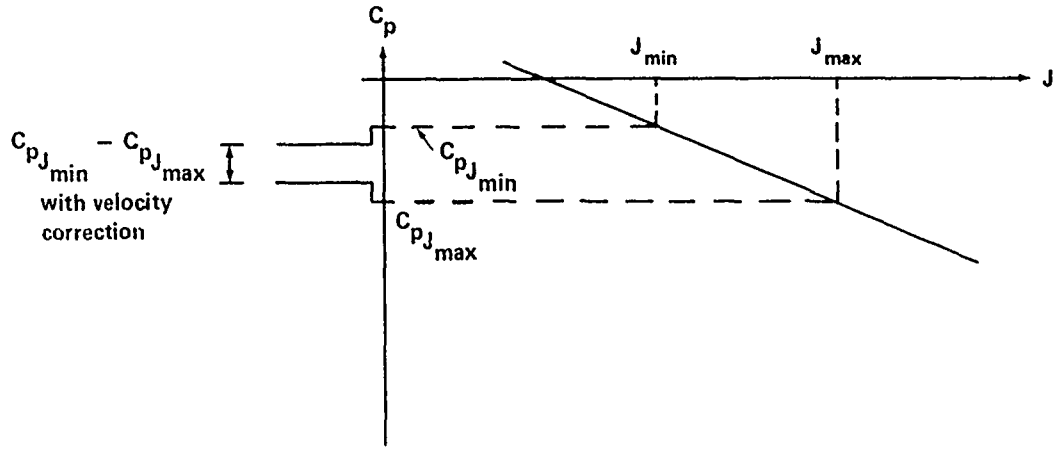

Figure 27a - Effect of Speed Correction on Pressure Side

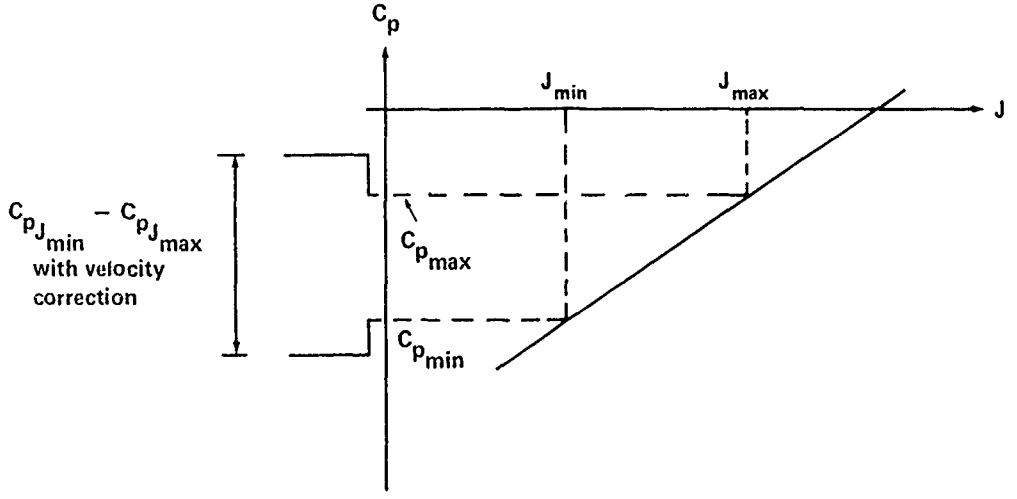

Figure 27b - Effect of Speed Correction on Suction Side

Figure 27 - Quasi-Steady Speed Correction Trends on Suction and Pressure Side of Propeller Blade

Figure 28 - First Harmonic Pressure Coefficients for Propeller 4718 Inclined 7.5 Degrees Over a Range of J

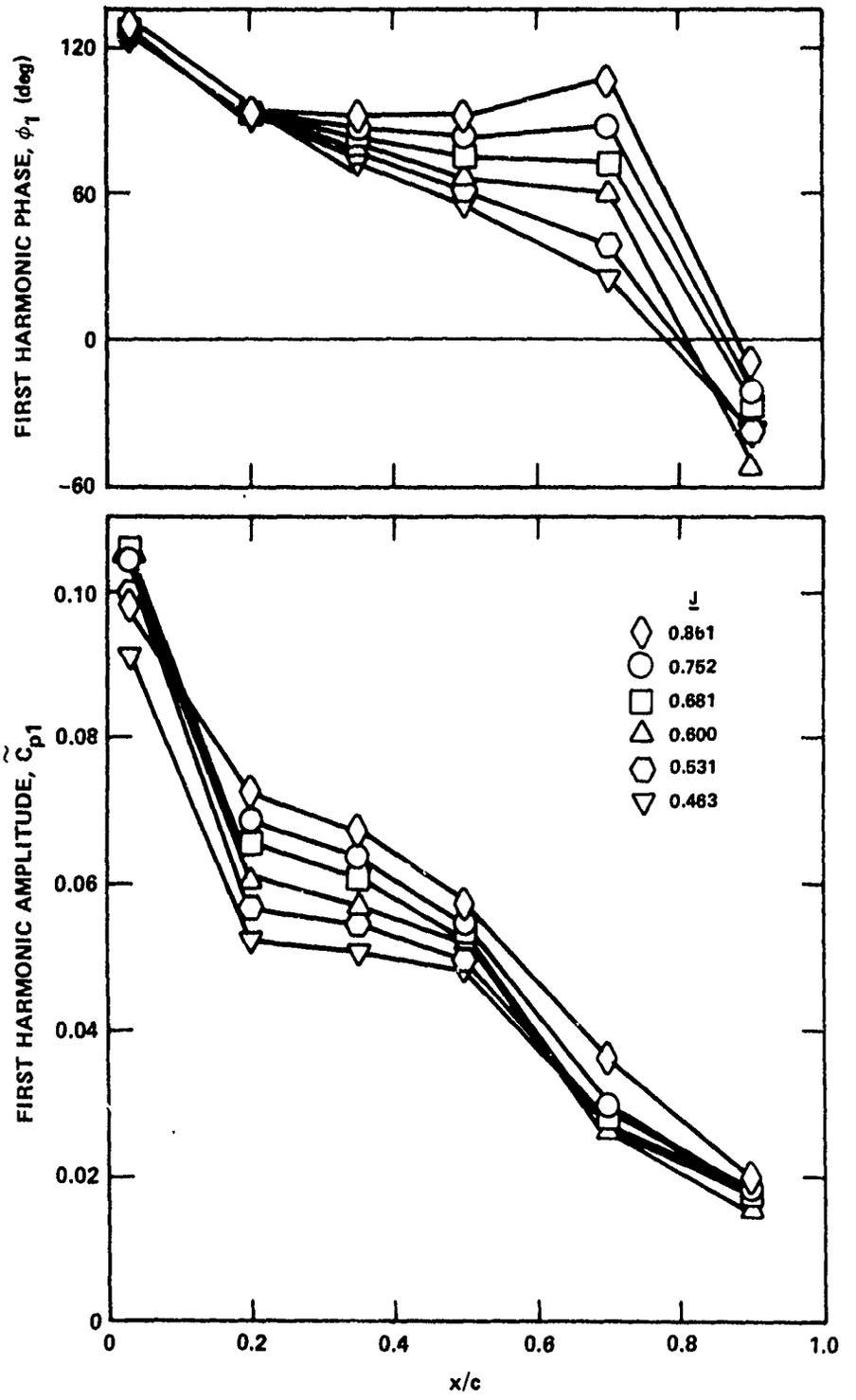

Figure 28a - r/R = 0.5, Suction Side

Figure 28 (Continued)

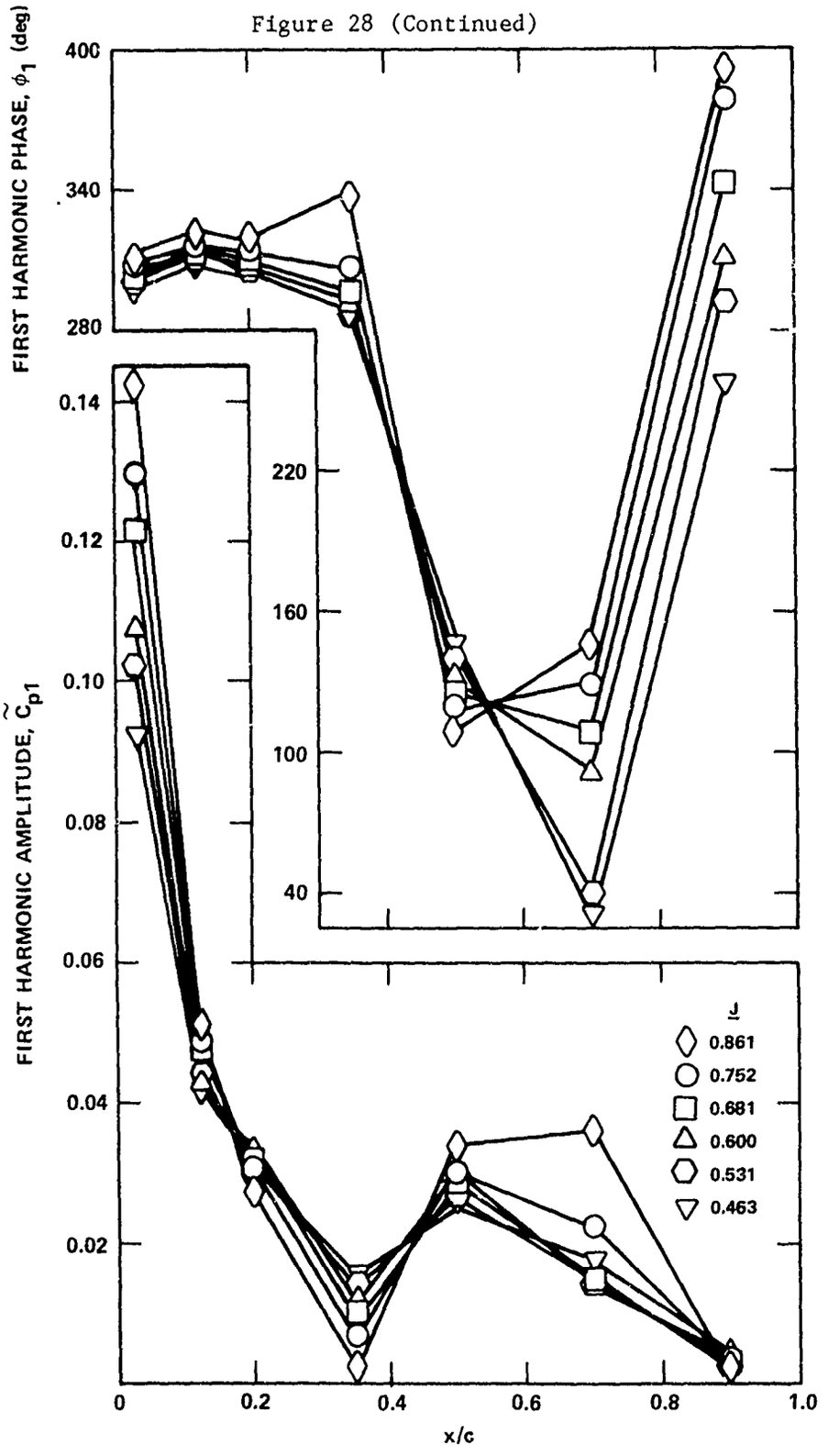

Figure 28b - r/R = 0.5, Pressure Side

Figure 28 (Continued)

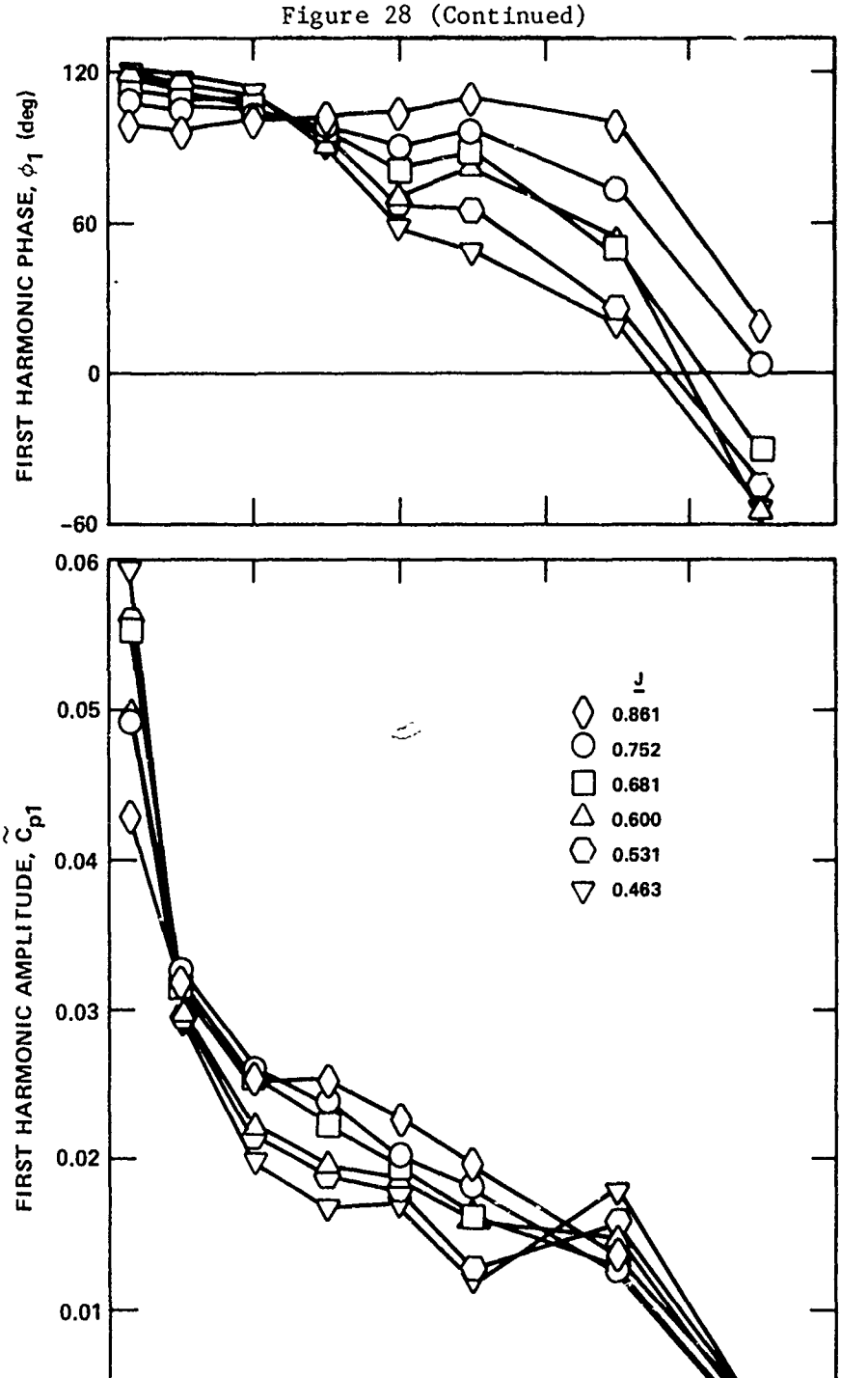

Figure 28c - r/R = 0.7, Suction Side

Figure 28 (Continued)

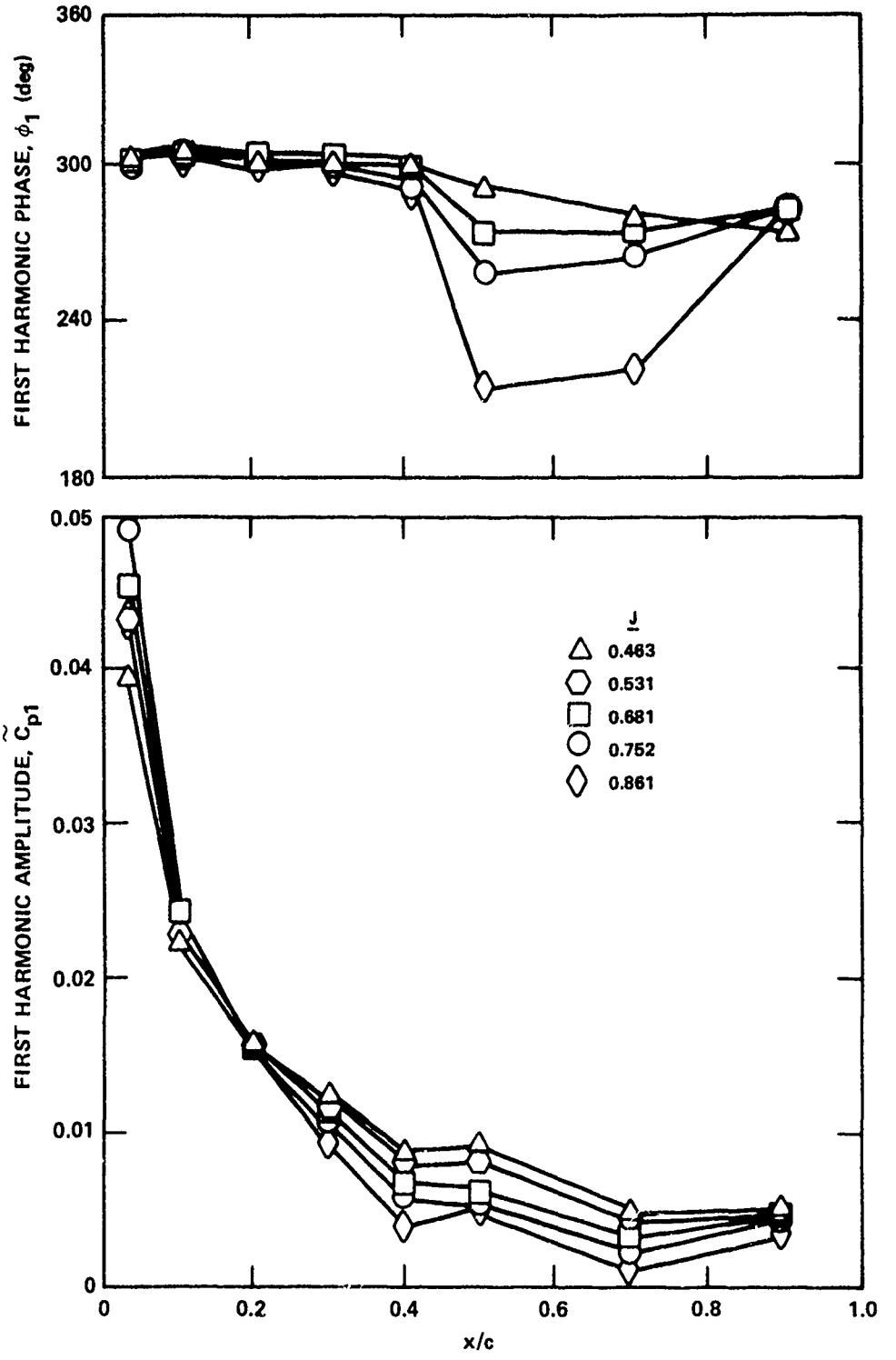

Figure 28d - r/R = 0.7, Pressure Side

Figure 28 (Continued)

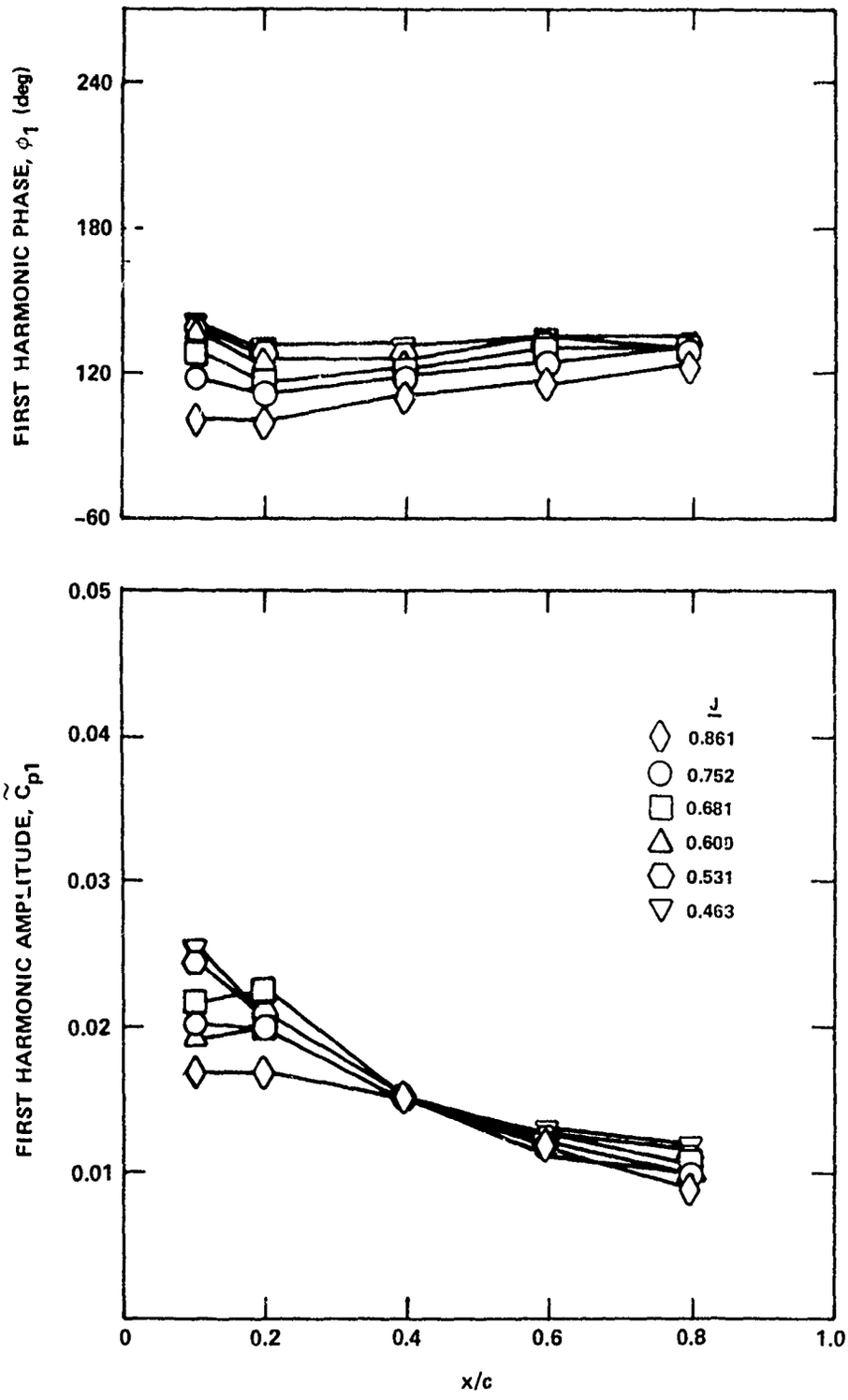

Figure 28e - r/R = 0.9, Suction Side

Figure 28 (Continued)

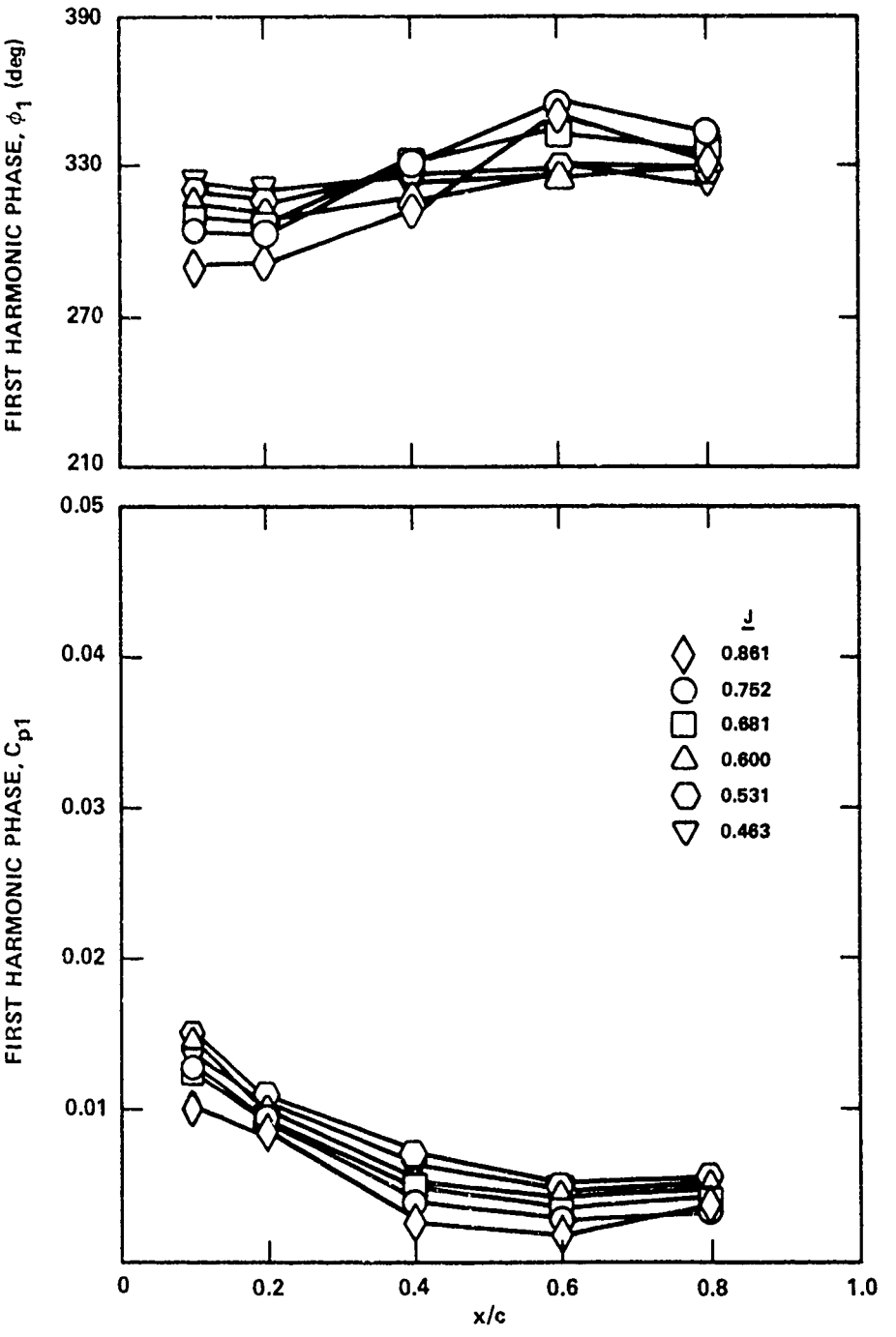

Figure 28f - r/R = 0.9, Pressure Side

Figure 29 - First Harmonic Pressure Coefficients for Propeller 4679 Inclined 7.5 Degrees Over a Range of J

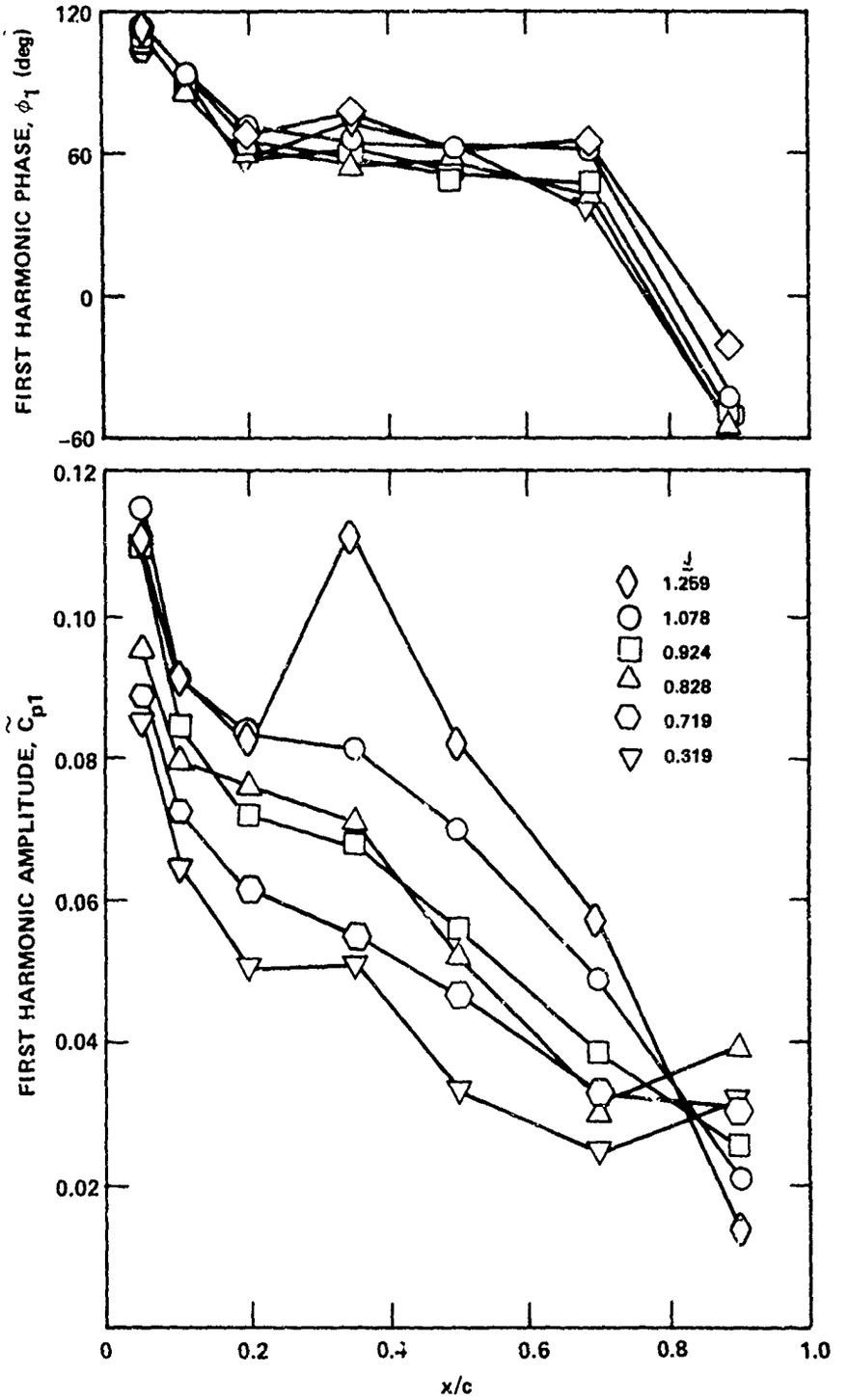

Figure 29a - r/R = 0.5, Suction Side

Figure 29 (Continued)

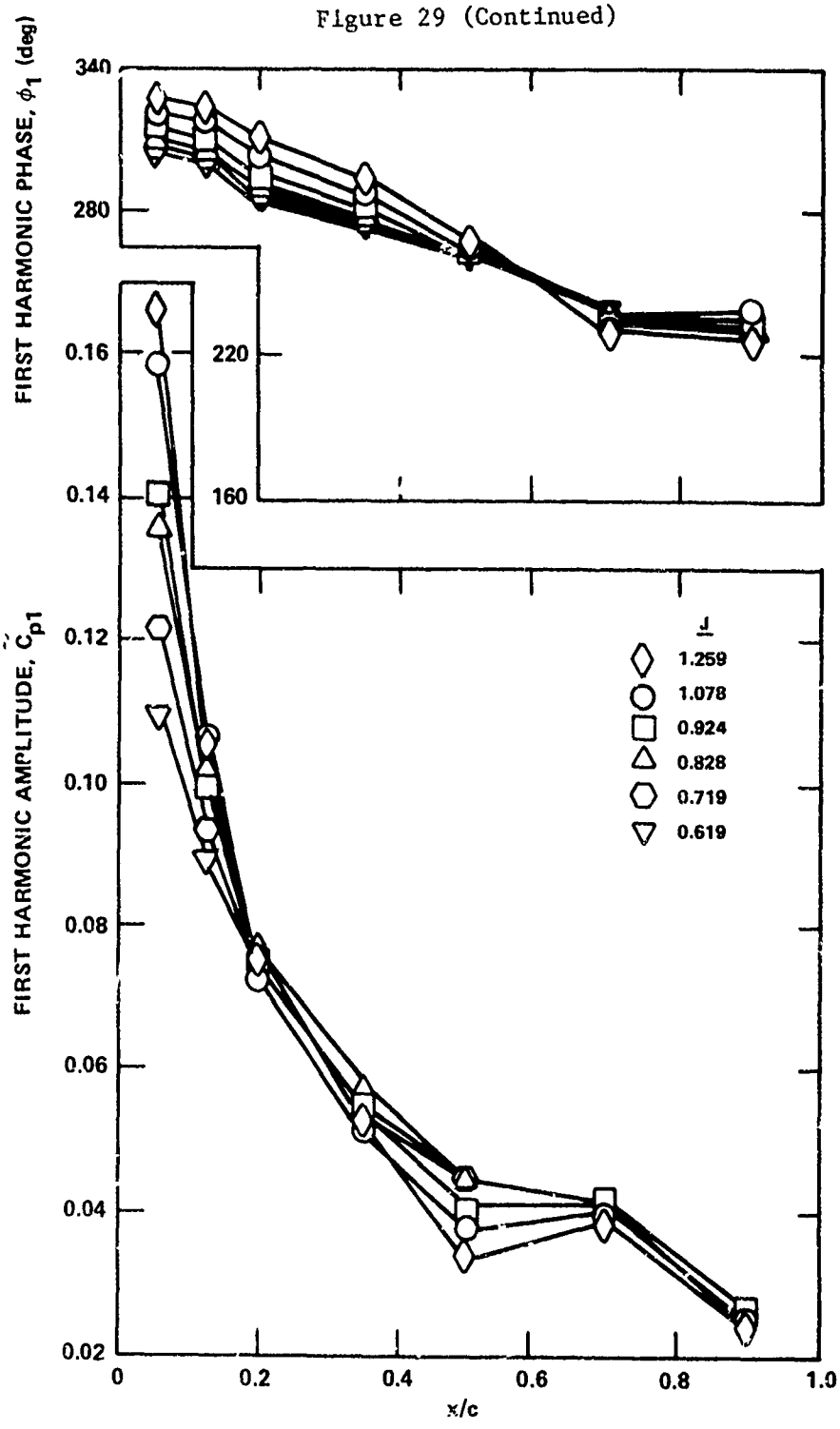

Figure 29b - r/R = 0.5, Pressure Side

Figure 29 (Continued)

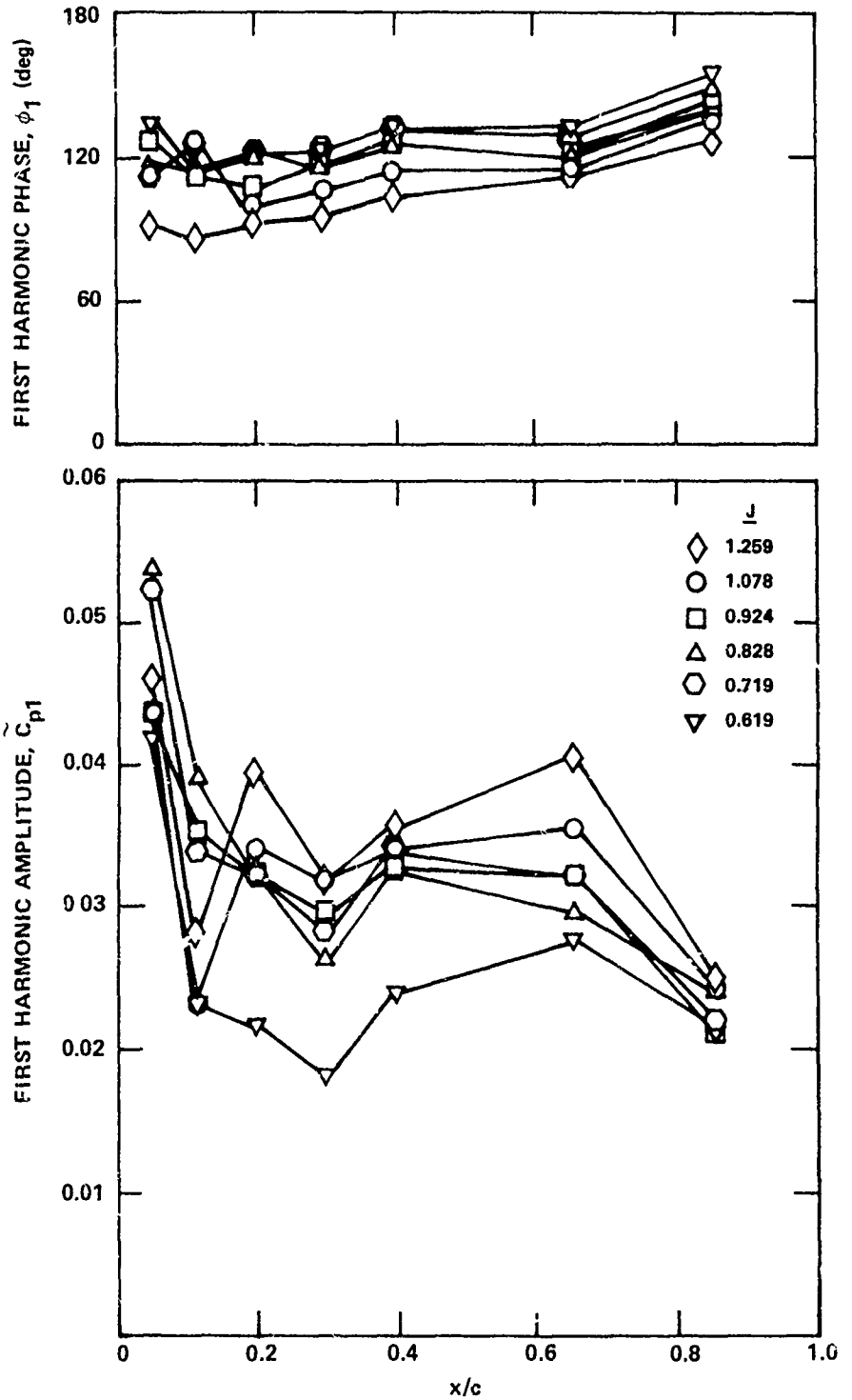

Figure 29c - r/R = 0.7, Suction Side

Figure 29 (Continued)

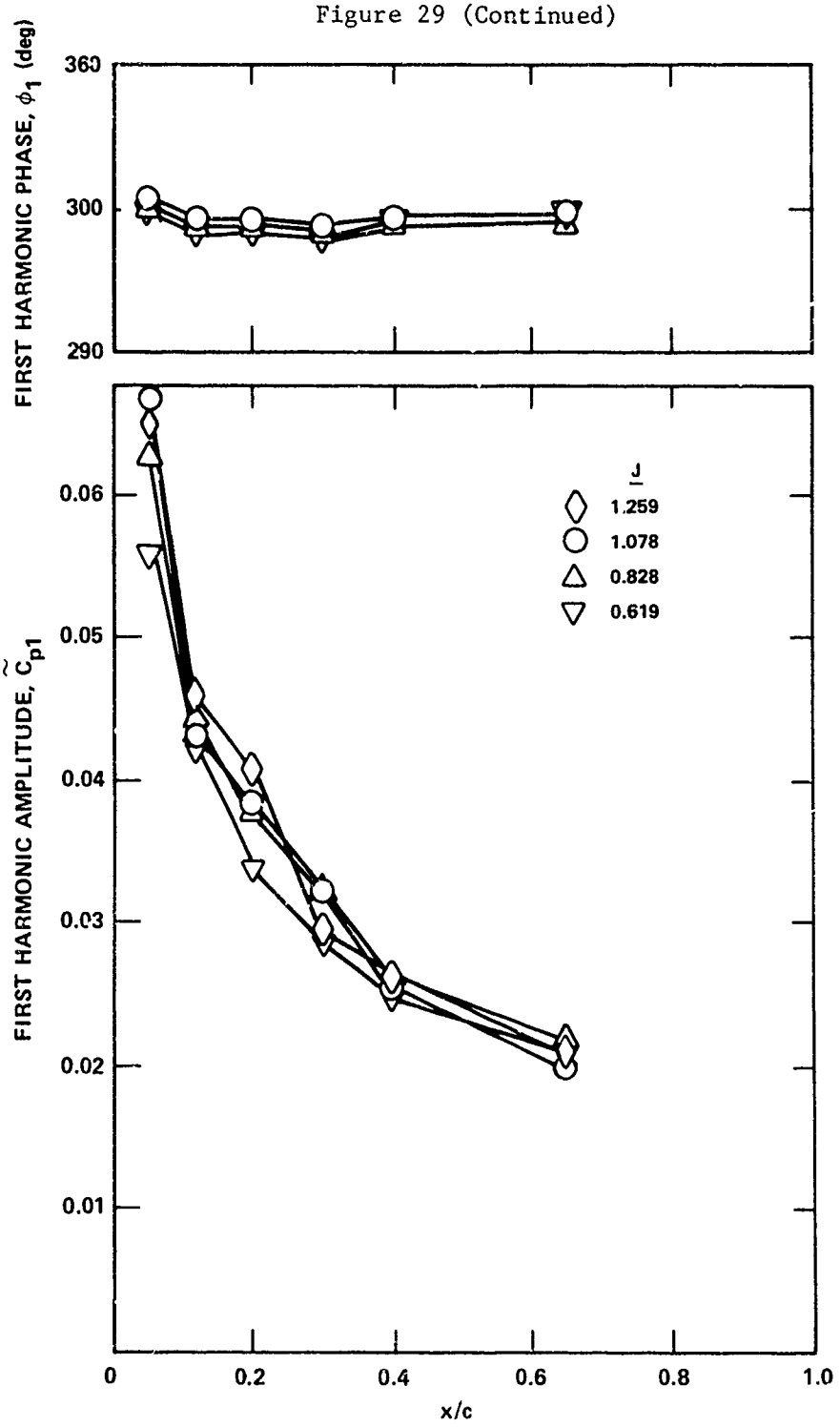

Figure 29d - r/R = 0.7, Pressure Side

Figure 29 (Continued)

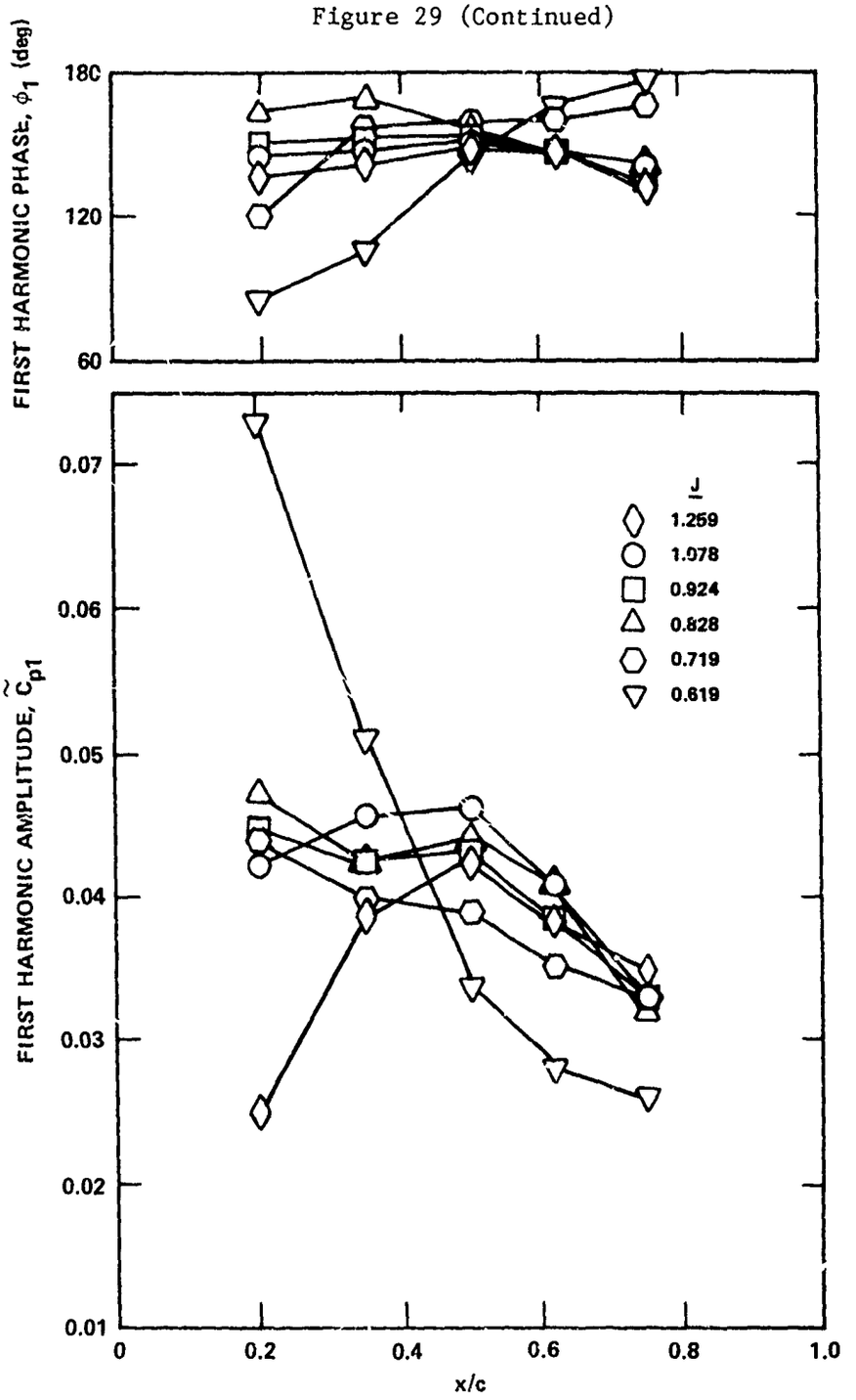

Figure 29e - r/R = 0.9, Suction Side

Figure 29 (Continued)

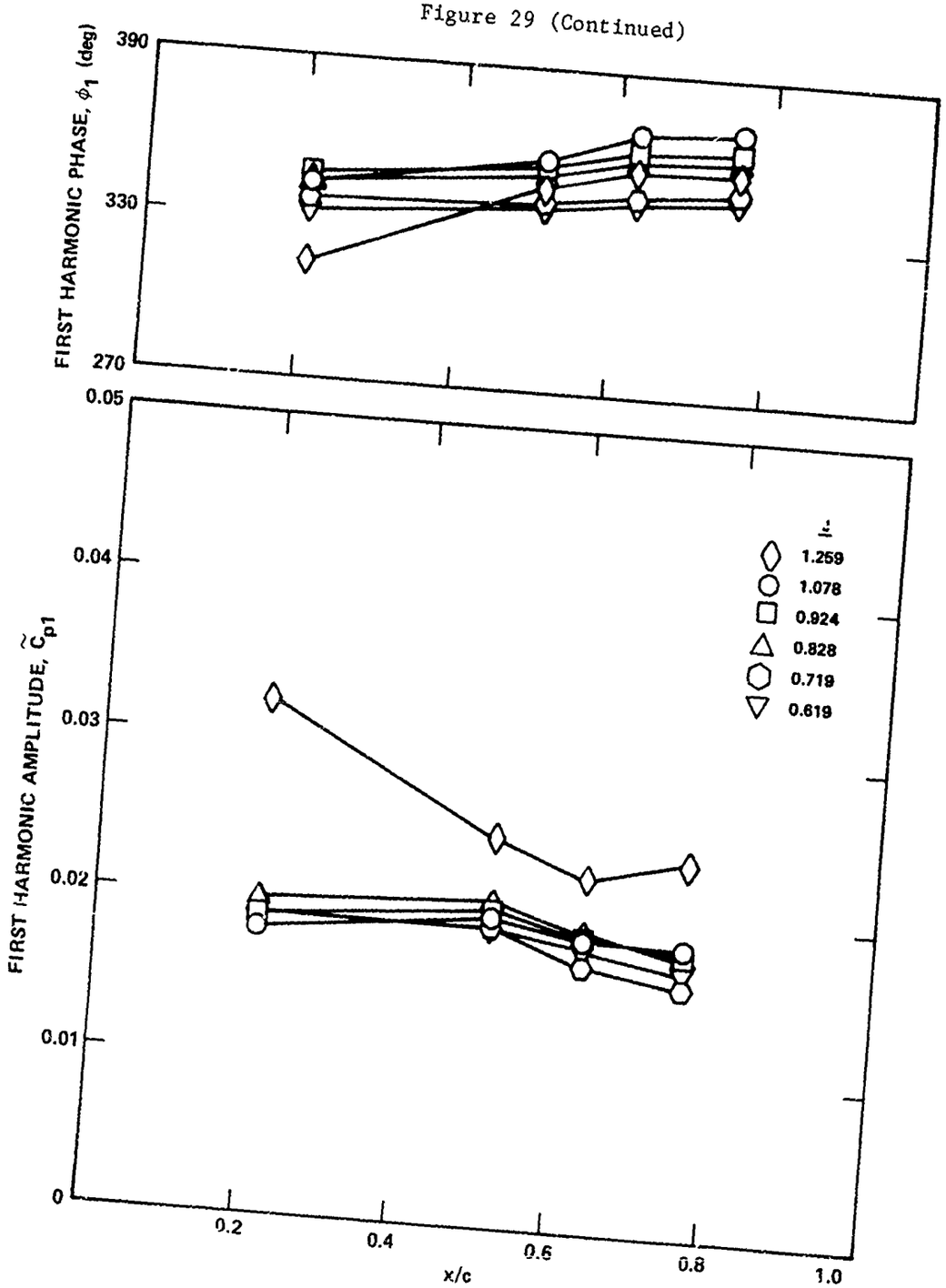

Figure 29f - r/R = 0.9, Pressure Side

Figure 30 - Quasi-Steady Predictions of First Harmonic Pressure Coefficients for Propeller 4718 Inclined 7.5 Degrees Over a Range of J; Based on First-Order Curve Fits of C_p versus J

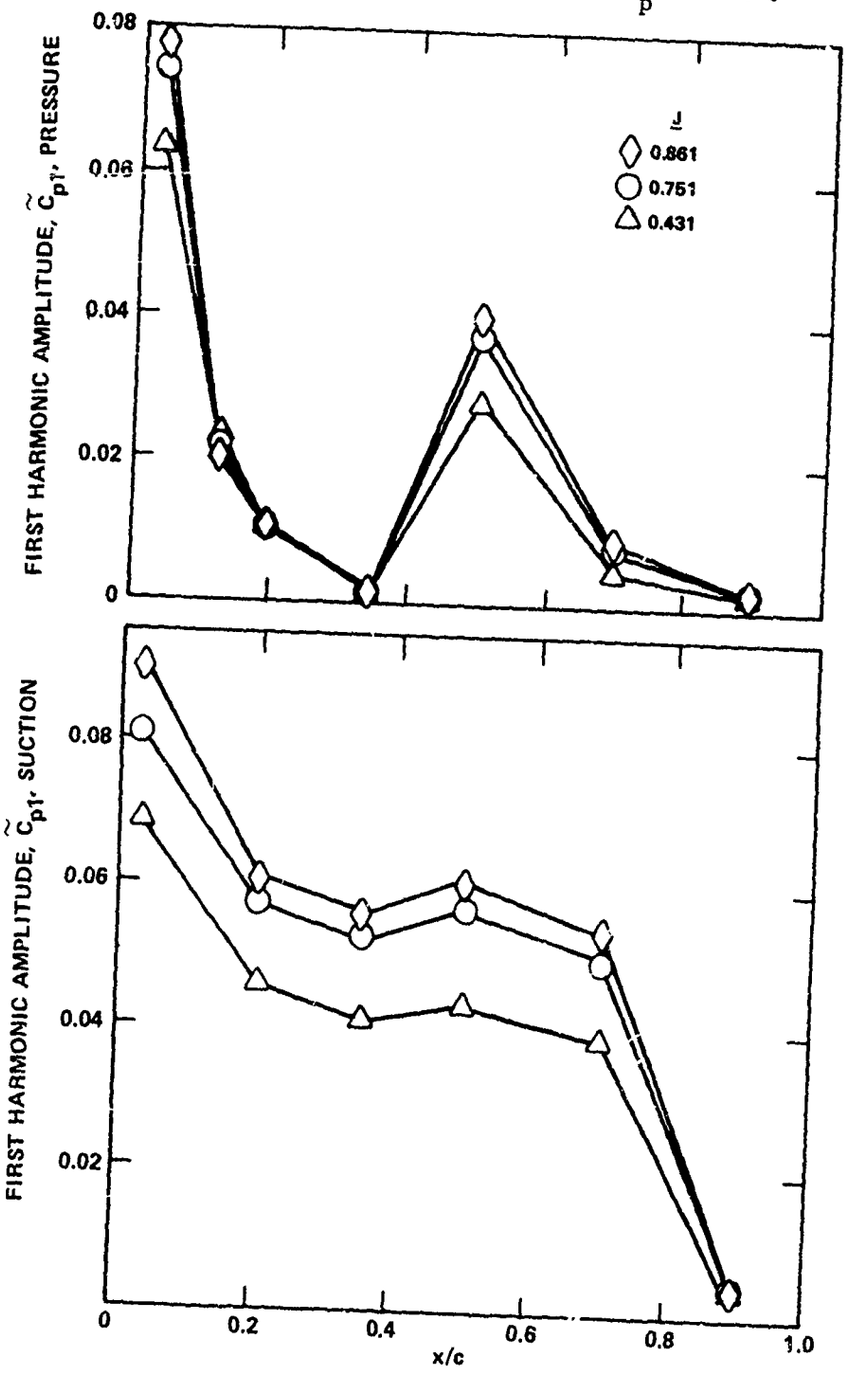

Figure 30a - $r/\dot{R} = 0.5$

Figure 30 (Continued)

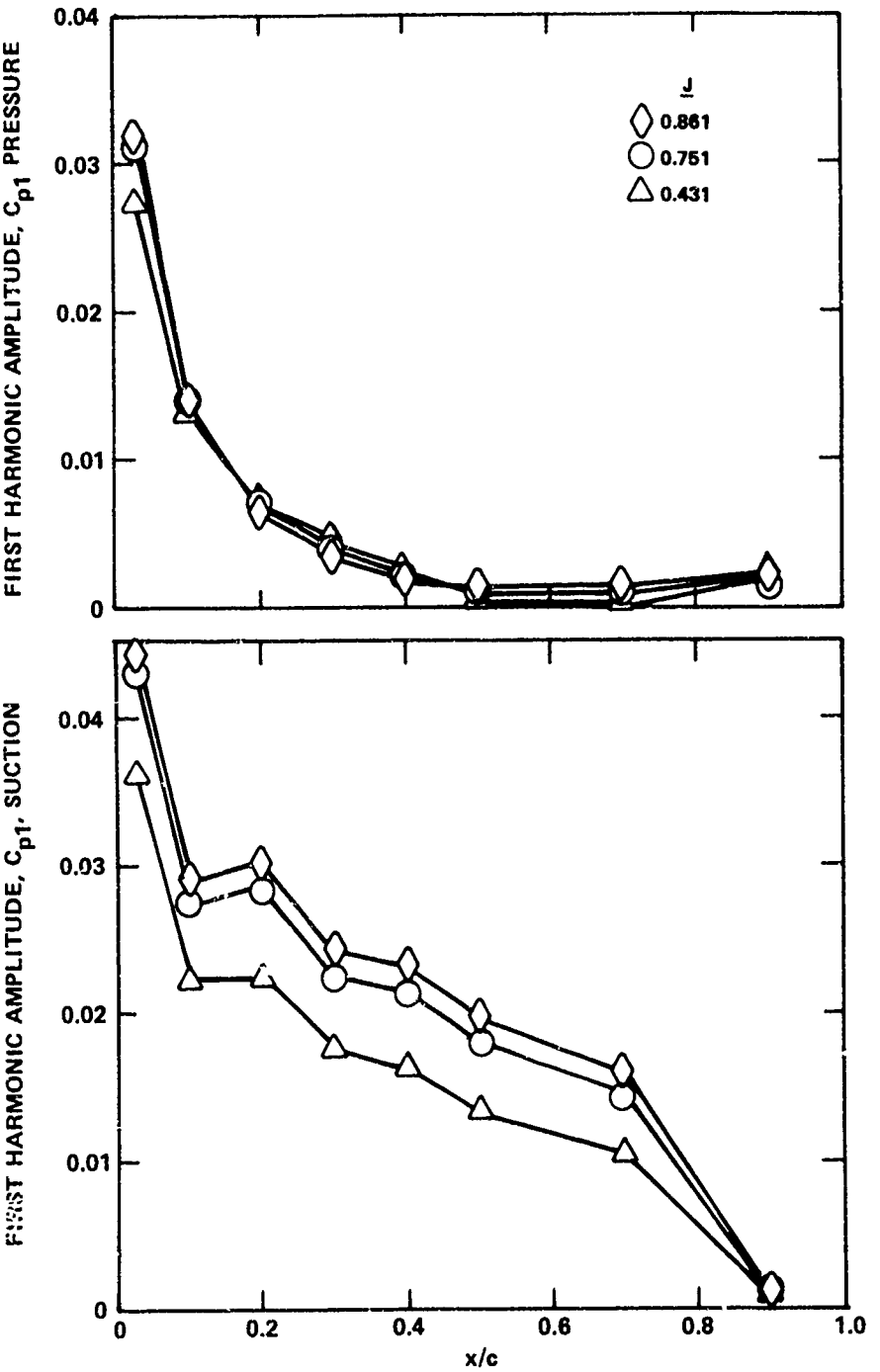

Figure 30b - r/R = 0.7

Figure 30 (Continued)

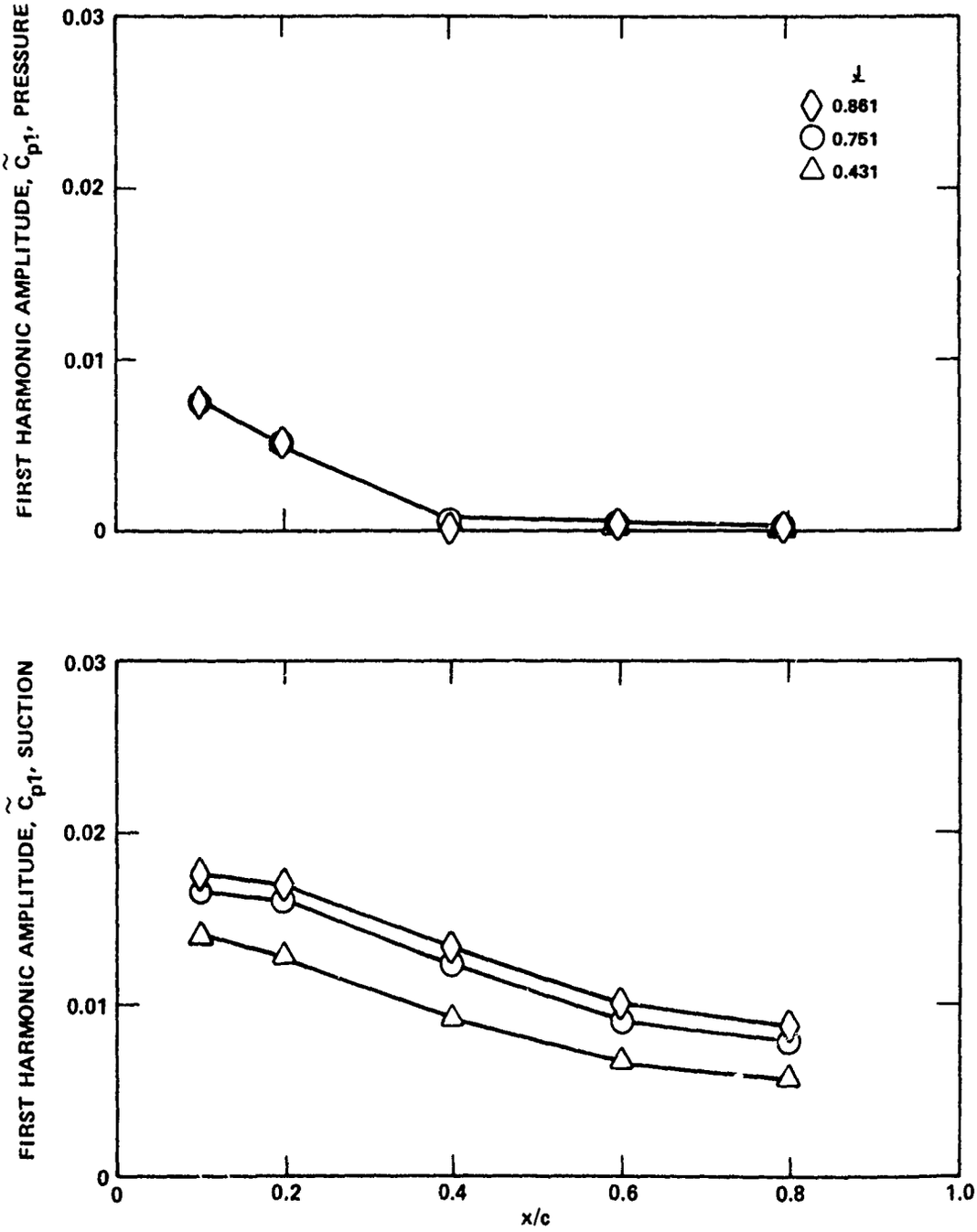

Figure 30c - r/R = 0.9

Figure 31 - Quasi-Steady Predictions of First Harmonic Pressure Coefficients for Propeller 4718 Inclined 7.5 Degrees Over a Range of J; Based on Second-Order Curve Fits of C_p versus J

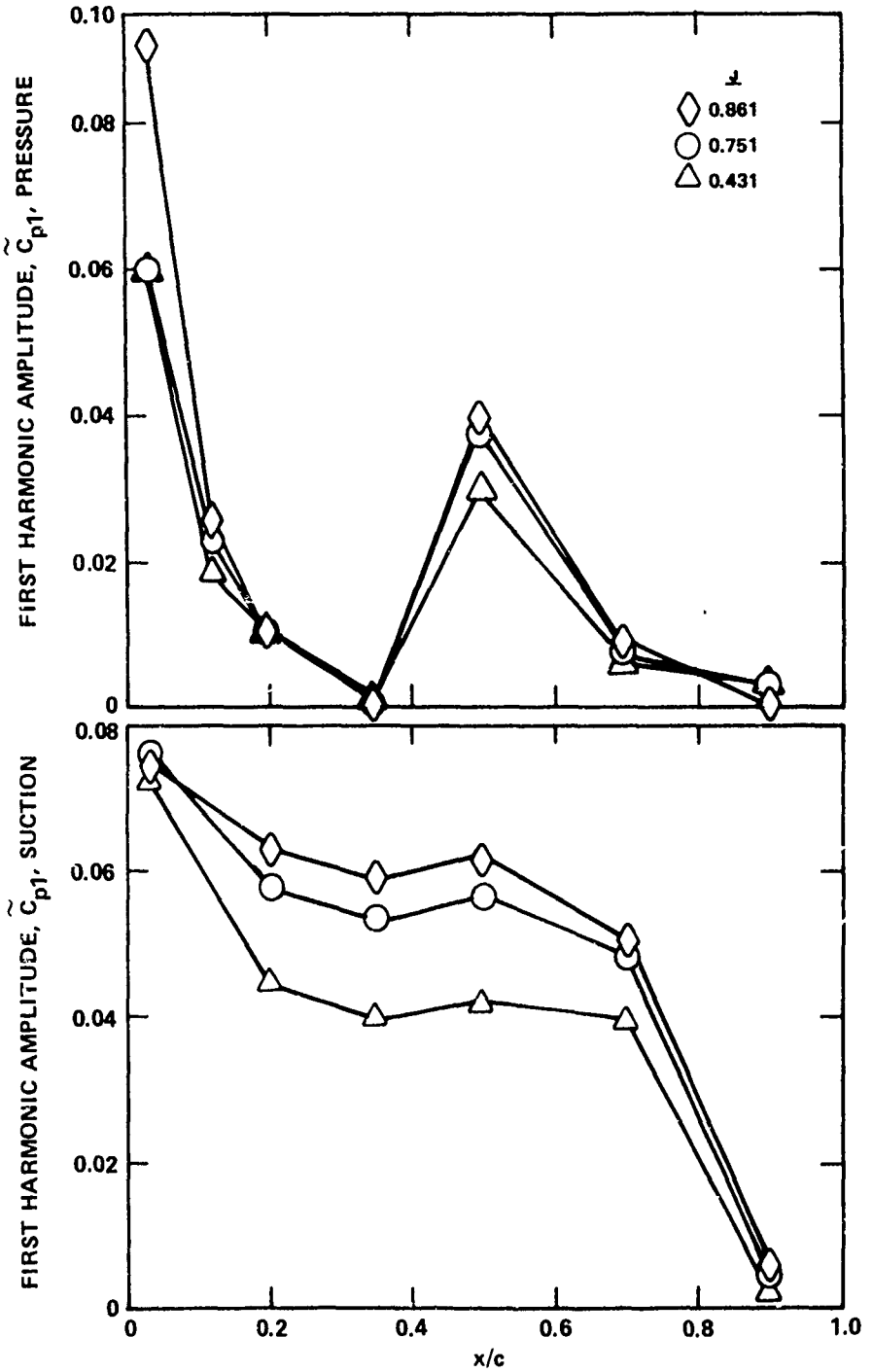

Figure 31a - r/R = 0.5

Figure 31 (Continued)

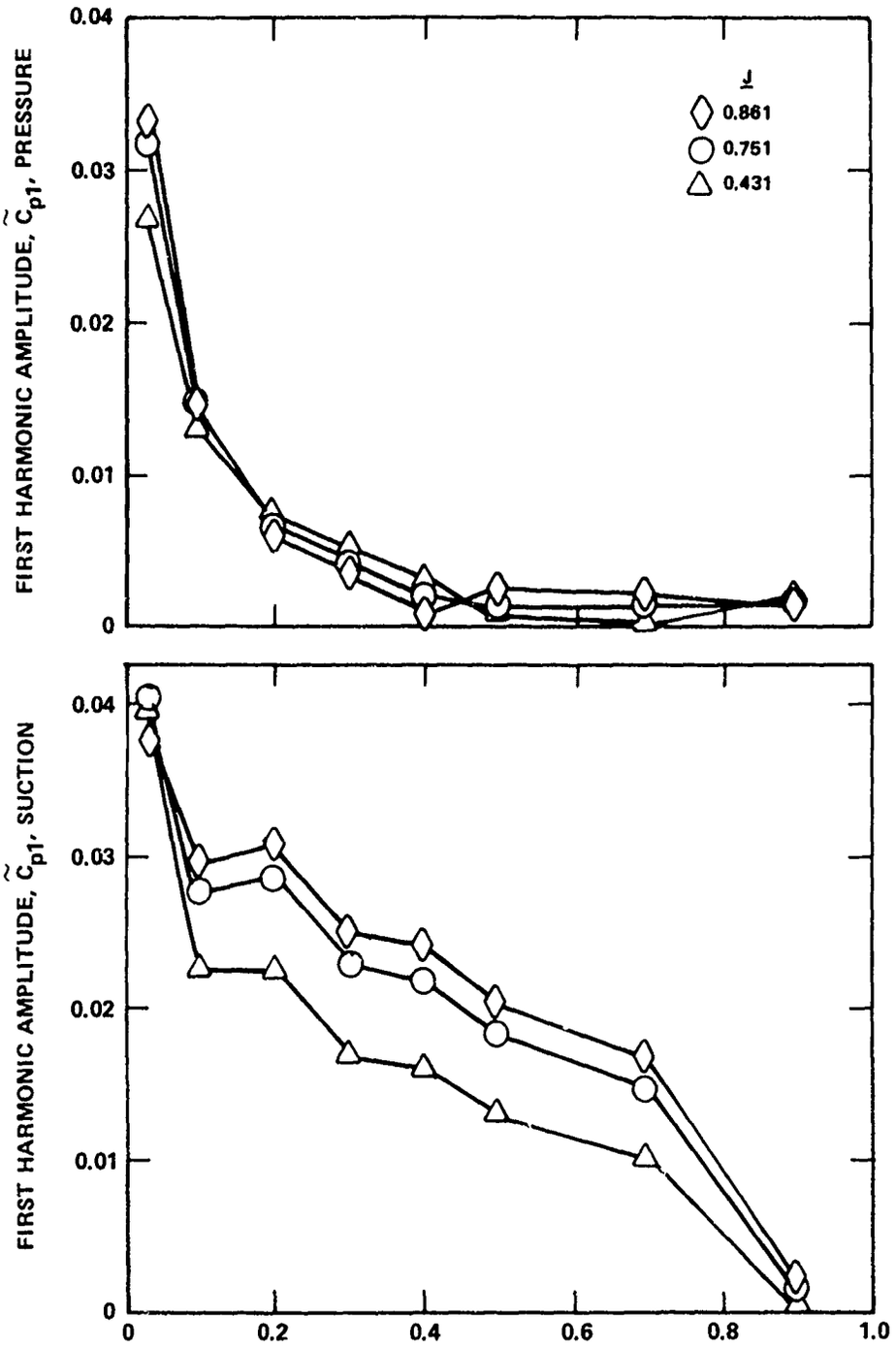

Figure 31b - r/R = 0.7

Figure 31 (Continued)

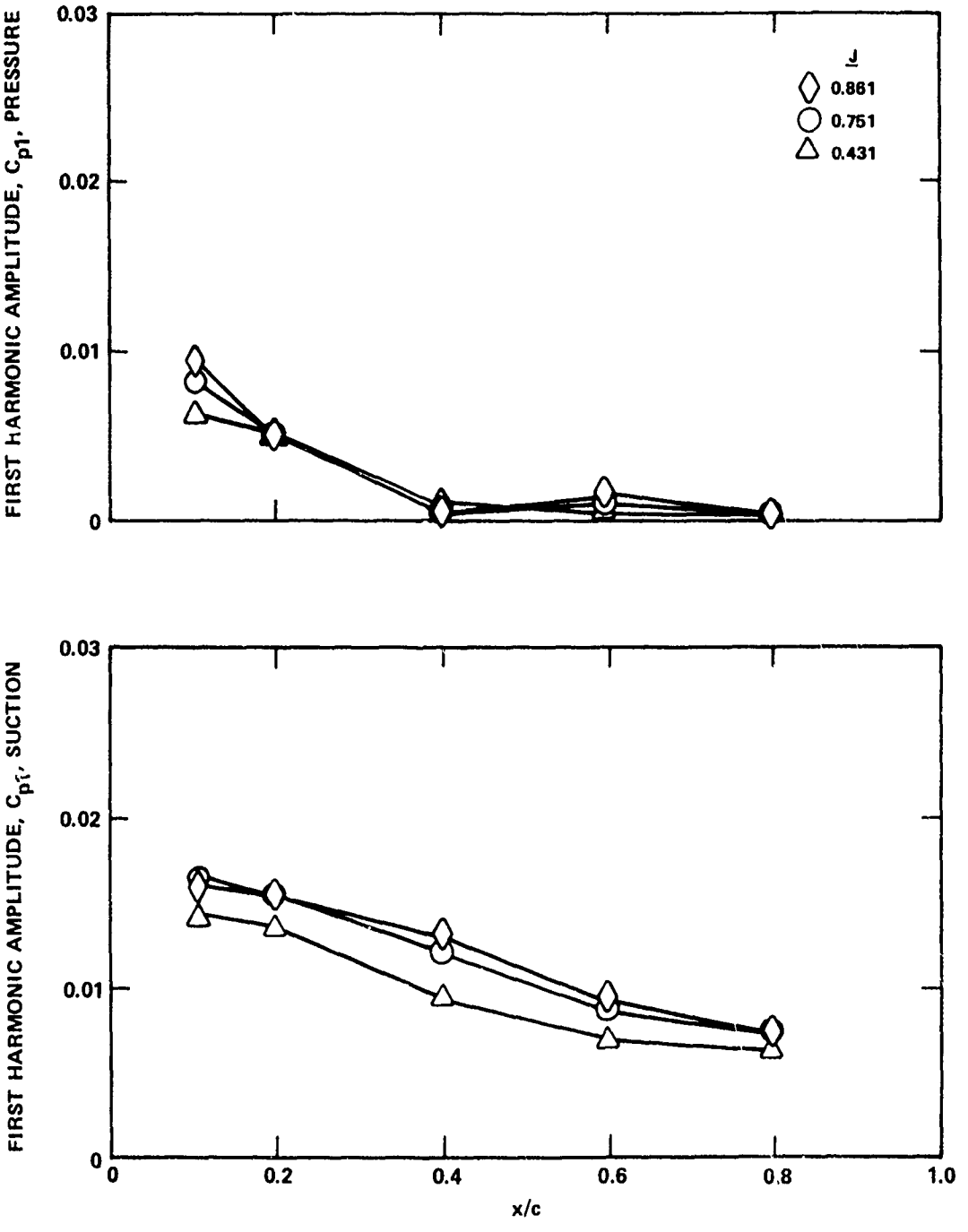

Figure 31c - r/R = 0.9

Figure 32 - Quasi-Steady Predictions of First Harmonic Pressure Coefficients for Propeller 4679 Inclined 7.5 Degrees Over a Range of J; Based on Second-Order Curve Fits of C_p versus J

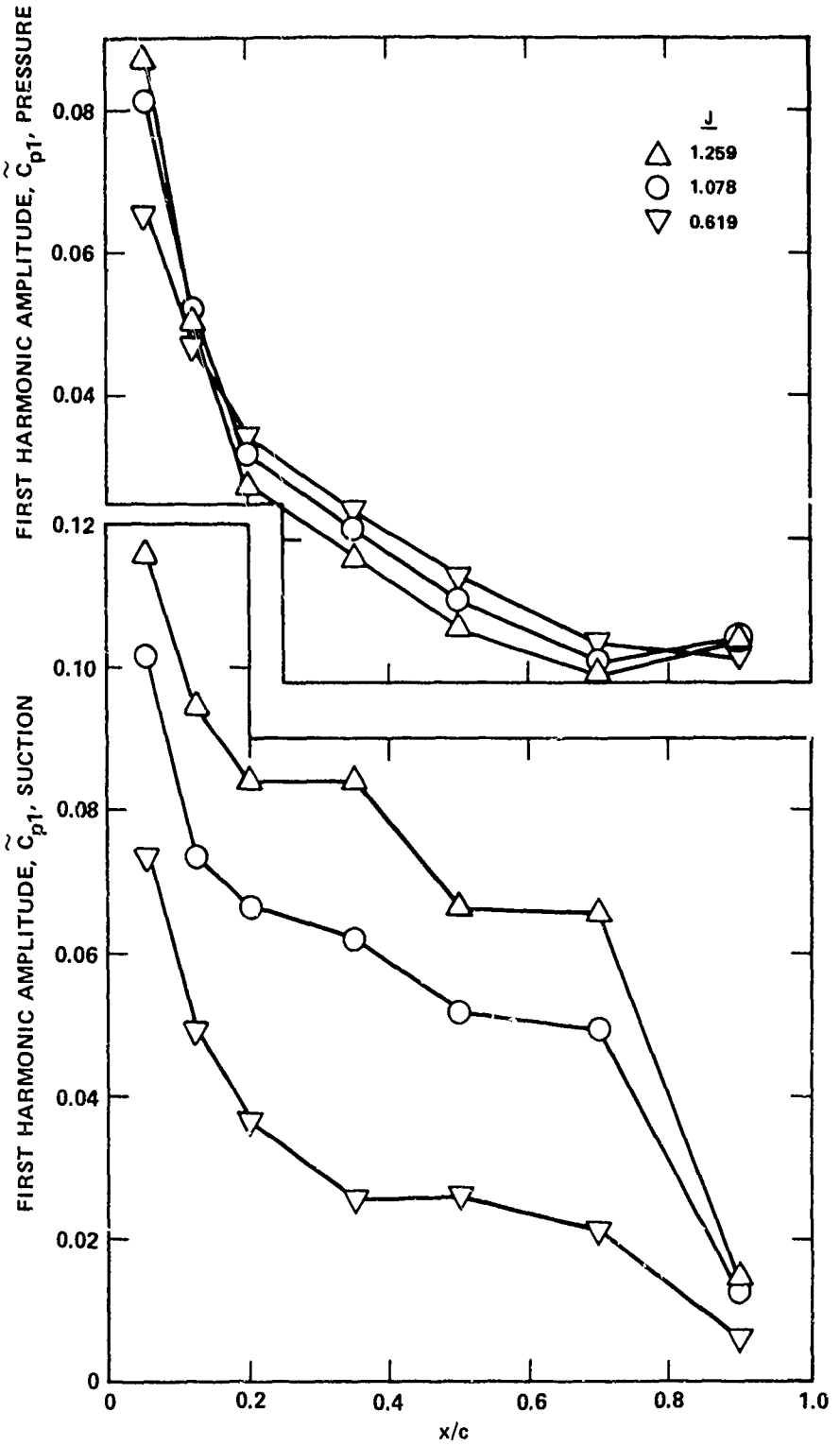

Figure 32a - r/R = 0.5

Figure 32 (Continued)

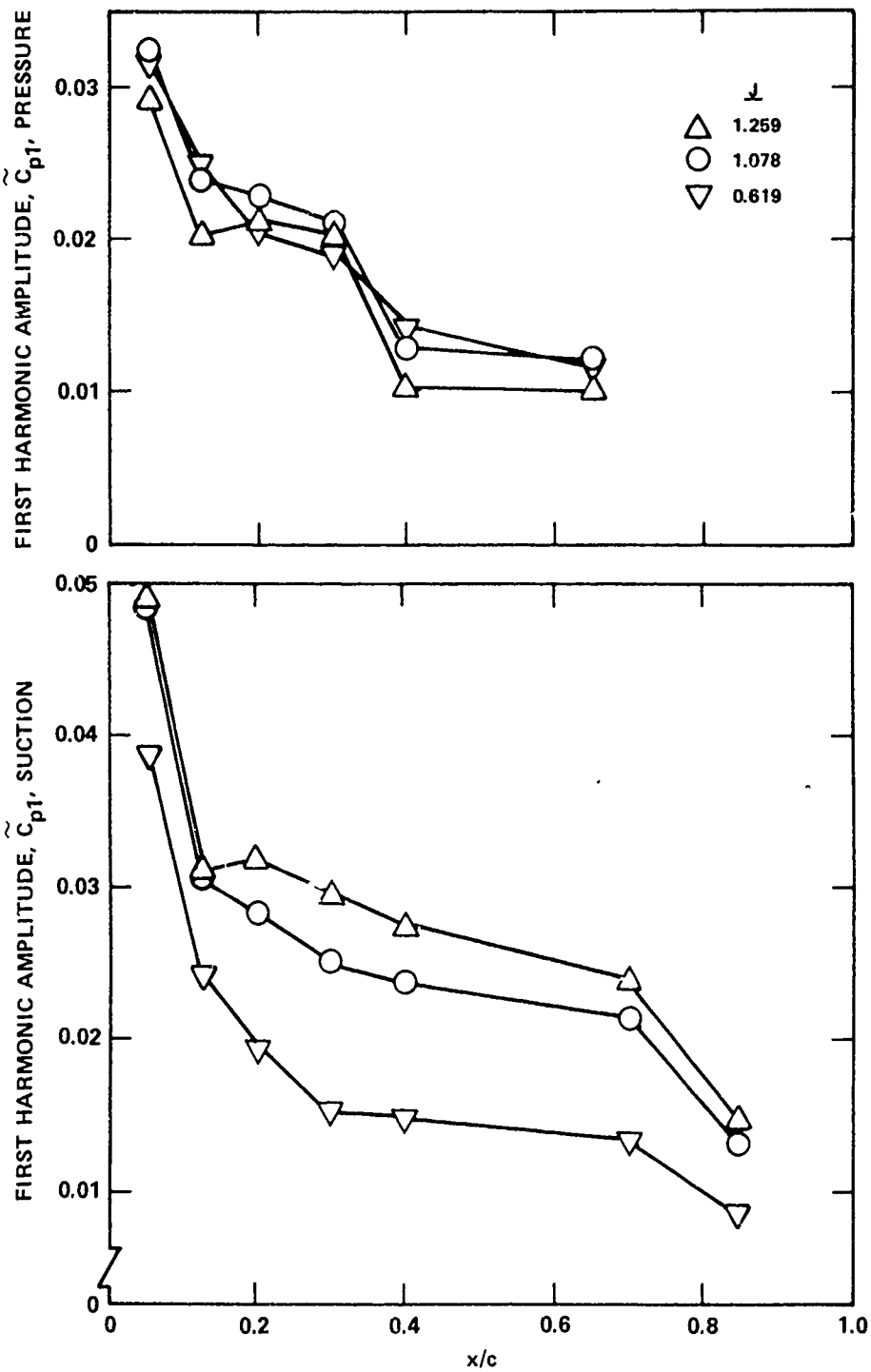

Figure 32b - r/R = 0.7

Figure 32 (Continued)

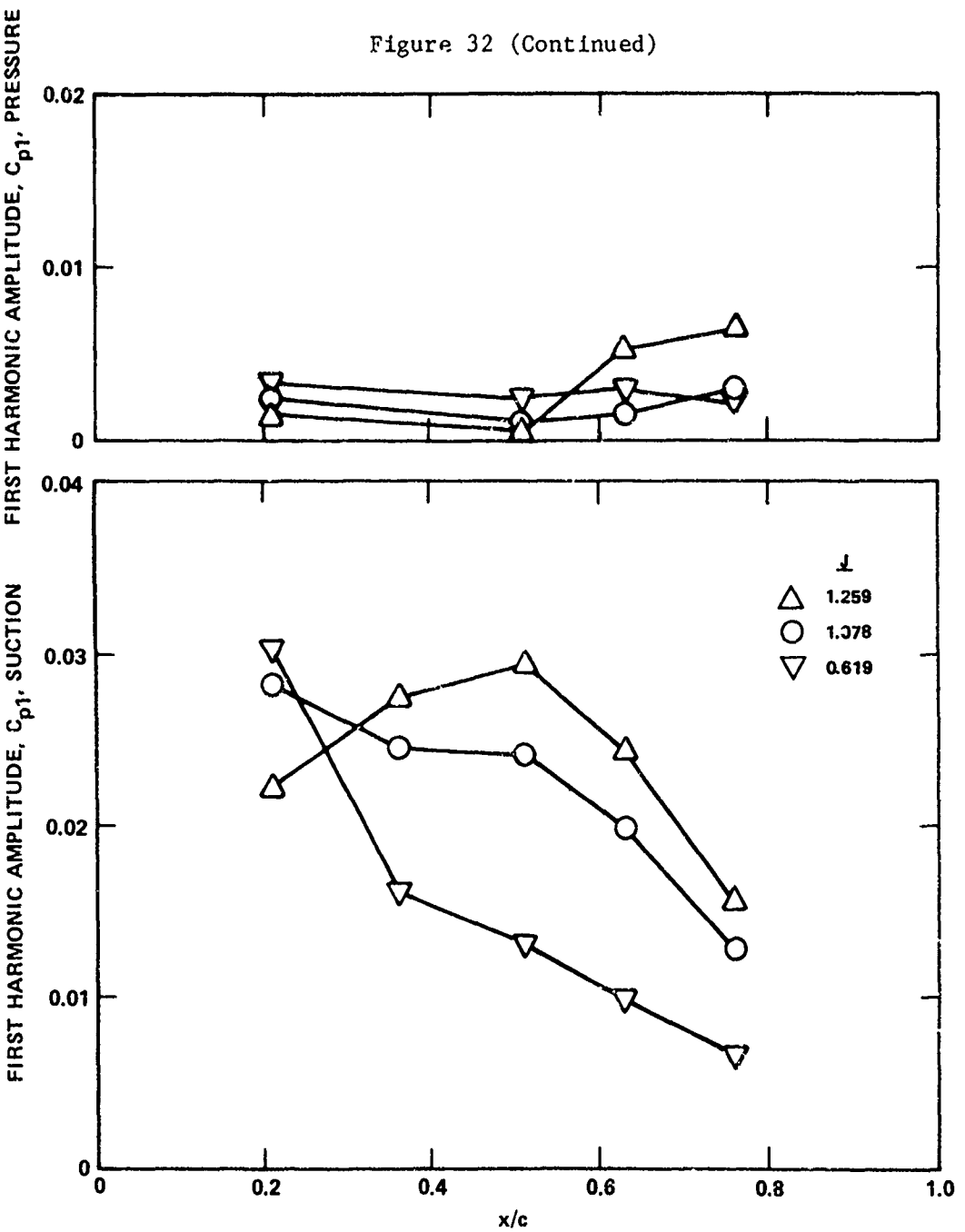

Figure 32c - r/R = 0.9

Figure 33a - Laboratory Arrangement

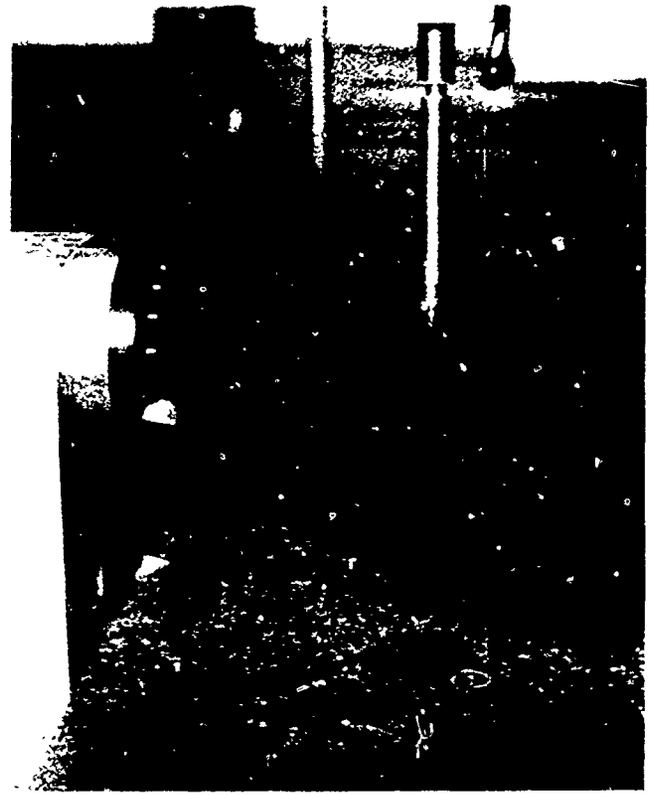

Figure 33b - Blade Mounted in Fixture

Figure 33 - Blade Measuring Arrangement

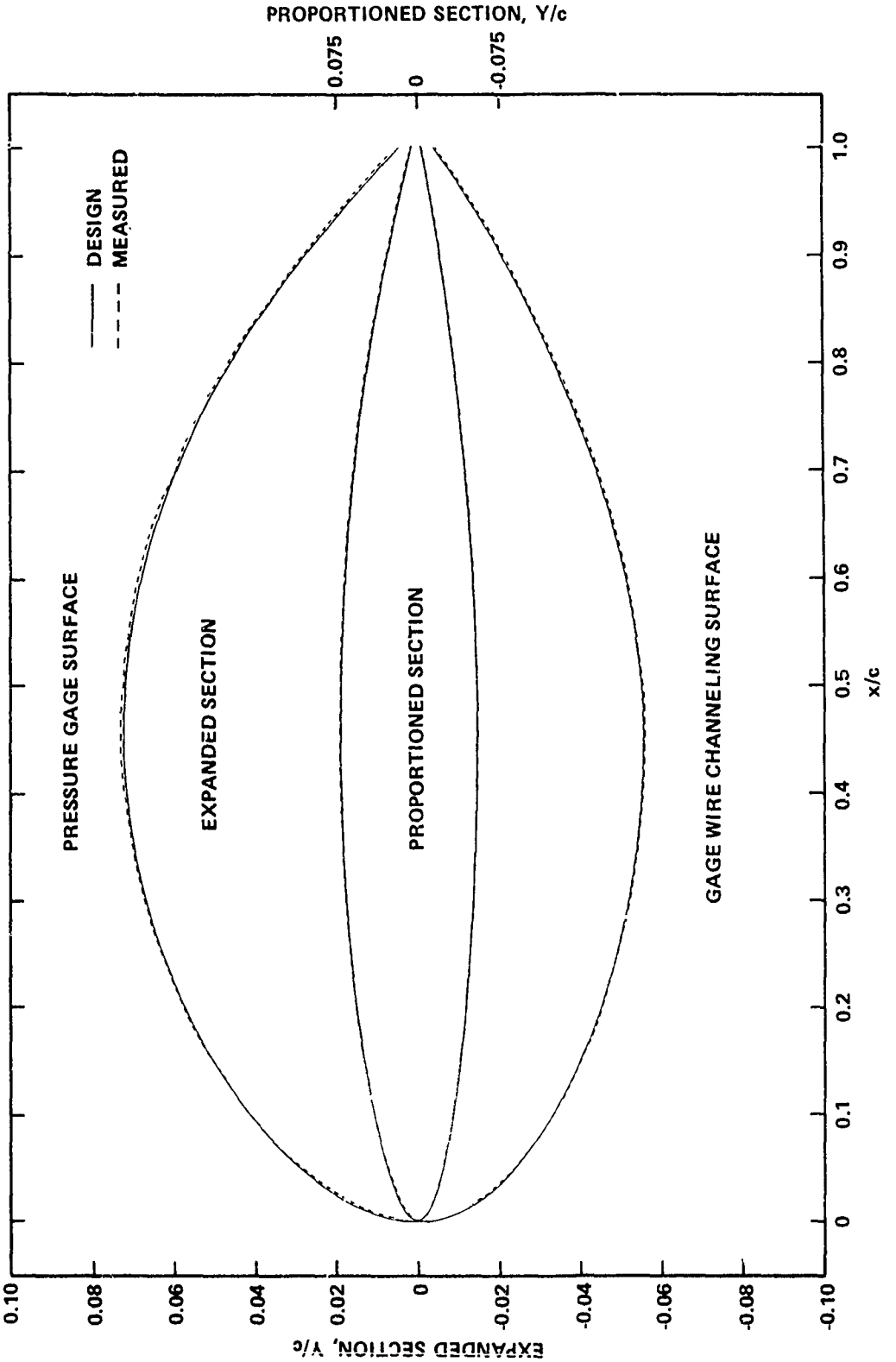

Figure 34 - Comparison of Measured and Design Blade Section Offsets

Figure 34a - r/R = 0.5, Blade C, Gages on the Suction Side

Figure 34 (Continued)

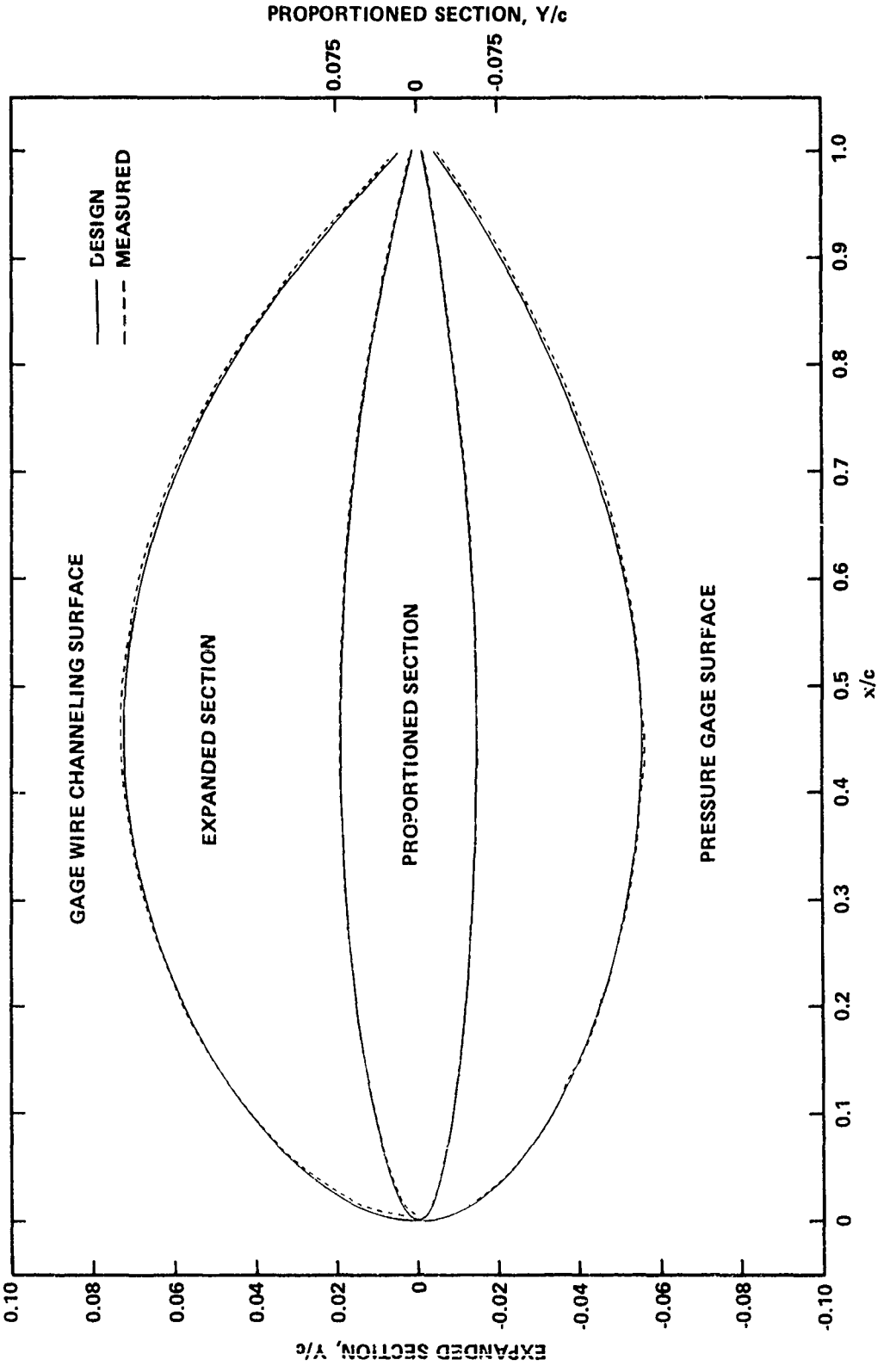

Figure 34b - r/R = 0.5, Blade B, Gages on Pressure Side

Figure 34 (Continued)

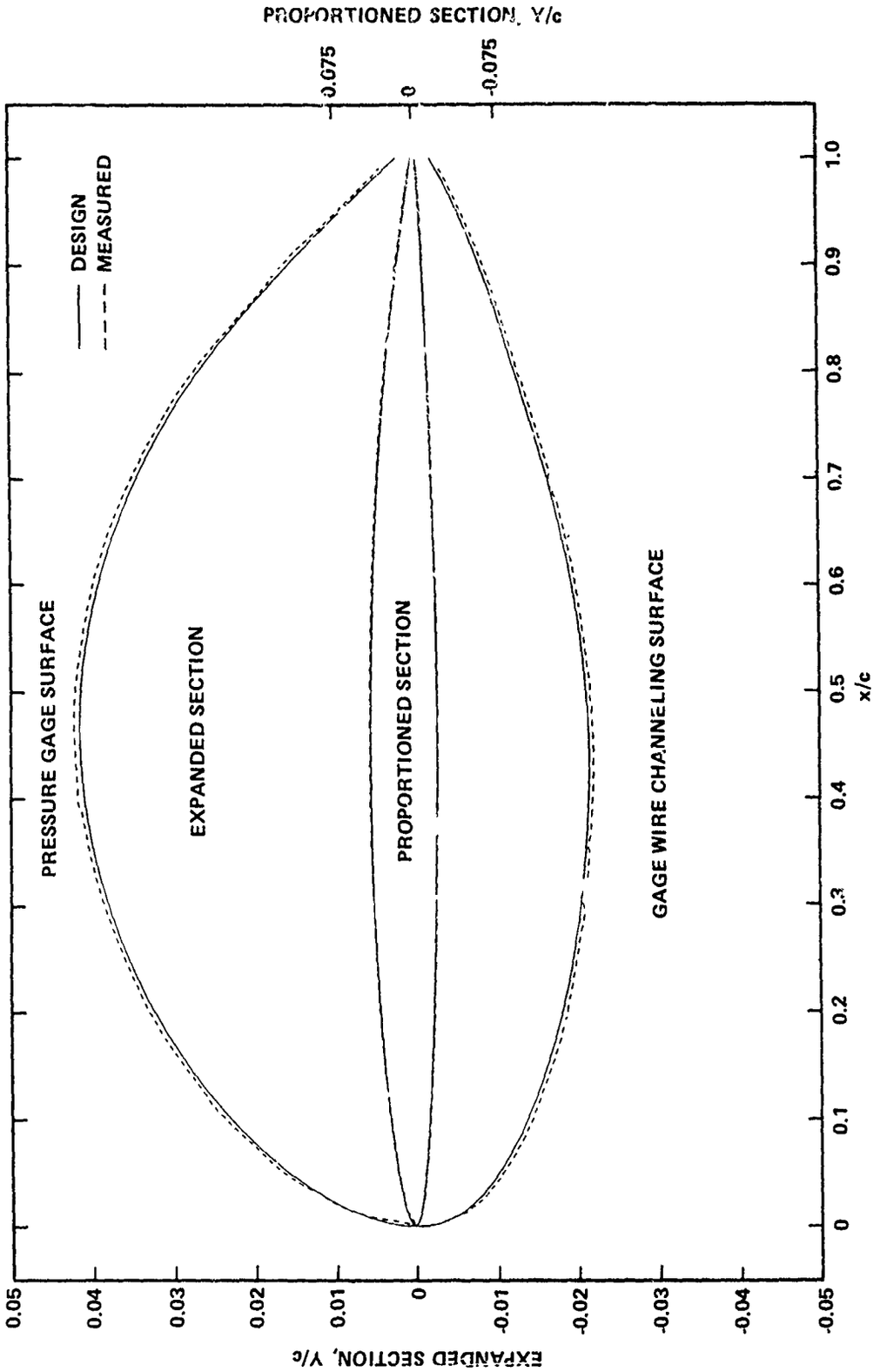

Figure 34c - r/R = 0.7, Blade C, Gages on Suction Side

Figure 34 (Continued)

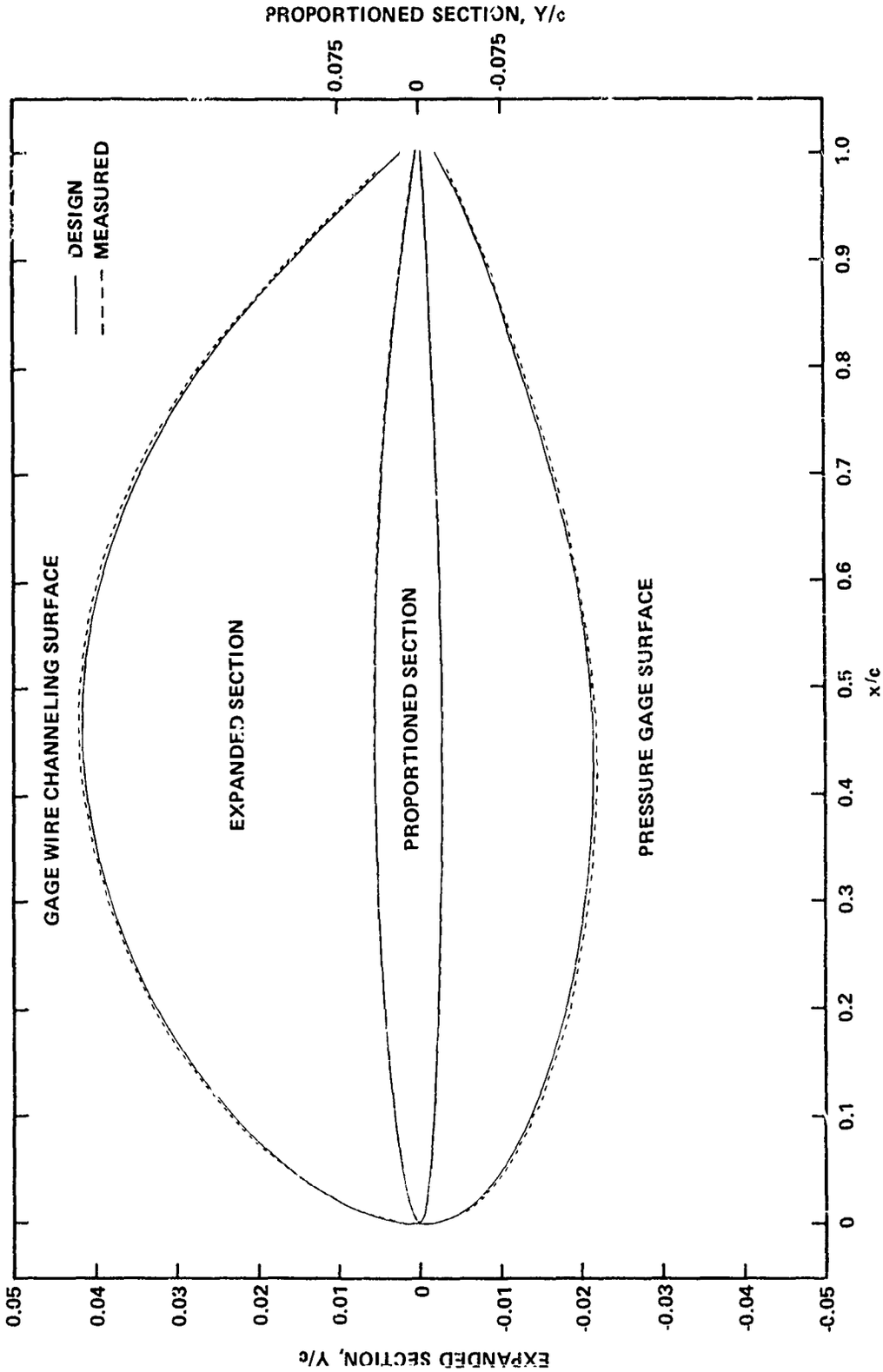

Figure 34d - r/R = 0.7, Blade B, Gages on Pressure Side

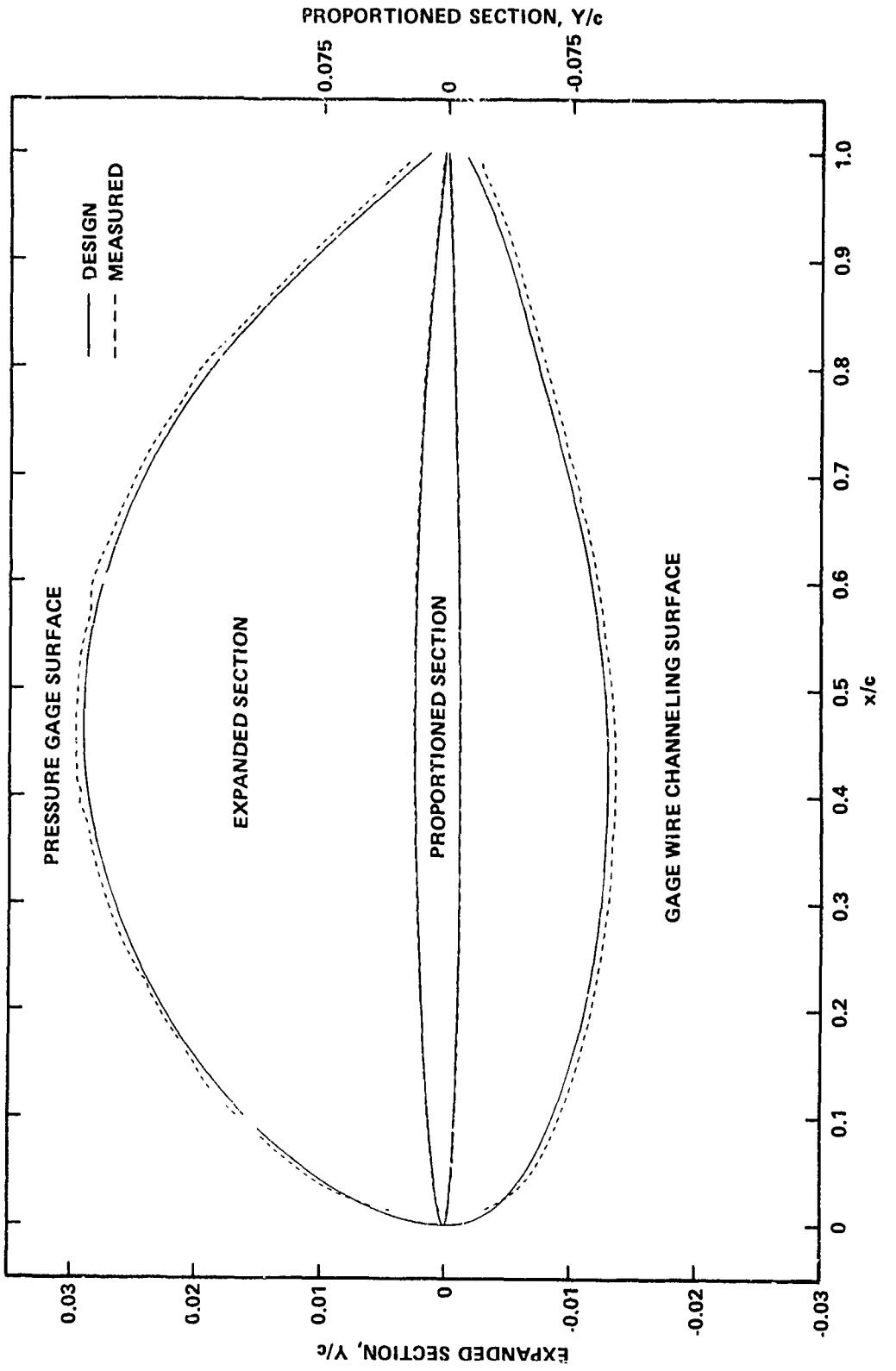

Figure 34 (Continued)

Figure 34e - r/R = 0.9, Blade C, Gages on Suction Side

Figure 34 (Continued)

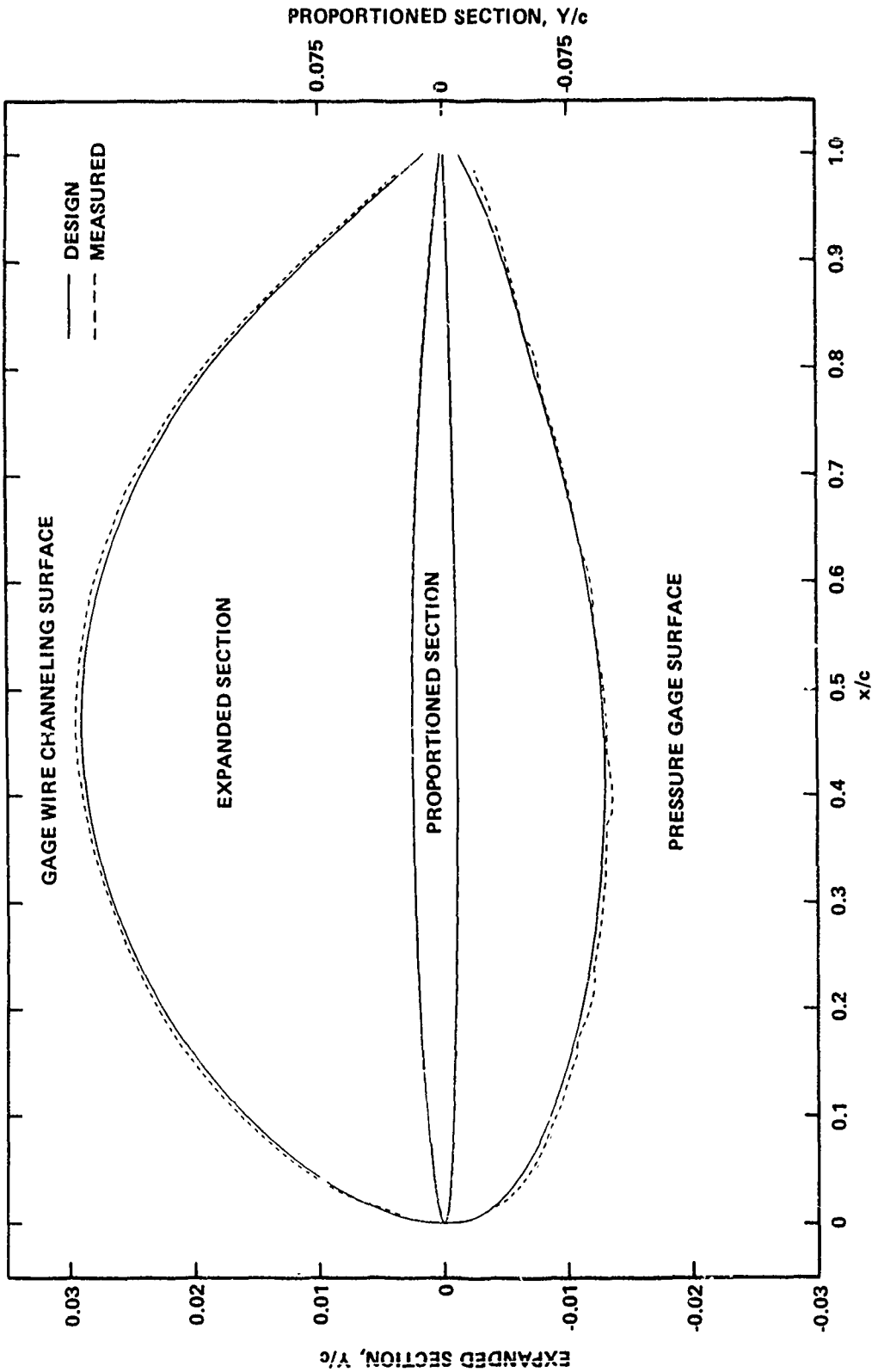

Figure 34f - r/R = 0.9, Blade B, Gages on Pressure Side

Figure 35 - Details of Leading Edges Produced from Interpolation of Measured Offsets

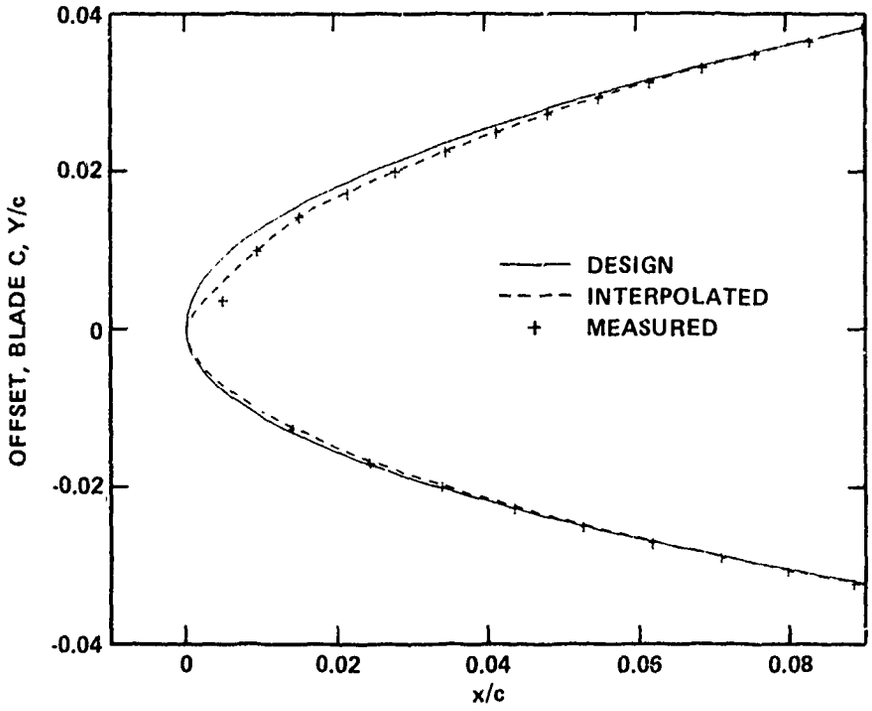

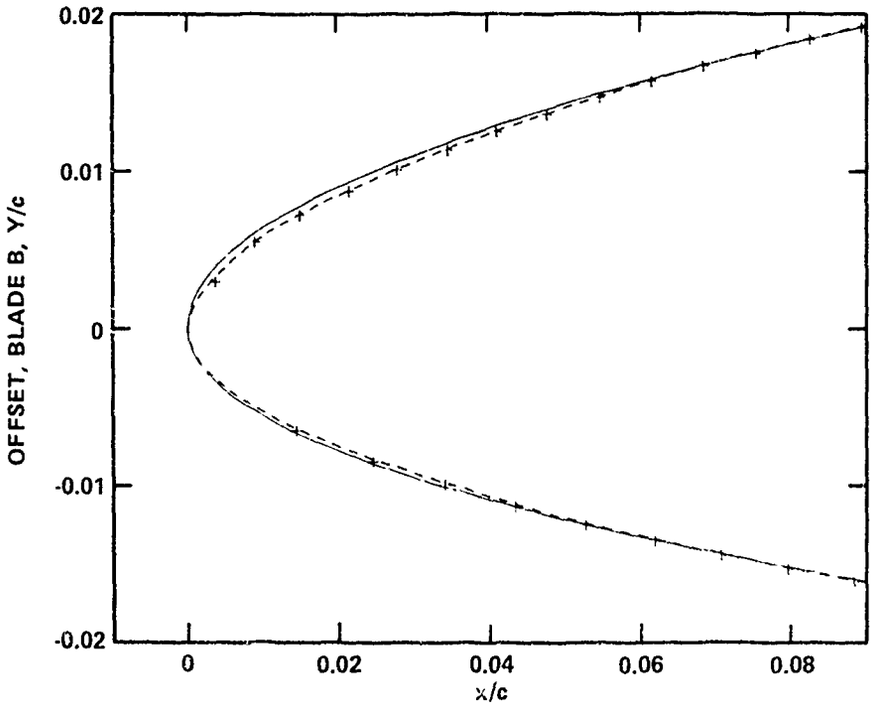

Figure 35a - r/R = 0.5

Figure 35 (Continued)

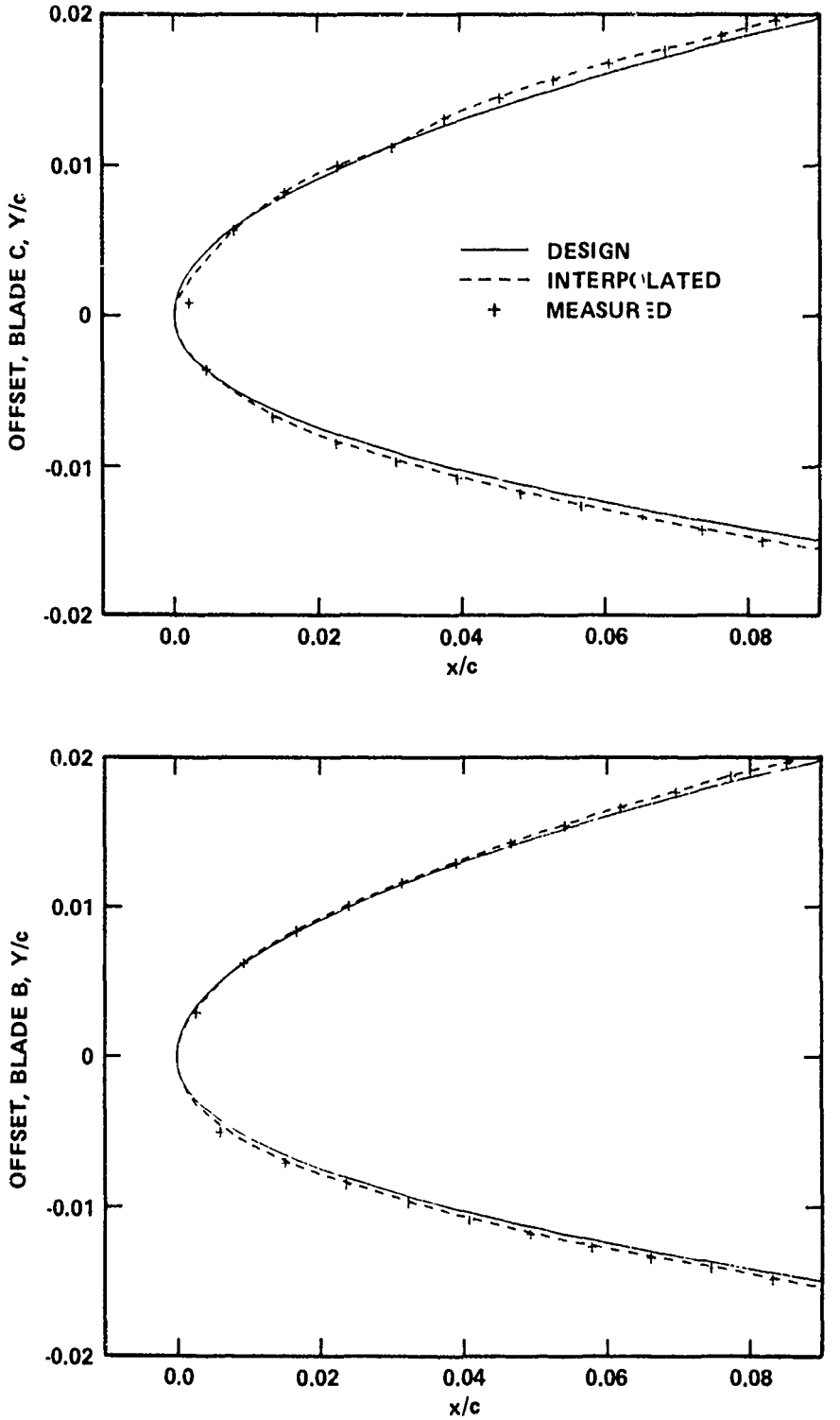

Figure 35b - r/R = 0.7

Figure 35 (Continued)

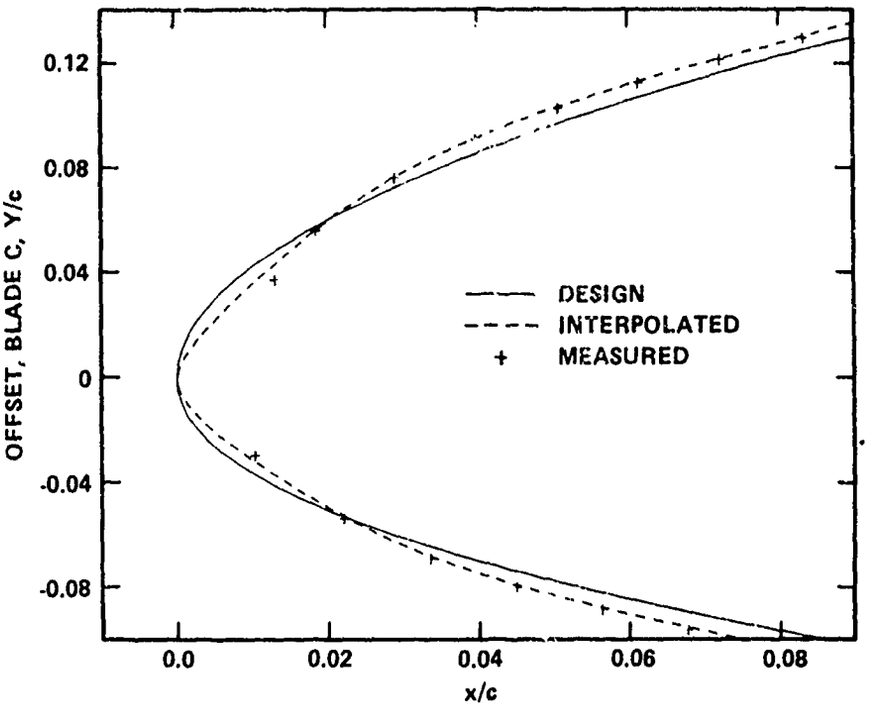

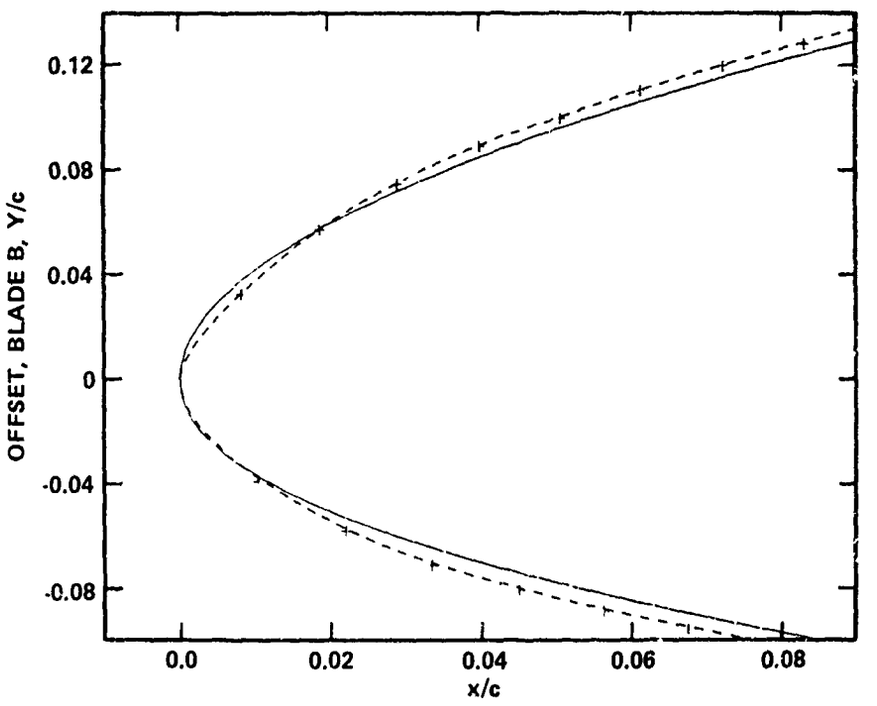

Figure 35c - r/R = 0.9

Figure 36 - Modification of Pressure Side Trailing Edges on Interpolated Offsets

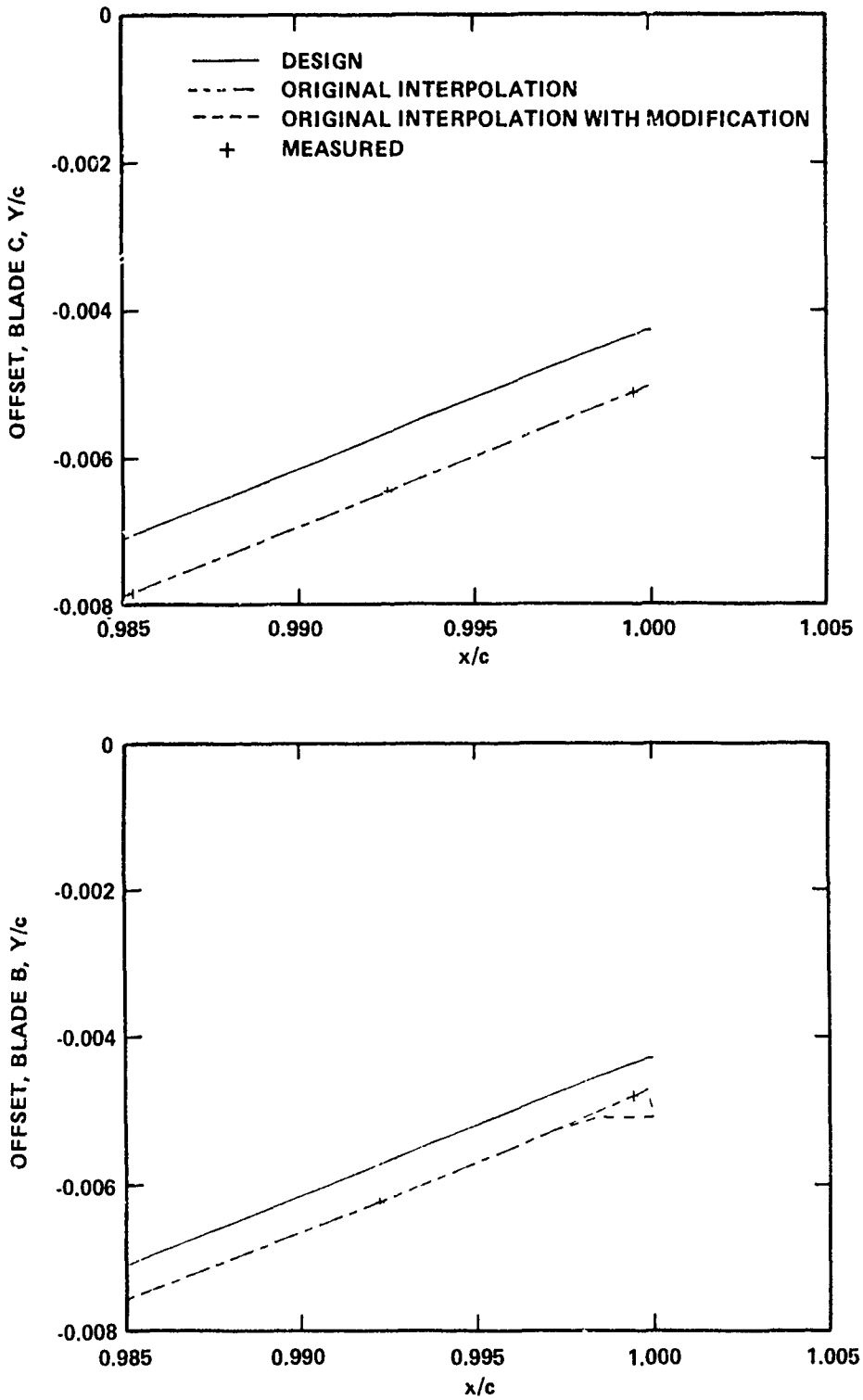

Figure 36a - r/R = 0.5

Figure 36 (Continued)

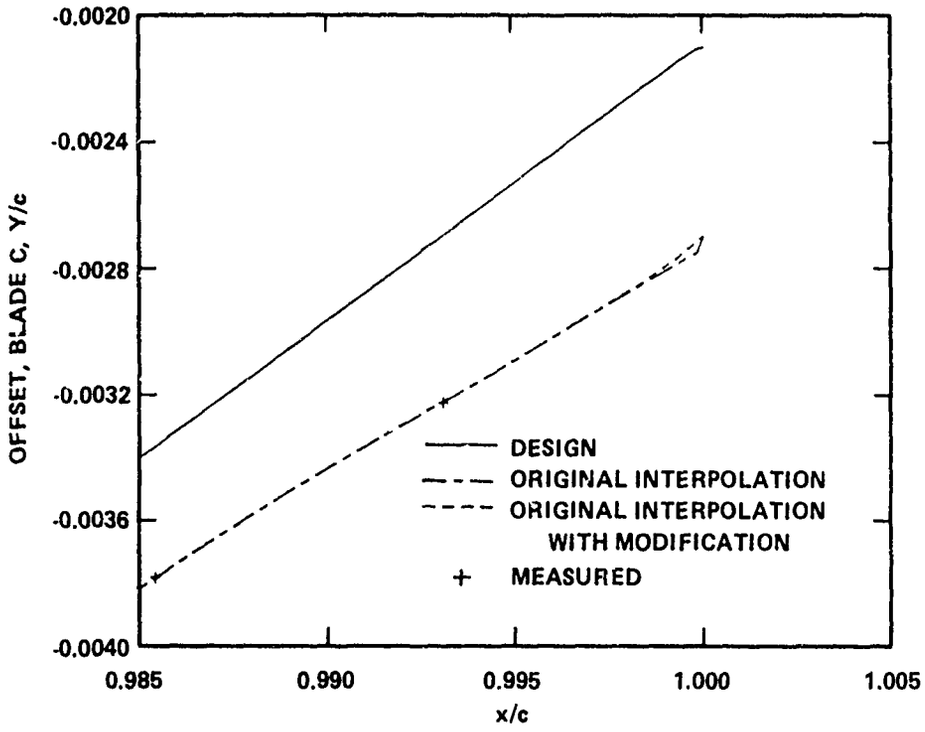

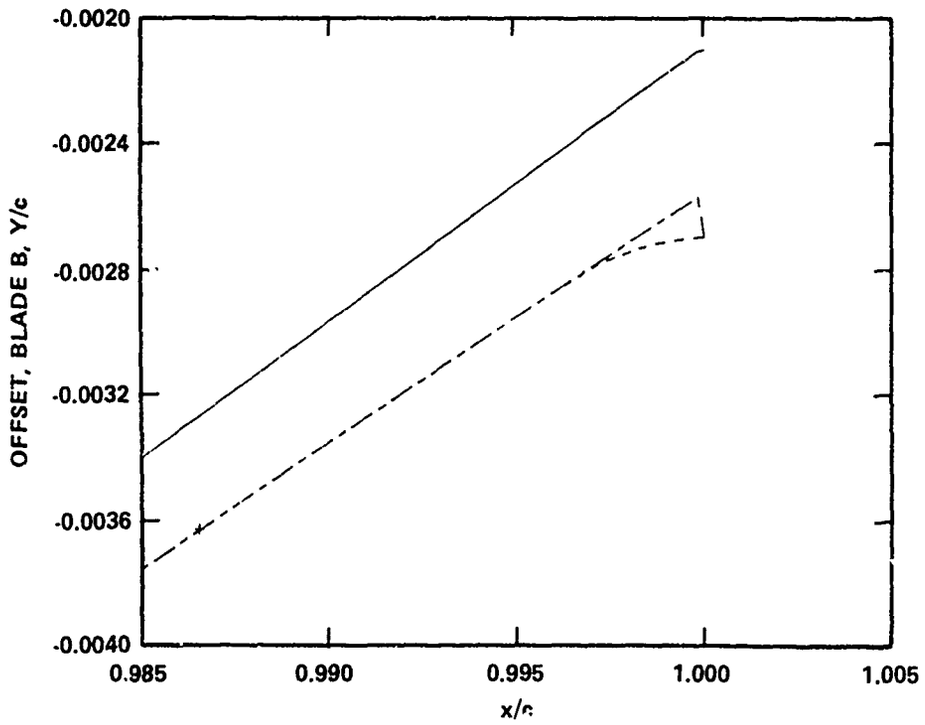

Figure 36b - r/R = 0.7

Figure 36 (Continued)

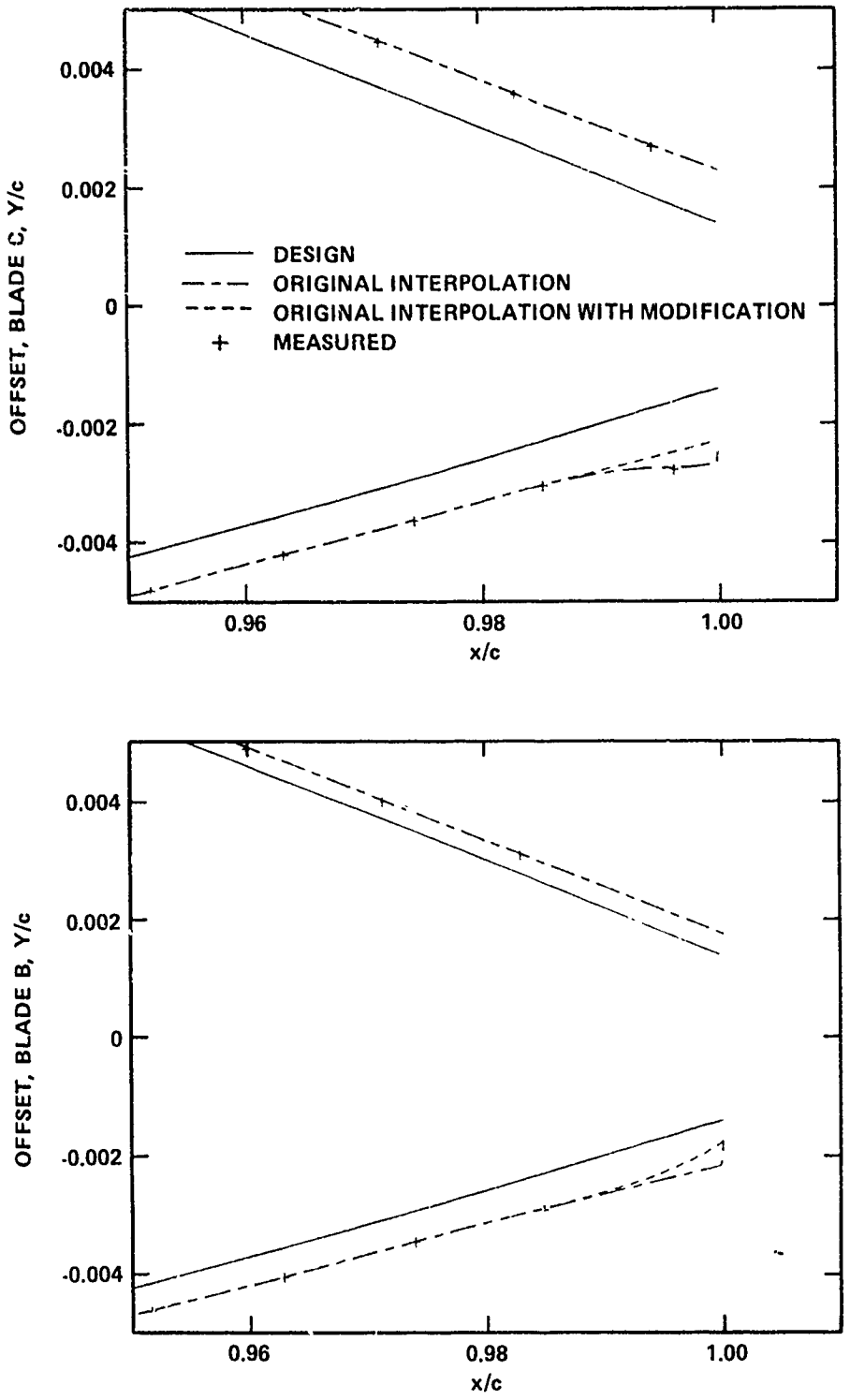

Figure 36c - r/R = 0.9

Figure 37 - Comparison of Pressure Distributions for Measured and Design Offsets

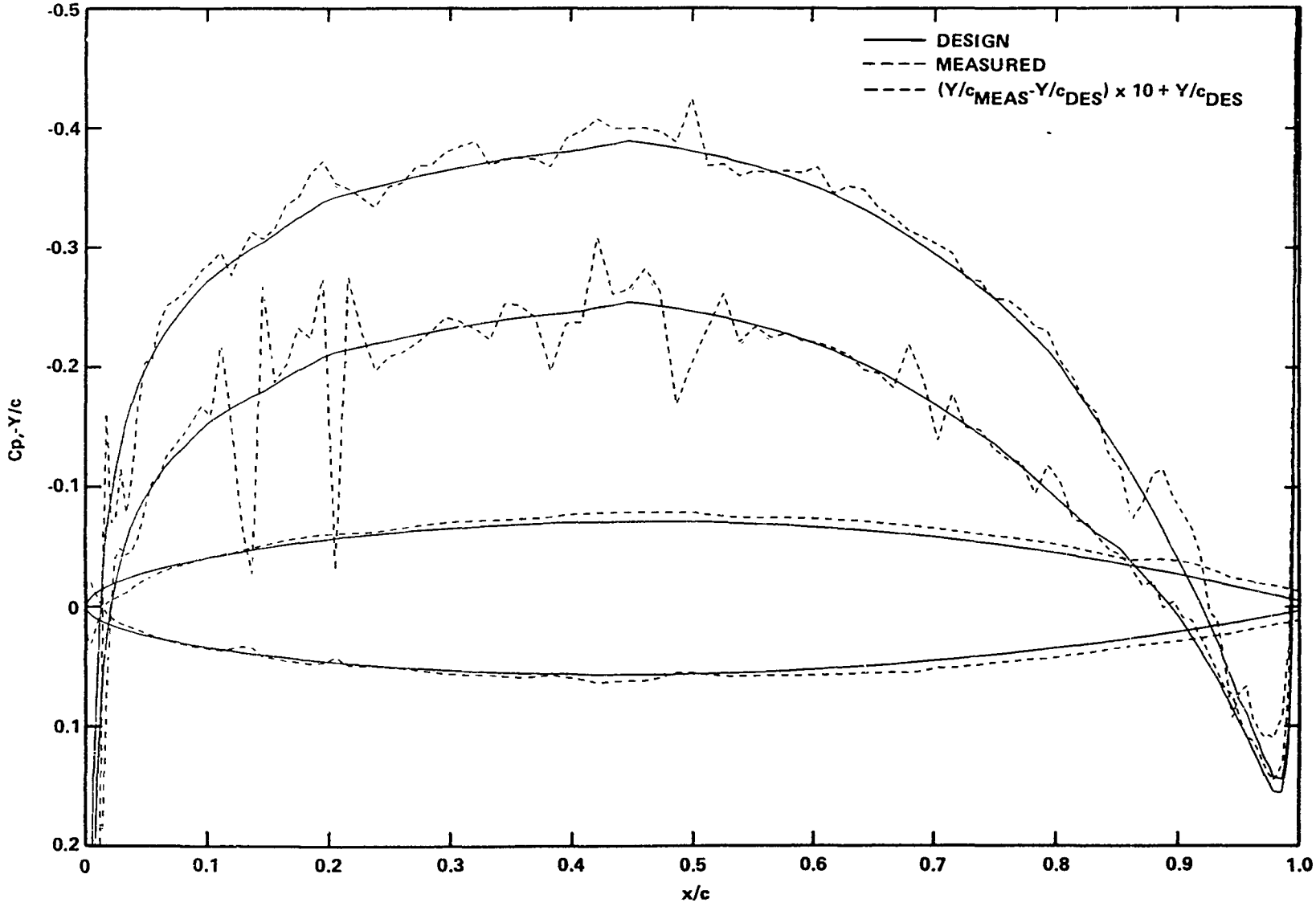

Figure 37a - r/R = 0.5, Blade C, Gages on Suction Side

Figure 37 (Continued)

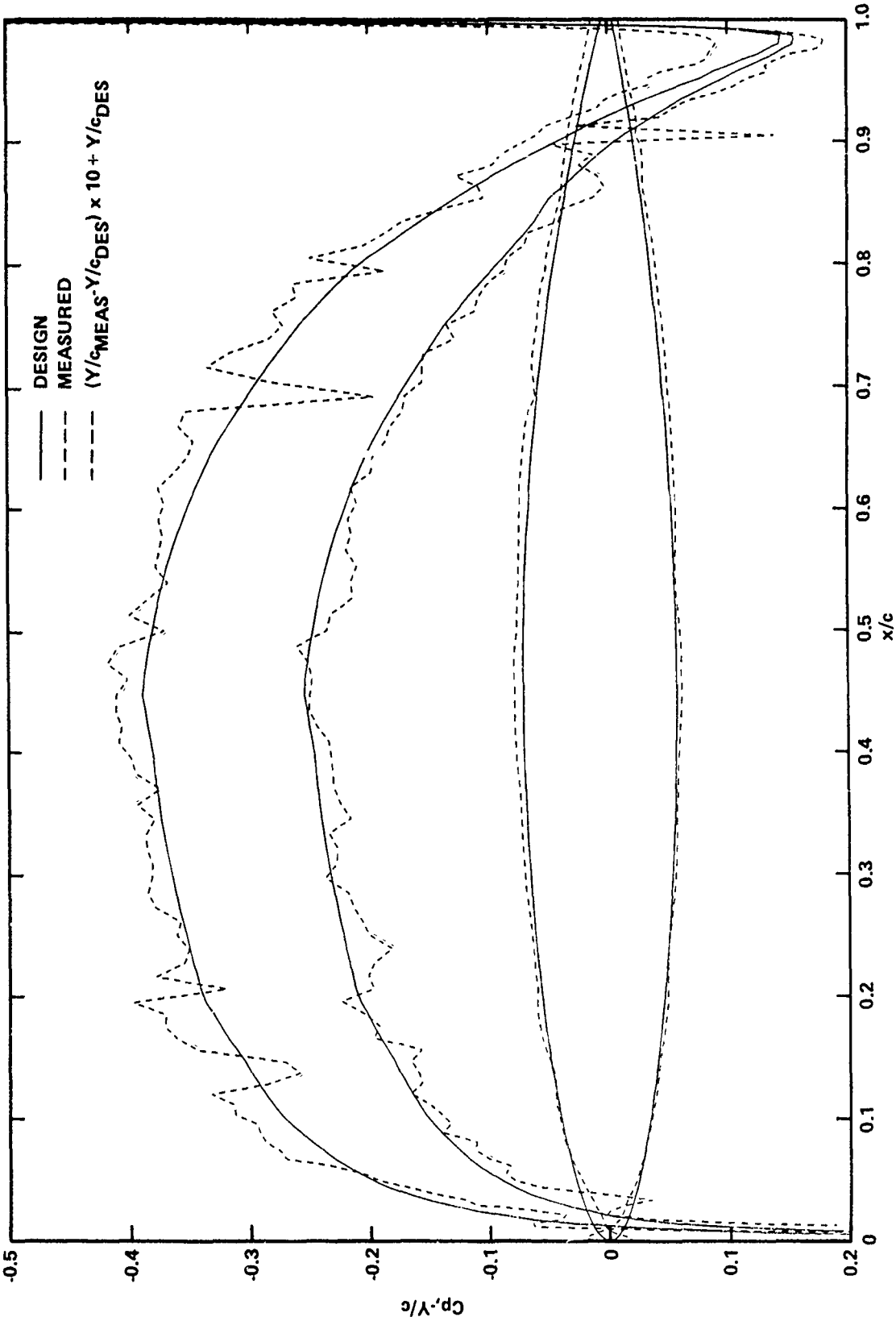

Figure 37b - $r/R = 0.5$, Blade B, Gages on Pressure Side

Figure 37 (Continued)

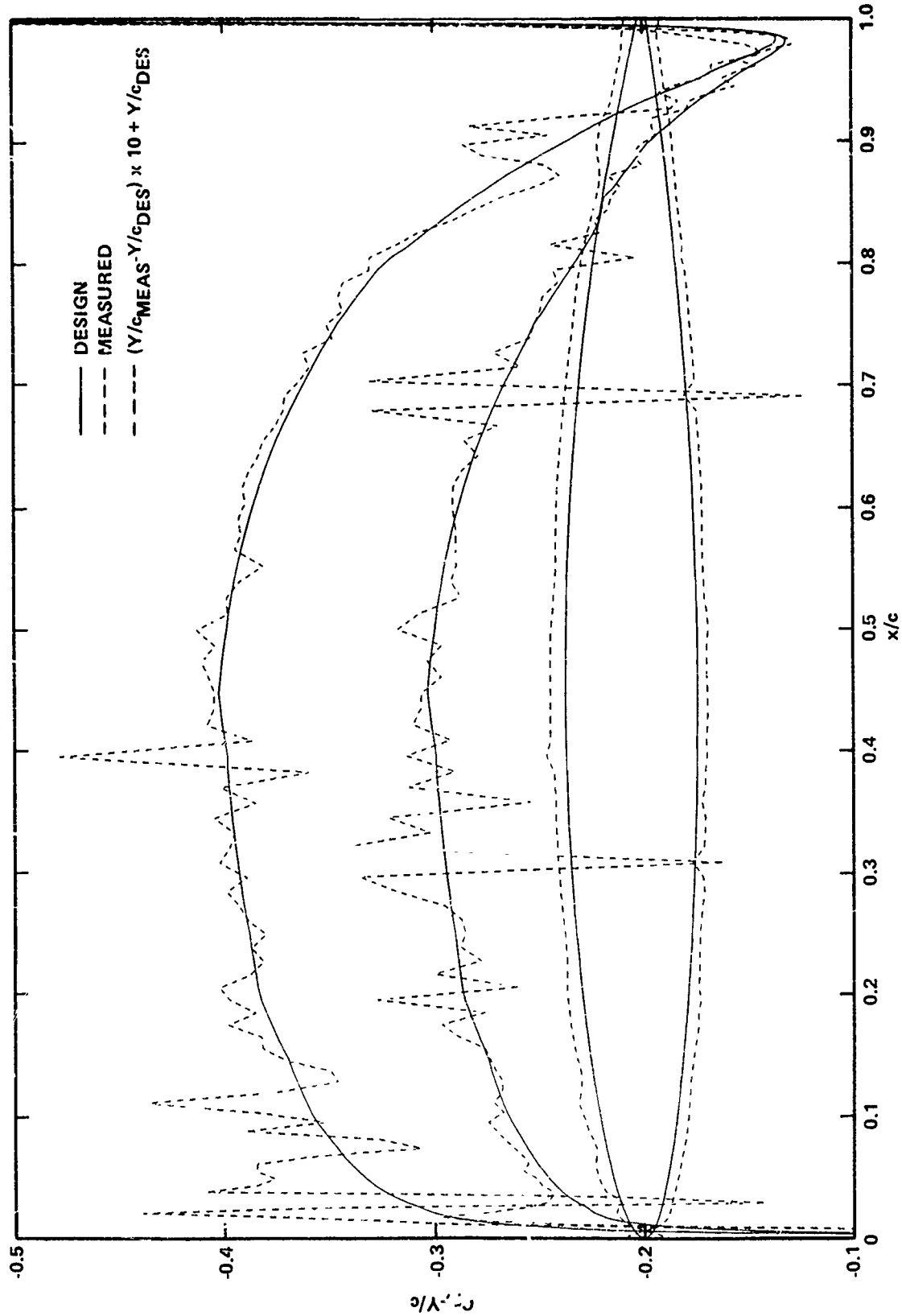

Figure 37c - r/R = 0.7, Blade C, Gates on Suction Side

Figure 37 (Continued)

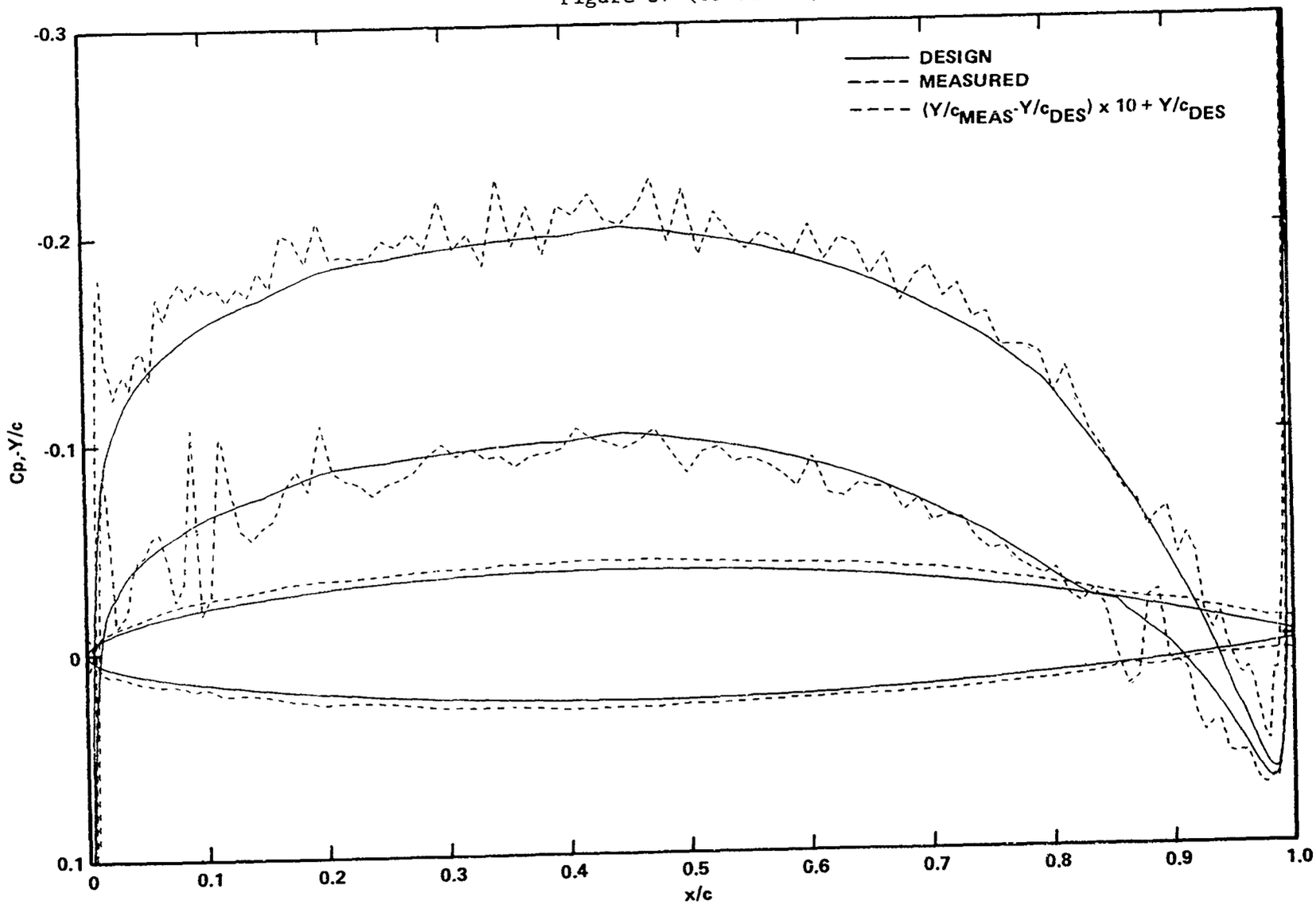

Figure 37d - r/R = 0.7, Blade B, Gages on Pressure Side

Figure 37 (Continued)

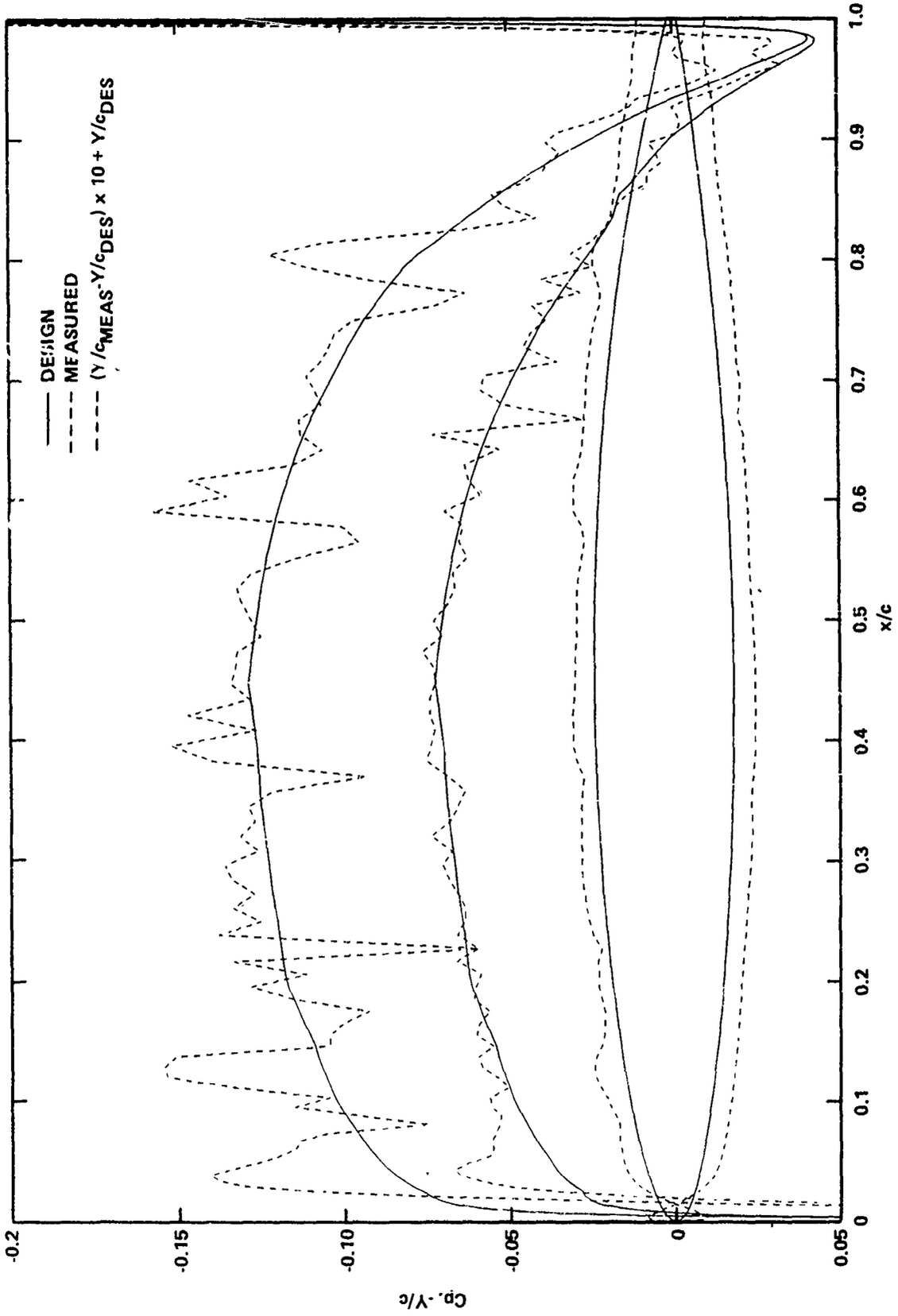

Figure 37e - r/R = 0.9, Blade C, Gages on Suction Side

Figure 37 (Continued)

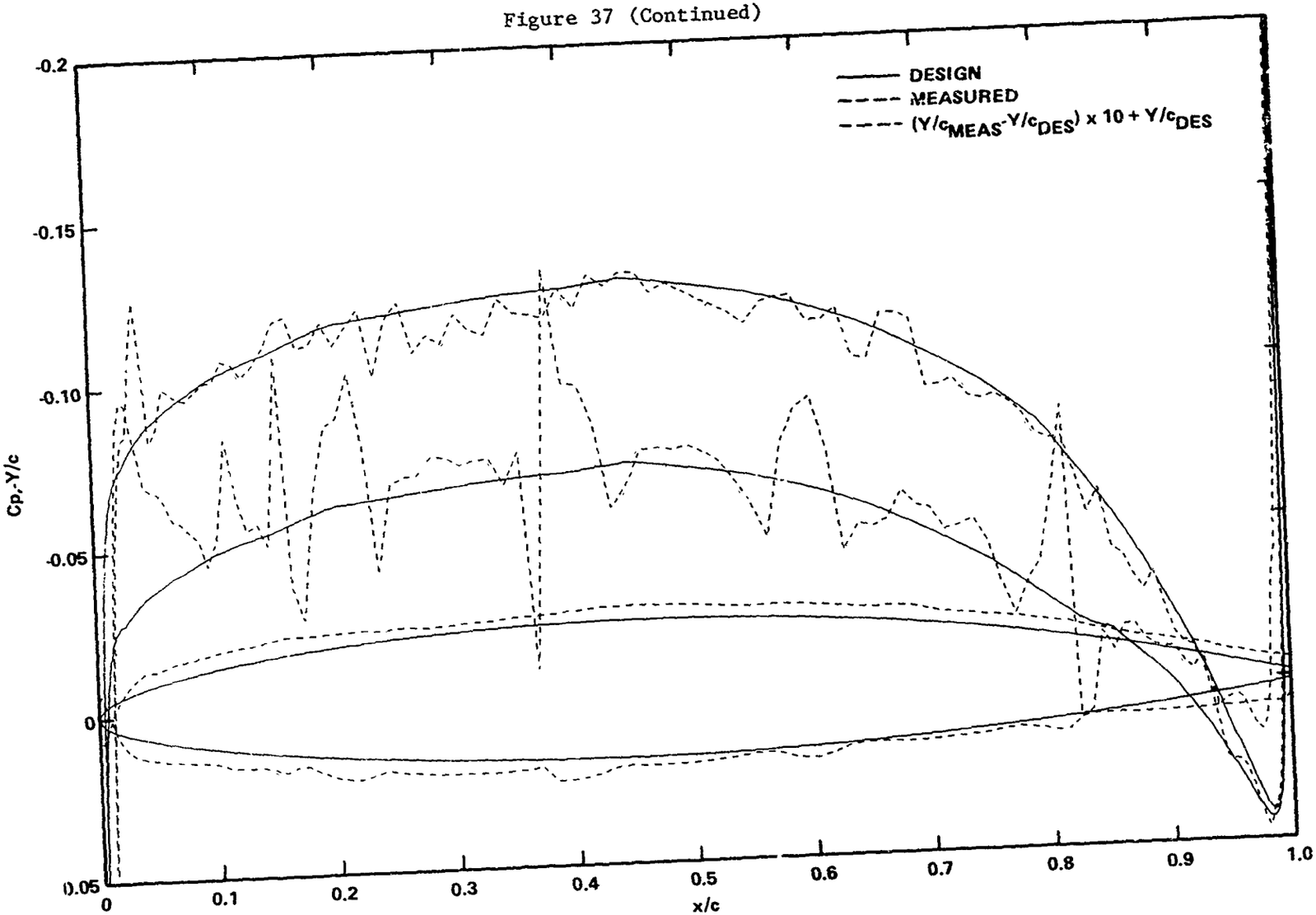

Figure 37f - r/R = 0.9, Blade B, Gages on Pressure Side

Figure 38 - Comparison of Measured Section Offsets to Series Representation
Used for Calculation of Predicted Pressure Distribution,
Blade C, r/R = 0.9

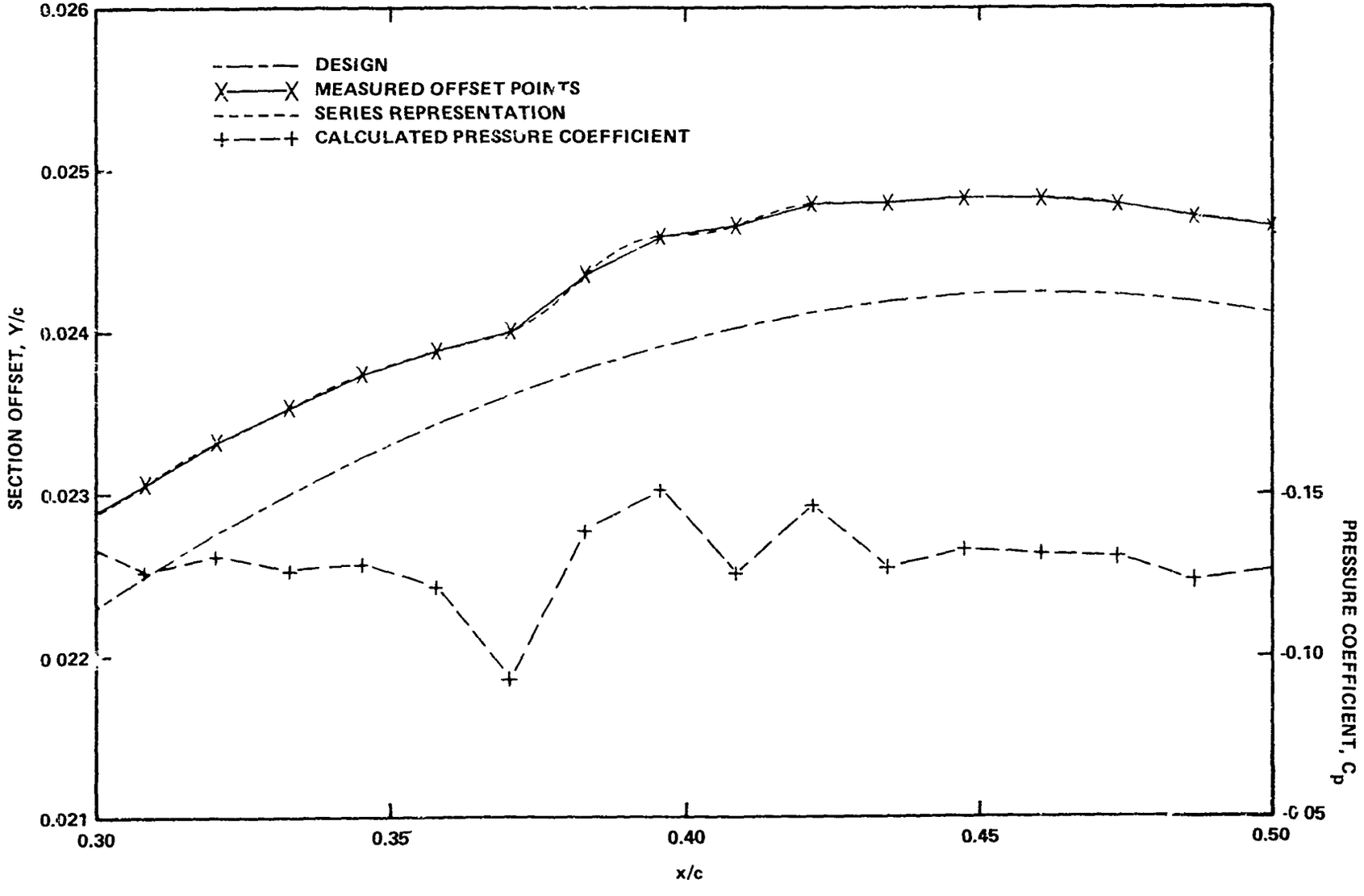

Figure 38a - 0.3 to 0.5 Chordwise Position

Figure 38 (Continued)

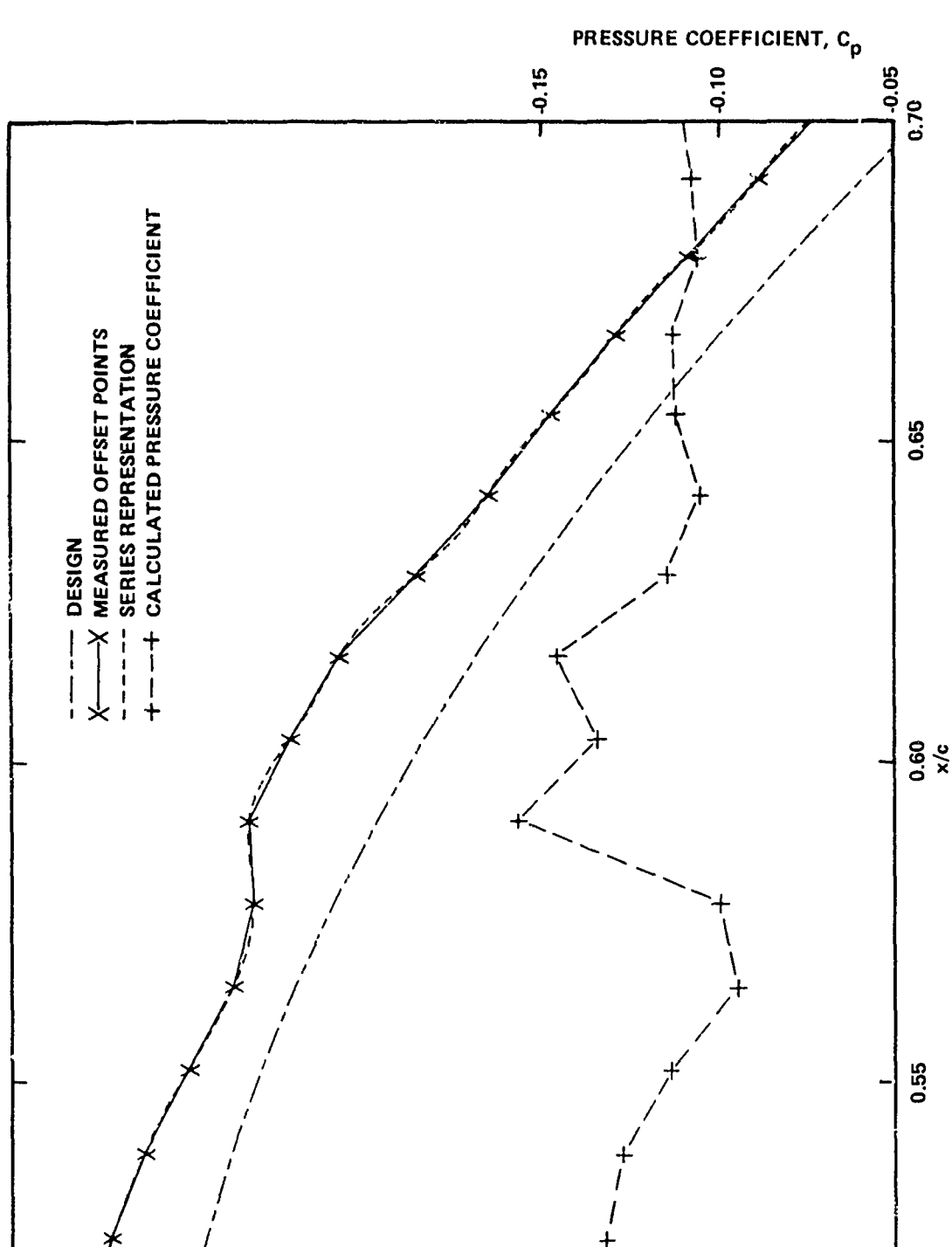

Figure 38b - 0.5 to 0.7 Chordwise Position

Figure 38 (Continued)

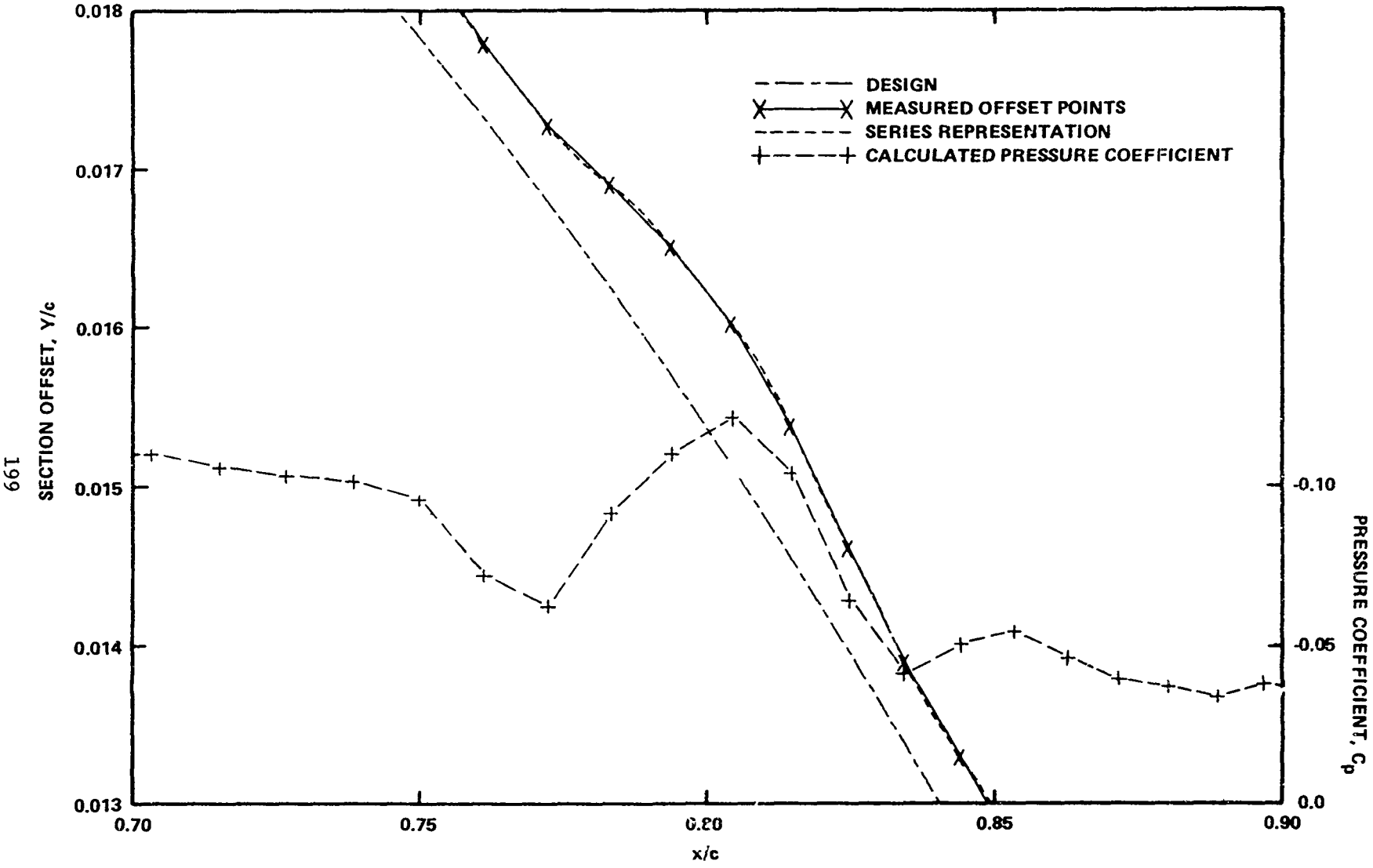

Figure 38c - 0.7 to 0.9 Chordwise Position

TABLE 1 - SUMMARY OF PREVIOUSLY REPORTED RESULTS OF EXPERIMENTAL PRESSURE MEASUREMENTS ON SUBCAVITATING MARINE PROPELLER BLADES

Investigator*	Gage Arrangement	Facility	Flow Pattern	Number of Locations at which Pressure Measured	Number of Propellers	Diameter of Propeller		Comments
						(ft)	(m)	
Auslander[3] (1959)	Water tubes in blade to scanning valve in hub to manometer board (Prandtl tubes)	Water Tunnel	Uniform flow	16 or more	1	1.000	(0.305)	Lack of repeatability (including unpublished data) and large effect of centrifugal force on rotating columns of water render these results useless.
Siekmann[5] (1969)	Air tubes in blade to scanning valve in hub to manometer board (Prandtl Tubes)	Wind Tunnel	Uniform flow	36	1	1.968	(0.600)	Accuracy poor due to use of air as fluid medium. Velocities deduced from measured pressures are presented but measured pressures are not presented.
Mavludoff[10, 11] (1965)	Water tubes in blade to ten pressure transducers in propeller hub	Water Tunnel	Uniform flow	36 or more	2 or more	0.886 1.017	(0.270) (0.310)	Very limited amount of data presented. Results questionable due to large effect of centrifugal force on rotating columns of water.
Weitendorf[12] Kienappel, et al[13, 14, 15] (1976)	Air tubes in blade to one pressure transducer in propeller hub	Wind Tunnel	Circumferentially nonuniform ship-like wake	235	1	4.593	(1.400)	Accuracy poor due to use of air as fluid medium. Pressure difference across blade is approximately 0.4 lb/in^2 (0.025 bar).
Kato[16, 17] (1977)	Transducer on blade extending beyond blade surface opposite to surface on which pressure measured	Towing Tank	Circumferentially nonuniform flow generated by model hull	2	1	0.820	(0.250)	Influence of gages on flow and scatter in data render these results useless.
Brandau and Leahy[18] (1970)	Transducers embedded in blade flush with surface	Wind Tunnel	Uniform flow	16	1	1.667	(0.508)	Lack of repeatability (including unpublished data) and very irregular blade section contours render these data useless.
Ito and Araki[19] (1976)	Transducers embedded in blade flush with surface	Towing Tank	Uniform flow and circumferentially nonuniform wake of flat plate	3	1	0.673	(0.205)	Substantial scatter in data. Preliminary studies for work of Takahashi and Oku.
Takei, et al[20, 21] (1977)	Transducers embedded in blade flush with surface	Cavitation Tunnel	Uniform flow and circumferentially nonuniform wake generated by screens	5	2	0.984 0.820	(0.300) (0.250)	Substantial scatter in data. No apparent systematic variation with speed. Includes measurement with cavitation in uniform flow.
Takahashi and Oku[22] (1977)	Transducers embedded in blades flush with surface	Towing Tank	Uniform flow	16	1	0.820	(0.250)	Significant scatter for limited number of repeat runs that are presented.
Hoxby[23] (1970)	Transducers embedded in cavities in blades with a hole to blade surface	Towing Tank	Uniform flow	54	1	1.855	(0.565)	Significant scatter in data.

*Superscripts refer to reference at end of report.

TABLE 2 - LIFTING-LINE DESIGN CALCULATIONS

TABLE 2A - LIFTING-LINE DESIGN CALCULATION CORRESPONDING TO DTNSRDC MODEL PROPELLER 4679

THRUST OPTION, DENSITY OF PROP(LBS/CUFT)= 484.0000

V = 2.0000E+01
P_E = 5.4950E+03
D (FT)= 16.5000 $1-W_T$ .8790 1-t .9300 H(FT)= 49.0000 ρ= 1.9384

Z= 3
A_E/A_o = 7.3420E-01 7.3966E-01
n = 1.1160E+02

x	$1-w_x$	c/D	t/c	$\tan\beta_i$ (PREL)	$\tan\beta$	θ_s (deg)	Z_R		C_D
3.0000E-01	9.7900E-01	3.1140E-01	2.5600E-01	1.0610E+00	1.1425E+00	0.	0.	0.	1.4406E-02
3.5000E-01	9.7900E-01	3.6361E-01	1.8700E-01	9.9600E-01	9.7931E-01	-4.7700E+00	0.	0.	1.1093E-02
4.0000E-01	9.7900E-01	4.1570E-01	1.4170E-01	9.3500E-01	9.5689E-01	-7.5600E+00	0.	0.	9.8202E-03
4.5000E-01	9.7900E-01	4.6730E-01	1.0840E-01	8.8100E-01	7.6168E-01	-9.1500E+00	0.	0.	9.2221E-03
5.0000E-01	9.7900E-01	5.1880E-01	8.5620E-02	8.3400E-01	8.8551E-01	-9.7300E+00	0.	0.	8.9099E-03
6.0000E-01	9.7900E-01	6.1840E-01	5.6680E-02	7.4000E-01	5.7126E-01	-7.9400E+00	0.	0.	8.5771E-03
7.0000E-01	9.7900E-01	6.7200E-01	3.7730E-02	6.3800E-01	4.8965E-01	-3.1400E+00	0.	0.	8.3798E-03
8.0000E-01	9.7900E-01	6.9140E-01	2.8100E-02	5.5100E-01	4.2845E-01	8.0000E+00	0.	0.	8.2816E-03
9.0000E-01	9.7900E-01	6.0960E-01	2.5400E-02	4.7000E-01	3.8084E-01	2.2280E+01	0.	0.	8.2544E-03
9.5000E-01	9.7900E-01	5.1780E-01	2.5000E-02	4.3200E-01	3.6080E-01	3.1480E+01	0.	0.	8.2504E-03
1.0000E+00	9.7900E-01	1.1670E-01	2.4500E-02	3.9200E-01	3.4276E-01	4.1160E+01	0.	0.	8.2454E-03

x	$\tan\beta_i$	$\tan\beta$	G	u_T/V	u_A/V	$d(C_{THSI})$	$d(C_{PSI})$	V_r	ω
3.0000E-01	1.0795E+00	1.1425E+00	0.	-2.6653E-02	-2.5499E-02	0.	0.	4.3880E+01	1.5525E+00
3.5000E-01	1.0131E+00	9.7931E-01	1.0590E-02	1.5534E-02	1.8029E-02	1.2507E-01	1.2665E-01	4.7290E+01	1.3297E+00
4.0000E-01	9.5104E-01	9.5689E-01	1.7520E-02	5.1396E-02	5.8688E-02	2.2950E-01	2.4936E-01	5.0829E+01	1.1424E+00
4.5000E-01	8.9611E-01	7.6169E-01	2.3865E-02	8.1811E-02	9.9469E-02	3.4466E-01	3.9697E-01	5.4550E+01	9.8537E-01
5.0000E-01	8.4831E-01	8.8551E-01	2.9541E-02	1.0952E-01	1.3974E-01	4.6750E-01	5.6637E-01	5.8378E+01	8.5375E-01
6.0000E-01	7.5264E-01	5.7126E-01	3.7602E-02	1.4277E-01	2.0347E-01	7.0887E-01	9.1439E-01	6.6373E+01	6.4850E-01
7.0000E-01	6.4494E-01	4.8965E-01	3.9913E-02	1.3926E-01	2.2811E-01	8.9092E-01	1.1560E+00	7.4853E+01	4.9944E-01
8.0000E-01	5.6045E-01	4.2845E-01	3.6665E-02	1.2269E-01	2.3286E-01	9.5137E-01	1.2184E+00	8.3672E+01	3.9163E-01
9.0000E-01	4.7900E-01	3.8084E-01	2.7024E-02	9.2136E-02	2.0584E-01	8.0372E-01	9.8770E-01	9.2731E+01	3.1220E-01
9.5000E-01	4.3941E-01	3.6080E-01	1.8962E-02	7.3775E-02	1.8589E-01	6.0063E-01	7.1614E-01	9.7327E+01	2.8047E-01
1.0000E+00	3.9873E-01	3.4276E-01	0.	5.0939E-02	1.5958E-01	0.	0.	1.0195E+02	2.5289E-01

C_{PTI} =4.1444E-01 C_{PSI} =5.3010E-01 n_i =7.8182E-01 C_{THSI} =4.2333E-01 C_{THSI}/C_{PSI} =7.9859E-01
C_{PT} =3.9911E-01 C_{PS} =5.8432E-01 n =6.8304E-01 C_{THS} =4.0767E-01 C_{THS}/C_{PS} =6.9769E-01

x	C_L	α_i	f_{M2D}/C	C_D/C_L	F	L	θ_s	C_{LE}/R	C_{TE}/R	t/R
3.0000E-01	0.	0.	0.	0.	0.	0.	0.	-3.1140E-01	3.1140E-01	1.5570E-01
3.5000E-01	1.3065E-01	2.7122E-01	4.8700E-03	9.4920E-02	5.5080E-01	2.8831E+02	-4.7700E+00	-4.0510E-01	3.2210E-01	1.3600E-01
4.0000E-01	1.7590E-01	2.7100E-01	1.1950E-02	5.5810E-02	3.5060E-01	4.4066E+02	-7.5600E+00	-4.8850E-01	3.4290E-01	1.1780E-01
4.5000E-01	1.9865E-01	3.1554E-01	1.3480E-02	4.5440E-02	2.8340E-01	5.7270E+02	-9.1500E+00	-5.6380E-01	3.7080E-01	1.0130E-01
5.0000E-01	2.0085E-01	3.1950E-01	1.4040E-02	4.3980E-02	2.4230E-01	6.4320E+02	-9.7300E+00	-6.3020E-01	4.0760E-01	8.8860E-02
6.0000E-01	1.9670E-01	3.0330E-01	1.3360E-02	4.3600E-02	1.9790E-01	8.5990E+02	-7.9400E+00	-7.1490E-01	5.0670E-01	6.9240E-02
7.0000E-01	1.6830E-01	2.5930E-01	1.1430E-02	4.9790E-02	1.8140E-01	9.1390E+02	-3.1400E+00	-7.1770E-01	6.2630E-01	5.0780E-02
8.0000E-01	1.3630E-01	2.0990E-01	9.2560E-03	6.0750E-02	1.6930E-01	9.2500E+02	8.0000E+00	-5.5380E-01	8.0980E-01	3.8320E-02
9.0000E-01	1.0160E-01	1.5640E-01	6.8960E-03	8.1280E-02	1.6420E-01	8.4640E+02	2.2280E+01	-2.2070E-01	9.9650E-01	3.0920E-02
9.5000E-01	7.9800E-02	1.2290E-01	5.4190E-03	1.0340E-01	1.5770E-01	7.3270E+02	3.1480E+01	5.2330E-02	1.0680E+00	2.5890E-02
1.0000E+00	0.	0.	0.	0.	0.	0.	4.1180E+01	6.5710E-01	8.9050E-01	5.7180E-03

n_D =6.4896E-01 P_D =8.4687E+03 1-t=9.3000E-01 1-W=9.7900E-01 V=2.0000E+01 DESIGN THRUST=9.6269E+04
Z = 3 n =1.1160E+02 A_E/A_o(DESIGN)=7.3420E-01 CALCULATED THRUST=9.6269E+04

TABLE 2 (Continued)

TABLE 2B - LIFTING-LINE DESIGN CALCULATION CORRESPONDING TO DTNSRDC MODEL PROPELLER 4718

THRUST OPTION, DENSITY OF PROP(LB#/FT3)= 484.0000

V = 2.0000E+01
P_E = 3.2970E+03

D = 16.5000 , $1-W_T$ =.9791 , 1-t =.9300 ,H(FT)= 49.0000 , ρ = 1.9905

Z 3
A_E/A_o 4.4024E-01
n 1.6000E+02

x	$1-w_x$	c/D	t/c	$\tan\beta_1$	$\tan\beta$	θ_sDEG	Z_R		C_D
3.0000E-01	9.7900E-01	1.8672E-01	2.5000E-01	7.7031E-01	7.9691E-01	-1.6500E+01	0.	0.	1.4406E-02
3.5000E-01	9.7900E-01	2.1801E-01	2.1100E-01	6.9119E-01	6.8307E-01	-2.9500E+01	0.	0.	1.2092E-02
4.0000E-01	9.7900E-01	2.4929E-01	1.7680E-01	6.2707E-01	5.9766E-01	-4.0500E+00	0.	0.	1.0745E-02
4.5000E-01	9.7900E-01	2.8018E-01	1.5100E-01	5.7154E-01	5.3127E-01	-4.7500E+00	0.	0.	1.0030E-02
5.0000E-01	9.7900E-01	3.1117E-01	1.2820E-01	5.2457E-01	4.7815E-01	-5.0000E+00	0.	0.	9.5521E-03
6.0000E-01	9.7900E-01	3.6525E-01	9.0500E-02	4.4988E-01	3.9946E-01	-3.5000E+00	0.	0.	8.9721E-03
7.0000E-01	9.7900E-01	4.0293E-01	6.3000E-02	3.9107E-01	3.4153E-01	4.0000E-01	0.	0.	8.6458E-03
8.0000E-01	9.7900E-01	4.0883E-01	4.6900E-02	3.4019E-01	2.9884E-01	5.7500E+00	0.	0.	8.4735E-03
9.0000E-01	9.7900E-01	3.6495E-01	4.2400E-02	2.9562E-01	2.6564E-01	1.2400E+01	0.	0.	8.4272E-03
9.5000E-01	9.7900E-01	3.1047E-01	4.1500E-02	2.7378E-01	2.5166E-01	1.6100E+01	0.	0.	8.4180E-03
1.0000E+00	9.7900E-01	6.9370E-02	4.1400E-02	2.5019E-01	2.3907E-01	2.0000E+01	0.	0.	8.4169E-03

x	$\tan\beta_1$	$\tan\beta$	G	u_T/V	u_A/V	$d(C_{ThSI})$	$d(C_{psi})$	V_r	σ
3.0000E-01	7.6994E-01	7.9591E-01	0.	-1.5849E-02	-2.1050E-02	0.	0.	5.3009E+01	1.3544E+00
3.5000E-01	6.9077E-01	6.8307E-01	3.7102E-03	5.0396E-03	7.5621E-03	6.3587E-02	6.2954E-02	5.6594E+01	8.6390E-01
4.0000E-01	6.2669E-01	5.9708E-01	6.5462E-03	2.0982E-02	3.4355E-02	1.2702E-01	1.3079E-01	5.4417E+01	7.3962E-01
4.5000E-01	5.7119E-01	5.3127E-01	9.1018E-03	3.1026E-02	5.5841E-02	1.9788E-01	2.0828E-01	7.0433E+01	5.8757E-01
5.0000E-01	5.2425E-01	4.7815E-01	1.1342E-02	3.7893E-02	7.4536E-02	2.7351E-01	2.9359E-01	7.6593E+01	4.9239E-01
6.0000E-01	4.4951E-01	3.9946E-01	1.4675E-02	4.5630E-02	1.0517E-01	4.2465E-01	4.6910E-01	9.3247E+01	3.5507E-01
7.0000E-01	3.9033E-01	3.4153E-01	1.6019E-02	4.6347E-02	1.2320E-01	5.4213E-01	6.0732E-01	1.0221E+02	2.6539E-01
8.0000E-01	3.3938E-01	2.9884E-01	1.4768E-02	3.9678E-02	1.2129E-01	5.7354E-01	6.3830E-01	1.1539E+02	2.0498E-01
9.0000E-01	2.9544E-01	2.6564E-01	1.0570E-02	2.8621E-02	1.0139E-01	4.6424E-01	5.0994E-01	1.2872E+02	1.6149E-01
9.5000E-01	2.7341E-01	2.5166E-01	7.2338E-03	2.0603E-02	7.9795E-02	3.3591E-01	3.5735E-01	1.3542E+02	1.4443E-01
1.0000E+00	2.5034E-01	2.3907E-01	0.	9.6897E-03	4.2490E-02	0.	0.	1.4215E+02	1.2975E-01

C_{PTI} =2.4512E-01 C_{PSI} =2.7464E-01 n_1 =8.9250E-01 C_{ThSI} =2.5335E-01 C_{ThSI}/C_{PSI} =9.1164E-01
C_{PT} =2.3323E-01 C_{PS} =2.7296E-01 n =8.2526E-01 C_{THS} =2.3823E-01 C_{THS}/C_{PS} =8.3867E-01

x	C_L	f_{MED}/C	C_D/C_L	F	L	θ_s	C_{LE}/R	C_{TE}/R	t/R
3.0000E-01	0.	0.	0.	0.	0.	-1.650E+00	-1.975E-01	1.758E-01	9.335E-02
3.5000E-01	6.1605E-02	9.447E-02	4.183E-03	1.963E-01	6.519E-01	-2.950E+00	-2.399E-01	1.961E-01	9.200E-02
4.0000E-01	8.6466E-02	1.331E-01	5.871E-03	1.243E-01	3.947E-01	-4.050E+00	-2.827E-01	2.159E-01	8.815E-02
4.5000E-01	9.7833E-02	1.507E-01	6.643E-03	1.025E-01	3.370E-01	-4.750E+00	-3.231E-01	2.372E-01	8.461E-02
5.0000E-01	1.0309E-01	1.594E-01	6.853E-03	9.464E-02	3.035E-01	-5.000E+00	-3.604E-01	2.619E-01	7.978E-02
6.0000E-01	9.5235E-02	1.466E-01	6.466E-03	9.422E-02	2.589E-01	-3.500E+00	-4.064E-01	3.261E-01	6.529E-02
7.0000E-01	8.2508E-02	1.276E-01	5.602E-03	1.048E-01	2.319E-01	4.000E-01	-3.977E-01	4.082E-01	5.377E-02
8.0000E-01	6.5403E-02	1.023E-01	4.509E-03	1.276E-01	2.206E-01	5.750E+00	-3.240E-01	4.936E-01	3.535E-02
9.0000E-01	4.4198E-02	7.419E-02	3.271E-03	1.749E-01	2.172E-01	1.240E+01	-1.618E-01	5.680E-01	3.095E-02
9.5000E-01	3.6496E-02	5.620E-02	2.479E-03	2.307E-01	2.204E-01	1.610E+01	-3.371E-02	5.872E-01	2.577E-02
1.0000E+00	0.	0.	0.	0.	0.	2.000E+01	2.899E-01	4.298E-01	5.794E-03

η_D=5.9336E-01 P_D =5.5508E+03 1-t =9.3000E-01 1-w =9.7900E-01 V =2.0000E+01 DESIGN THRUST =5.7761E+04
Z= 3 n =1.6000E+02 A_E/A_o (DESIGN)=4.4024E-01 CALCULATED THRUST =5.7751E+04

TABLE 3 - CHARACTERISTICS OF DTNSRDC MODEL PROPELLERS 4679 AND 4718

TABLE 3A - PROPELLER 4679

Diameter, D: 2.000 ft (0.610m)

Rotation: Right Hand

Number of Blades, Z: 3

Hub-Diameter Ratio, D_h/D: 0.30

Expanded Area Ratio: 0.755

Blade Thickness Fraction: 0.099

Design Advance Coefficient, J: 1.077

Design Thrust Loading Coefficient, C_{Th}: 0.425

Design Thrust Coefficient, K_T: 0.194

Design Torque Coefficient, K_Q: 0.0486

r/R	c/D	P/D	θ_s (deg)	i_G/D	t/c	t/D	f/c M	f/D M
0.3	0.274	0.950	0.0	0.0	0.2496	0.0684	0.0000	0.0000
0.4	0.404	1.225	-7.56	0.0	0.1418	0.0573	0.0171	0.0069
0.5	0.519	1.449	-9.73	0.0	0.0855	0.0444	0.0287	0.0149
0.6	0.611	1.356	-7.94	0.0	0.0566	0.0346	0.0321	0.0196
0.7	0.672	1.572	-3.14	0.0	0.0378	0.0254	0.0306	0.0206
0.8	0.682	1.475	8.0	0.0	0.0281	0.0192	0.0293	0.0200
0.9	0.609	1.270	22.28	0.0	0.0254	0.0155	0.0287	0.0185
0.95	0.518	1.120	31.48	0.0	0.0249	0.0129	0.0287	0.0149
1.0	0.117	0.965	41.18	0.0	0.0248	0.0029	0.0274	0.0032

TABLE 3 (Continued)

TABLE 3B - PROPELLER 4718

Diameter, D: 2.000 ft (0.610m)

Rotation: Right Hand

Number of Blades, Z: 3

Hub-Diameter Ratio, D_h/D: 0.30

Expanded Area Ratio: 0.44

Blade Thickness Fraction: 0.069

Design Advance Coefficient, J: 0.751

Design Thrust Loading Coefficient, C_{Th}: 0.248

Design Thrust Coefficient, K_T: 0.055

Design Torque Coefficient, K_Q: 0.0106

r/R	c/D	P/D	θ_s (deg)	i_G/D	t/c	t/D	f_M/c	f_M/D
0.3	0.187	0.718	-1.65	0.0	0.2497	0.0467	0.0	0.0
0.4	0.249	0.796	-4.05	0.0	0.1771	0.0441	0.0044	0.0011
0.5	0.311	0.855	-5.00	0.0	0.1280	0.0398	0.0085	0.0027
0.6	0.366	0.886	-3.50	0.0	0.0910	0.0333	0.0099	0.0036
0.7	0.403	0.888	0.40	0.0	0.0630	0.0254	0.0101	0.0041
0.8	0.409	0.870	5.75	0.0	0.0469	0.0192	0.0097	0.0090
0.9	0.365	0.825	12.40	0.0	0.0419	0.0153	0.0082	0.0030
0.95	0.311	0.786	16.10	0.0	0.0418	0.0130	0.0065	0.0020
1.0	0.070	0.734	20.00	0.0	0.0414	0.0029	0.0090	0.0006

TABLE 3 (Continued)

TABLE 3C - THICKNESS AND CAMBER DISTRIBUTIONS USED FOR PROPELLERS 4679 AND 4718

y	E_T/t*	E_c/f_M**
0.0000	0.0000	0.0000
0.005	0.0665	0.0423
0.0075	0.0812	0.0595
0.0125	0.1044	0.0907
0.025	0.1466	0.1586
0.05	0.2066	0.2712
0.075	0.2525	0.3657
0.1	0.2907	0.4482
0.15	0.3521	0.5869
0.2	0.4000	0.6993
0.25	0.4363	0.7905
0.3	0.4367	0.8635
0.35	0.4832	0.9202
0.4	0.4952	0.9615
0.45	0.5	0.9881
0.5	0.4962	1.0
0.55	0.4846	0.9971
0.6	0.4653	0.9786
0.65	0.4383	0.9434
0.7	0.4035	0.8892
0.75	0.3612	0.8121
0.8	0.3110	0.7027
0.85	0.2532	0.5425
0.9	0.1877	0.3586
0.95	0.1143	0.1713
0.975	0.0748	0.0823
1.0	0.0333	0

*NACA 66 Section (DTNSRDC modified).

**NACA a = 0.8 meanline: the design procedure determines the magnitude of the camber at each radius and uses the two-dimensional chordwise distribution of camber.

TABLE 4 - LOCATIONS AT WHICH PRESSURES WERE MEASURED

Fractional radius, r/R	0.5		0.7		0.9	
Propeller	4718	4679	4718	4679	4718	4679
Fraction of chord from leading edge, x/c	0.03	0.05	0.03	0.05	0.1	0.21
	0.12	0.12	0.1	0.12	0.2	0.36
	0.2	0.2	0.2	0.2	0.4	0.51
	0.35	0.35	0.3	0.3	0.6	0.63
	0.5	0.5	0.4	0.4	0.8	0.76
	0.7	0.7	0.5	0.5		
	0.9	0.9	0.7	0.65		
			0.9	0.85		

TABLE 5 - EXPERIMENTAL CONDITIONS

TABLE 5A - PROPELLER 4718

V_c (ft/sec)	N (rps)	$V_{R_{0.7}}$ (ft/sec)	$R_N \times 10^{-6}$	J	Number of Runs		
					Uniform Flow	Inclined Flow	Taped Gages
10.13	6.68	31.08	2.50	0.751	6	4	4
11.82+	7.88	36.62	2.95	0.751	8	17	6*
13.50	9.00	41.82	3.37	0.751	5	6	4
15.19	10.13	47.07	3.79	0.751	5	5	3
16.88	11.23	52.20	4.20	0.751	9	6	4
18.57	12.35	57.40	4.63	0.751	7	4	3
10.13	11.21	50.33	4.06	0.451	4	-	-
10.13	10.95	49.21	3.96	0.463	4	4	2*
8.44	7.87	35.63	2.87	0.326	3	4	-
11.82	11.23	50.79	4.09	0.532	4	5	3*
13.50	11.21	51.12	4.12	0.607	4	5	3*
10.97	8.09	37.23	3.00	0.677	4	-	2*
15.19	11.18	51.46	4.15	0.685	3	5	2*
12.66	7.85	36.77	2.97	0.806	3	-	2*
13.50	7.80	36.87	2.98	0.855	2	4	2*
14.35	7.88	37.51	3.01	0.919	3	-	2*
15.19	7.80	37.52	3.02	0.980	4	-	2*

*Conditions plotted in Figure 7.

+Baseline design J condition.

TABLE 5 (Continued)

TABLE 5B - PROPELLER 4679

V_c (ft/sec)	N (rps)	$V_{R_{0.7}}$ (ft/sec)	$R_N \times 10^{-6}$	J	Number of Runs		
					Uniform Flow	Inclined Flow	Taped Gages
10.13	4.68	22.94	3.08	1.081	3	-	-
11.82	5.45	26.73	3.59	1.086	6	5	4
13.47	6.23	30.53	4.10	1.080	4	7	4
15.14	7.02	34.39	4.62	1.078	4	6	4
17.70+	8.20	40.17	5.40	1.080	4	7	5
20.28	9.407	46.08	6.20	1.078	2	-	1
10.13	8.21	37.50	5.04	0.617	4	2	3
11.81	8.21	37.99	5.10	0.719	4	4	2
13.48	8.19	38.46	5.17	0.823	4	5	3
15.15	8.21	39.16	5.26	0.923	4	3	2
17.17	7.02	35.33	4.74	1.262	5	2	4

+Baseline design J condition.

TABLE 6 - COMPARISON OF MEASURED MEAN PRESSURE COEFFICIENTS AT DESIGN CONDITION WITH AND WITHOUT SAND ON BLADE LEADING EDGES

Gage	x/c	r/R	Propeller 4718*			Propeller 4679+		
			c_p w/o sand	w/o sand-w/sand	largest σ	c_p w/o sand	w/o sand-w/sand	largest σ
1	0.900	0.500	-0.0189	-0.004	0.004	-0.0492	-0.001	0.003
2	0.700	0.500	-0.1662	-0.001	0.006	-0.0489	-0.002	0.004
3	0.500	0.500	-0.2957	-0.013	0.006	-0.0737	0.001	0.003
4	0.350	0.500	-0.2152	-0.003	0.008	-0.0651	0.003	0.003
5	0.200	0.500	-0.2308	-0.009	0.007	-0.0712	0.003	0.003
6	0.080	0.500	-0.1932	-0.008	0.008	-0.0187	-0.012	0.002
7	0.030	0.500	-0.0184	-0.029	0.010	-0.0015	-0.017	0.005
8	0.900	0.700	0.0065	0.003	0.003	-0.0055		0.005
9	0.700	0.700	-0.0632	0.000	0.002	0.0422	0.000	0.004
10	0.500	0.700	-0.0949	-0.001	0.003	0.0106		
11	0.400	0.700	-0.0765	0.000	0.002	0.0094	-0.001	0.004
12	0.300	0.700	-0.0774	0.003	0.004	0.0338	0.002	0.001
13	0.200	0.700	-0.0813	-0.003	0.003	0.0363	0.002	0.003
14	0.100	0.700	-0.0661	-0.001	0.004	0.0053	-0.010	0.005
15	0.030	0.700	-0.0173	-0.041	0.009	0.0207	-0.018	0.002
16	0.800	0.900	-0.0051	0.001	0.001	-0.0029	0.000	0.003
17	0.600	0.900	-0.0335	0.000	0.001	0.0035	0.001	0.002
18	0.400	0.900	-0.0458	-0.001	0.003	0.0162	0.001	0.002
19	0.200	0.900	-0.0261	0.008	0.003	-0.1043		
20	0.075	0.900	-0.0217	-0.005	0.003	-0.0273	-0.003	0.001
21	0.030	0.500	0.0073	-0.007	0.008	-0.1714	-0.003	0.006
22	0.080	0.500	-0.0015			-0.2064	0.022	0.019
23	0.200	0.500	-0.2687	0.001	0.004	-0.2416	-0.009	0.021
24	0.350	0.500	-0.3240	0.004	0.006	-0.2981	0.001	0.029
25	0.500	0.500	-0.4447	0.009	0.016	-0.3340	0.008	0.007
26	0.700	0.500	-0.4220	0.009	0.008	-0.3762	0.007	0.012
27	0.900	0.500	-0.0862	-0.011	0.003	-0.1513	-0.007	0.011
28	0.030	0.700	-0.0840	-0.025	0.004	-0.1933	-0.009	0.003
29	0.100	0.700	-0.1081	0.001	0.002	-0.1335	-0.005	0.006
30	0.200	0.700	-0.1799	-0.005	0.005	-0.1332	0.014	0.015
31	0.300	0.700	-0.1631	0.002	0.006	-0.1328	0.001	0.002
32	0.400	0.700	-0.1867	-0.003	0.007	-0.1456	0.000	0.001
33	0.500	0.700	-0.1739	0.005	0.008	-0.1611		0.007
34	0.700	0.700	-0.1700	-0.010	0.005	-0.1837	-0.005	0.006
35	0.900	0.700	-0.0306	-0.002	0.002	-0.1384	-0.005	0.003
36	0.075	0.900	-0.0707	-0.005	0.002	-0.0946		
37	0.200	0.900	-0.1112	0.005	0.003	-0.1209	0.029	0.031
38	0.400	0.900	-0.1209	-0.001	0.002	-0.1702	0.001	0.005
39	0.600	0.900	-0.0963	0.000	0.001	-0.1482	0.000	0.006
40	0.800	0.900	-0.0963	-0.003	0.001	-0.1083	-0.007	0.001

*$R_{N_{0.7}} = 2.79 \times 10^6$.

+$R_{N_{0.7}} = 5.1 \times 10^6$.

TABLE 7 - STANDARD ERROR AT A 95 PERCENT CONFIDENCE LEVEL OF MEASURED MEAN PRESSURE COEFFICIENTS FROM C_p VERSUS J CURVES

TABLE 7A - PROPELLER 4718

Gage	x/c	r/R	Uniform Flow (c_p)		Inclined Flow (c_p)	
			1st Order	2nd Order	1st Order	2nd Order
1	0.900	0.500	0.0059	0.0058	0.0106	0.0094
2	0.700	0.500	0.0108	0.0107	0.0193	0.0192
3	0.500	0.500	0.0700	0.0054	0.0205	0.0205
4	0.350	0.500	0.0205	0.0205	0.0174	0.0174
5	0.200	0.500	0.0061	0.0061	0.0147	0.0147
6	0.080	0.500	0.0093	0.0069	0.0177	0.0163
7	0.030	0.500	0.0261	0.0091	0.0419	0.0394
8	0.900	0.700	0.0041	0.0032	0.0062	0.0060
9	0.700	0.700	0.0031	0.0028	0.0070	0.0069
10	0.500	0.700	0.0057	0.0049	0.0076	0.0073
11	0.400	0.700	0.0046	0.0034	0.0073	0.0069
12	0.300	0.700	0.0039	0.0032	0.0093	0.0090
13	0.200	0.700	0.0039	0.0033	0.0070	0.0068
14	0.100	0.700	0.0038	0.0037	0.0076	0.0076
15	0.030	0.700	0.0118	0.0094	0.0271	0.0271
16	0.800	0.900	0.0038	0.0029	0.0061	0.0061
17	0.600	0.900	0.0045	0.0033	0.0059	0.0056
18	0.400	0.900	0.0036	0.0029	0.0070	0.0069
19	0.200	0.900	0.0029	0.0027	0.0064	0.0058
20	0.075	0.900	0.0064	0.0048	0.0147	0.0121
21	0.030	0.500	0.0248	0.0082	0.0259	0.0179
22	0.080	0.500	*	*	*	*
23	0.200	0.500	0.0069	0.0042	0.0119	0.0111
24	0.350	0.500	0.0119	0.0075	0.0150	0.0146
25	0.500	0.500	0.0104	0.0079	0.0220	0.0219
26	0.700	0.500	*	*	0.0217	0.0211
27	0.900	0.500	0.0050	0.0044	0.0099	0.0095
28	0.030	0.700	0.0237	0.0054	0.0240	0.0141
29	0.100	0.700	0.0041	0.0041	0.0131	0.0130
30	0.200	0.700	0.0066	0.0064	0.0110	0.0110
31	0.300	0.700	0.0054	0.0042	0.0116	0.0114
32	0.400	0.700	0.0046	0.0036	0.0112	0.0112
33	0.500	0.700	0.0089	0.0078	0.0140	0.0140
34	0.700	0.700	0.0055	0.0046	0.0141	0.0140
35	0.900	0.700	0.0031	0.0027	0.0074	0.0072
36	0.075	0.900	0.0095	0.0061	0.0090	0.0082
37	0.200	0.900	0.0070	0.0036	0.0097	0.0080
38	0.400	0.900	0.0033	0.0030	0.0072	0.0072
39	0.600	0.900	0.0040	0.0027	0.0067	0.0065
40	0.800	0.900	0.0065	0.0031	0.0081	0.0065

*Damaged gage.

TABLE 7 (Continued)

TABLE 7B - PROPELLER 4679

Gage	x/c	r/R	Uniform Flow (c_p)		Inclined Flow (c_p)	
			1st Order	2nd Order	1st Order	2nd Order
1	0.900	0.500	0.0173	0.0173	0.0111	0.0111
2	0.700	0.500	0.0184	0.0177	0.0179	0.0177
3	0.500	0.500	0.0206	0.0185	0.0137	0.0120
4	0.350	0.500	0.0236	0.0202	0.0148	0.0128
5	0.200	0.500	*	*	0.0175	0.0142
6	0.080	0.500	0.0273	0.0231	0.0568	0.0561
7	0.030	0.500	0.0203	0.0192	0.0314	0.0205
8	0.900	0.700	0.0260	0.0260**		*
9	0.700	0.700	0.0133	0.0111	0.0115	0.0112
10	0.500	0.700		*		*
11	0.400	0.700	0.0172	0.0152	0.0283	0.0279
12	0.300	0.700	0.1209	0.1170**	0.0091	0.0081
13	0.200	0.700	0.0167	0.0148	0.0124	0.0114
14	0.100	0.700	0.0223	0.0171	0.0199	0.0187
15	0.030	0.700	0.0259	0.0200	0.0406	0.0398**
16	0.800	0.900	0.0144	0.0094	0.0102	0.0074
17	0.600	0.900	0.0151	0.0100	0.0104	0.0080
18	0.400	0.900		*	0.0261	0.0258+
19	0.200	0.900		*		*
20	0.075	0.900	0.0151	0.0146	0.0147	0.0147
21	0.030	0.500	0.0178	0.0177	0.0205	0.0205
22	0.080	0.500	0.0207	0.0173	0.0438	0.0425**
23	0.200	0.500	0.0214	0.0167	0.0570	0.0532**
24	0.350	0.500	0.0322	0.0235	0.1376	0.1351**
25	0.500	0.500	0.0243	0.0205	0.0236	0.0184
26	0.700	0.500	0.0275	0.0223	0.0346	0.0307**
27	0.900	0.500	0.0222	0.0219	0.0456	0.0456**
28	0.030	0.700	0.0194	0.0167	0.0195	0.0182
29	0.100	0.700	0.0153	0.0139	0.0175	0.0173
30	0.200	0.700	0.0120	0.0119	0.0290	0.0290**
31	0.300	0.700	0.0125	0.0120	0.0104	0.0095
32	0.400	0.700	0.0145	0.0142	0.0135	0.0131
33	0.500	0.700	0.0287	0.0282+		*
34	0.700	0.700	0.0175	0.0175	0.0188	0.0187
35	0.900	0.700	0.0178	0.0177	0.0121	0.0121
36	0.075	0.900	0.0409	0.0323		*
37	0.200	0.900	0.0156	0.0151	0.0245	0.0244**
38	0.400	0.900	0.0163	0.0148	0.0196	0.0178
39	0.600	0.900	0.0170	0.0160	0.0196	0.0165
40	0.800	0.900	0.0172	0.0171	0.0140	0.0121

*Damaged gage.

**Numerous bad runs.

+Improper speed correction.

TABLE 8 - STANDARD ERROR AT A 95 PERCENT CONFIDENCE LEVEL OF MEASURED MEAN PRESSURE FROM C_p VERSUS J CURVES

TABLE 8A - PROPELLER 4718

Gage	x/c	r/R	78 Runs Uniform Flow (psi)		69 Runs Inclined Flow (psi)		
			1st Order	2nd Order	1st Order	2nd Order	
1	0.900	0.500	0.0417	0.0418	0.0579	0.0564	
2	0.700	0.500	0.0744	0.0742	0.1319	0.1317	
3	0.500	0.500	0.0518	0.0413	0.1209	0.1208	
4	0.350	0.500	0.1399	0.1400	0.0913	0.0913	
5	0.200	0.500	0.0444	0.0442	0.0892	0.0892	
6	0.080	0.500	0.0741	0.0542	0.1064	0.0935	
7	0.030	0.500	0.1954	0.0695	0.3377	0.3204	
8	0.900	0.700	0.0575	0.0476	0.0696	0.0646	
9	0.700	0.700	0.0434	0.0408	0.0679	0.0671	
10	0.500	0.700	0.0762	0.0642	0.0835	0.0771	
11	0.400	0.700	0.0633	0.0481	0.0736	0.0672	
12	0.300	0.700	0.0567	0.0488	0.0975	0.0993	
13	0.200	0.700	0.0545	0.0481	0.0752	0.0725	
14	0.100	0.700	0.0544	0.0532	0.0885	0.0881	
15	0.030	0.700	0.1726	0.1337	0.3814	0.3850	
16	0.800	0.900	0.0874	0.0627	0.1044	0.0998	
17	0.600	0.900	0.1018	0.0713	0.1025	0.0890	
18	0.400	0.900	0.0855	0.0701	0.1084	0.1034	
19	0.200	0.900	0.0596	0.0581	0.0955	0.0913	
20	0.075	0.900	0.1251	0.1014	0.2723	0.2826	
21	0.030	0.500	0.1722	0.0669	0.1637	0.1475	
22	0.080	0.500	*	*	*	*	
23	0.200	0.500	0.0531	0.0320	0.0793	0.0736	
24	0.350	0.500	0.0841	0.0502	0.0962	0.0931	
25	0.500	0.500	0.0712	0.0540	0.1342	0.1345	
26	0.700	0.500	*	*	0.1148	0.1113	
27	0.900	0.500	0.0376	0.0338	0.0586	0.0562	
28	0.030	0.700	0.3075	0.0742	0.2921	0.1913	
29	0.100	0.700	0.0491	0.0491	0.1440	0.1406	
30	0.200	0.700	0.0804	0.0743	0.1157	0.1179	
31	0.300	0.700	0.0691	0.0531	0.1177	0.1159	
32	0.400	0.700	0.0606	0.0479	0.1097	0.1101	
33	0.500	0.700	0.1143	0.0944	0.1525	0.1526	
34	0.700	0.700	0.0693	0.0697	0.1434	0.1455	
35	0.900	0.700	0.0440	0.0402	0.0736	0.0734	
36	0.075	0.900	0.2102	0.1435	0.1962	0.1851	
37	0.200	0.900	0.1433	0.0838	0.1760	0.1615	
38	0.400	0.900	0.0773	0.0690	0.1377	0.1385	
39	0.600	0.900	0.0936	0.0628	0.1261	0.1167	Calibration Error
40	0.800	0.900	0.1481	0.0742	0.1517	0.1101	
Average			0.093	0.065	0.132	0.125	0.050 - 0.070

*Damaged gage.

TABLE 8 (Continued)

TABLE 8B - PROPELLER 4679

Gage	x/c	r/R	44 Runs Uniform Flow (psi)		41 Runs Inclined Flow (psi)		
			1st Order	2nd Order	1st Order	2nd Order	
1	0.900	0.500	0.0799	0.0799	0.0539	0.0539	
2	0.700	0.500	0.0833	0.0793	0.0734	0.0722	
3	0.500	0.500	0.0959	0.0840	0.0646	0.0543	
4	0.350	0.500	0.1132	0.0942	0.0706	0.0582	
5	0.200	0.500		*	0.0918	0.0718	
6	0.080	0.500	0.1337	0.1107	0.2691	0.2646	
7	0.030	0.500	0.1000	0.0938	0.1059	0.1003	
8	0.900	0.700	0.2161	0.2160**		*	
9	0.700	0.700	0.1012	0.0792	0.0960	0.0926	
10	0.500	0.700		*		*	
11	0.400	0.700	0.1274	0.1088	0.2059	0.2016	
12	0.300	0.700	1.1588	1.1212**	0.0760	0.0677	
13	0.200	0.700	0.1259	0.1097	0.1022	0.0928	
14	0.100	0.700	0.1829	0.1406	0.1450	0.1356	
15	0.030	0.700	0.2119	0.1644	0.3094	0.2995**	
16	0.800	0.900	0.1817	0.0971	0.1356	0.0886	
17	0.600	0.900	0.1940	0.1122	0.1317	0.0904	
18	0.400	0.900		*	0.3295	0.3156+	
19	0.200	0.900		*		*	
20	0.075	0.900	0.1712	0.1645	0.1578	0.1579	
21	0.030	0.500	0.0852	0.0843	0.1027	0.1026	
22	0.080	0.500	0.0984	0.0774	0.1955	0.1874**	
23	0.200	0.500	0.1060	0.0785	0.2942	0.2741**	
24	0.350	0.500	0.1623	0.1127	0.7463	0.7326**	
25	0.500	0.500	0.1192	0.0956	0.1253	0.0982	
26	0.700	0.500	0.1312	0.0903	0.1857	0.1655**	
27	0.900	0.500	0.0964	0.0946	0.1919	0.1919**	
28	0.030	0.700	0.1749	0.1391	0.1719	0.1595	
29	0.100	0.700	0.1144	0.0990	0.1463	0.1445	
30	0.200	0.700	0.0994	0.0985	0.2422	0.2422**	
31	0.300	0.700	0.0936	0.0884	0.0897	0.0825	
32	0.500	0.700	0.1052	0.1030	0.1185	0.1166	
33	0.500	0.700	0.2028	0.1967+		*	
34	0.700	0.700	0.1247	0.1247	0.1543	0.1536	
35	0.900	0.700	0.1281	0.1262	0.0965	0.0962	
36	0.075	0.900	0.5993	0.4757		*	
37	0.200	0.900	0.1923	0.1812	0.3007	0.2989**	
38	0.400	0.900	0.2029	0.1723	0.2440	0.2141	
39	0.600	0.900	0.2138	0.1919	0.2838	0.2355	
40	0.800	0.900	0.2135	0.2115	0.2066	0.1762	Calibration Error
Average			0.150	0.126	0.135	0.123	0.050 - 0.070

*Damaged gages, excluded from average.

**Numerous bad runs, excluded from average.

+Improper speed correction, excluded from average.

TABLE 9 - MEASURED OFFSETS OF PROPELLER 4718, BLADE C, AT THE 0.7 RADIUS

Suction Side		Pressure Side	
x/c	Y/c	x/c	Y/c
0.002441	0.001019	0.004729	-0.003345
0.008682	0.006085	0.013996	-0.006269
0.015666	0.008774	0.022852	-0.007764
0.023067	0.010773	0.031272	-0.008811
0.038701	0.012119	0.039836	-0.009744
0.037993	0.014185	0.048503	-0.010591
0.045679	0.015720	0.056888	-0.011329
0.053197	0.017052	0.065424	-0.012005
0.060936	0.018262	0.073707	-0.012628
0.068723	0.019302	0.082136	-0.013214
0.076462	0.020322	0.090489	-0.013753
0.084103	0.021503	0.099007	-0.014247
0.091940	0.022630	0.107278	-0.014685
0.099622	0.023549	0.115702	-0.015128
0.107390	0.024659	0.123878	-0.015515
0.115254	0.025484	0.132201	-0.015920
0.123150	0.026133	0.140527	-0.016314
0.130994	0.026861	0.149001	-0.016704
0.138952	0.027657	0.157262	-0.017078
0.146701	0.028458	0.165667	-0.017462
0.154621	0.029240	0.173854	-0.017789
0.162535	0.029974	0.182174	-0.018096
0.170434	0.030679	0.190459	-0.018349
0.178321	0.031358	0.198758	-0.018698
0.186228	0.031955	0.206921	-0.018767
0.194101	0.032550	0.215330	-0.019071
0.202108	0.033221	0.223489	-0.019242
0.209995	0.033643	0.231824	-0.019442
0.218019	0.034265	0.239957	-0.019657
0.226040	0.034641	0.248244	-0.019843
0.234048	0.035100	0.256518	-0.020045
0.242014	0.035588	0.264758	-0.020239
0.250007	0.036019	0.272992	-0.020435
0.257944	0.036461	0.281200	-0.020609
0.265893	0.036819	0.289581	-0.020858
0.274012	0.037335	0.297672	-0.020799
0.281946	0.037720	0.305803	-0.020480
0.290026	0.038130	0.313990	-0.020762
0.297948	0.038444	0.322423	-0.021268
0.306024	0.038819	0.330678	-0.021367

TABLE 9 (Continued)

Suction Side		Pressure Side	
x/c	Y/c	x/c	Y/c
0.649698	0.037834	0.672495	-0.017771
0.658089	0.037400	0.680434	-0.017506
0.666321	0.036969	0.688418	-0.016866
0.674726	0.036540	0.696313	-0.016419
0.683018	0.036033	0.704710	-0.016761
0.691496	0.035556	0.712669	-0.016400
0.699829	0.035032	0.720838	-0.016120
0.708175	0.034513	0.728863	-0.015810
0.716541	0.033957	0.736892	-0.015498
0.724938	0.033403	0.744926	-0.015150
0.733379	0.032788	0.752995	-0.014844
0.741829	0.032166	0.761069	-0.014525
0.750315	0.031536	0.769005	-0.014217
0.758654	0.030869	0.777111	-0.013852
0.767187	0.030224	0.785064	-0.013537
0.775591	0.029506	0.793225	-0.013194
0.784014	0.028784	0.801158	-0.012687
0.792481	0.027990	0.809263	-0.012523
0.800985	0.027189	0.817295	-0.012176
0.809544	0.026321	0.825367	-0.011835
0.818147	0.025403	0.833294	-0.011509
0.826607	0.024473	0.841424	-0.011179
0.835296	0.023479	0.849404	-0.010853
0.843817	0.022495	0.857397	-0.010522
0.852372	0.021492	0.865431	-0.010186
0.860978	0.020475	0.873478	-0.009844
0.869601	0.019465	0.881537	-0.009464
0.878032	0.018557	0.889652	-0.009106
0.886663	0.017673	0.897600	-0.008738
0.895137	0.016804	0.905554	-0.008344
0.903708	0.015696	0.913547	-0.007958
0.912310	0.014677	0.921586	-0.007530
0.921063	0.013408	0.929611	-0.007064
0.929643	0.012103	0.937677	-0.006603
0.938394	0.010944	0.945583	-0.006118
0.947017	0.009778	0.953553	-0.005662
0.955655	0.008596	0.961526	-0.005161
0.964360	0.007430	0.969535	-0.004667
0.972886	0.006259	0.977543	-0.004107
0.981605	0.005132	0.985444	-0.003568
0.990190	0.003995	0.993153	-0.003128

TABLE 9 (Continued)

Suction Side		Pressure Side	
x/c	Y/c	x/c	Y/c
0.314098	0.039139	0.338745	-0.021452
0.322169	0.039434	0.346958	-0.021512
0.330240	0.039330	0.355077	-0.021364
0.338306	0.039978	0.363365	-0.021639
0.346375	0.040251	0.371563	-0.021716
0.354453	0.040448	0.379739	-0.021791
0.362498	0.040678	0.388070	-0.021826
0.370534	0.040904	0.396252	-0.021931
0.378565	0.041127	0.404389	-0.021977
0.386791	0.041318	0.412509	-0.021940
0.394712	0.041776	0.420815	-0.022019
0.402975	0.041814	0.428925	-0.022020
0.411078	0.041822	0.437198	-0.022022
0.419120	0.041938	0.445284	-0.021988
0.427362	0.042046	0.453358	-0.021959
0.435407	0.042108	0.461592	-0.021899
0.443657	0.042152	0.469677	-0.021887
0.451711	0.042207	0.477899	-0.021810
0.459951	0.042236	0.485963	-0.021785
0.468030	0.042245	0.494131	-0.021551
0.476285	0.042235	0.502447	-0.021714
0.484550	0.042196	0.510449	-0.021569
0.492661	0.042129	0.518616	-0.021335
0.500936	0.042072	0.526660	-0.021207
0.509076	0.041938	0.534850	-0.021075
0.517382	0.041815	0.542885	-0.020939
0.525530	0.041674	0.551085	-0.020792
0.533862	0.041505	0.559139	-0.020660
0.542033	0.041329	0.567333	-0.020504
0.550197	0.041126	0.575367	-0.020357
0.558550	0.040967	0.583412	-0.020195
0.566726	0.040792	0.591611	-0.020037
0.574924	0.040581	0.599681	-0.019876
0.583322	0.040361	0.607742	-0.019674
0.591548	0.040117	0.615973	-0.019481
0.599803	0.039851	0.624022	-0.019262
0.608074	0.039570	0.632074	-0.019029
0.616360	0.039272	0.640141	-0.018780
0.624658	0.038945	0.648223	-0.018569
0.632978	0.038594	0.656305	-0.018303
0.641319	0.038218	0.664401	-0.018042

REFERENCES

1. Angelo, J.J., et al., "U.S. Navy Controllable Pitch Propeller Programs," Presented at a Joint Session of the Chesapeake Section of the Society of Naval Architects and Marine Engineers and the Flagship Section of the American Society of Naval Engineers, Bethesda, Maryland (19 Apr 1977).

2. Noonan, C., et al., "The BARBEY Report - An Investigation into Controllable Pitch Propeller Failures from the Standpoint of Full-Scale Underway Propeller Measurements," DTNSRDC Report 77-0080 (Aug 1977).

3. Boswell, R.J., et al., "Experimental Determination of Mean and Unsteady Loads on a Model CP Propeller Blade for Various Simulated Modes of Ship Operation," The Eleventh Symposium on Naval Hydrodynamics sponsored jointly by the Office of Naval Research and University College London, Mechanical Engineering Publications Limited, London and New York, pp. 789-823 and 832-834 (Apr 1976).

4. Boswell, R.J., et al., "Experimental Unsteady and Mean Loads on a CP Propeller Blade of the FF-1088 for Simulated Modes of Operation," DTNSRDC Report 76-0125 (Oct 1976).

5. Boswell, R.J. and S.D. Jessup, "Experimental Determination of Periodic Propeller Blade Loads in a Towing Tank," Presented to the 18th American Towing Tank Conference, Annapolis, Maryland (23 Aug 1977).

6. Jessup, S.D., et al., "Experimental Unsteady and Time-Average Loads on the Blades of the CP Propeller on a Model of the DD-963 Class Destroyer for Simulated Modes of Operation," DTNSRDC Report 77-0110 (Dec 1977).

7. Boswell, R.J., et al., "Experimental Unsteady and Time-Average Loads on the Blades of a CP Propeller Behind a Model of the DD-963 Class Destroyer," Propellers '78 Symposium, The Society of Naval Architects and Marine Engineers, Virginia Beach, Virginia (24-25 May 1978).

8. Auslander, J., "Measurement of the Pressure Distribution on the Blades of a Marine Propeller," Presented to the American Towing Tank Conference, Berkely, California (1-2 Sep 1959).

9. Siekmann, J., "Relativestromung in Schiffsschrauben Stronumgsmechanik and Stromungsmaschinen, No. 7 (Aug 1969), pp. 28-56; also, "Relative Flow in Ship Propellers," Naval Intelligence Command, Translation 3048 (May 1970).

10. Mavlyduoff, M.A., "Measurement of Pressure Distribution on the Blades of a Marine Propeller Model," Sbornik Statey po Gidrodinamike Dvirhiteley, Sudostroyaniye (Publishing House), pp. 67-72 (1965) (in English).

11. Mavlyduoff, M.A., "Measurement of Pressure on the Blade Surface of Noncavitating Propeller Model," Proceedings of the 11th International Towing Tank Conference, pp. 290-292 (1965).

12. Weitendorf, E.A., "Cavitation and Its Influence on Induced Hull Pressure Amplitudes," Presented to the Symposium on Hydrodynamics of Ship and Offshore Propulsion Systems, Det Norske Veritas, Oslo, Norway (Mar 1977).

13. Kienappel, K., et al., "Messung der Instationären Druckverteilung und der Kräfte an einem Propeller im Schiffsnachstrom (Measurements of the Unsteady Pressure Distribution and Forces on a Propeller in a Ship's Wake)," Deutsche Forschungs-und Versuchsanstalt für Luft-und Raumfahrt E.V., AVA-Göttingen, Report IB-253-76-C-04 (Mar 1976) (in German).

14. Kienappel, K., "Wiederholungsmessung der Instationären Druckverteilung eines Propellers im Schiffsnachstrom (Repeat Measurement of the Unsteady Pressure Distribution on a Propeller in a Ship's Wake)," Deutsche Forschungs-und Versuchsanstalt für Luft-und Raumfahrt E.V., AVA-Göttingen Report IB-253-76-J-09 (Sep 1976) (in German).

15. Kienappel, K., "Untersuchung zur Messung Instationaerer Druecke in Rotierenden Systenen (Investigations of Unsteady Pressure Distribution in Rotating Systems)," Deutsche Forschungs-und Versuchsanstalt für Luft-und Raumfahrt E.V., AVA-Göttingen Report DLR-FB-77-43 (1977) (in German).

16. Yamasaki, T., "On Some Tank Test Results with a Large Model Propeller - 0.95m in Diameter," Journal of the Society of Naval Architects of Japan, No. 144, pp. 70-77 (Dec 1978).

17. Kato, H., "An Experimental Study of the Pressure Fluctuation on a Propeller Blade in a Wake," Presented at the Symposium on Hydrodynamics of Ship and Offshore Propulsion Systems, Det Norske Veritas, Oslo, Norway (Mar 1977).

18. Kato, H., "Measurement of Pressure on Propeller Blade Surfaces," Zosen Gakkai Suiso Iinkai Shiryo (Materials of the Water Tank Committee, Society of Naval Architects of Japan) (1974).

19. Brandau, J.H. and J.L. Leahy, "Measurement of Marine Propeller Blade Pressure Distribution," American Society of Mechanical Engineers Cavitation Forum, Presented at the Joint ASME Fluids Engineering Heat Transfer and Lubrication Conference, Detroit, Michigan, pp. 10-12 (24-27 May 1970).

20. Ito, Y. and S. Araki, "On Measurement of Surface Pressure of an Operating Model Propeller," The Shipbuilding Research Center of Japan, Tokyo, Japan, No. 4 (Jul 1976) pp. 25-34 (in Japanese).

21. Takei, Y., et al., "Measurement of Pressure on a Propeller Blade Surface (First Report)," Papers of Shipbuilding Research Institute of Japan, No. 24, pp. 95-98 (undated).

22. Takei, Y., et al., "Measurement of Pressure Distribution on the Blades of a Model Propeller," Presented to the Autumn Meeting of the Shipbuilding Research Institute of Japan, No. 28 (1976) and No. 30 (1977).

23. Takahashi, M. and M. Oku, "Studies of Cavitation Characteristics of MAU Type Propellers - First Report; Pressure Distribution on Blade Surface in Uniform Flow," Journal of the Society of Naval Architects of Japan, No. 141, pp. 19-29 (1977) (in Japanese).

24. Hoiby, O.W., "Three-Dimensional Effects in Propeller Theory," Norwegian Ship Model Experimental Tank Publication 105 (May 1970).

25. Boswell, R.J., "Exploratory Measurement of the Pressure Distribution on DTNSRDC Model Controllable-Pitch Propeller 4679," Report DTNSRDC/SPD-0834-01 (May 1978, Unpublished).

26. Denny, S.B., et al., "Hydrodynamic Design Considerations for the Controllable-Pitch Propeller for the Guided Missile Frigate," Naval Engineers Journal, pp. 72-81 (Apr 1975).

27. Boswell, R.J., et al., "Experimental Spindle Torque and Open Water Performance of Two Skewed Controllable-Pitch Propellers," DTNSRDC Report 4753 (Dec 1975).

28. Caster, E.B., et al., "A Lifting-Line Computer Program for Preliminary Design of Propellers," DTNSRDC Report SPD-595-01 (Nov 1975).

29. Kerwin, J.E., "Computer Techniques for Propeller Blade Section Design," Proceedings of the Second LIPS Propeller Symposium, Drunen, Holland, Vol. 1, pp. 7-31 (May 1973); also, International Shipbuilding Progress, Vol. 20, No. 227, pp. 227-251 (Jul 1973).

30. Brockett, T., "Steady Two-Dimensional Pressure Distributions on Arbitrary Profiles," David Taylor Model Basin Report 1821 (Oct 1965).

31. Meyne, K., "Untersuchung der Propellergrenzschichtströmung und der Einfluss der Reibung auf die Propellerkenngrössen (Investigation of Propeller Boundary Layer Flow and Friction Effect on Propeller Characteristics)," Jahrbuch der Schiffbautechnischen Gesellschaft 66, 317 (1972); also DTNSRDC Translation 352 (Sep 1980).

32. McCarthy, J.H., "On the Calculation of Thrust and Torque Fluctuations of Propellers in Nonuniform Wake Flow," David Taylor Model Basin Report 1533 (Oct 1961).

33. Tsakonas, S., et al., "An Exact Linear Lifting Surface Theory for Marine Propellers in a Nonuniform Flow Field," Journal of Ship Research, Vol. 17, No. 4, pp. 196-207 (Dec 1974).

34. Tsakonas, S., et al., "Documentation of a Computer Program for the Pressure Distribution, Forces and Moments on Ship Propellers in Hull Wakes," Stevens Institute of Technology, Davidson Laboratory Report SIT-DL-76-1863, in Four Volumes (Jan 1976), Revised (Apr 1977).

35. Kerwin, J.E. and C.S. Lee, "Prediction of Steady and Unsteady Marine Propeller Performance by Numerical Lifting Surface Theory," Transactions, The Society of Naval Architects and Marine Engineers, Vol. 86, pp. 218-253 (1978).

INITIAL DISTRIBUTION

Copies	
1	ARMY CHIEF OF RES & DIV
1	ARMY ENGR R&D LAB
2	CHONR
	1 Code 438
	1 Lib
1	NRL
4	ONR BOSTON
4	ONR CHICAGO
4	ONR LONDON, ENGLAND
2	USNA
	1 Lib
	1 JOHNSON
1	NAVPGSCOL/Lib
1	NROTC & NAVADMINU, MIT
1	NADC
5	NOSC
	1 1311 Lib
	1 6005
	1 13111 Lib
	1 2501/HOYT
	1 NELSON
1	NWC
38	NAVSEA
	1 SEA 032
	1 SEA 0321
	1 SEA 03D
	1 SEA 052
	3 SEA 0521
	1 SEA 0522
	3 SEA 0524
	1 SEA 0525
	3 SEA 05D
	3 SEA 05H
	5 SEA 05R
	1 SEA 52P
	1 PMS-378
	1 PMS-380
	1 PMS-381
	1 PMS-383
	1 PMS-389
	1 PMS-391
	1 PMS-392
	1 PMS-393
	1 PMS-397
	1 PMS-399
	1 PMS-400
	1 SEA TECH REP BATH, ENGLAND
	2 DET NORFOLK (SEC 6660)
1	FAC 032C
1	MILITARY SEALIFT COMMAND (M-4EX)
1	NAVSHIPYD/PTSMH
1	NAVSHIPYD/PHILA
1	NAVSHIPYD/NORVA
1	NAVSHIPYD/CHASN
1	NAVSHIPYD/LBEACH
1	NAVSHIPYD/MARE
1	NAVSHIPYD/PUGET
1	NAVSHIPYD/PEARL
12	DTIC
2	HQS COGARD
1	US COAST GUARD (G-ENE-4A)
1	LC/SCI & TECH DIV

Copies

8 MARAD
- 1 DIV SHIP DES
- 1 COORD RES
- 1 SCHUBERT
- 1 FALLS
- 1 DASHNAW
- 1 HAMMER
- 1 LASKY
- 1 SIEBOLD

2 MMA
- 1 Lib
- 1 MARITIME RES CEN

2 NASA STIF
- 1 DIR RES

1 NSF ENGR DIV Lib

1 DOT Lib

1 U BRIDGEPORT/URAM

2 U CAL BERKELY/DEPT NAME
- 1 NAME Lib
- 1 WEBSTER

1 U CAL SAN DIEGO/ELLIS

2 UC SCRIPPS
- 1 TECHNICAL Lib
- 1 POLLACK

1 U MARYLAND/GLEN MARTIN INST

4 CIT
- 1 AERO Lib
- 1 ACOSTA
- 1 PLESSET
- 1 WU

1 CATHOLIC U

1 COLORADO STATE U/ALBERTSON

1 U CONNECTICUT/SCOTTRON

1 CORNELL U/SEARS

1 FLORIDA ATLANTIC U OE LIB

Copies

3 HARVARD U
- 1 MCKAY Lib
- 1 BIRKOFF
- 1 CARRIER

2 U HAWAII/BRETSCHNEIDER

1 U ILLINOIS/ROBERTSON

8 U MICHIGAN
- 1 NAME Lib
- 1 NAME/COUCH
- 1 DEPT/HAMMITT
- 1 NAME/OGILVIE
- 1 WILLOW RUN LABS
- 1 NAME/VORUS
- 1 NAME/PARSONS
- 1 NAME/LATORRE

2 U IOWA
- 1 IHR/KENNEDY
- 1 IHR/LANDWEBER

2 JOHNS HOPKINS U
- 1 PHILLIPS
- 1 ISNT COOP RES

1 U KANSAS CIV ENGR LIB

1 KANSAS ST U ENGR EXP/Lib

1 LEHIGH U FRITZ ENGR LAB/Lib

5 ORI, INC.
- 2 KIM
- 1 SCHNEIDER
- 1 WILLIAMS
- 1 KOBAYASHI

7 MIT
- 1 BARKER ENGR LIB
- 2 OCEAN ENGR/KERWIN
- 1 OCEAN ENGR/LEEHEY
- 1 OCEAN ENGR/NEWMAN
- 1 OCEAN ENGR/BURKE
- 1 OCEAN ENGR/VAN HOUTON

Copies	
3	U MINNESOTA SAFHL 1 KILLEN 1 SONG 1 WETZEL
1	U MISSISSIPPI, M.E. DEPT/FOX
2	STATE U MARITIME COLL S U ARL LIB 1 ENGR DEPT 1 INST MATH SCI
1	U NEBRASKA, M.E. DEPT/PETERS
1	NOTRE DAME ENGR/Lib
6	PENN STATE U ARL 1 Lib 1 PARKIN 1 HENDERSON 1 GEARHART 1 MCBRIDE 1 THOMPSON
1	PRINCETON U/MELLOR
1	RENSSHLAER/DEPT MATH
1	FLORIDA STATE/OCEAN ENGR
1	ST JOHNS U
3	SWRI 1 APPLIED MECH REVIEW 1 ABRAMSON 1 BURNSIDE
1	BOEING ADV AMR SYS DIV
2	BOLT BERANEK AND NEWMAN 1 BROWN 1 JACKSON
1	BREWER ENGR LAB
1	CALSPAN, INC/RITTER
1	STANDFORD U/ASHLEY
1	STANDFORD RES INST/Lib

Copies	
5	SIT DAVIDSON LAB 1 Lib 1 BRESLIN 1 TSAKONAS
1	TEXAS U ARL/Lib
1	UTAH STATE U/JEPPSON
3	WEBB INST 1 Lib 1 WARD 1 HADLER
1	WHOI OCEAN ENGR DEPT
1	WPI ALDEN HYDR LAB/Lib
1	ASME/RES COMM INFO
1	ASNE
1	SNAME
1	AERO JET GENERAL/Lib
1	ALLIS CHALMERS, YORK, PA
1	AVCO LYCOMING
1	BAKER MANUFACTURING
2	BATH IRON WORKS CORP 1 HANSEN 1 FFG PROJECT OFFICE
1	BETHLEHEM STEEL SPARROWS
3	BIRD-JOHNSON CO 1 CASE 1 RIDLEY 1 NORTON
2	DOUGLAS AIRCRAFT 1 TECHNICAL Lib 1 SMITH
2	EXXON RES DIV 1 Lib 1 FITZGERALD

Copies	
1	FRIEDE & GOLDMAN/MICHEL
1	GEN DYN CONVAIR/ASW-MARINE SCIENCES
3	GIBBS & COX 1 TECHNICAL Lib 1 OSLON 1 CAPT NELSON
1	GRUMMAN AEROSPACE/CARL
3	HYDRONAUTICS 1 ETTER 1 SCHERRER 1 Lib
1	INGALLS SHIPBUILDING
1	INST FOR DEFENSE ANAL
1	LITTLETON R & ENGR CORP/REED
1	LITTON INDUSTRIES
1	LOCKHEED/WAID
1	MARITECH, INC./VASSILOPOULIS
2	HYDRODYNAMICS RESEARCH ASSOCIATES, INC. 1 COX 1 VALENTINE
1	NATIONAL STEEL & SHIPBLDG
2	NEWPORT NEWS SHIPBLDG 1 Lib 1 BORDEAUX
1	NIELSEN ENGR/SPANGLER
1	HYDROMECHANICS, INC./KAPLIN
1	NAR SPACE/UJIHARA
1	PROPULSION DYNAMICS, INC.
1	PROPULSION SYSTEMS, INC.

Copies	
1	SCIENCE APPLICATIONS, INC./STERN
1	GEORGE G. SHARP
1	SPERRY SYS MGMT LIB/SHAPIRO
2	SUN SHIPBLDG 1 Lib 1 NEILSON
1	ROBERT TAGGART
1	TETRA TECH PASADENA/CHAPKIS
1	TRACOR
1	UA HAMILTON STANDARD/CORNELL

CENTER DISTRIBUTION

Copies	Code	Name
1	11	Ellsworth
1	1102.1	Nakonechny
1	15	Morgan
1	1509	Powell
1	152	Lin
1	1521	Pien
1	1521	Reed
1	1522	Dobay
1	1522	Jenkins
1	1522	Wilson
1	1522	Thomason
1	154	McCarthy
1	1542	Huang
1	1542	Shen
1	1543	Cumming
1	1543	Santore
1	1543	Wisler
1	1543	Jeffers
1	1544	Brockett
1	1544	Boswell
30	1544	Jessup

Copies	Code	Name
1	172	Krenzke
1	1720.6	Rockwell
1	19	Sevik
1	19	Strasberg
1	1903	Chertock
1	1962	Zaloumis
1	1962	Noonan
1	2814	Czyryca
30	5211.1	Reports Distribution
1	522.1	Unclassified Library (C)
1	522.2	Unclassified Library (A)

*U.S GOVERNMENT PRINTING OFFICE:1982 361-334/536 1-3

DTNSRDC ISSUES THREE TYPES OF REPORTS

1. DTNSRDC REPORTS, A FORMAL SERIES, CONTAIN INFORMATION OF PERMANENT TECHNICAL VALUE. THEY CARRY A CONSECUTIVE NUMERICAL IDENTIFICATION REGARDLESS OF THEIR CLASSIFICATION OR THE ORIGINATING DEPARTMENT.

2. DEPARTMENTAL REPORTS, A SEMIFORMAL SERIES, CONTAIN INFORMATION OF A PRELIMINARY, TEMPORARY, OR PROPRIETARY NATURE OR OF LIMITED INTEREST OR SIGNIFICANCE. THEY CARRY A DEPARTMENTAL ALPHANUMERICAL IDENTIFICATION.

3. TECHNICAL MEMORANDA, AN INFORMAL SERIES, CONTAIN TECHNICAL DOCUMENTATION OF LIMITED USE AND INTEREST. THEY ARE PRIMARILY WORKING PAPERS INTENDED FOR INTERNAL USE. THEY CARRY AN IDENTIFYING NUMBER WHICH INDICATES THEIR TYPE AND THE NUMERICAL CODE OF THE ORIGINATING DEPARTMENT. ANY DISTRIBUTION OUTSIDE DTNSRDC MUST BE APPROVED BY THE HEAD OF THE ORIGINATING DEPARTMENT ON A CASE-BY-CASE BASIS.